A Data-Mining Framework for Uncertainty Analysis in Pipeline Erosion Modeling

By

Wei Dai

A dissertation submitted to the Graduate Faculty of
Auburn University
in partial fulfillment of the
requirements for the Degree of
Doctor of Philosophy

Auburn, Alabama
August 4, 2018

Keywords: Erosion, Uncertainty Quantification, Dimensional Analysis, Gaussian Process Modeling, Data Mining, Machine Learning.

Approved by

Selen Cremaschi, Chair and B. Redd Associate Professor of Chemical Engineering
Mario R. Eden, Joe T. and Billie Carole McMillan Professor of Chemical Engineering
Jin Wang, Walt and Virginia Woltosz Endowed Professor of Chemical Engineering
Qinghua He, Associate Professor of Chemical Engineering
Haijing Gao, Facilities Engineer of Chevron Energy Technology Company

ABSTRACT

The transport of solids in multiphase flows is common practice in energy industries due to the unavoidable extraction of solids from oil and gas bearing reservoirs either from onshore or offshore sites. The safe and efficient operation requires reliable estimates of erosion happening in the pipelines. The phenomenon that leads to erosion, especially in multiphase flow systems, is very complex and depends on many factors including the fluid and solid characteristics, the pipeline material properties, and the geometry of the flow lines. Semi-mechanistic models have been developed to quantify the erosion rate within pipelines that transport solids in both single-phase and multiphase flows. However, due to the process complexity, most of the developed models tend to have large model uncertainties, even in interpolated regions, and fail to provide an accurate estimates of confidence levels of their predictions based on sound uncertainty analysis.

The overall goal of this dissertation is to develop uncertainty quantification and propagation approaches for multiphase flow model predictions focusing on cases where solids are present in the system. Three sources of uncertainty identified and implemented are model form uncertainty, input uncertainty, and experimental data uncertainty. The first two uncertainties are resolved based on the Gaussian Process Modeling (GPM) framework, where data clustering, data transformation and dimensional analysis are applied to enhance the prediction reliability. For data uncertainty, a unique approach to estimate and combine variable-dependent data uncertainty is proposed.

The proposed framework is applied to one commonly used erosion model. Uncertainty of the model, which spans six orders of magnitude has been accurately captured by the framework. By using a novel clustering approach, prediction accuracy has been further enhanced according to grouping data from a wide spread of operating conditions. The physical explanation for regions that lead to high uncertainty has also been investigated using the dimensionless numbers obtained from dimensional analysis.

The methodology developed as a result of this dissertation can be applied to uncertainty analysis for other erosion models. For given operating conditions, uncertainty of erosion predictions can be obtained together with confidence intervals. The uncertainty analysis can be used as a guideline for field production and future research on erosion process.

ACKNOWLEDFEMENTS

First of all, I would like to thank my advisor, Dr. Selen Cremaschi, for her dedicated and professional guidance and support since my graduate study. I learn and grow a lot from her mentorship. Her enthusiasm in work is incredibly contagious and I feel deeply honored to be her doctoral student.

I would also express my gratitude to my committee members, Dr. Mario Eden, Dr. Jin Wang, Dr. Qinghua He and Dr. Haijing Gao, for their continuous guidance throughout my research work. I would also express my sincere appreciation to my dissertation reader, Dr. Daniel Silva.

Finance support from NSF CAREER Award #1623417, and Chevron Energy Technology Company are highly acknowledged. Without their continuous support and trust, I cannot finish my degree.

I would also like to thank my lab mates from Auburn University and the University of Tulsa, it was great time to spend with all of you.

Finally, my deep thanks go to my friends and family. This adventure is not lonely with all your support and encouragement.

TABLE OF CONTENTS

LIST OF TABLES

LIST OF FIGURES

LIST OF SYMBOLS

μ_w	water viscosity (cp)
μ_g	gas viscosity (cp)
ρ_w	water density (kg/m^3)
ρ_g	gas density (kg/m^3)
ρ_p	density of sand particles (kg/m^3)
d_p	particle size (µm)
D	pipe diameter (inch)
v_w	water velocity (m/s)
v_g	gas velocity (m/s)
h_B	pipeline hardness
g	gravitation constant
σ	surface tension
θ	inclination of pipe
C	concentration of particle
f_s	coefficient of static friction
sf_s	particle sharpness factor

LIST OF ABBREVATIONS

ANG	Angle of measurement
AS	Aluminum specimens
CFD	Computational Fluid Dynamics
DI	Direct Impingement
ER	ER Probe
ERR	Erosion Rate
EXP	Experimenters
FPR	False Positive Rate
GEO	Geometry
GP	Gaussian Process
GPM	Gaussian Process Modeling
HOR	Horizontal to Horizontal Orientation
MA	Measurement Approach
PO	Pipe Orientation
NA	Not Available
NLML	Negative Log Marginal Likelihood
TPR	True Positive Rate
UTL	Ultrasonic Thickness Loss
UT	Ultrasonic Technique
VER	Vertical to Horizontal Orientation
WL	Weight Loss Measurement

CHAPTER 1

INTRODUCTION

1.1 Uncertainty Quantification

Uncertainty analysis is a critical step in modeling a physical process. When developing models, information on the data reliability, model uncertainty and assumptions of model parameters should be provided as these factors have been shown essential for uncertainty quantification. However, this type of information is normally scarce due to limited understanding of the process being modeled or inadequate data collection.

The uncertainty in model predictions stems from three sources in general: (1) model form uncertainty (i.e., incomplete presentation of the actual system due to lack of knowledge or imprecise experimental observations), (2) uncertainty in experimental measurements of both input conditions and observations, and (3) model parameter uncertainty [1]. The experimental data uncertainty usually consists of measurement errors due to both instrumental and human errors. The reliability of the models largely depends on the ability of the model form to capture the details of the process being modeled in enough granularity. The uncertainty in the model parameters results from an inability to measure or understand certain factors in the process accurately [2].

1.2 Challenges and motivations

In multiphase transportation, sand particles extracted during production from oil and gas reservoirs can cause significant erosion damage to the pipelines. Erosion in pipelines is defined as the material removal from the inner surface of the pipeline due to solid particle impingement. This phenomenon, especially in multiphase flow systems, is very complex and depends on many factors including fluid and solid characteristics, the pipeline material properties and the geometry of the flow lines. The safe and efficient operation and design of these pipelines requires reliable estimates of erosion rates.

Given the complexity, most of the modeling work focuses on developing empirical or semi-mechanistic models to predict erosion rates. For example, Oka et al. [3] developed their erosion model using particle impingement in air with empirical constants based on particle properties and hardness of the target materials. Their model is one of the most commonly cited models in the literature. Another semi-mechanistic model [4], which is widely used for predicting erosion rates by the oil and gas industry, was developed with several empirically estimated parameters, like the sharpness factor of particles, Brinell hardness and the empirical constants in the impact angle function. These empirical parameters are calculated using experimental observations. However, the experimental data used in these calculations and for model validation and uncertainty quantification are, for the most part, collected in small pipe diameters (from 2 to 4 inches). These small pipe sizes do not coincide with the field conditions, where the pipe diameters generally exceed 8 inches. Hence, the predictions of erosion models are routinely extrapolated to conditions where experimental data or even operating experience is not available, and the estimation of erosion-rate prediction uncertainty becomes crucial for offshore deep-water production due to the limited access to fields. The quantification of this uncertainty is especially

important during the design phase for subsea applications, as erosion rate allowance, which is set using the erosion rate predictions and its uncertainty, directly impacts the integrity of the designed facility.

To evaluate the model uncertainty, we collected a database from literature reviews. Due to the number of factors affecting the scale of erosion rate and tremendous changes in the operating conditions, within our database, the measured erosion rate ranges over six orders of magnitude. To use this set of data for uncertainty quantification and model validation, a single model might not be complex and reliable enough for all the considered conditions. Special data preprocessing, separation and model partition should be applied to develop models more representative under certain input regions. However, question remains on the generality capability of the models, especially for uncertainty estimation in the extrapolated regions while securing their prediction performance at the same time.

1.3 Scope and Objectives

In this work, a systematic framework is introduced to quantify erosion-rate prediction uncertainty for operating conditions where experimental data are scares or not available. The uncertainties considered from the overall model predictions are:

(1) Model form uncertainty,

(2) Input uncertainty, and

(3) Experimental data uncertainty.

This work will investigate the impact of all these components on the overall erosion-rate model prediction, and develop tools and algorithms to incorporate these uncertainties for generating confidence intervals of the erosion model predictions.

More specifically, the planned project activities are:

(1) Collect publicly available experimental data regarding erosion rate,

(2) Develop novel approaches to quantify experimental data uncertainty when experimental repetitions are not available,

(3) Estimate model prediction discrepancy and its confidence interval using Gaussian process modeling incorporating experimental uncertainty,

(4) Investigate strategies to reduce model prediction discrepancy and its confidence interval which include:

    a. Novel data clustering approaches,

    b. Established and new data transformation methods,

    c. Model evaluation techniques,

(5) Generate model prediction and its confidence interval that considers the impact of model discrepancy and experimental data uncertainty,

(6) Incorporate the impact of input condition uncertainty on the model prediction confidence interval,

(7) Investigate the feasibility of using dimensionless numbers as the input variables in the Gaussian process modeling to extend the applicable range uncertainty estimates,

(8) Compile the methodology in a tool and develop a user interface.

1.4 Significance of the Research

The United States has the world's largest network of energy pipelines with approximately 72,000 miles of crude oil lines. Sand particles transported together with the flow is an unplanned event and it is nearly impossible to fully get rid of those particles with filtration equipment or chemical inhibitors which are commonly used approaches to

remove the sand particles produced. If the erosion prediction fails, it may have adverse environment impacts due to unexpected pipeline rapture, may lead to lost production and high repair costs. Our observations show that for the same operating condition, the most commonly used erosion models can give predictions spanning several orders of magnitude. Therefore, the reliability of these models' predictions should be estimated. Uncertainty quantification approaches should be applied to reduce the model prediction uncertainty at laboratory conditions. Furthermore, uncertainty quantification approaches should also help people to understand and estimate uncertainty when models are extrapolated to conditions where experimental data is scarce or not available. This is often the case for very remote operations such as deep-water applications, where information on pressure, fluid properties, pipe sizes, and other operating conditions may be scarce or unavailable.

1.5 Organization

CHAPTER 2 provides the general theoretical background on the erosion phenomena and the modeling development. Section 2.2 introduces the development of erosion modeling from empirical view to semi-empirical scheme, and to computational fluid dynamics (CFD) simulation based approaches. To calculate the model prediction discrepancy and validate the model's capability in uncertainty quantification, a database covered a large range of operating conditions is introduced in section 2.3. Section 2.4 discusses in detail one selected erosion-rate prediction model used for elaborating methodologies developed for uncertainty quantification in this dissertation.

In CHAPTER 3, we define the three main sources of uncertainty in models and the approaches to deal with each uncertainty source. The model form uncertainty, due to the lack of knowledge in mimicking the reality, is visited in section 3.2. Surrogate modeling

approaches are introduced, and Gaussian process modeling is utilized to quantify the model form uncertainty in erosion-rate prediction. The second type of uncertainty is the input uncertainty and will be discussed in section 3.3. Section 3.4 introduces a novel approach to quantify data uncertainty without repeated measurements. Due to the cost in conducting erosion experiments, most measurements, even under lab conditions, are not repeated for more than three times. Considering this situation, traditional statistical approaches to quantify the measurement uncertainty is not applicable. Therefore, we come up with a new approach considering the characteristics of the data points collected. This approach yields experimental data uncertainty estimates for four commonly used erosion measurement approaches.

CHAPTER 4 elaborates the details of implementing the Gaussian process modeling for model uncertainty quantification. The basic theories of Gaussian process modeling (GPM) are discussed in section 4.2. Gaussian process modeling as a Bayesian approach, relies on the selection of kernel functions and the hyperparameters in the kernel functions (section 4.3). Section 4.4 introduces two criteria to assess the quality of GPM predictions. Gaussian Process models are then developed with two different clustering approaches where the novel clustering approach shows better performance as illustrated in section 4.5. A Gaussian process classification approach is introduced in section 4.6 to further improve the model form uncertainty estimates. To achieve prediction accuracy and reliability at the same time, a bi-objective optimization approach is implemented in section 4.7.

To extend the applicability of uncertainty estimates based on GPM, especially to untested regions, dimensional analysis is conducted and introduced in CHAPTER 5. The procedure for applying dimensional analysis and forming dimensionless numbers are

illustrated in detail in section 5.2. The framework of uncertainty analysis with dimensionless numbers as the input to GPM is given in section 5.3. To obtain the dimensionless group with the highest correlation to the model discrepancy, a feature selection analysis is implemented and discussed in section 5.4. Gaussian Process models with the selected dimensionless groups as the candidate inputs are developed. Section 5.6 shows improved results in combining dimensional analysis with Gaussian Process modeling for quantifying erosion model uncertainty.

Conclusions and future work for extending the analyses introduced in this dissertation are given in CHAPTER 6. The proposed work is to locate the regions with high uncertainty based on all the conducted analyses and the obtained results. As a result, specific suggestions for aiding future erosion experimental design and modeling are proposed for future work.

CHAPTER 2

EROSION PROCESS

In this chapter, theoretical background on erosion phenomenon and development of erosion models are discussed along with the erosion experimental database constructed for developing uncertainty estimation approaches. One of the most commonly used erosion prediction models is introduced and used for the erosion-rate predictions.

2.1 The Complexity of Erosion Process

The solid transport and management system (STMS) is an important component of production systems for energy industry because of the unavoidable extraction of solids from oil and gas bearing reservoirs either onshore or offshore sites [5,6]. In STMS, one of the integral design and operational decisions is the maximum fluid flow rate [7,8]. If the amount and velocity of the solids traveling with the fluids (oil, water and gas) in the transportation lines are too high, they might cause erosion in the pipelines resulting in facility integrity issues [9]. The erosion risks can result in high operation costs for repairing pipelines and equipment, especially for offshore deep-water production due to the limited access to fields.

The erosion process, especially in conduits with multiphase flows, is a complex phenomenon. It depends on many factors including fluid characteristic, solid characteristics, the construction material properties, and the geometry of the flow lines

[10,11]. Given this complexity, most of the modeling work in this area focuses on developing empirical or semi-empirical models.

2.2 Modeling of Erosion in Pipeline Transportation

The American Petroleum Institute Recommended Practice 14E [12] provided a guideline for the calculation of threshold erosional velocity, the velocity above which erosion will occur, using a simple relation. Salama and Venkatech [13] proposed an empirical model as an improvement of the erosional velocity prediction based on API RP 14 E. This empirical model is shown to be accurate for predicting erosion-rate for gas-solid flows in elbows and tees. Bourgoyne [14] developed an empirical model that predicts thickness loss using an empirical "specific erosion factor" which was only valid for limited flow properties and pipe geometries at single phase and gas-mist flow conditions. Additionally, the model did not consider the impacts of sand hardness and flow viscosity. Salama [8] expanded the Salama and Venkatech [13] model to multiphase flows using mixture density and velocity of the liquid and gas phases. Ahlert's [15] from the Erosion/Corrosion Research Center (E/CRC) at the University of Tulsa proposed an exponential relation of the erosion ratio to the particle impact velocity under different impingement angles, where the erosion ratio was defined as the mass loss of the material divided by the total mass of the solid particles entrained in the fluid. McLaury et al. [7] extended Ahlert's [15] empirical erosion model to account for the maximum penetration rate that represented the thickness loss for a unit time (also referred as erosion rate). They introduced the "equivalent stagnation length" to calculate the particle impact velocity considering both flow stream velocity and pipe geometry type and diameter. With the introduction of computational fluid dynamics (CFD) methods, the simulation of fluids in

dynamic state became possible. Thus, the multiphase flow modeling and trajectory of particles in the flow were included in the erosion predictions. Edwards et al. [16] applied a commercial CFD simulator (CFX, [17]) to model fluid-solid flows and incorporated a stochastic rebound model to simulate particle rebound behavior to improve the particle impact trajectories. They also studied the effect of near-wall fluid on the particles' impingement, as the particles must pass through the fluid layer near the wall to cause the impingement. Wang and Shirazi [18] came up with a CFD based correlation to extend erosion calculations to non-common geometries, e.g. the long radius elbows. Zhang et al. [19] performed several CFD-based erosion predictions where the particle trajectories were validated against experimental data recorded using laser diagnostics. They also investigated particle motion in the near-wall region, and the results revealed that, for turbulent flow in a 90° bend, the near-wall particle size effect and turbulent particle interactions play a significant role in the scale of erosion rate [20].

The brief discussion of models for predicting erosion rate highlights that: (1) even the most complex mechanistic or semi-mechanistic model may not be general enough to accurately predict erosion rates under all flow conditions due to the complexity of the multiphase flow behavior coupled with particle movement, and hence requiring model simplifications and reliance on empirical constants [21], and that (2) the accurate modeling of particle impact trajectories and velocities is crucial to precise erosion predictions [22]. Meng and Ludema's critical review [10] of 28 sand–wall erosion models where they went through 33 basic and general parameters and summarized the mechanical relations in erosion process also emphasized the modeling complexity and the limitations of using empirical parameters. Several studies compared different erosion models under the same

operating condition, and they have observed large prediction mismatches in those models. Zhang and Liu [23] compared the erosion-rate predictions of four erosion models (SPPS 2D [19], DNV [24], Oka et al. [3] and Grant and Tabakoff [25]) in single-phase carrier-fluid conditions. The results revealed that for the same input set, Oka et al. [3] tends to over-predict the erosion rate while results from SPPS 2D [19], DNV [26] and Grant and Tabakoff [25] models are less conservative. Arabnejad et al. [11] compared four empirical and semi-mechanistic models (SPPS 1D [27], SPPS 2D [19], DNV [24] and Salama [8]) to predict erosion rate in multiphase flow. The analysis showed that, for certain operating conditions, the predictions of Salama's [8] model was 50 times greater than the predictions of SPPS 2D [19], while SPPS 1D model was less conservative and DNV model even under predicted most of the data. A similar mismatch in model predictions was observed by Parsi et al. [28]. They observed that, on average, the maximum erosion prediction is about 20 times the minimum prediction. Similarly, the comparison of SPPS 1D predictions and the experimental data in our previous work [27] revealed that the predictions may be up to three orders of magnitude higher (resulting in considerable overdesign) for some input sets and up to one order of magnitude lower (causing facility integrity issues) for others. It is hypothesized that these discrepancies are mostly due to the model form uncertainty in erosion models considering the simplifications and assumptions in model development. However, none of the existing models includes a comprehensive uncertainty analysis.

2.2.1 Factors Important to Erosion-Rate Predictions

The following factors are important to the quantification of erosion happened in the pipeline transportation:

- Pipeline material, geometry and orientation

- Particle properties
- Flow conditions

Based on these factors, we collected experimental data from open literature and build a database using which the capability of uncertainty estimation framework developed in this dissertation is validated. One of the commonly used erosion prediction models is selected to predict erosion rates. The details of this model are given in section 2.4.

2.3 Data Collection

Approximately 700 experimental erosion rate measurements in single or multiphase flows with detailed operating conditions from open literature have been collected. Table 2.1 lists the sources, and the ranges of operating conditions and resulting erosion rates for these experimental data. The independent variables are geometry and diameter of the pipe (D), hardness of the pipe material (h_B), particle size (d_p) and rate, densities and viscosities of the liquid (ρ_l, μ_l) and gas (ρ_g, μ_g), and liquid (V_{sl}) and gas superficial flow rates (V_{sg}). The dependent variable is the measured erosion rate (experimental ER), and it is provided in mils/lb units. The database also includes the approach used to measure erosion rate, flow orientation and particle impingement angle, if provided by the experimenters. Most of the experiments were conducted by E/CRC and used the following particle types: Silica Flour, Oklahoma #1, and California 60 Mesh with average particle sizes of 20 µm, 150 µm, and 300 µm, respectively. Most data were collected at elbow geometry with pipe diameters ranging from one to four inches. The liquid viscosities are {1, 10, 20, 40} cp. The superficial gas velocities range from five to 200 m/s, however experimental data at higher

gas velocities (>100 m/s) are limited. The superficial liquid velocities are between 0.0001 to 1.0 m/s.

Table 2.1: Summary of database (sorted by year)

Experimenters	Measurement Approach	Geometry	D (inch)	h_B (vicker)	d_p (μm)	ρ_g (kg/m^3)	V_{sg} (m/s)	μ_l (cp)	V_{sl} (m/s)	Erosion rate (mils/lb)
Bikbaev [29]	NA[1]	Long elbow	2	120	295	1	33-54	0	0	1×10^{-1}-5×10^{-1}
Tolle et al. [30]	WL[2]	Elbow	2	109	300	1	9-30	0	0	4×10^{-2}-4×10^{-1}
Bourgoyne [14]	UTL[3]	Long elbow	2	120, 140	350	1	32-222	1	1×10^{-1}-14	8×10^{-6}-5
Salama [31]	NA[1]	Elbow	1, 2	160, 330	150, 250	2, 10	8-52	1	2×10^{-1}-6	2×10^{-4}-2×10^{-1}
Antezana [32]	ER[4]	Elbow & Tee	1	330	150	4	15-30	1	1×10^{-1}-3×10^{-1}	6×10^{-4}-1×10^{-2}
Mazumder [4]	AS[5]	Elbow	1	230	150	1	10-34	1	3×10^{-2}-3×10^{-1}	2×10^{-4}-1×10^{-1}
Evans [33]	ER[4]	Long elbow	4	222	150	46	23-63	0	0	2×10^{-4}-7×10^{-3}
Reuterfors [34]	ER[4]	DI[6]	0.315	330	20, 150	1	0	1	2-10	1×10^{-4}-2×10^{-3}
Pyboyina [35]	ER[4]	Elbow & Tee	1, 2	90, 123	150	3	19-34	1	3×10^{-2}-3×10^{-1}	1×10^{-3}-1×10^{-1}
Nuguri [36]	ER[4]	Elbow	2	330	150, 300	1	24-58	1	3×10^{-4}-3×10^{-1}	1×10^{-3}-6×10^{-2}
Dosila [37]	ER[4]	Elbow	2	330	150, 300	1	29	1, 10	3×10^{-4}-2×10^{-1}	9×10^{-4}-7×10^{-2}
Rodriguez [38]	Angle-head ER[4]	Elbow	3	330	20, 300	1	15-45	10, 40	4×10^{-1}-8×10^{-1}	8×10^{-6}-4×10^{-3}
Zhang [20]	ER[4]	DI	0.315	330	150	1	0	1	3-10	2×10^{-5}-2×10^{-3}
Fan [39]	ER[4]	Elbow	4	330	150, 300	1	15-23	1	4×10^{-3}-8×10^{-2}	5×10^{-5}-6×10^{-3}
Throneberry [40]	Angle-head ER[4]	Elbow	3	330	150, 300	1	15-45	20, 40	4×10^{-1}-8×10^{-1}	3×10^{-5}-8×10^{-3}
Kesana [41]	ER[4] & UT[7]	Elbow	3	230	20, 150	1	15-48	1, 10	4×10^{-1}-8×10^{-1}	8×10^{-6}-4×10^{-2}
Vieira [42]	UT[7]	Elbow	3	230	150, 300	1	11-49	1	4×10^{-3}-2×10^{-1}	4×10^{-5}-5×10^{-2}

[1] Not available
[2] Weight loss measurement
[3] Ultrasonic thickness loss
[4] ER Probe
[5] Aluminum specimens
[6] Direct impingement
[7] Ultrasonic Technique

The data is preprocessed to consolidate erosion-rate measurement discrepancies because Gaussian Process modeling is prone to ill-conditioning as the distances between its training points decrease. The training points with the same or very similar independent

variable values and different dependent variable values result in linearly-dependent equations and cause instability in the predictions of Gaussian Process modeling [43]. The following steps avoid that the training points overlap with each other:

(1) For experiments performed at identical operating conditions, the average of the erosion rate measurements is used as the dependent variable value.

(2) For data points with the same operating conditions except flow orientation, the erosion rate from vertical orientation is selected because the erosion-rate prediction model used in this dissertation for demonstrating our approaches was developed for predicting maximum erosion rate under vertical orientation.

(3) For data points that have the same operating conditions except their particle flow-rates, the one with the highest measured erosion rate is kept. The fluid with a low particle flow rate has a smaller number of particles impinging the pipeline. However, due to the reduced particle concentration [20], the interaction between the particles also decreases. Thus, each particle collides the pipeline with greater momentum and causes larger thickness loss, which translates to a larger erosion rate. To represent the worst thickness loss to be caused by the two effects, the highest measured erosion rate is kept.

(4) For experiments conducted at the same conditions except their particle impingement angles, the one with the highest erosion rate is selected.

After the data preprocessing steps, the database contains 585 linearly-independent experimental data points (for more details, please refer to Table A.1 in appendix).

2.4 Overview of the Erosion-Rate Prediction Model

The Sand Production Pipe Saver in One Dimension (SPPS 1D) erosion model is extensively used in the oil and gas industry for erosion-rate predictions [19]. The model predicts maximum erosion rate given system geometry and materials, flow conditions, and particle properties [27]. It calculates the maximum erosion rate by defining how a hypothetical representative particle will impinge the target material. The abrasion caused by this particle is defined by thickness loss in the target specimen, and is calculated using the momentum of impingement. This calculation requires the so-called "characteristic impact velocity" of the representative particle. Given flow conditions, particle and pipe properties, the model first calculates the characteristic impact velocity. The erosion ratio, which is defined as the ratio of measured target material mass loss to the mass of all particles in the carrier fluid, is calculated using a power law correlation of the characteristic impact velocity. Here, the carrier fluid can be single phase (liquid or gas), or multiphase (liquid/gas mixture). The maximum erosion rate (predicted ER), which is defined as the target specimen thickness loss per particle weight, is calculated using the erosion ratio and accounts for pipe geometry, size and material; fluid properties (density and viscosity); and sand sharpness, density and rate via empirical constants. The calculation process is imbedded in a VBA-enriched Excel software. There are several versions of the software that have been developed and implemented. SPPS 1D version 5.1 is the latest version where model empirical constants have been updated based on the data collected to date. For the remainder of the dissertation, we'll refer to this set of erosion-rate prediction models as SPPS 1D version 5.1.

2.5 Prediction Comparisons

Figure 2.1 gives the comparison of the erosion-model, SPPS 1D version 5.1, predictions with the experimental erosion rates for all the data points in the database after the pre-processing step. The blue circles in Figure 2.1 represent the 585 data points collected. Both axes are plotted in logarithmic scale. The dotted line on the graph is the parity line, where data points lie above this line are over-predicted by the erosion model while below this line under-predicted. The point dotted lines show the 1000% over or under values of the model predictions. This figure clearly shows the over-predicting feature of the SPPS 1D version 5.1, as most of the data points scattered above the parity line. Comparing model predictions to observed erosion-rates reveals that the model over-predicts the erosion rates for 63% of the data points by an average of 900%. For the 37% under-predicted data points, the average is -60%. The model's predictions are widely conservative for over-predicted data points suggesting significant over-design of facilities. On the other hand, the regions where the model under-predicts may require maintenance sooner than anticipated by the original design. For either case, the model does not provide any information on prediction uncertainty or its confidence interval.

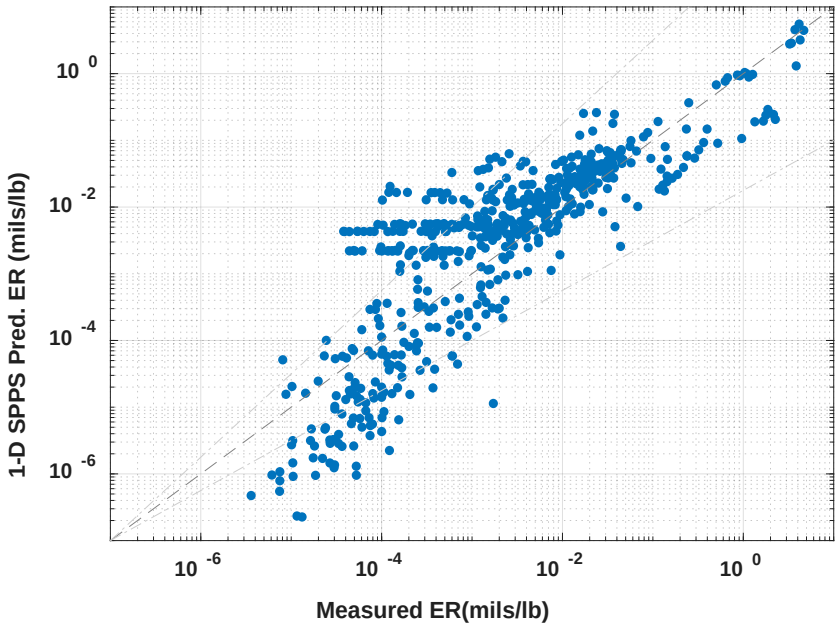

Figure 2.1: Comparison of experimental measured erosion-rate (Measured ER) to SPPS 1D version 5.1 predictions (Pred. ER)

To incorporate the impacts of flow regime on the velocity of the representative particle, SPPS 1D provides three approaches for predicting erosion rates. The first one uses a flow regime independent prediction, where a "equivalent flowstream velocity" represents the initial velocity as a mixture of gas and liquid flows. This velocity is applied to data from all the possible flow regimes [44]. The second is a flow regime dependent prediction where characteristics from multiphase flow has been considered [27]. This type of model first determines the flow regime based on a given set of input conditions, and then makes prediction for the initial velocity according to the model from consistent flow regime. The flow regime considered are: mist, annular, churn, slug, dispersed bubble, and bubbly flows. The last type of model is also flow regime dependent, but it uses the flow regime specified by the model user instead. The flow regime of a certain set of input condition can be

determined by other flow regime prediction models (like the Barnea unified model [45]) or from experimental observations.

Figure 2.2 gives the histogram of the absolute values of model discrepancy (the difference between SPPS 1D version 5.1 predictions and the corresponding experimental erosion rate measurements) for all the 585 data points (of the database) grouped based on the predicted flow regimes by the SPPS 1D version 5.1 along with the root-mean-square-error values (discussed in section 4.4). The magnitude of model discrepancy differs for the six flow regimes as both experimental measurements and model predictions tend to have large values in gas dominated flows (i.e., mist (Mi), annular (An), and churn flows). Therefore, the absolute model discrepancies in gas, mist, annular and churn flows are greater compared to the ones in slug and liquid flows.

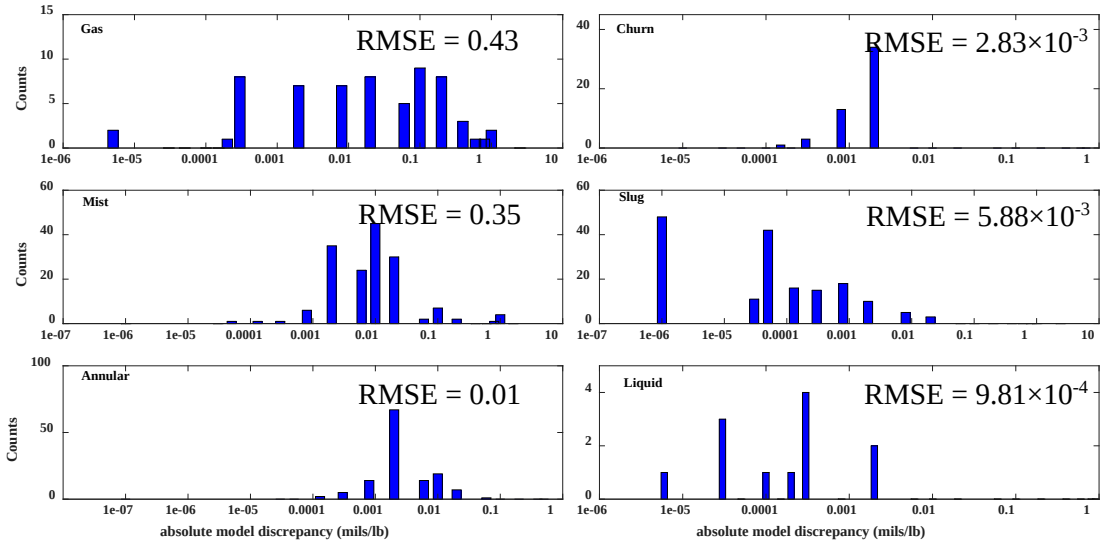

Figure 2.2: Histogram of absolute model discrepancy between SPPS 1D version 5.1 predictions and experimental data in each flow regime where the flow regimes are predicted using SPPS 1D version 5.1

We also compared the predictions of erosion rate (y^m) based on the three model types (the last model type is used only when observed flow regime is given) to experimental

measurements (y^e). The prediction error in percentage is calculated as the ratio of model discrepancy (δ) to experimental measurements in percentage.

$$Error\% = \frac{\delta}{y^e} \cdot 100\% = \frac{y^e - y^m}{y^e} \cdot 100\% \quad (2.1)$$

The mean error in percentage for the three model types is summarized in Table 2.2. Especially, the mean error in percentage is calculated for each flow regime as predicted by the second model type (flow regime dependent model). Flow regime is abbreviated as FR.

Table 2.2: Mean error in percentage for three erosion rate calculation approaches of SPPS 1D version 5.1

Mean Error%	FR Independent	FR by SPPS 1D	FR as observed
Mist	-160%	-388%	-
Annular	-344%	-1039%	-
Churn	-431%	-2154%	-
Slug	-	-	-85%

Slug flow differs from other flow regimes as it is based on experimental observation, and a special measurement approach - angle head ER probe - is used to measure erosion rates in experiments for slug flow regime [46]. The angle head ER probe is placed in the straight part of the pipeline where the flow has been fully developed. This measurement approach must be indicated as a geometry type in SPPS 1D's input and can only be combined with slug flow. Therefore, there is no FR Independent and FR by SPPS 1D predictions for data collected for this type of measurement approach. In other words, only the third approach of SPPS 1D model, where the flow regime has been specified as slug flow by the users, can give erosion-rate predictions for these data points. Therefore, we separate data under slug flow regime based on their measurement approaches, i.e., ER probe measurement approach or the angle head ER probe measurement approach.

The results based on SPPS 1D flow regime predictions generate the largest mean error in percentages. The prediction error is by average 20 times larger than the experimental measurements in churn flow. The large error might result from the inappropriate flow regime determination and flow-regime dependent erosion-rate model used in SPPS 1D. As erosion-rate prediction is sensitive to the flow regime used, the flow regime prediction based on the Barnea unified model is compared to that from SPPS 1D. Barnea unified model can predict flow regime for a given condition as stratified smooth, stratified wavy, annular, dispersed bubble, bubbly flow and slug flow. This model is applied to all the data points except for the ones that were observed experimentally to be in slug flow regime. Table 2.3 gives the predicted flow regimes as a comparison to the flow regimes predicted by SPPS 1D version 5.1. The parentheses followed by the predicted flow regimes are the number of data points.

Table 2.3: Comparison of flow regime predictions of SPPS 1D version 5.1 to Barnea unified model

Flow regime dependent on SPPS 1D	FR by Barnea model
Mist (162)	Annular (149) Stratified wavy (8) Slug (5)
Annular (129)	Annular (77) Stratified wavy (26) Slug (26)
Churn (51)	Annular (1) Stratified wavy (35) Slug (15)

It can be concluded from Table 2.3, that since Barnea model doesn't predict mist flow regime, most of data predicted as mist flow by SPPS 1D are predicted as annular flow. Forty percent of data points predicted as annular flow by SPPS 1D are either predicted as stratified wavy or slug flow. Nearly 70% of data points predicted as churn flow by SPPS

1D are not consistent with the flow-regime predictions based on Barnea model. Due to the great differences in the two models' flow-regime predictions, the predictions of erosion rates using flow-regimes predicted by from Barnea model have been calculated using the third approach of SPPS 1D version 5.1. Since SPPS 1D model does not include stratified wavy flow regime and erosion-rate predictions in this flow regime, data points predicted as stratified wavy flow by the Barnea model are treated as slug flow in the SPPS 1D. Table 2.4 gives the mean error in percentage of erosion-rate predictions calculated as outlined above.

Table 2.4: Mean error in percentage for three erosion rate calculation approaches of SPPS 1D version 5.1 and Barnea unified model

Mean Error%	FR Independent	FR by SPPS 1D	FR by Barnea model
Mist	-160%	-388%	-156%
Annular	-344%	-1039%	-284%
Churn	-431%	-2154%	97%

The erosion-rate predictions based on the Barnea model yield the smallest mean error in percentages for all three flow regimes. These results may suggest that the large model discrepancies observed in SPPS 1D may be due to the flow-regime model used in SPPS 1D version 5.1 than the flow-regime dependent erosion-rate prediction models. However, if we take a close look at the data points being predicted as stratified wavy by Barnea model, they are, in fact, all experimentally collected from horizontal to horizontal orientations of the pipeline. The remaining erosion rates are mostly measured from horizontal to vertical and vertical to horizontal orientations. The orientation separates these data points from the others and may explain the large model discrepancies observed when the SPPS 1D flow regime dependent model is used. Therefore, we repeated the previous

analysis excluding the data points from horizontal to horizontal orientation. Table 2.5 gives the results. Though the number of data points considered is decreased, the prediction errors in percentages have greatly decreased and are in general below 200%. These results suggest that the SPPS 1D version 5.1 model may not be applicable for estimating erosion rates for data points that are experimentally collected from horizontal to horizontal orientation.

Table 2.5: Mean error in percentage for three erosion rate calculation approaches of SPPS 1D version 5.1 and Barnea unified model excluding data collected from horizontal to horizontal orientation

Mean Error%	FR Independent	FR by SPPS 1D	FR by Barnea model
Mist (146)	-42%	-79%	24%
Annular (89)	-211%	-169%	-92%
Churn (16)	39%	-206%	96%

The flow-regime dependent SPPS 1D model has relatively larger prediction errors among the three approaches considered. However, to prove GPM capability in quantifying model discrepancy and to identify the most relevant dimensionless numbers for each flow regime, the flow-regime dependent SPPS 1D version 5.1 (y^m) model is used to calculate the model discrepancy for the remainder of the dissertation.

For slug flow, the model discrepancies are calculated for data collected from both the ER probe measurement approach and the angle head ER probe measurement approach. Table 2.6 gives the mean errors in percentages for the two measurement approaches. Though the angle head ER probe gives relatively larger prediction errors among the two measurement approaches, in general, the SPPS 1D version 5.1 model can be used to estimate erosion rates for data from slug flows.

Table 2.6: Mean error in percentage for the third erosion rate calculation approach of SPPS 1D version 5.1 with data observed as slug flow

Mean Error%	FR specified as slug flow in SPPS 1D
ER probe (100)	65%
Angle head ER probe (68)	-306%
All data (168)	-85%

CHAPTER 3

SOURCES OF UNCERTAINTY

3.1 Introduction

The discrepancies between experimental data and erosion-rate predictions are due to the complexity of the erosion process, and due to the models' inabilities to capture these complexities accurately. This sort of imperfection is normally categorized as the model form uncertainty. Other sources of uncertainty include the model inputs, assumptions, equations, the data used to develop the model, and the computational methods used to solve the governing equation sets [47]. Furthermore, the models are routinely extrapolated beyond their capabilities as they are originally developed and validated using data collected from bench-scale or at best pilot-scale experiments. The experiments are usually conducted at pipe diameters of one to four inches, while in field applications, the diameter of a deep-water riser, as an example, is normally greater than eight inches [42]. Few erosion models explicitly address the prediction uncertainty or discuss the model's performance when extrapolated.

Mazumder [27] developed a mechanistic model to predict erosion rates in single- and multiphase flows, and propagated the input uncertainties. The study revealed that the uncertainties in sand sizes, liquid rates and gas rates are, respectively, 21%, 6% and 4% of the total erosion-rate prediction uncertainties, and they may yield 20% to 70% uncertainty in erosion-rate predictions depending on input conditions. However, the impact of model-

form uncertainty was not considered. Zhang et al. [19] extrapolated the model developed by Oka et al. [3] to predict erosion rates caused by fine particles at low flowrates although the original model was developed for relatively large particles traveling at high flowrates. Zhang et al. [19] concluded that the model's predictions closely matched the experimentally observed erosion rates in the extrapolated regions, but the uncertainty of these predictions was not addressed. We in a previous study [48] estimated the model uncertainty of SPPS 1D version 5.1 [27] using Gaussian Process Modeling (GPM). The analysis yielded an average GPM estimate of model uncertainty that was four times the model predictions for the experimental data considered.

In the following sections, the uncertainties from input, model form, and experimental data is discussed respectively with approaches developed to estimate uncertainty from each source. Because the approaches introduced in this dissertation consider the erosion-rate prediction models as black-boxes for ease of use and implementation, the model parameter uncertainty is considered to be included in the model form uncertainty and is not addressed separately.

3.2 Model Form Uncertainty

In this section, several commonly used approaches to quantify model form uncertainty is discussed. Gaussian process method, as a machine learning approach, is shown to capture the nonlinearity of processes with its flexible structure by using kernel functions, and it can provide the distribution of the predicted model form uncertainty.

A linear correlation analysis of each input variable to the model discrepancy using the Pearson correlation analysis is conducted. The plot in Figure 3.1 shows the strength of the linear correlations between all the input variables and the model discrepancy (δ) for the

data points. It can be observed that the gas superficial velocity (V_g) and pipe hardness (H_b) have relatively strong correlations with the model discrepancy while there are no apparent linear correlations between other input variables and the outputs. Therefore, a more complex modeling approach is necessary to identify the underlying nonlinear relationships between the inputs and the output.

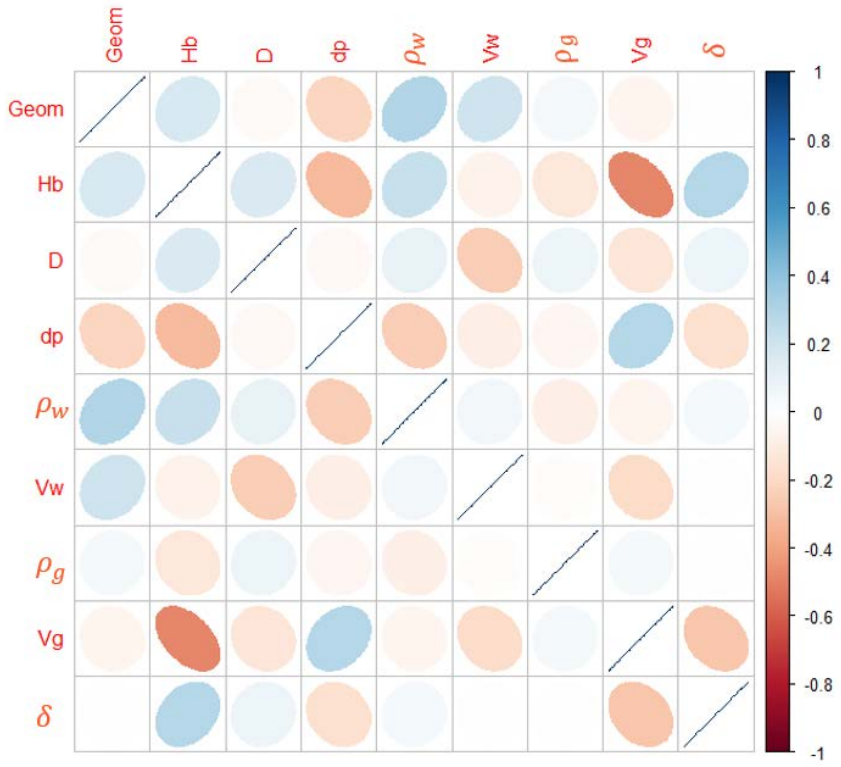

Figure 3.1: Correlation between model inputs and model discrepancy

3.2.1 Surrogate Modeling

For predictions and simulations which are expensive to evaluate, surrogate modeling methods [49,50] can be used as a replacement for the original model for more cost efficient computation. These methods rely on experimental design to obtain samples from the input space. The response surface is developed based on the sampled inputs and uncertainty analysis can be carried out directly from the developed response surface. However, due to

the difficulty in collecting erosion experimental data, approaches like Latin hypercube sampling [51], importance sampling [52] and other iterative sampling [53] to improve the response surface modeling cannot be applied.

3.2.2 Gaussian Process Modeling

The Gaussian process (GP) is a natural generalization of the Gaussian distribution, where the GP is fully characterized by its mean and covariance functions [54]. Once we specify the mean and covariance functions using the available data, the GP can be used to predict values at untested locations, and its prediction variance, i.e., uncertainty, can be calculated by the covariance function. The process of finding the mean and covariance function estimates using available data is referred to as the Gaussian Process Modeling.

Gaussian Process Modeling (GPM), an expansion of Kriging models, has been shown to successfully account for model uncertainty [55]. Gaussian Process Modeling has also been widely used in uncertainty quantification of engineering processes. For example, Rasmussen and Williams [54] investigated the uncertainty in predictions of atmospheric concentrations of CO_2 using GPM. The GPM provided the prediction and was simultaneously used to quantify the interpolation uncertainty even under data-limited conditions. Jiang et al. [56] applied GPM to estimate the model bias of vehicle-frontal-impact predictions (measurements of Chest G and Crush Distance), and used the trained GPM to remove the bias. The resulting predictions were shown to be in good agreement with experimental data through both interpolation and extrapolation validation studies. Thacker et al. [57] compared GPM to *n*-degree polynomial interpolation approach to quantify the uncertainties of the concentrations of oil at the sea surface at a certain spill site in the Gulf of Mexico. Both approaches provided reliable estimates of the uncertainties,

and the authors concluded that the GPM was less likely to exhibit erratic behavior in uncertainty estimates when extrapolated. Therefore, Gaussian Process Modeling is selected for estimating the model form uncertainty in this dissertation.

3.3 Input Uncertainty

The input variables considered are listed in Table 3.1. Pipe geometry and orientation are categorical variables and the remaining are continuous variables. In this section, we consider the uncertainty from the continuous input variables.

Table 3.1: List of input variables

	Pipe Geometry	**Pipe Orientation**	**Pipe Diameter**	**Pipe Hardness**	**Particle Size**	**Gas Density**	**Gas Viscosity**	**Gas Velocity**	**Liquid Density**	**Liquid Viscosity**	**Liquid Velocity**
Symbol	-	-	D	h_B	d_p	ρ_g	μ_g	V_{sg}	ρ_l	μ_l	V_{sl}
Unit	-	-	Inch	Vicker	μm	kg/m^3	cp	m/s	kg/m^3	cp	m/s

In general, the inputs are assumed to be noise free in the Gaussian process modeling. However, data measured under either lab environment or field condition unavoidably contains noise. The uncertainty can be from (1) stochastic nature of the operating condition and (2) measurement inaccuracy. For the first kind of input uncertainty, we usually rely on the experience from the experimental operators who normally have an approximated uncertainty scale for each input variable. For the second source of input uncertainty, a GP based framework [58] is adopted to consider input data corrupted by a Gaussian noise.

The standard GP framework does not consider the noise from each input variable or treat each input variable as a distribution. The GP based framework developed by Mchutchon and Rasmussen [58] tranports the uncertainty from input variables to the GP model output by holding the input variables deterministic and inflating the corresponding

output variance. Thus, the framework leads to a GP model with heteroscedastic output uncertainty, i.e., the noise of output varying across the input space. Furthermore, it is observed that the input noise has a much greater effect in areas where the GP model has a steep gradient than in areas where the GP model is nearly flat. Therefore, the framework can infer the input noise variance from the gradient of the GP posterior mean. The GP posterior mean is estimated using a first order Taylor expansion, which is expected to be a good approximation for any function provided that the input noise levels are not too large. More details can be found in [58]. Becasue gas viscosity and liquid density of the experimental data in the collected database remain constants, their uncertainties are not estimated. Table 3.2 summarizes the estimated uncertainty of the remaining input variables using the GP based framework of [58]. The estimated uncertainty falls into a noraml distribution (N) with the mean value specified by the first term of the bracket and the variance given in the second term of the bracket in each column. For example, the estimated uncertainty of pipe diameter is a normal distribution, with the mean value equal to zero and the standard deviation equal to 0.0023. To incorporate the uncertainty from this input variable (pipe diameter), the upper and lower extreme values of pipe diameter considering the uncertainty can be used to calculate the ranges of erosion rate values. A similar analysis can be applied to incorporate the influence from other input variables.

Table 3.2: Estimated uncertainty of input variables

	Pipe Diameter	**Pipe Hardness**	**Particle Size**	**Gas Density**	**Gas Velocity**	**Liquid Viscosity**	**Liquid Velocity**
Symbol	D	h_B	d_p	ρ_g	V_{sg}	μ_l	V_{sl}
Unit	Inch	Vicker	µm	kg/m^3	m/s	cp	m/s
Uncertainty	$N(0, 0.0023^2)$	$N(0, 0.1660^2)$	$N(0, 1.3320^2)$	$N(0, 0.0128^2)$	$N(0, 1.3066^2)$	$N(0, 0.0233^2)$	$N(0, 0.0410^2)$

The uncertainty from gas superficial velocity has been analyzed by Arabnejad [11] and he reported an uncertainty around 10% of the measurement. The 95% confidence interval of the gas superficial velocity estimated from the GP approach overlaps with the measurement uncertainty reported for 80% of the data points in the database. The estimation difference for the remaining 20% is smaller than 3% in average. Therefore, the estimated uncertainty for the gas superficial velocity is comparable to the uncertainty reported by Arabnejad [11]. Though no similar analysis has been found for uncertainty estimation of other input variables, the results give credit to the adopted framework for the input uncertainty estimation.

3.4 Data Uncertainty

Measurement uncertainty is irreducible no matter how accurate or precise the instruments become, and can be the result of gauge sensitivities, calibration accuracies, drifts due to environmental turbulence, and manipulation of the recorded data [59]. There are, in general, two kinds of uncertainties in measurements of engineering variables: random uncertainty and systematic uncertainty. Random uncertainty captures the random variations in the measurements while systematic uncertainty quantifies the inaccuracies inherent in the system [60]. For example, instruments with finite precision or measurements taken over a limited range (fails to reveal the physical variations) lead to random errors; whereas failure to account for all controllable factors or instrument drifts result in systematic errors. A more detailed description of uncertainty classification can be found in Bell [61].

There are, in general, two ways to quantify the measurement uncertainty [62]. First, if a variable is easy to measure, replicate measurements are conducted. The experimental

uncertainty can be estimated from design of replicate experiments [63]. In replicate experiments, the process variable is measured in several experiments carried out under the same conditions. Average of these measurements is treated as the best estimate value of the variable with the standard deviation representing the measurement uncertainty [62]. Most recent experimental studies include a section that discusses the uncertainty of their measurements. However, there are many data sets in the literature without proper uncertainty information, and, in field conditions, it may not be possible to replicate experiments due to considerable costs. Besides, to quantify the variation of the measurement in all possible aspects, the measurements should be taken in more than one fixed condition where different combinations of the influencing variables are incorporated. The second approach uses Taylor series expansion, and this approach is used when it is difficult to measure a variable directly. This section focuses on estimating measurement uncertainty for experimental data where the first approach would have been employed.

To discover the mathematical relationship between a dependent variable and one independent (influencing) variable, measurements can be taken from different values of an independent variable while keeping other independent variables constant. The same approach can also be used for the estimation of measurement uncertainty if we can validate the discovered relationship based on theoretical principles or prior knowledge [62].

However, in reality, the dependent variable can be influenced by several independent variables simultaneously. The measurement uncertainty obtained from each relationship of the dependent variable to the independent variable may be aggregated to approximate the measurement uncertainty to a general case. For a physical/chemical phenomenon, the dependent variable generally changes smoothly with small variations in each independent

variable if other independent variables are kept constant. For example, in the heating of process streams, the heat flow per unit time is linearly correlated to the temperature gradient for a given surface area [64]. In analytical chemistry, absorbance of analyzed samples is found to change smoothly with the samples' concentration for a small absorbance range [65]. If experimental data in this form is available, we hypothesize that the relationship between the dependent variable and each independent variable may be approximated using regression analysis using a limited number of basis functions, and that the modified residuals of the regression models can be used to estimate the distribution of the dependent-variable data uncertainty. This section introduces an approach used for estimating these residuals and aggregating them to estimate data uncertainty and tests this hypothesis using simulated data. The simulated data sets mimicking experiments are generated from different regions of five model functions: four commonly used for conducting computer experiments and another one modeling the circular motion of a piston within a cylinder. The experimental uncertainty is modeled as a Gaussian distribution with zero mean and a certain standard deviation (ranging from 1% to 100% of the average of sample outputs). The results reveal that the estimated distributions of the dependent-variable uncertainty are mostly consistent with that generated from Gaussian distribution.

The approach is, then, used to estimate uncertainty of erosion-rate measurements in conduits. Due to limited access to the field pipelines, most erosion-rate measurements have no replication. Even under lab conditions, replicate experiments, especially three or more times, are rarely carried out because each measurement takes considerable time and expense [66]. Erosion rate is commonly measured via Electrical Resistance probe (ER probe), Angle ER probe, mass loss, or Ultrasonic Non-Destructive Testing (UT) [11].

Based on experience, Rincon [67] stated that the uncertainty for erosion rates using ER probe ranges from 10% to 30% of the measurement. Arabnejad et al. [68] investigated the uncertainty in mass loss measurement by fitting through the cumulative mass loss versus the sand throughput. It shows the average standard relative error in the regression line's coefficients is around 9%. They stated that this value was consistent with the weight measurement scale uncertainty. However, the particle velocities being tested are in limited ranges (< 30 m/s). Mazumder [4] gave the uncertainty of balance used for mass loss measurements with the nominal level equal to 20.0 mg. A 2.5% uncertainty was calculated as the combination of systematic uncertainty (0.1 mg) and random uncertainty (0.4 mg). Ultrasonic Non-Destructive Testing [42] is a newly developed erosion measurement approach. The random uncertainty from three repetition erosion experiments in annular flow were estimated as 20% of the average.

The proposed approach is applied to estimate distribution of data uncertainty for each of the four commonly used measurement approaches and the results are compared to the estimates above and are discussed with experts for consistency. Using the proposed approach and the database (section 2.3), erosion-rate measurement uncertainty is estimated for each measurement approach.

3.4.1 Analysis of Dependent-Variable Data Uncertainty

Figure 3.2 plots the change in dependent variable y with a single independent variable x for a linear system. Four distinct measurements of y are taken, and they are shown with the black dots in Figure 3.2. The error bars give the two-thirds confidence interval of each measured value. It is assumed that the error variance is constant, and hence, the error bars have the same length. The dotted line represents the least squares regression line for these

four measurements. The difference between the measurement and the dotted line is the model residual. For example, the residual for measurement y_1 is $e_1 = y_1 - (ax_1 + b)$.

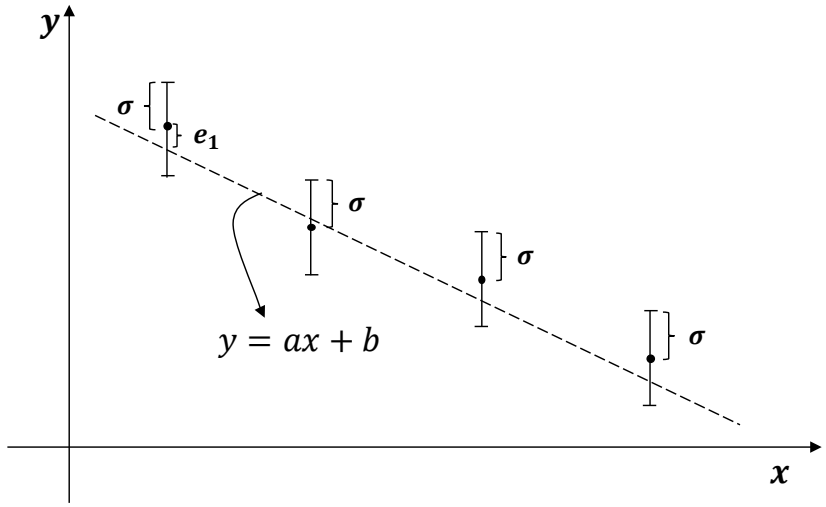

Figure 3.2: **Illustration of linear regression based on four measurements**

In general, for a system with n observations, the regression can be expressed as

$$y = X\theta + e \tag{3.1}$$

where $y = [y_1, y_2, \dots, y_n]$ is the vector of dependent-variable measurements, $X_{n\times p}$ is the matrix of p independent-variable values, θ is to-be-determined parameter vector of $p \times 1$, and e is the model-residual vector. The model residuals are assumed to be independent and identically distributed (iid), and if the best-fit regression model is identified, they follow a normal distribution with a mean of zero and a standard deviation of σ. That is to say, $e \sim N(0, \sigma^2)$.

The ordinary least squares (OLS) estimate of θ, $\hat{\theta}$, is given by Eq. (3.2). The predicted values of y, $\hat{y}$, can be obtained using Eq. (3.3), where $H=X(X^TX)^{-1}X^Ty$ is defined as the hat matrix. The OLS residuals, $\hat{e}$, are calculated using Eq. (3.4).

$$\hat{\theta} = (X^T X)^{-1} X^T y \tag{3.2}$$

$$\hat{y} = X\hat{\theta} = X(X^T X)^{-1} X^T y = Hy \tag{3.3}$$

$$\hat{e} = y - \hat{y} = y - Hy = (I - H)y \tag{3.4}$$

where I is a matrix of ones of the same size of H. Then, the variance of OLS residuals is

$$var(\hat{e}) = var\big((I - H)y\big) = \sigma^2 (I - H)^2 = \sigma^2 (I - H) \tag{3.5}$$

because $I - H$ is idempotent, i.e., $I - H = (I - H)^2$. For the i^{th} observation, the variance of its OLS residual is

$$var(\hat{e}_i) = \sigma^2 (1 - h_{ii}) \tag{3.6}$$

where h_{ii} is the i^{th} diagonal element of H. Based on Eq. (3.6), the distribution of i^{th} residual is $\hat{e}_i \sim N\big(0, \sigma^2 (1 - h_{ii})\big)$. Because $0 \leq h_{ii} \leq 1$ is dependent on the location of x_i, the variance for each estimated residual might be different. To correct for this variance inequality, each residual is scaled by dividing it with its corresponding$\sqrt{(1 - h_{ii})}$. The scaled residuals (which will be referred to as modified residuals) are consistently of variance σ^2.

The modified residuals, calculated as outlined above, correspond to the case where the dependent variable changes only as a result of changes in one independent variable while all others are kept constant. For physical/chemical phenomena, there may be, and in general are, numerous independent variables that impact the dependent variable, and most experimental work studies the impact of at least some of these independent variables on the dependent variable. A similar analysis is conducted to calculate modified residuals for each of the independent variables for which experimental data is available. The main assumption of our hypothesis is that for a physical/chemical phenomenon, the dependent

variable generally changes smoothly with small variations in each independent variable if other independent variables are kept constant. If experimental data in this form is available, we hypothesize that the relationship between the dependent variable and each independent variable may be approximated using regression analysis using a limited number of basis functions. We hypothesize that the modified residuals of the regression models can be used to estimate the distribution of the dependent-variable data uncertainty.

To find out the best-fit regression model for each independent variable, regression functions based on four basis functions are developed. The four basis functions are: polynomial $(\theta_1 x^a + \theta_0)$, power $(\theta_1 x^{\theta_2} + \theta_0)$, exponential $(\theta_1 exp(x) + \theta_0)$, and logarithmic $(\theta_1 ln(x) + \theta_0)$. The four basis functions we select are commonly used in describing physical/chemical processes. For example, based on the principles of chemical thermodynamics, the measurement of the dilute concentration of a chemical in one of a two-phase system is linearly related to another. A power equation can be used to link the solute concentration (C) in the aqueous phase to measure the mass of solute (q) in the solid phase ($q = K_F C^n$, K_F and n are constants). The regression functions are developed using the four basis functions. For a single independent variable, polynomial basis functions up to the third order are used. The higher order polynomial terms can be transformed to the form given in Eq.(3.1) by setting x^2 and x^3 as a column in X. Because $x, x^2,$ and x^3 are linearly independent, X is full column rank. Similarly, the nonlinearity of the other basis functions can be linearized by setting x^{θ_2}, $exp(x)$, and $ln(x)$ as a column in X. It should also be noted that in the selection of best-fit regression model, the number of input-output data pairs should be greater than the number of columns to ensure a unique determination of the parameters (e.g. θ_0, θ_1). The adjusted-R^2 statistic of all the fitted basis functions is

calculated. This statistical measure evaluates the scatter of data to the regression line considering the number of parameters estimated in the model. The basis function with the largest adjusted-R^2 value is selected as the best-fit regression model. Based on the selected basis function, the modified residuals are calculated.

To ensure sampling from a smooth region of the model function, we apply residual analysis [69] to locate possible outliers from the simulated input-output data pairs. Residual analysis is based on the calculation of leverage for each observation. A data point with high leverage yields a high variance for the prediction of the dependent variable, indicating the observation as an outlier, i.e. an abrupt change of the model function. Leverage is defined as the diagonal element of the hat matrix H for the selected basis function, where H_{ii} is the leverage for observation i. From the trace of H (trH in Eq.(3.7)) we can calculate the average leverage of all the observations, as $\bar{H}_{ii} = p/N$, where N is the number of observations. Generally, for observations with $H_{ii} > 2\bar{H}_{ii}$is categorized as outliers [69]. In this analysis, we deem data points with three times the average leverage as outliers, i.e. $H_{ii} > 3\bar{H}_{ii}$. Then, the identified outliers are removed from the input-output data pairs and the regression model is updated. The modified residuals from the updated regression model is used for estimation of uncertainty distribution.

$$trH = \sum_{i=n}^{n} H_{ii} = p \tag{3.7}$$

All modified residuals are used to construct a histogram, which we hypothesize gives an estimate of the dependent variable measurement uncertainty distribution. However, the uncertainty distribution cannot be directly obtained from the histogram as the number of bins used affects the shape of histograms. Kernel density plots [70] are employed as an effective way to obtain the distribution of data uncertainty in percentages. Kernel density

estimation is a non-parametric method of estimating the probability density function of a continuous random variable. The kernel function estimates the density at a point x_0 by taking the density of the points within the distance of λ to x_0 and assigning a weight to each point which relies on their proximity to x_0. The estimated density at x_0 ($\hat{f}(x_0)$) can be expressed as:

$$\hat{f}(x_0) = \frac{1}{n\lambda}\sum_{i} K\left(\frac{x_i - x_0}{\lambda}\right) \tag{3.8}$$

where n is the number of points considered, λ is the bandwidth which controls the size of the neighborhood around x_0, and K is the kernel function which controls the weight given to each point x_i at x_0 based on the distance. A Gaussian kernel is used in this analysis to construct probability density function of the dependent variable uncertainties.

The value of λ is important in the density estimation as a large λ will over-smooth the density estimation and mask the underlying structure of the data, and on the other hand, a small λ will result in a density estimation too spiky and hard to interpret. Therefore, the optimal value of λ is found by minimizing the error between the estimated density and the true one. If the true distribution is assumed to be Gaussian, with a Gaussian kernel, it can be shown [70] that the optimal value of λ is λ^* as shown in Eq.(3.9).

$$\lambda^* = 1.06\sigma N^{-1/5} \tag{3.9}$$

where σ is the sample standard deviation and N is the number of samples.

3.4.2 Computational Experiments

To test our hypothesis and the proposed approach for estimating measurement uncertainty, we constructed simulated data using several model functions. The functions are chosen to ensure that (1) they have a smooth surface under the simulation domain, and

(2) their dependent variables change differently with changes in each dimension. Simulated data sets are generated from the functions in a way that agrees with our underlying assumptions. The five model functions used are: Branin function [71], Three-hump camel function [72], Friedman function [73], Dette & Pepelyshev's eight dimension function [74], and Piston simulation model [75].

The Branin function (Eq.(3.10)) has two independent variables and has three global minima. The independent variable ranges used for data generation are [-5, 10] for the first variable and [0, 15] for the second one. Three-hump camel function (Eq.(3.11)) also has two independent variables and three local minima. The function varies smoothly in a small region of the design space. The independent variable ranges used for data generation are [-2, 2] for both variables. The Friedman function (Eq.(3.12)) has five independent variables and the data sets are sampled from a hypercube with variable values ranging from 0 to 1. Dette & Pepelyshev's eight dimension function (Eq.(3.13)) is shown to be influenced greatly by some variables and less influenced by others and is evaluated on a hypercube with variable values ranging from 0 to 1. Piston simulation model (Eq.(3.14)) models the circular motion of a piston within a cylinder and contains three nonlinear functions. The response (C) is the time it takes for the piston to complete one cycle in seconds. This model has seven independent variables: the piston weight, piston surface area, initial gas volume, spring coefficient, atmospheric pressure, ambient temperature and filling gas temperature. The data sets are sampled from the ranges of independent variables given in Table 3.3.

Branin function:

$$f_1(x) = a(x_2 - bx_1^2 + cx_1 - r)^2 + s(1-t)\,cos(x_1) + s \tag{3.10}$$

where a = 1, b = $\frac{5.1}{4\pi^2}$, c = $\frac{5}{\pi}$, r = 6, s = 10 and t = $\frac{1}{8\pi}$. This function is evaluated on the square $x_1 \in [-5, 10]$, $x_2 \in [0, 15]$.

Three-hump Camel function:

$$f_2(x) = 2x_1^2 - 1.05x_1^4 + \frac{x_1^6}{6} + x_1x_2 + x_2^2 \tag{3.11}$$

where $x_i \in [-5, 5]$, for all i = 1, 2.

Friedman function:

$$f_3(x) = 10\,sin(\pi x_1 x_2) + 20(x_3 - 0.5)^2 + 10x_4 + 5x_5 \tag{3.12}$$

This function is evaluated on the hypercube $x_i \in [0, 1]$, for all i = 1, …, 5.

Dette & Pepelyshev's eight dimension function:

$$f_4(x) = 4(x_1 - 2 + 8x_2 - 8x_2^2)^2 + (3 - 4x_2)^2 + 16\sqrt{x_3 + 1}(2x_3 - 1)^2 + \sum_{i=4}^{8} i\,ln\left(1 + \sum_{j=3}^{i} x_j\right) \tag{3.13}$$

This function is evaluated on the hypercube $x_i \in [0, 1]$, for all i = 1, …, 8.

Piston simulation function:

$$C = 2\pi\sqrt{\frac{M}{k + S^2\frac{P_0V_0}{T_0}\frac{T_0}{V^2}}}\,where$$

$$V = \frac{S}{2k}\left(\sqrt{A^2 + 4k\frac{P_0V_0}{T_0}T_a} - A\right) \tag{3.14}$$

$$A = P_0S + 19.62M - \frac{kV_0}{S}$$

Table 3.3: Ranges of inputs for Piston simulation function

Input variables	Ranges of the inputs
M, piston weight (kg)	$M \in [30, 60]$
S, piston surface area (m^2)	$S \in [0.005, 0.020]$
V_0, initial gas volume (m^3)	$V_0 \in [0.002, 0.010]$
k, spring coefficient (N/m)	$k \in [1000, 5000]$
P_0, atmospheric pressure (N/m^2)	$P_0 \in [90000, 110000]$
T_a, ambient temperature (K)	$T_a \in [290, 296]$
T_0, filling gas temperature (K)	$T_0 \in [340, 360]$

For each model function, the numbers of input-output pairs in simulated data, emulating individual experimental campaigns, range from three to 20. Latin hypercube sampling [76] of three values from the given range is used to generate the locations of simulated data as a combination of all the independent variables. For one pair of the simulated data from functions with two or more independent variables, one of the independent variables is varied based on the Latin hypercube sampling and the remaining independent variables are kept constant using one of the sample values.

The experimental uncertainty is modeled as a Gaussian distribution with zero mean and a certain standard deviation generated as a percentage of the mean value of the function outputs (the dependent variables) as the standard deviation level. The percentage levels used in the computational study are: 1%, 2%, 5%, 10%, 20%, 50%, and 100%. Random samples of experimental uncertainty are added to the calculated values of dependent variables.

3.4.2.1 Statistic Tests Used in Computational Experiments

The experimental uncertainty in simulated data is generated from a normal distribution with zero mean and given variance. Therefore, the first statistical test is a normality check of the estimated data uncertainty distribution. For the normality check, Shapiro-Wilk test (SW-test) is used because Shapiro-Wilk test has been shown to have better power properties (as the power increases, there are decreasing chances of a Type II error) in the test of normality compared to other tests [77]. If the modified residuals are normally distributed, then the t-test [78] is used to check whether its mean is equal to zero (null hypothesis), and the Chi-squared test [78] is used to check whether its variance is equal to σ^2 (null hypothesis). Three significance levels (α: 0.01, 0.05 and 0.1) are used for all tests. The overall process - generation of sample input-output pairs, development of regression model, calculation of modified residuals and applying corresponding statistical tests - is repeated for 1000 times with different Monte Carlo samples of experimental uncertainty. For each statistical test, a pass is defined as failing to reject the null hypothesis at the specific significance level. The probability of pass is calculated after 1000 repetitions for each test.

3.4.2.2 Results of the computational experiments

The probabilities of passing each of the three tests at significance level 0.1 for different variance levels are compiled as bar plots given in Figure 3.3 - 3.5 for Brannin function. In each bar plot, the standard deviation used to generate experimental uncertainty increases from 1% to 100%. The number of independent variables is equal to two for Branin function. In each bar, the x-axis differentiates the number of input-output pairs used in the simulated

data. Due to limited space, the plots only show number of input-output pairs for three, six, nine, 12, 15, and 18.

Figure 3.3 shows the probability of passing the SW-test. It can be observed that the probability is close to one for all conditions, except for data generated with very small standard deviations (i.e. 1%, 2% and 5%). For data with larger standard deviations, the probability of passing the SW test increases with increasing number of input-output pairs. For example, at the standard deviation of 10%, the probability of passing the SW test increases starting from the case with six input-output pairs. The reason a smaller number of input-output pairs fails to pass the SW test for very small standard deviations is that the obtained modified residuals are all very small and are distributed narrowly around zero. The probability of passing the SW test is close to 1 for the simulated data generated with only three samples under all standard deviation levels. This is an artifact of the perfect fit of the linear basis function for three data points. Similar observations can be made for probability of passing SW test at significance levels 0.01 (in supplementary Figure B.1) and 0.05 (in supplementary Figure B.2). As expected, with a decrease in the significance level, the probability of passing the SW test increases compared to that in Figure 3.3. For t-test (Figure 3.4), the results are equal to one and not influenced by the number of input-output pairs, significance level and the variance. The same conclusion can be made for t-test with the significance level equal to 0.01 (in supplementary Figure B.4) and 0.05 (in supplementary Figure B.5). For χ^2-test (Figure 3.5), the probability of passing the test is close to or greater than 0.7 starting from 10% standard deviation. However, the probability decreases with the increase in standard deviation percentage starting from the case with six input-output pairs.

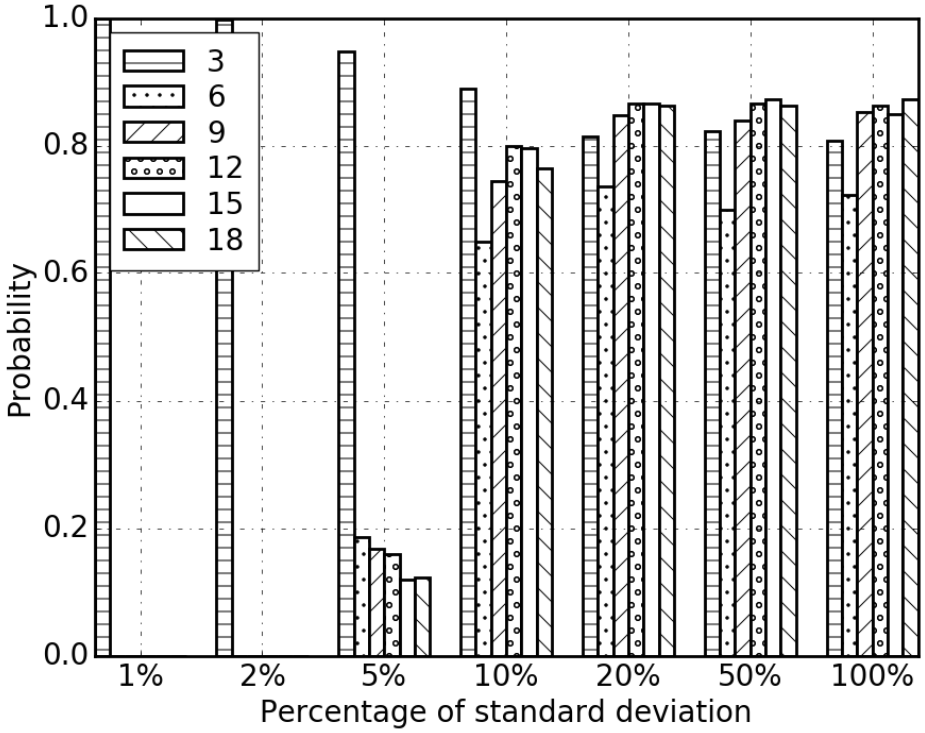

Figure 3.3: Probability of passing SW-test of Branin function (α = 0.1)

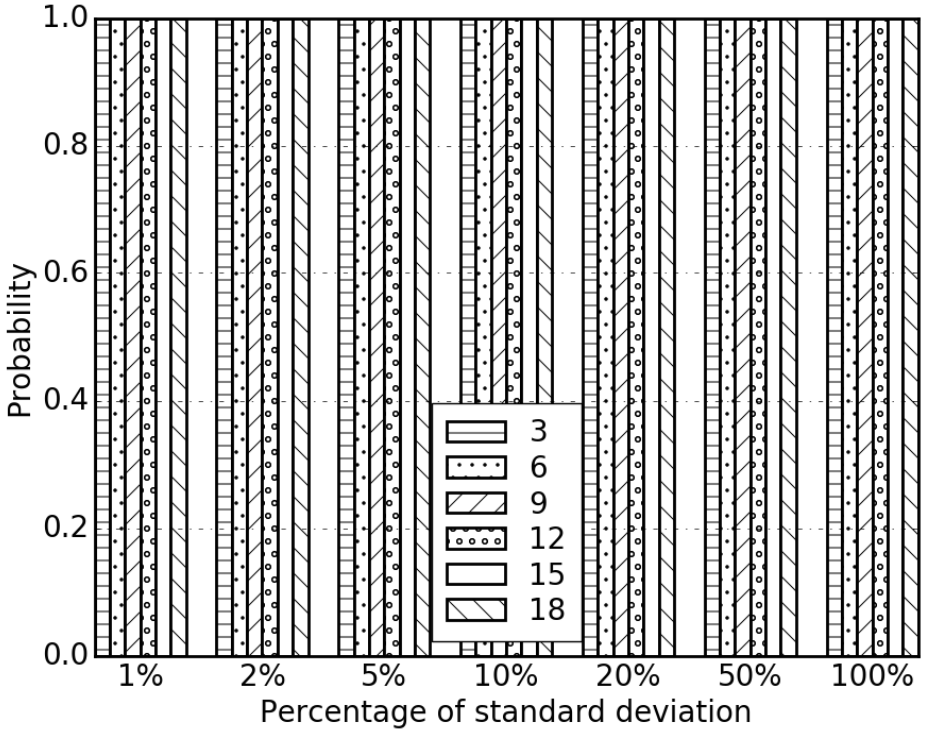

Figure 3.4: Probability of passing t-test of Branin function (α = 0.1)

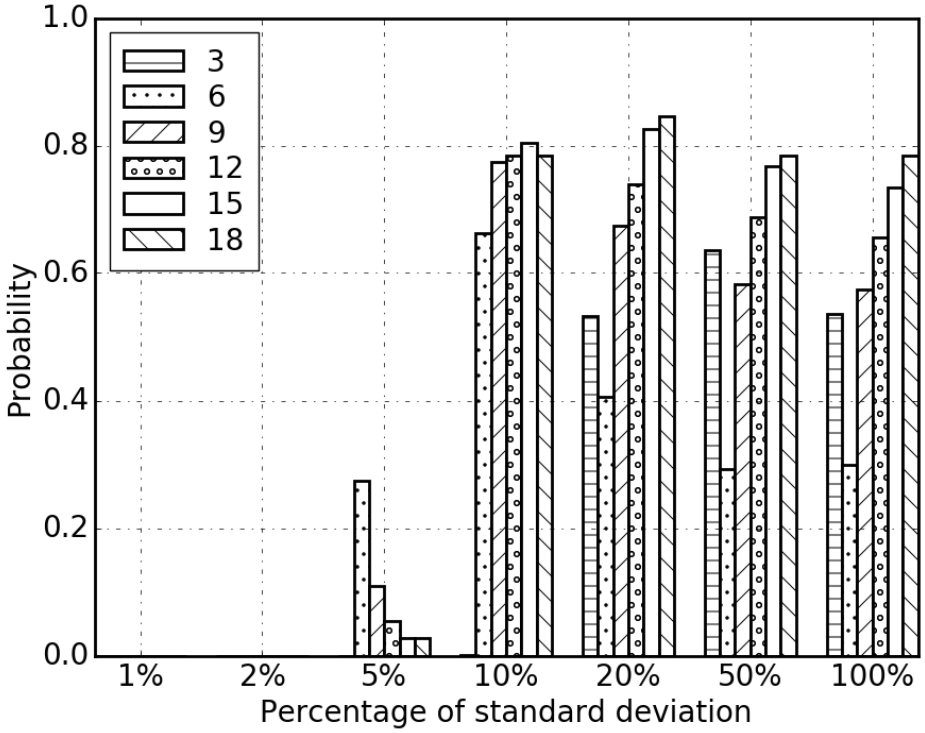

Figure 3.5: Probability of passing χ^2-test of Branin function ($\alpha = 0.1$)

For Piston simulation model, the probability of passing the SW-test is given in Figure 3.6. The probability is close to 0.8 for all conditions, except for data generated with very small standard deviations (i.e. 1%, 2% and 5%). For data with larger standard deviations, the probability of passing the SW test increases with increasing number of input-output pairs and a slight increase with the increasing percentage of standard deviations. A similar observation can be found for SW test with the significance level equal to 0.01 (in supplementary Figure B.38) and 0.05 (in supplementary Figure B.39). As the significance level has decreased, the probability of passing the SW test for all the cases has increased compared to that in Figure 3.6. For t-test (Figure 3.7), the results are equal to one and not influenced by the number of input-output pairs, significance level and the variance. The same conclusion can be made for t-test with the significance level equal to 0.01 (in

supplementary Figure B.40) and 0.05 (in supplementary Figure B.41). In χ^2-test (Figure 3.8), the probability of passing the test is influenced by the level of standard deviations and number of input-output pairs. The probability decreases with the increase in the percentage of standard deviation starting from 2% for the case with six input-output pairs, 5% for the case with nine, 12, and 15 input-output pairs, and, 10% for the case with 18 input-output pairs. Though the probability of passing the test increases when the standard deviation increases from 2% to 5%, when the standard deviation continues to increase, the probability of passing the test decreases. For results obtained from high dimensional function (i.e., the Dette & Pepelyshev's eight dimension function), we also observe that the probabilities of passing the χ^2-test are close to or less than 0.6. However, the probability of passing the test is greater to 0.7 with increased level of significance, especially when α is equal to 0.01 (in supplementary Figure B.43).

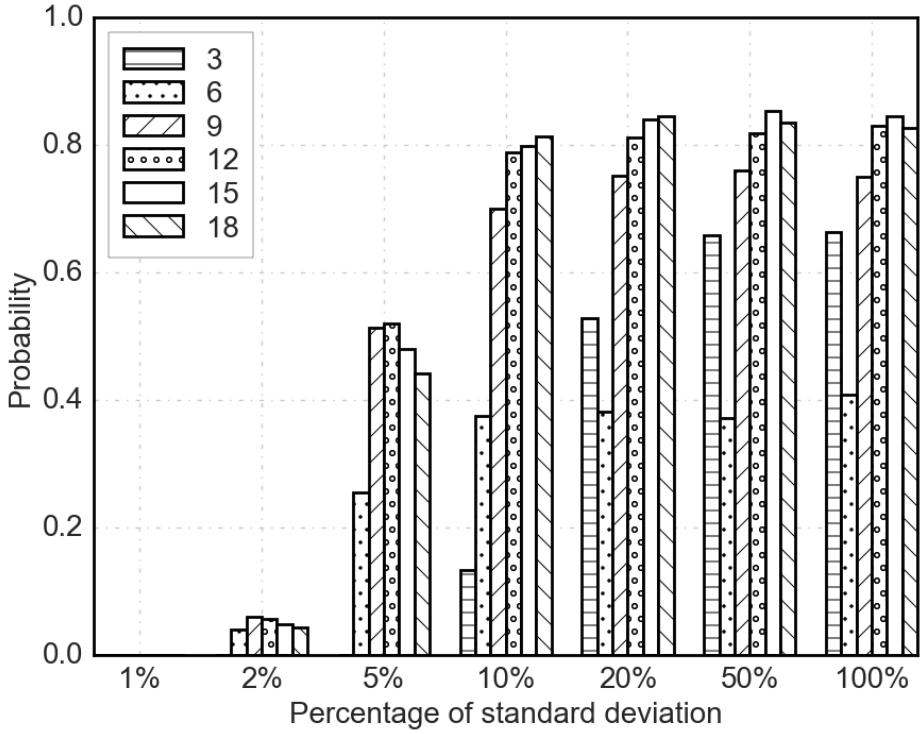

Figure 3.6: Probability of passing SW-test of Piston simulation function (α = 0.1)

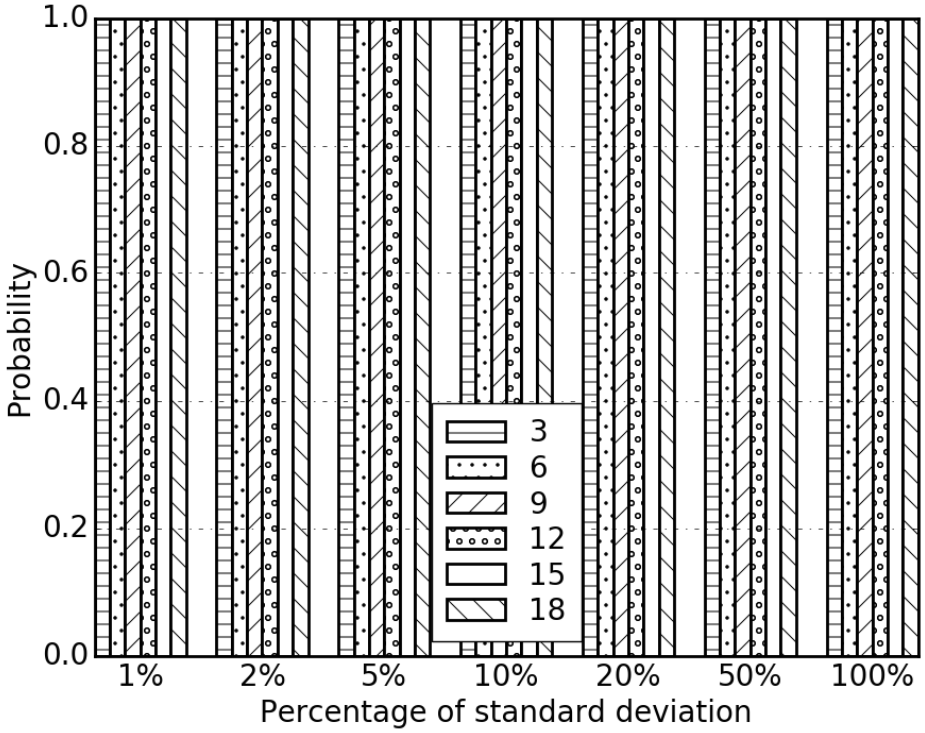

Figure 3.7: Probability of passing t-test of Piston simulation function (α = 0.1)

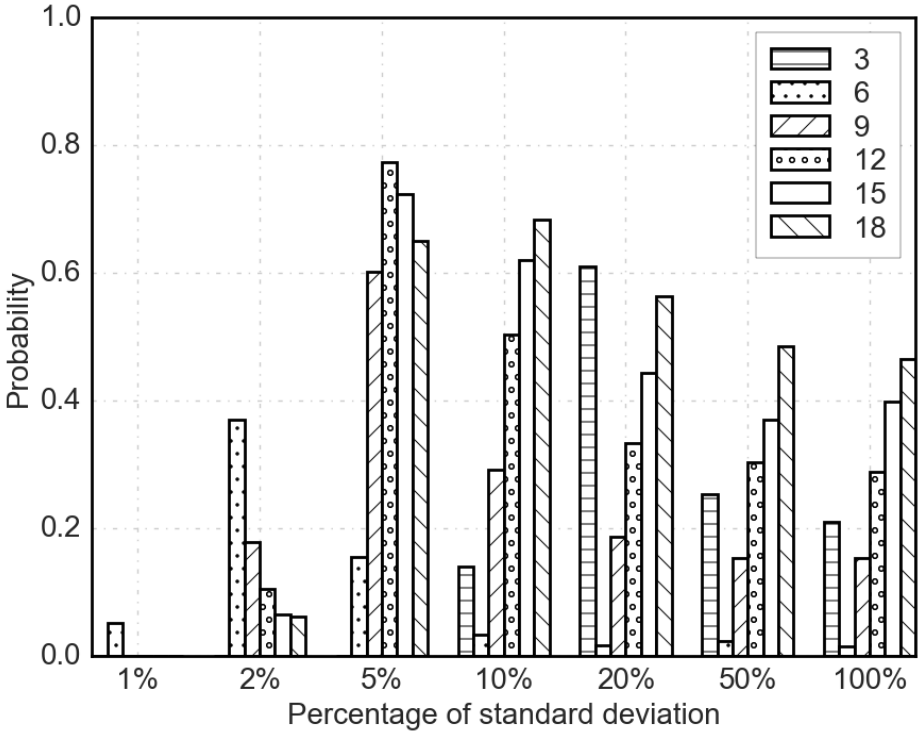

Figure 3.8: Probability of passing χ^2-test of Piston simulation function (α = 0.1)

Similar results were observed, and hence similar conclusions can be drawn for Three-hump camel function, Friedman function, and Dette & Pepelyshev's eight dimension function. The probabilities of passing each of the three tests under seven different standard deviation levels for these model functions are provided in the supplementary material.

Based on the computational experiments, data with more than nine input-output pairs and with moderate to high uncertainty levels (5% - 100%) are more likely to pass all the three statistical tests. Data with three input-output pairs under all uncertainty levels are also showed high passing probabilities.

These results provide strong support for the hypothesis, and for the use of the proposed approach in estimating experimental data uncertainty as the uncertainty level is moderately high (>10%) based on previous analysis [67,68]. In the next section, the proposed approach is applied to estimate uncertainties of erosion measurements in the absence of repetition experiments.

3.4.3 Estimation of Erosion-Rate Measurements Uncertainty

Figure 3.9 illustrates the application of our approach using four erosion-rate measurements taken at an elbow geometry using ultrasonic technique. A 3-inch stainless steel pipe was eroded under gas flow [42]. The liquid viscosity was 1 cp. The particle size was 300 microns. The independent variable that changes was superficial gas velocity, which were 11, 15, 23 and 27 m/s. In Figure 3.9, the dots represent measured erosion rate (y^e) in mils/lb at different gas rates. The dotted line gives the best curve that fits the data, in this case, a linear trend line. The function and the adjusted-R^2 are given in Figure 3.9. All other things being equal, it is expected that the erosion rate increases monotonically with increasing gas rates because particles traveling at higher gas rates have greater

momentum, resulting in more severe erosion when impinging the pipe wall. The linear trend line, in agreement with this expectation, also increases monotonically with increasing gas velocities. The adjusted-R^2 is close to one suggesting a good fit. Based on our hypothesis, the difference between the experimental erosion rate and predicted erosion rate using the trend line is calculated ($\hat{e}$). The difference at 23 m/s is illustrated in Figure 3.9. This value is then adjusted by the hat matrix to obtain the modified residual ($\hat{\varepsilon}$). In this case, a total of four modified residuals for UT are obtained. Similar analysis is performed with different independent variables or at other experimental conditions for each measurement approach.

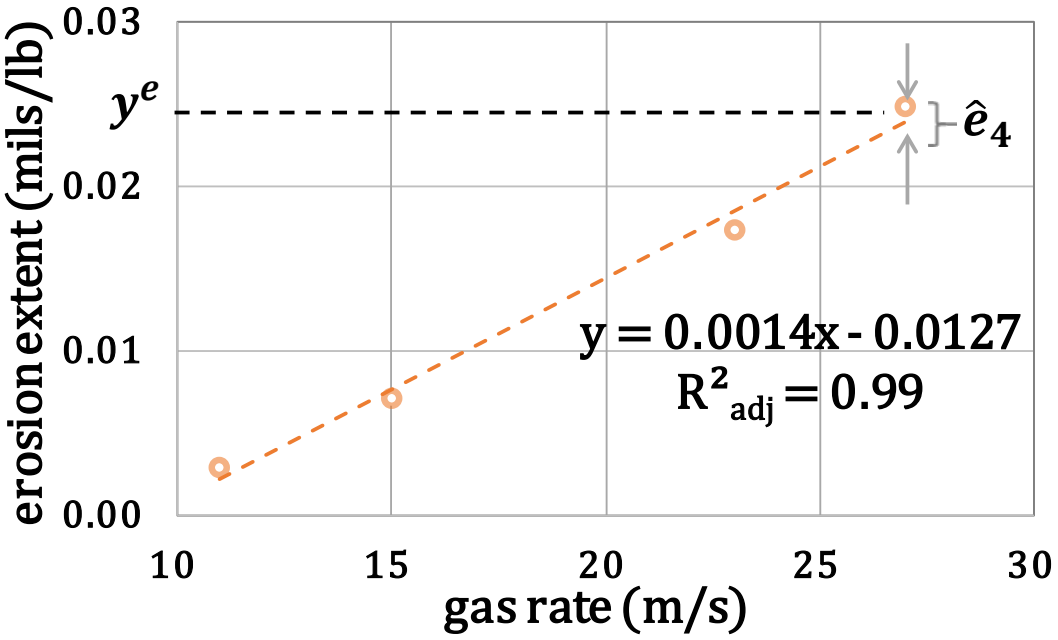

Figure 3.9: Estimation of experimental uncertainties using one set of data from Vieira [79]

In the erosion database, we define a set as the experimental data points with only one changing independent variable (when all other independent variables are the same). For example, the four data points shown in Figure 3.9 form a set. There are 105 sets with gas

rate, liquid rate and particle size as the changing independent variable, respectively. Out of 105 sets, there are 51 sets with only two data points. The sets with only two data points cannot be used for our analysis, because a linear trend line would fit the data perfectly. We grouped the remaining 54 data sets based on measurement approaches because the measurement uncertainty strongly depends on the measurement instrument used. The sets obtained with the total number of data points considered for each measurement approach are given in Table 3.4. The analysis, then, yields the estimates of erosion-rate measurement uncertainty for each of the four measurement approaches.

Table 3.4: Number of data points and sets obtained for each measurement approach

Measurement Approach	ER probe	Angle ER probe	Mass loss	Ultrasonic technique
No. of data points	306	29	24	55
Sets obtained	36	9	5	14

The basis functions identified by the best-fit regressions models for each measurement approach and the corresponding independent variable considered are given in Table 3.5. For example, an exponential trend line is used for representing how erosion rate changes with gas rate in multiphase flows, which is in agreement with the models developed in literature for this relationship [3]. The modified residuals for each measurement technique are combined to construct histograms and estimate probability distributions of experimental uncertainty for that measurement approach.

Table 3.5: Best-fit regression model identified with the corresponding independent variable for each measurement approach

Measurement approach / Independent variable	Gas	Liquid	Sand size
ER probe	linear/ exponential	logarithmic	NA
Angle ER probe	exponential	linear	NA
Mass loss	linear/ exponential	linear	NA
UT	linear	logarithmic/ linear	linear

3.4.4 Results and Comparisons to Literature Reviews

For each estimate, the experimental uncertainty in percentage is calculated via $\hat{\varepsilon}\% = \frac{\hat{\varepsilon}}{y^e} \times 100\%$. The resulting histogram of data uncertainty in percentage ($\hat{\varepsilon}\%$) for each measurement approach is given in Figure 3.10. The data uncertainty for ER probe, Angle ER probe, mass loss and UT measurements are estimated to be in the ranges of [-400%, 200%], [-100%, 60%], [-30%, 40%], and [-150%, 100%] of the measurements, respectively. To remove the influence of histograms by number of bins used, Kernel density plots [70] are employed as an effective way to view the distribution of data uncertainty in percentage. The optimal value of bandwidth, λ^*, is determined for each measurement approach (equal to 0.4022, 0.3848, 0.4788 and 0.0888 for ER probe, Angle ER probe, mass loss and UT measurements, respectively). The corresponding kernel density plots are generated and are given in Figure 3.11. It can be seen that UT measurement approach yields relatively smaller data uncertainty in percentage.

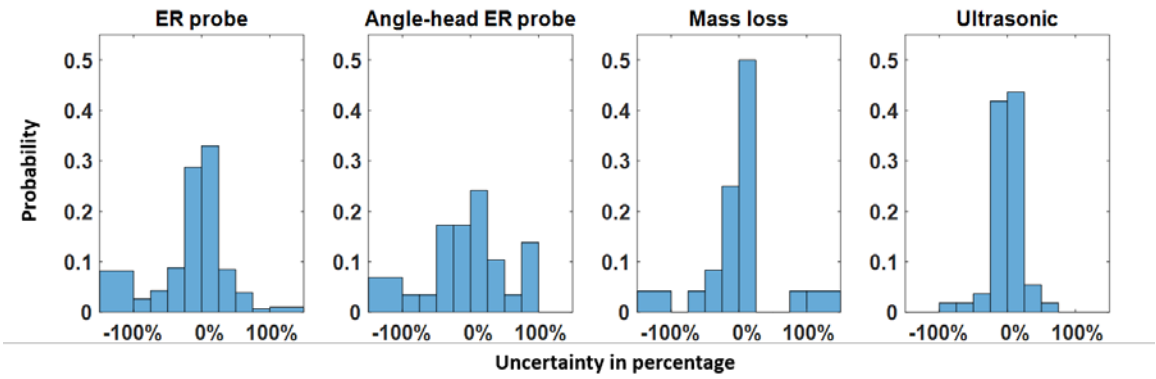

Figure 3.10: Histogram of experimental uncertainty estimation in percentage for each of the four measurement approaches

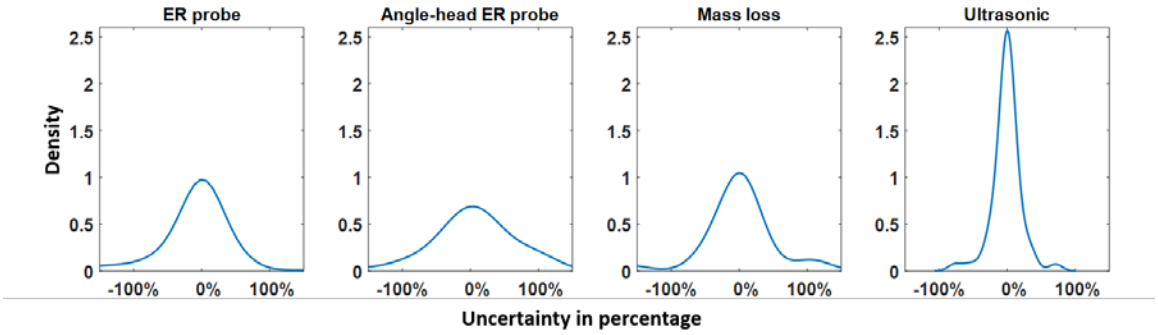

Figure 3.11: Kernel density plots of experimental uncertainty estimation in percentage for each of the four measurement approaches

Near 70% of experimental uncertainty for ER probe measurements are ranging from -30% to 30%, which is comparable to Rincon [67]'s statement that the uncertainty for erosion rates using ER probe ranges from 10% to 30% of the measurement. Khanouki [80] analyzed the experimental uncertainty for mass loss measurements. Based on this study, the average uncertainty for all materials and particle velocities measured by mass loss approach (by a digital scale) was about 9%. In our analysis, the average estimate of experimental uncertainty for mass loss measurements is 10%, and the probability that the experimental uncertainty percentage of mass loss measurements is within [-50%, 50%] is 83%. These results are comparable to the conclusions presented in Khanouki [80]. The

estimate of experimental uncertainty for UT measurements shows that more than 80% of experimental uncertainty percentage is within [-20%, 20%]. This value is comparable to the estimated random uncertainty from repeated erosion experiments [42] as 20% of the average. The results have also been consulted with experts on erosion experimental design and erosion-rate measurements. They concurred that the estimated data uncertainties are consistent with their expectations.

3.5 Summary

This section is focused on the quantification of uncertainty in modeling erosion occurring in pipeline transportation. Three major sources of uncertainty: model form, input, and experimental data have been investigated. The Gaussian process modeling is proposed to quantify the model form uncertainty. Then, a Gaussian process with noisy input framework is introduced to estimate uncertainty from input variables. The estimated input uncertainty is shown in line with other independent studies. For estimating uncertainty from experimental data, a novel approach is proposed which can be used for data uncertainty estimation without repetitive experimental measurements. The credibility of this approach is validated by computational experiments. Comparable results from this study to expert opinions and values given in literature also present strong support for the proposed approach.

CHAPTER 4

UNCERTAINTY QUANTIFICATION USING GAUSSIAN PROCESS MODELING

4.1 Introduction

Reliable estimates of erosion rates are essential for designing and safely operating pipelines that transport solids. Prediction of erosion rates in multiphase flow is a complex problem due to the lack of accurate models for predicting particle movements in the flow and their impact velocities to the wall. The erosion-rate calculations also depend on the accuracy of the flow regime predictions in the pipeline. The comparisons of existing model predictions to experimental data revealed that the predictions might differ by several orders of magnitude for some operating conditions. The goal of this chapter is to introduce a computational framework that estimates the model-prediction uncertainty of erosion-rate models. The framework utilizes a non-parametric regression analysis, Gaussian Process Modeling (GPM), for estimating the model-prediction uncertainty. Three different approaches are employed to estimate erosion-rate model discrepancies using GPM. The first approach utilizes all data points in the database without clustering to train and test a single GPM using four-fold cross-validation. For the second and third approaches, the data are clustered prior to training and testing GPMs using two different metrics. Data is clustered prior to training the non-parametric Gaussian Process based model because it has been suggested that robustness and accuracy of the predictions are greatly enhanced by

performing clustering analysis prior to modeling when analyzing large data sets [81]. We compare two approaches for clustering the data prior to training GPMs: (1) a flow regime based clustering, and (2) a unified similarity metric that is shown to perform well with datasets containing both numerical and categorical attributes. The results reveal that the new data clustering approach significantly shrinks the confidence intervals of the uncertainty estimates.

4.2 Gaussian Process Modeling (GPM)

According to general model uncertainty quantification formulation [82], the experimental response, y^e can be expressed as

$$y^e = y^m + \delta' + \varepsilon \tag{4.1}$$

where y^m is the model response, δ' is the model bias, and ε is the experimental uncertainty. In the uncertainty quantification of erosion-rate predictions, the measured erosion rate is used as the experimental response, and the model response is the predicted erosion rate by the SPPS 1D models. In this chapter, the experimental uncertainty is assumed to follow a zero-mean normal distribution. The model bias includes the uncertainties associated with estimated model parameters, the numerical errors and the model-form discrepancies, and is expressed as a Gaussian random process [56]. Because the experimental uncertainty is assumed to follow a zero-mean normal distribution, the model bias and the experimental uncertainty can be combined into one term, which we will refer as the model discrepancy (δ).

The Gaussian process, $GP(m, K)$, is a natural generalization of the Gaussian distribution [54]. Let x denote a point in multidimensional space, then $m(x)$ is the mean

function of the $GP(m,K)$, and $k(x,x')$ is the covariance function of the $GP(m,K)$, representing the spatial covariance between any two points (x and x') at the process. Therefore, we can express the model discrepancy using a multivariate Gaussian distribution with its characteristics determined by a mean function and a covariance function.

$$\delta(x) \sim GP(m(x), K(x,x')) \tag{4.2}$$

For prediction of model discrepancy δ_* at N_* untested locations (x^*), δ_* also follows the Gaussian distribution $\delta_* \sim N(m_*, K(x_*, x_*))$. The joint distribution of the observed δ and the to-be-predicted δ_* can be expressed as:

$$\begin{bmatrix} \delta \\ \delta_* \end{bmatrix} \sim GP\left(\begin{pmatrix} m(x) \\ m(x_*) \end{pmatrix}, \begin{bmatrix} K & K_* \\ K_*^T & K_{**} \end{bmatrix} \right) \tag{4.3}$$

where K is a $N \times N$ symmetric positive definite covariance matrix, K_* is a $N \times 1$ covariance matrix, and K_{**} is a $N_* \times N_*$ matrix. The element of covariance function $k_{ij} = k(x_i, x_j)$ measures the correlation between variable x_i and x_j. The posterior distribution of δ_* can then be obtained as:

$$P(\delta_* | x_*, x, f) = N(\mu_*, \Sigma_*) \tag{4.4}$$

where $\mu_* = m(x_*) + K_*^T K^{-1}(f - m(x)), \Sigma_* = K_{**} - K_*^T K^{-1} K_*$.

Since the covariance function is a positive definite matrix satisfying the Mercer Theorem, it is also a kernel function. The performance of GP prediction relies on the selection of kernel function [83] as shown in Eq.(4.4). Squared exponential, Matern and rational quadratic kernels are among the most commonly used kernel functions [54]. Kernel function in GP model should be selected based on the knowledge of the underlying

phenomena that is modeled and the characteristic of the data. Once the format of the kernel function is decided, the hyperparameters in the kernel function and the mean function can be optimized via the maximum-likelihood estimation using the available data, and this procedure is referred to as training the GPM. The trained GPM can be used to estimate the expected value ($\hat{\delta}$) of the model discrepancy (δ_*) and its variance ($\hat{\sigma}^2$), at conditions which are not in the training data set.

4.3 Implementation of GPMs

As mentioned in section 4.2, the distribution of the measurements can be expressed as

$$p(f|x,\theta) = N(m(x), K) \tag{4.5}$$

Eq.(4.5) is also called the marginal likelihood function. Its log marginal likelihood is

$$\log\big(p(f|x,\theta)\big) = -\frac{1}{2}f^T K^{-1} f - \frac{1}{2} log\det|K| - \frac{n}{2} log 2\pi \tag{4.6}$$

The optimal set of hyperparameters are obtained when the log marginal likelihood gets maximized. The conjugated gradient approach is commonly used to solve the partial derivatives of the log marginal likelihood with respect to the hyperparameters.

A constant mean function and a neural network covariance function (shown in Eq.(4.7) given in [54]) are determined to be appropriate for estimating model discrepancy for the dataset and model used in this study through a trial-and-error procedure.

$$\delta(x) \sim GP(m, K),$$
$$m(x) = a, \text{ and } K(x,x') = \sigma_y \sin^{-1}\left(\frac{2\mathrm{x}^{\mathrm{T}}\mathrm{diag}(\sigma_0^2)\mathrm{x}'}{\sqrt{(1+2\mathrm{x}^{\mathrm{T}}\mathrm{diag}(\sigma_0^2)\mathrm{x})(1+2\mathrm{x}'^{\mathrm{T}}\mathrm{diag}(\sigma_0^2)\mathrm{x}')}}\right), \tag{4.7}$$

where $\mathrm{x} = (1, x_1, \ldots, x_d)^T$ is an augmented input vector, and diag is the diagonal matrix with σ_0^2 times the unit matrix. In Eq. (4.7), we have introduced hyperparameters $\theta =$

$\{a, \sigma_y, \sigma_0\}$, where σ_y and σ_0 specify the magnitude of the covariance function and the amount of offset from the origin. The values of hyperparameters are determined via the maximum likelihood estimation approach.

Both categorical and numerical attributes and the corresponding actual model discrepancies are used to train the GPM. The actual model discrepancy (δ) is defined as the difference between experimental erosion rates and the corresponding erosion rate predictions of the model. The experimental database covers a wide range of input conditions resulting in significantly different erosion rates, and, up to five orders of magnitude differences in actual model discrepancies. For example, in gas only flow, with a gas flow rate of 70 m/s, the erosion rate is around 1 mil (1/1000th inch) length loss per pound of particles transported. In slug flow, which is under a liquid dominated condition, the erosion rate shrinks to 10^{-4} mils/lb. To minimize the impact of scaling issues on the GPM training, both numerical attributes and the actual model discrepancies are normalized to the range [0.1, 1].

For each GPM, the normalized data set is divided into two subsets: (1) a training set (3/4th of the data points), and (2) a test set (1/4th of the data points). The data in the training set is used to calculate the maximum-likelihood estimators of the GPM hyper-parameters, and the test set is used to assess the performance of the trained GPM. A four-fold cross validation [84] is used to generate GPM predictions for all data points in the dataset. The process is repeated for 30 times, and the results are averaged to minimize the impact of local solutions on GPM predictions. A MATLAB® based toolbox, Gaussian Process for Machine Learning - GPML [54], is used to train the GMPs. The same toolbox is used to calculate the expected mean ($\hat{\delta}$) and variance ($\hat{\sigma}^2$) at the test data points. The expected

mean gives the model discrepancy prediction, and the confidence interval of the prediction at α significance level is calculated using the estimated variance ($\hat{\sigma}$).

4.4 Assessing the Quality of GPM Predictions

To assess the quality of GPM predictions, the area metric [85] and root-mean-square-error [86] are introduced. Area metric (AM) is a measure that quantifies how well a model estimates the experimental observation of a physical variable at one input condition [85]. It is defined as the disagreement area between the estimated variable ($\hat{y}^e$) and experimental observation (y^e).

In Figure 4.1, the experimental measurement and the model estimate are expressed as two probability distributions. The area of the shaded region gives the AM value. A smaller AM value indicates a better prediction by the model for that input condition. An overall AM value can be calculated by summing the AM values for a set of input conditions, and it can be used to compare the prediction capabilities of different models.

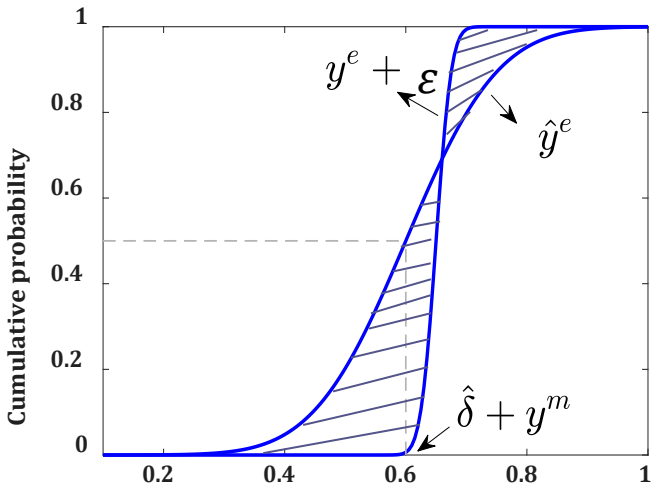

Figure 4.1: Area metric defined as the disagreement area between the estimated erosion-rate ($\hat{y}^e$) and experimental observation (y^e)

Here, we calculate the AM value for each data point with each approach, and use these AM values to calculate the overall AM for each approach.

The second criterion used is the root-mean-square-error (RMSE), which is calculated as the difference between the estimated predictions and the experimental observations using Eq. (4.8), where N is number of data points. For calculation RMSE, the mean experimental observations and predictions are used.

$$RMSE = \sqrt{\frac{\sum_i^n (\hat{y}_i^e - y_i^e)^2}{N}} \tag{4.8}$$

4.5 Data Clustering using GPM

To quantify prediction uncertainty and its confidence interval using GPM for erosion models under a wide range of input conditions, three different clustering approaches are introduced and compared in this section. As mentioned, the database covers operating conditions from different erosion rate measurement approaches, flow regimes and experimental set-up. For the first approach, data is used to train a non-parametric model based on Gaussian Process to estimate the prediction uncertainty and its confidence interval. For the second and third approaches, data is clustered prior to training the non-parametric Gaussian Process based model, because, it has been suggested that robustness and accuracy of the predictions are greatly enhanced by performing clustering analysis prior to modeling when analyzing large data sets [81]. The data are clustered using: (a) the flow regime in the pipeline, and (b) a unified similarity metric that is shown to perform well with datasets containing both numerical and categorical attributes [87]. For each cluster, a non-parametric model based on Gaussian Process is trained to estimate the prediction uncertainty and its confidence interval. Three approaches are applied to quantify

the prediction uncertainty and its confidence interval of SPPS 1D version 5.1 [27], which is commonly used by oil and gas industry.

Figure 4.2 gives the overview of these approaches. The first approach (Figure 4.2a) utilized all data points in the database without clustering to train and test a single GPM using four-fold cross-validation. For the second (Figure 4.2b) and third (Figure 4.2c) approaches, the data are clustered prior to training and testing GPMs using two different metrics.

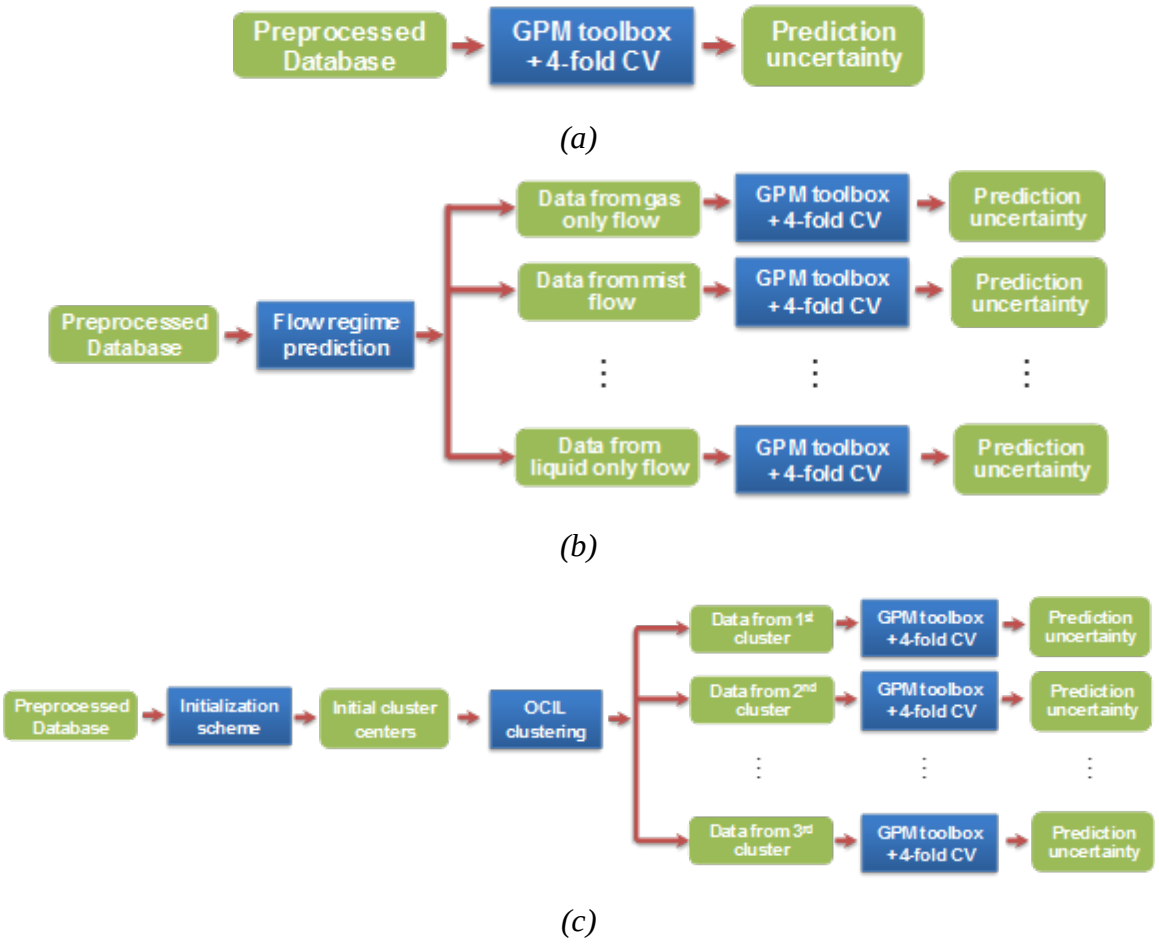

Figure 4.2: Approaches employed to estimate erosion-rate model discrepancy with GPM trained using data (a) without clustering, (b) clustered based on flow-regime, and (c) clustered based on object-cluster similarity metric.

The first set of clusters are constructed based on predicted flow regimes because it has been shown that the impact velocity of particles depends on the flow regime. In addition to single-phase (liquid only or gas only) flow regimes, the multiphase flow mixtures exhibit different flow patterns in the conduit depending on the relative ratios of liquid and gas amounts, their densities and viscosities [88]. These flow regimes are gas, mist, annular, churn, slug and liquid. The flow regime for a given data point is determined by a flow map embedded in SPPS 1D version 5.1 model because it was (generally) not available with the experimental data. In this approach, data points that predicted to exhibit the same flow regime are grouped into different clusters, and clusters are used to develop GPMs (Figure 4.2 (b)).

The second clustering method utilizes object-cluster similarity metric (OCIL) [87] as the measure to cluster data with the proposed density-peak [89] based initialization scheme, and the resulting clusters are used to develop GPMs (Figure 4.2 (c)). The details of the clustering approach and the initialization scheme introduced to significantly enhance its computational performance is discussed in detail in Section 4.5.2.

All approaches, algorithms, and analysis are implemented in MATLAB R2016a. The algorithms are executed, and the analysis are carried out on a 2.30GHz Intel Xeon E5 PC with 32GB memory running Windows 10 Enterprise.

4.5.1 Clustering Data Based on Flow-Regime

The erosion model can predict the erosion rate based on flow regimes. There are gas, mist, annular, churn, slug and liquid flows based on the collected data. When there is only gas in the pipeline, the sand particles are assumed to travel at the gas velocity. This leads to high erosion rates at high gas flow rates [90]. With the introduction of liquid, the flow

regime changes from gas flow to mist flow. In mist flow, gas normally travels at a high velocity, and liquid is entrained as droplets in the gas flow. The particles entrained in both the liquid droplets and the gas flow can lead to erosion when impinging on the pipe wall. With increased liquid flow rate, liquid forms a thin film adjacent to the pipe wall [91]. The erosion model defines the transition boundary between mist and annular flow by comparing the liquid film thickness to the average particle size; if the film thickness is larger than particle size, the regime is classified as annular flow, otherwise as mist flow [92]. In annular flow, the sand particles are entrained both in the liquid droplets and in the gas core. To determine the amount of liquid entrained as droplets in the gas core, Ishi's entrainment correlation [93] is used. Given the entrainment rate and velocities of sand particles in the liquid film and gas core, the total erosion rate is calculated.

Slug flow is characterized by unsteady flow behavior. It is composed of an alternate flow of a gas pocket, named Taylor bubble, and liquid slugs that contain numerous small gas bubbles [94]. Erosion is assumed to be caused by particles uniformly distributed in the liquid slug body. Since slug flow displays transient behavior, segmented calculation of representative impact velocity is conducted [95].

Churn flow are more chaotic than slug flow with no clear boundaries between the gas and liquid phases. At high gas flow rates, when the liquid slugs bridging the pipe become short and frothy, churn flow occurs [96]. In churn flow, sand particles are assumed to be uniformly distributed in the liquid phase and lead to erosion with the movement of the liquid flow. The velocities of the liquid and sand particles in churn flow are assumed to be at the mixture velocity of the gas and liquid flows.

4.5.2 Clustering Data Based on Object-Cluster Similarity Metric

The object-cluster similarity metric (OCIL) is developed by Cheung and Jia [87]. The clustering problem of N data points, $\{\mathbf{x}_1, \mathbf{x}_2, \ldots, \mathbf{x}_N\}$, with mixed attributes into k different clusters, denoted with $C_1, C_2, \ldots, C_k$, can be formulated as

$$\mathbf{Q}^* = \arg\max_{\mathbf{Q}} F(\mathbf{Q}) = \arg\max_{\mathbf{Q}} \left[\sum_{j=1}^{k} \sum_{i=1}^{N} q_{ij} s(\mathbf{x}_i, C_j) \right] \tag{4.9}$$

In Eq. (4.9), $s(\mathbf{x}_i, C_j)$ is the OCIL between data point $\mathbf{x}_i$ and cluster C_j, and $\mathbf{Q} = (q_{ij})$ is an $N \times k$ partition matrix satisfying

$$\sum_{j=1}^{k} q_{ij} = 1, \quad \text{and} \quad 0 < \sum_{i=1}^{N} q_{ij} < N \tag{4.10}$$

where $q_{ij} \in \{0,1\}$, $i = 1,2,\ldots,N$, and $j = 1,2,\ldots,k$. Equation (4.10) ensures that each data point is assigned to one and only one cluster and the number of clusters is greater than or equal to two.

The OCIL is calculated as a combination of the similarity measures obtained for categorical, $\mathbf{x}_i^c$, and numerical, $\mathbf{x}_i^u$, attributes. The similarity between $\mathbf{x}_i^c$ and C_j, $s(\mathbf{x}_i^c, C_j)$ is defined as

$$s(\mathbf{x}_i^c, C_j) = \sum_{r=1}^{d_c} w_r s(x_{ir}^c, C_j) \tag{4.11}$$

where the weight factor, w_r, accounts for possible unequal importance of each attribute, and d_c is the number of categorical attributes. The similarity between a categorical attribute value x_{ir}^c and cluster C_j, $i \in \{1,2,\ldots,N\}$, $j \in \{1,2,\ldots,k\}$, $r \in \{1,2,\ldots,d_c\}$, is defined as

$$s\left(\mathrm{x}_{ir}^{\mathrm{c}}, C_j\right) = \frac{\tau_{A_r = x_{ir}^c}\left(C_j\right)}{\tau_{A_r \neq NULL}\left(C_j\right)} \tag{4.12}$$

where $\tau_{A_r = x_{ir}^c}\left(C_j\right)$ is the number of data points that have the value x_{ir}^c for attribute A_r in cluster C_j, NULL refers to the empty set, and $\tau_{A_r \neq NULL}\left(C_j\right)$ is the number of data points that have the attribute A_r whose value is not equal to NULL in cluster C_j. The value of $s\left(\mathrm{x}_{ir}^{\mathrm{c}}, C_j\right)$ becomes one when all the data points have the value $\mathrm{x}_{ir}^{\mathrm{c}}$ for attribute A_r in cluster C_j, and becomes zero when none of the data points has the value $\mathrm{x}_{ir}^{\mathrm{c}}$ for attribute A_r in cluster C_j.

The similarity measure between numerical attribute $\mathbf{x}_i^u$ and cluster C_j , $i \in \{1,2,\dots,N\}, j \in \{1,2,\dots,k\}$ is given by

$$s\left(\mathbf{x}_i^u, C_j\right) = \frac{\exp(-0.5\mathrm{Dis}(\mathbf{x}_i^u, \mathbf{c}_{\mathrm{j}}))}{\sum_{t=1}^{k} \exp(-0.5\mathrm{Dis}(\mathbf{x}_i^u, \mathbf{c}_{\mathrm{t}}))} \tag{4.13}$$

where $\mathbf{c}_{\mathrm{j}}$ is the cluster center and is defined as

$$\mathbf{c}_{\mathrm{j}} = \frac{\sum_{i=i}^{N} \mathbf{x}_i^u(C_j)}{\mathrm{num}(C_j)} \tag{4.14}$$

where $\mathbf{x}_i^u(C_j)$ represents the numerical attributes in cluster C_j and $\mathrm{num}(C_j)$ is the number of data points assigned to clusterC_j. Dis(·) in Eq. (4.13) stands for the Euclidean distance. The value of $s\left(\mathbf{x}_i^{\mathrm{u}}, C_j\right)$ is within the interval [0,1].

The OCIL between $\mathbf{x}_i$ and cluster C_j can be obtained as the average of the similarity measures calculated based on each feature,

$$s\left(\mathbf{x}_i, C_j\right) = \frac{d_c}{d_f} s\left(\mathbf{x}_i^{\mathrm{c}}, C_j\right) + \frac{1}{d_f}\, s\left(\mathbf{x}_i^u, C_j\right) \tag{4.15}$$

where d_f denotes the total number of attributes. Because the numerical attributes are often treated as a vector and handled together in clustering analysis, $d_f = d_c + 1$.

We use the iterative clustering algorithm of Cheung and Jia [87]. The optimal $\mathbf{Q}^* = \{q_{ij}^*\}$ in Eq. (4.9) is defined by

$$q_{ij}^* = \begin{cases} 1 & \text{if } s(\mathbf{x}_i, C_j) \geq s(\mathbf{x}_i, C_r) \quad \forall 1 \leq r \leq k \\ 0 & \text{otherwise} \end{cases} \tag{4.16}$$

Each data point $\mathbf{x}_i$ is assigned to the cluster with the largest OCIL among the *k* clusters for that data point (Eq. (4.16)). The number of clusters is determined by a penalization mechanism that gradually eliminates redundant clusters. The algorithm assumes that the number of clusters, *k*, is initialized to a value greater than the true value (i.e., $k \geq k^*$), and assigns an equal weight to each cluster. This weight measures the importance of each cluster to the whole clustering structure. After a data point is assigned to the cluster (the winning cluster), which has the largest OCIL for that data point, the weight of the winning cluster is increased and the weight of the cluster with the second largest OCIL is decreased as a penalty. As the algorithm proceeds, the clusters with very low weights are assigned fewer data points, and hence, may eventually be eliminated. The algorithm terminates when the changes (α_r) in the ratio of data points assigned to each cluster are smaller than 1% and has stabilized for 10 continuous epoch times.

$$\alpha_r = \frac{\sum_{i,j=r}^{N} q_{ij}(epoch+1) - \sum_{i,j=r}^{N} q_{ij}(epoch)}{N} \tag{4.17}$$

$\forall 1 \leq r \leq k$

In general, the algorithm is executed several times, because the data points are randomly assigned to clusters at initialization. In this work, we propose a special initialization scheme based on the concept that cluster centers are surrounded by more data

points with a greater density and positioned relatively far away from other centers [89]. The local density and the distance between high density points are calculated to determine the number of clusters, cluster centers, and to make the initial data point assignments to clusters. A parameter, cutoff distance, controls the average number of neighboring data points that is used for density calculations. The number of clusters obtained and cluster centers change when the cutoff distance is changed. As a rule of thumb, Rodriguez and Laio [89] recommend selecting a cut-off distance such that the average number of neighboring data points is around 1-2% of the total number of data points.

For the erosion data set, eleven different initial cluster sets are obtained by changing the cut-off distance so that the average number of neighboring data points increased from 1% to 2% with an interval of 0.1%. The corresponding operating conditions of each cluster center is compiled, and the overlapping centers are removed. The Euclidean distances between the remaining cluster centers are calculated, and the cluster centers that are deemed very close to each other based on these distances are consolidated to a single cluster center. After the consolidation step, the remaining unique cluster centers are used to determine the initial number of clusters, and the initial cluster centers to initialize the OCIL clustering algorithm. For initialization, the data points are assigned to the clusters that yielded the highest OCIL value based on the initial cluster centers.

4.5.3 Results and Discussions

4.5.3.1 Estimating Model Prediction Uncertainty without Data Clustering

Figure 4.3 provides the histogram of average individual-data AM values (i.e., the average AM value of 30 repetitions for each data point in the database) when a GPM is trained using all data points using a four-fold cross validation repeated 30 times. The

histogram of the average AM is grouped by the flow regime prediction of each data point (also used in section 4.5.3.2). Data points predicted as liquid flow have larger average AM, because the average AM are all above 0.01 mils/lb. The largest counts for average AM from gas and slug flows is around 0.01 mils/lb, while for average AM from mist flow is around 0.001 mils/lb and for churn flow is around 0.0001 mils/lb. The annular flow has two peaks around AM values of 0.0001 mils/lb and 0.01 mils/lb, respectively. The maximum average AM is 2.37 mils/lb, and it is in gas flow. The overall average AM is 28.85 mils/lb, yielding an average value of 4.93×10^{-2} mils/lb. The RMSE value for each flow regime is also shown on the plot. The RMSE is generally greater than the average AM with the largest counts, except for the slug flow, where the prediction uncertainty contributes more than the prediction discrepancy. The RMSE for the overall data set is 0.13 mils/lb. It is almost half of the RMSE (which is equal to 0.24 mils/lb – Section 2.3) when the model bias was not corrected using the GMP model.

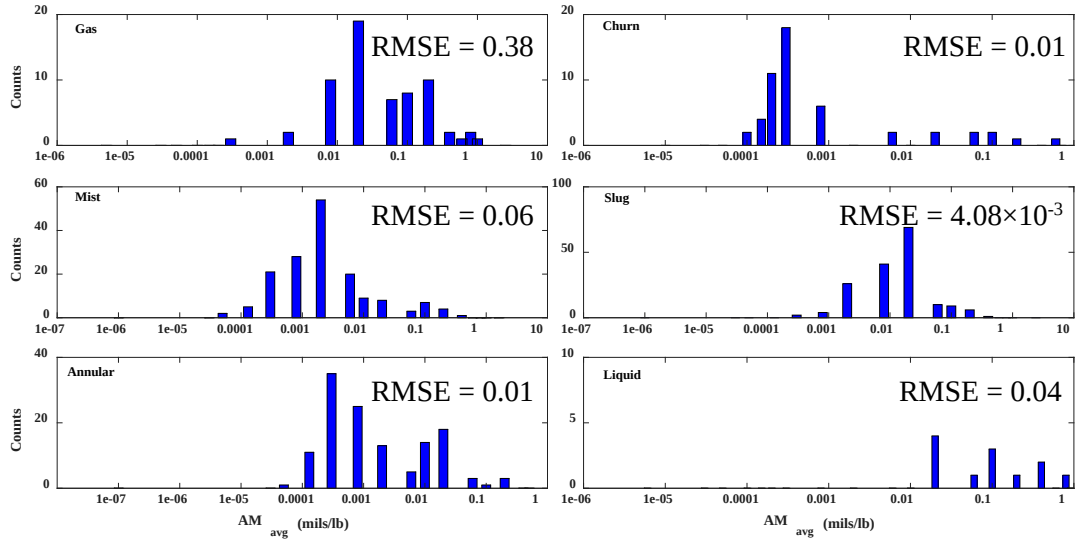

Figure 4.3: Histogram of average individual-data AM values without data clustering

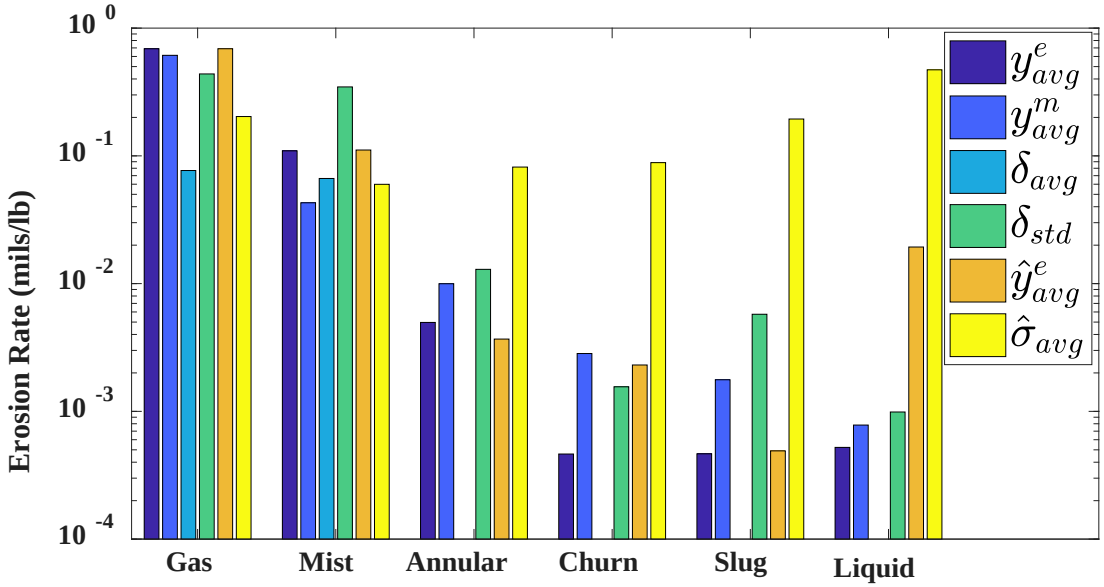

Figure 4.4: Averaged erosion rate prediction using GPM without data clustering

Figure 4.4 shows the average measured (y^e_{avg}) and predicted (y^m_{avg}) erosion rates, average (δ_{avg}) and standard deviations (δ_{std}) of actual model discrepancies, average predicted erosion rates using GPM ($\hat{y}^e_{avg} = avg(y^m + \hat{\delta})$) and the prediction uncertainties (represented by the average standard deviation: $\hat{\sigma}_{avg}$) for each cluster. Figure 4.4 suggests that the predicted erosion rates using GPM (5th set) are closer to measured values (1st set) than model predictions (2nd set) for gas, mist, annular and slug flow regimes. However, churn and liquid flow regimes are highly over-predicted. It can also be observed that the model tends to under-predict erosion rates in gas and mist flows. There are significant differences in actual model discrepancies (δ) in each flow regime that yield large variances (measure of which could be the standard deviation of the actual model discrepancies: δ_{std}). Partially due to the large variance in model discrepancies, the predicted erosion rates using GPM also have large standard deviations (as evidenced by $\hat{\sigma}_{avg}$).

Another reason is as mentioned in Section 2.2.1, the experimental database covers a wide range of operating conditions resulting in five orders of magnitude change in actual model discrepancies. Therefore, the training set of the GPM contains vastly different actual model discrepancies. For example, data points from gas dominated flows, where the actual model discrepancies range between -1.4 and 2.5, are used to estimate model discrepancies of data points from liquid only flow, where the actual model discrepancies range from -2.4×10^{-3} to 7.7×10^{-4}. Particle tracking and impingement in horizontal flow orientations are different from the ones in vertical flow orientations. Therefore, the GPM trained using one type of orientation may not be appropriate to estimate model discrepancy of another flow orientation. These results and discussions suggest that, clustering of data points based on the operating conditions prior to the development of GPMs may improve model-discrepancy estimates.

4.5.3.2 Clustering Based on Flow Regimes

We clustered the data based on the predicted flow regimes, and trained a GPM for each cluster [48]. According to the predicted flow regimes, eighty percent of the data are collected at gas dominated flows (i.e., gas only, annular, mist and churn flow) and the prediction results in six different clusters: gas, mist, annular, churn, slug and liquid. Figure 4.5 gives the histogram of average individual-data AM values based on each flow regime. We can see the counts shift to smaller AM values for gas, slug and liquid flows compared to Figure 4.3. There are also more number of data points to the left of AM values 0.001 mils/lb in mist flow. Even though annular and churn flow do not show great improvement, we have observed AM values as small as in the magnitudes of 1×10^{-7}. In this case, the overall AM has decreased to 23.03 mils/lb and leads to an average value of 3.94×10^{-2}

mils/lb. The RMSE for each flow regime is also calculated and displayed in Figure 4.5. Compared to the RMSE obtained in section 4.5.3.1, the improper determination of flow regimes and grouping of data points to generate the GP models result in larger RMSE in all multiphase flow regimes. The RMSE of erosion rate prediction for all data points is also increased to 0.14 mils/lb.

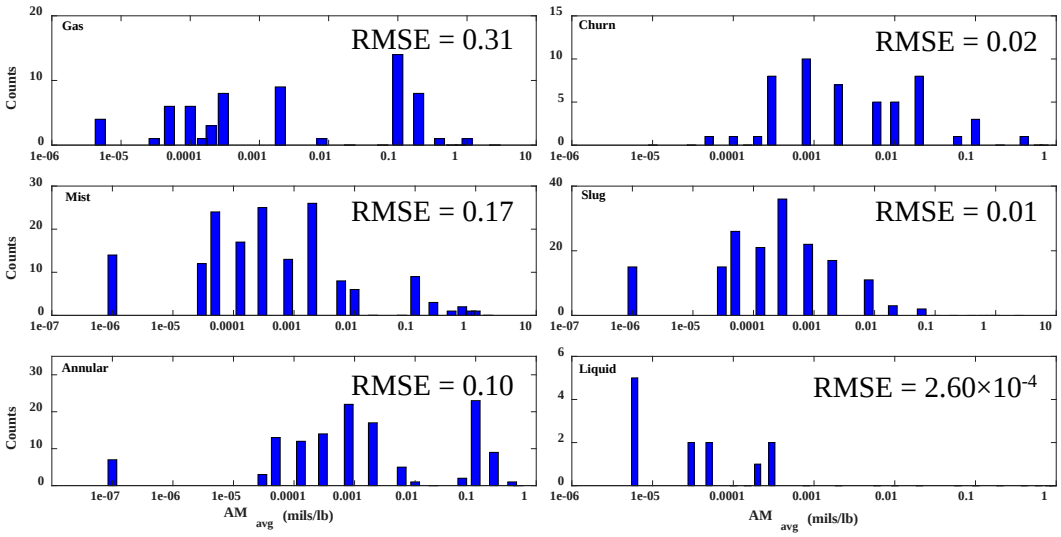

Figure 4.5: Histogram of average individual-data AM values with flow regime based clustering

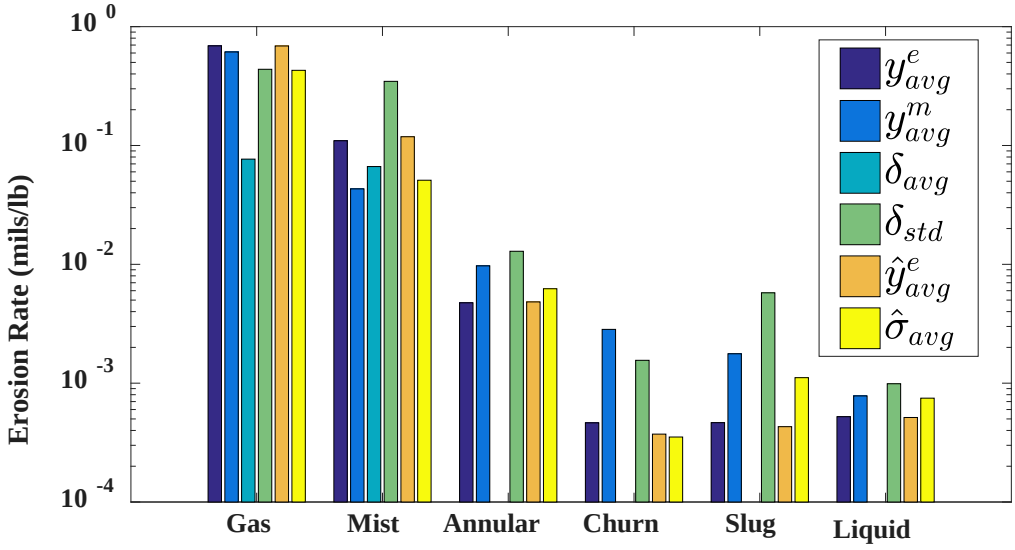

Figure 4.6: Averaged erosion rate prediction using GPM with flow regime based clustering

Figure 4.6 shows the similar information as in Figure 4.4: average measured (y_{avg}^{e}) and predicted (y_{avg}^{m}) erosion rates, average (δ_{avg}) and standard deviations (δ_{std}) of actual model discrepancies, average predicted erosion rates using GPM ($\hat{y}_{avg}^{e}$) and the prediction uncertainties ($\hat{\sigma}_{avg}$) for each cluster. Figure 4.6 suggests that, on average, the predicted erosion rates using GPM (5th set) are closer to measured values (1st set) than model predictions (2nd set) for all flow regimes. The model also tends to under-predict erosion rates in gas and mist flows. Though the predicted erosion rates using GPM still have large standard deviations (as evidenced by $\hat{\sigma}_{avg}$), these values have been greatly reduced compared to the predictions without data clustering and add up to a smaller overall AM.

4.5.3.3 Clustering Based on OCIL approach

We clustered the data using the OCIL metric as outlined in Figure 4.2 (c), and trained a GPM for each cluster. The numerical attributes used for clustering were pipe material hardness and size, particle diameter, liquid viscosity and velocity, gas density and velocity. The categorical attributes were pipe geometry, flow regime and flow orientation. Because experimentally observed flow regime is not available for most data points, it is not included as one of the categorical inputs.

Using the proposed cut-off values yielded 11 cluster sets. Three of these sets contained seven, nine and eleven elements, respectively. Two of them contained eight elements, and six of them contained ten elements. Therefore, the analysis resulted in 103 points as potential cluster centers. Out of these potential cluster centers, 17 of them were identical (appeared in several sets) reducing the number of distinct potential cluster centers to 27.

Figure 4.7 plots pair-wise Euclidean distances between potential cluster centers using a color scale on a 27-by-27 matrix. The color of each small square corresponds to the

Euclidean distance between the potential cluster centers of its corresponding column and row. In Figure 4.7, darker shades of gray correspond to smaller Euclidean distances. Therefore, the pairs of potential cluster centers with darker shades have similar operating conditions, and they may be consolidated to a single potential cluster center. On the other hand, a lighter gray scale indicates that the pair is away from each other yielding a large Euclidean distance representing unique operating conditions and distinct potential cluster centers. In general, Figure 4.7 suggests that the Euclidean distances of potential cluster centers around the diagonal are smaller while the distances between off-diagonal centers are relatively large. For example, potential cluster center 2 is close to centers 3 and 4 (with Euclidean distances less than 0.5), and away from the remaining cluster centers (with Euclidean distances greater than 0.5). Hence, we consolidate cluster centers 2, 3, and 4 into one cluster center, by removing cluster centers 3 and 4. Repeating this analysis for the rest of the potential cluster centers yields 12 unique cluster centers for initialization. Table 4.1 gives the values of pipeline orientation, pipe and particle diameters (D, d_p), liquid viscosity (μ_l), superficial liquid and gas velocity (v_{sl}, v_{sg}) for these 12 cluster centers. All cluster centers have elbow geometry.

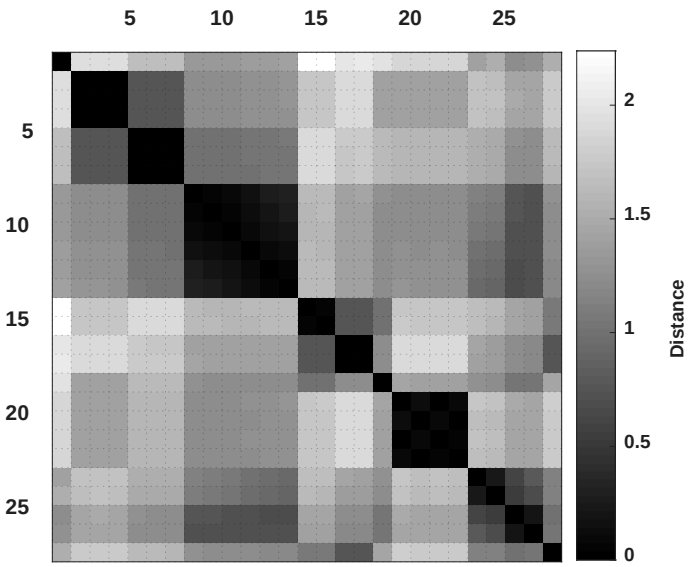

Figure 4.7: Paired distances of 27 cluster centers

Table 4.1: Cluster centers for initialization

	Orientation	***D* (in)**	**d_p (μm)**	**v_{sl} (m/s)**	**v_{sg} (m/s)**
1	vertical	2.1	350	0	107.0
2	vertical	2	150	3.9×10^{-3}	28.9
3	vertical	2	300	4.1×10^{-3}	28.9
4	vertical	2	300	5.2×10^{-3}	28.9
5	horizontal	4	150	8.8×10^{-3}	15.2
6	horizontal	4	300	1.2×10^{-2}	15.2
7	vertical	4	150	1.2×10^{-2}	22.9
8	vertical	2	150	3.1×10^{-3}	30.5
9	vertical	3	300	4.1×10^{-2}	49.0
10	vertical	3	300	4.0×10^{-2}	27.0
11	vertical	3	300	1.8×10^{-2}	27.0
12	horizontal	3	300	1.8×10^{-2}	40.0

The OCIL clustering algorithm constructed the final cluster set, which contained twelve clusters. The feature weights used for numerical and categorical attributes is 0.33, 0.26 and 0.4 (Eq. (4.4)). Table 4.2 gives the cluster centers of pipe and particle diameters (D, d_p), and the number of data points, flow regime(s) and the average AM for each cluster. Nine clusters have around or more than 30 data points, which are enough to develop highly non-

linear relationships using GPMs [97]. For the remaining three clusters, the variances of the GPMs may decrease with additional data points. However, if the additionally collected data points fail to provide extra information about the underlying model, the variance still cannot be guaranteed to decrease. Table 4.2 also reveals that there are six clusters (cluster 2, 3, 4, 8, 9 and 12) with data points from both mist and annular flows. The overlap of flow regimes in the clustering results may suggest a problem in the flow pattern predictions, especially for mist and annular flows. We hypothesize that a sharp decrease in prediction error trends can be expected if more accurate boundaries can be predicted between different flow regimes. Since the erosion-rate prediction model is flow regime dependent, if the model can better capture the differences between flow regimes, especially between the mist and annular flows, the model discrepancy may become more representative of the input conditions. Thus, a smaller predictive variance from GPM and a smaller overall AM can be obtained. Clusters six and seven contain data mostly collected from slug flow and have the highest average AMs. The data points with higher AM values are from conditions of very small particle sizes (20 μm) and relatively larger liquid viscosity (40 cp) where SPPS 1D version 5.1 model used tends to under predict. The particle movement and impingement under these conditions may not follow the model assumptions for larger particles (>50 μm).

Figure 4.8 shows the histogram of the average AM values. Again, we grouped the data based on flow regimes as an easy comparison to the results without clustering (Figure 4.3) and results from clustering based on flow regimes (Figure 4.5). There are more number of data points spreading in ranges between AM values of 0.0001 mils/lb and 0.001 mils/lb for gas, annular, churn and slug flows. Mist flow exhibits smaller maximum average AM values. However, liquid flow fails to show an improvement compared to the previous

approach. The overall AM is 14.57 mils/lb and the average AM is 2.49×10^{-2} mils/lb. The total RMSE of erosion rate prediction is 0.13 mils/lb. Though the total RMSE value is comparable to the flow regime based clustering, we obtain the minimum RMSE in each flow regime out of the three approaches except for the slug and liquid flows and the prediction uncertainty has greatly reduced using the OCIL clustering approach.

Table 4.2: Cluster centers and relevant data obtained by the OCIL approach

	D (in)	d_p (μm)	No.	Flow regime	AM_{avg}
1	1	150	12	Gas, An	1.0×10^{-2}
2	1	250	20	Gas, Mi, An, Ch	9.3×10^{-3}
3	2	150	95	Mi, An	6.7×10^{-3}
4	2	300	83	Mi, An, Ch, Sl	3.3×10^{-2}
5	2	350	28	Gas, Mi	5.2×10^{-3}
6	3	20	15	Sl	2.4×10^{-1}
7	3	300	85	Sl, liquid	7.5×10^{-2}
8	3	300	71	Gas, Mi, An, Sl	3.7×10^{-3}
9	3	300	32	Mi, An (horizontal)	1.5×10^{-3}
10	4	150	37	An, Ch (horizontal)	4.6×10^{-3}
11	4	150	78	Gas, An, Sl	3.6×10^{-3}
12	4	300	29	Mi, An (horizontal)	2.9×10^{-3}

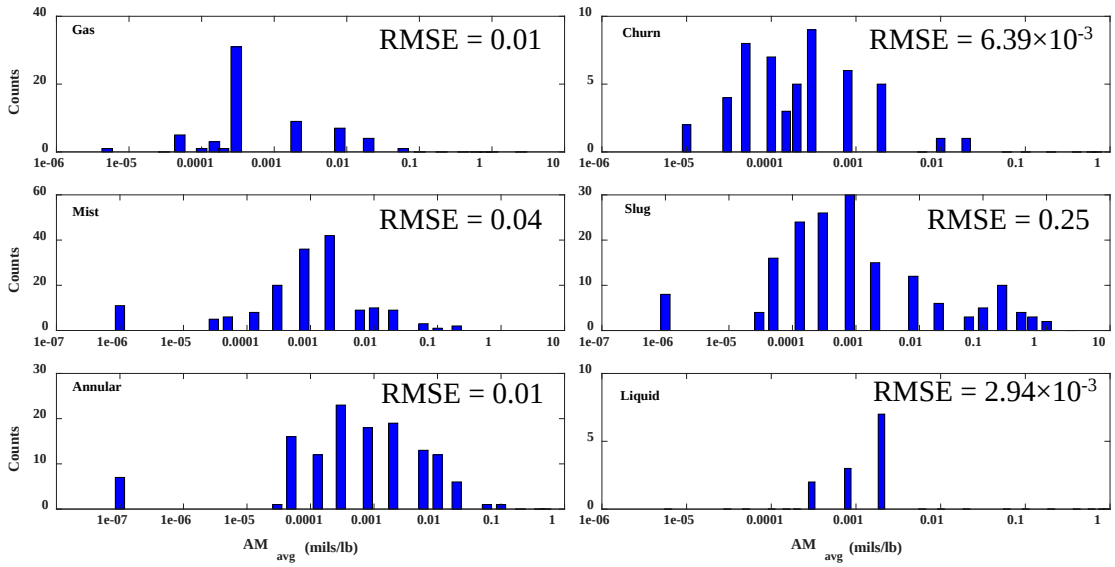

Figure 4.8: Histogram of average individual-data AM values with OCIL clustering

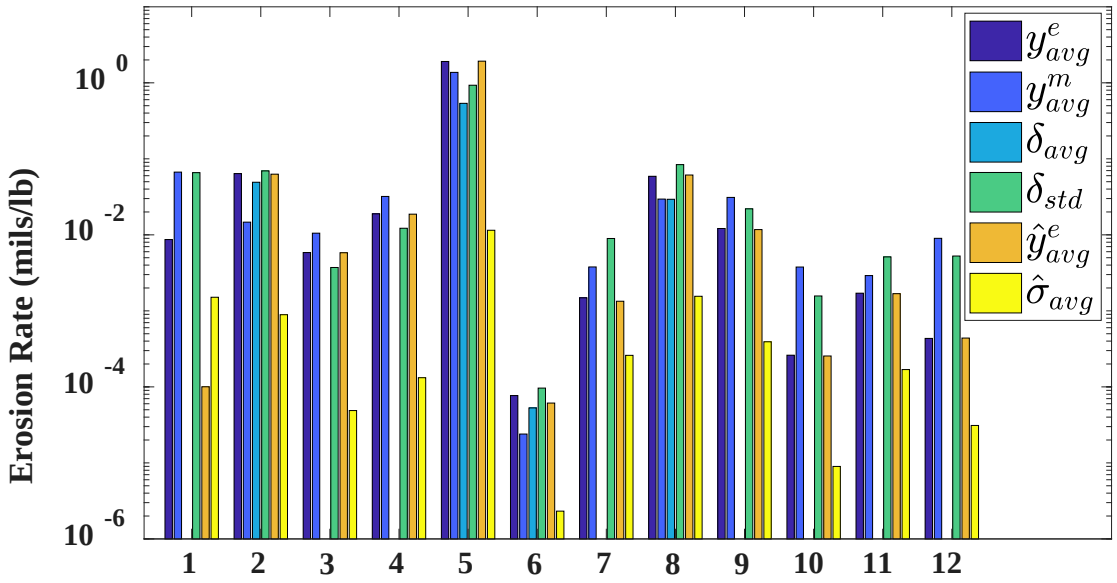

Figure 4.9: Averaged erosion rate prediction using GPM with OCIL clustering

In Figure 4.9, the prediction results for each cluster are given in a similar format of Figure 4.6 for the OCIL clustering approach. This plot also suggests that, on average, the predicted erosion rates using GPM are closer to measured values than model predictions for all clusters except for the first cluster, which is developed with limited number of data points. It can also be observed that the model tends to under-predict erosion rates of the 2nd, 5th, 6th and 8th clusters. The variances of actual model discrepancies (δ) of each cluster are still large. However, the variances ($\hat{\sigma}$) of predicted erosion rates using GPM have shrunk, which means the predicted erosion rates using GPM, in general, have smaller uncertainties. The OCIL based clustering approach reduced the overall AM by 36.7% compared to flow regime based clustering and 49.5% compared to predictions without clustering.

The prediction results separated by the flow regimes are given in Figure 4.10 for easy comparisons to the results of the first two approaches (Figure 4.4 and Figure 4.6). Figure 4.10 suggests that, on average, the predicted erosion rates using GPM (5th set) are closer to

measured values (1st set) than model predictions (2nd set) for all flow regimes except for liquid flow. The model also tends to under-predict erosion rates in gas and mist flows. However, using OCIL clustering, the standard deviations ($\hat{\sigma}_{avg}$) have been greatly reduced compared to the results obtained without data clustering (Figure 4.4) or flow regimes based clustering (Figure 4.6). Thus, these improvements lead to a smaller overall AM and give more confidence in the predicted model discrepancy of the erosion-rate model.

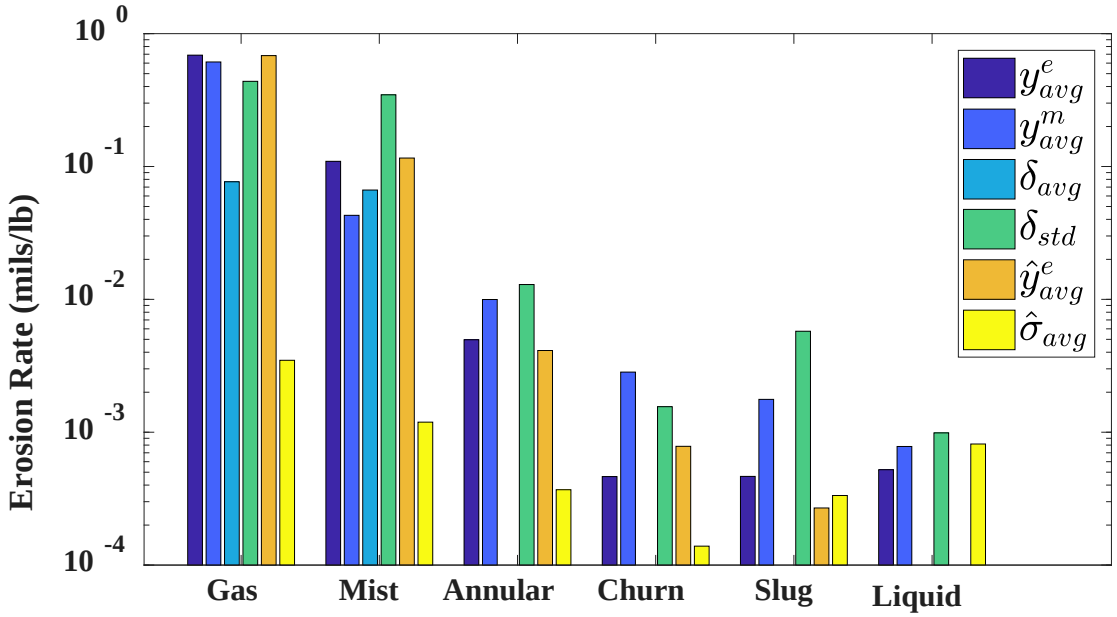

Figure 4.10: Averaged erosion rate prediction using GPM with OCIL clustering separated by the flow regimes

4.5.3.4 Impact of Proposed Initialization Scheme

To assess the performance of the proposed initialization scheme, the OCIL clustering algorithm is run 50 times using randomly generated 12 initial cluster centers. The GPMs are trained for each cluster, and the overall AM is calculated for each cluster set. The cluster set with the minimum overall AM value is selected. This cluster set contained nine clusters with an overall AM of 13.84 mils/lb.

Both approaches (i.e., proposed schema (Table 4.2) and random initialization (Table 4.3)) yielded clusters with similar operating conditions, where data are separated based on material hardness, pipe diameters and particle sizes. The proposed initialization scheme grouped data points in horizontal orientation into three clusters, while the random initialization grouped data points in horizontal orientation into one cluster. The overall AMs are comparable to each other. However, the proposed initialization scheme should only be run once and takes a considerable shorter computational time (30 CPUs) compared to the random one that requires multiple initializations (for 50 random initializations, it takes 4170 CPUs). The results recommend clustering the data using the OCIL metric and using the proposed initialization scheme for obtaining the best predictive capability for erosion rates most efficiently.

Table 4.3: Cluster centers and relevant data obtained by the random initialization

	D (in)	d_p (μm)	No.	Flow regime	AM_{avg}
1	3	300	81	Gas, Mi, An, Sl	1.8×10^{-2}
2	2	150	96	Mi, An	2.1×10^{-3}
3	3	300	79	An, Sl	3.4×10^{-3}
4	4	150	21	Gas, Mi, An	1.4×10^{-2}
5	2	350	28	Gas, Mi	3.8×10^{-1}
6	3	20	30	An, Sl	1.6×10^{-4}
7	4	150	178	Gas, Mi, An, Sl (partially horizontal)	4.0×10^{-3}
8	1	150	11	Liquid	6.5×10^{-4}
9	2	300	61	Mi, An	4.7×10^{-3}

4.5.3.5 Physical interpretation of AM

To display the physical meaning of the AM value, we devise a variable AM_{div} and define it as the division of the individual-data AM value to its experimentally measured average erosion-rate. The variable AM_{div} considers both prediction bias and uncertainty,

and its comparison to the experimental measurement is easier to show the difference in magnitude. In cases when we have more confidence in the predicted erosion-rate, the prediction is closer to the measured data, and a smaller AM_{div} is obtained. However, there are cases where AM_{div} is orders of magnitude higher than the measured value. It can be caused by either or both of the following facts: (1) a big discrepancy between the predicted erosion-rate and the measured data; (2) a large prediction uncertainty. We draw the histogram of AM_{div} for each of the three approaches in Figure 4.11. The three differently shaded bars show the number of data points falling into a certain range when all data points or data clustered based on flow regimes or data clustered based on OCIL clustering are used to train the GPM. Some data points have very large prediction mismatch or uncertainties with the AM_{div} greater than 10000. When not using any clustering, the AM_{div} spans the range from 0.01 to 10000. However, AM_{div} from both clustering approaches shrink to a minimum at the order of 10^{-6}, which indicates a very reliable uncertainty prediction. There are more number of data points from the OCIL clustering in the range from 1×10^{-6} to 1×10^{-1}. This is in line with our conclusion that the results from the clustering based on OCIL are more accurate and reliable.

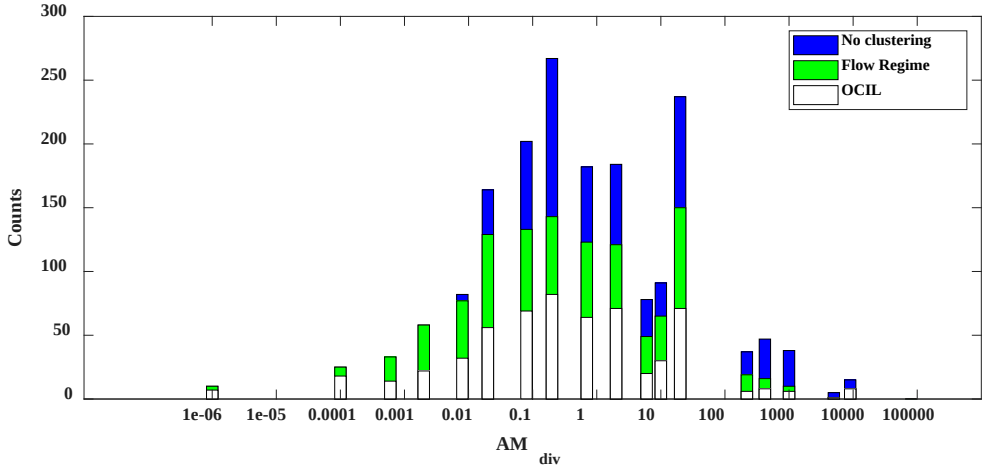

Figure 4.11: AM_{div} of the three approaches

4.6 Incorporation of Gaussian process classification approach

In the previous studies, the training data is normalized to [0.1, 1] to remove the influence from variables exhibiting different orders of magnitude. Although the normalization approach reduces the range of the data points, it still masks some important information, especially in regions around the origin, i.e., where erosion-model prediction discrepancies are very small. The absolute model discrepancies range from 1.32×10^{-6} to 2.54 with the smallest pairwise difference equal to 1.57×10^{-6}. There are significant inconsistencies in GPM predictions in these regions, and, GPM fails to estimate the correct sign of the model-discrepancy resulting in contradicting conclusions on whether the used erosion model (in this case, the SPPS 1D version 5.1) under or over-predicts the erosion rate. Correct identification of regions where an erosion-rate prediction model over- or under- predicts the actual erosion rates has significant engineering consequences. Significant of over-predictions may result in overdesign, increased capital costs, and production limitation. On the other hand, even small under-estimations can lead to facility integrity issues, and, may result in considerable downtime for equipment repairs.

In this section, we introduce a new approach to overcome these challenges. The approach distributes the data into a finer grid, yet still resolves the challenges associated with large data ranges, and hence, it enhances differentiability of data when constructing GPM. It combines GPM classification and log transformation, and introduces them to our previously developed systematic framework for model-uncertainty quantification. After log transformation of model discrepancies, the data ranges from -13.54 to 0.93, and the smallest pairwise difference in the transformed data grows to 1.38×10^{-3}. Figure 4.12 shows the transformed model discrepancy values, which are easier to differentiate (larger smaller

pairwise difference) between different operating conditions and which span a smaller range.

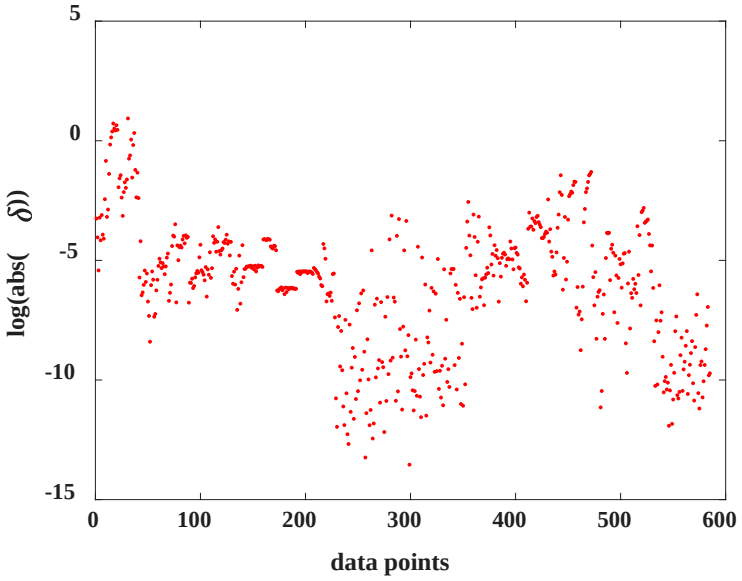

Figure 4.12: Log transformation applied to the absolute value of model discrepancy

In the developed approach, GPM-based classification [98] is applied to estimate the sign of the discrepancy, while GPM regression [99] trained using log-transformed absolute values of model discrepancy is employed to estimate the magnitude of the discrepancy. These approaches, comprising our new systematic framework, is still employed for uncertainty estimation of SPPS 1D version 5.1 model [27]. Our analysis indicates that using the log-transformed data improves the uncertainty quantification of erosion-rate modeling, and results in an additional 20% reduction in prediction uncertainties when compared to the previous approach.

4.6.1 Gaussian Process Classification Approach

We first compare three commonly used classification approaches for binary classification problems. They are classification tree, logistic regression and Gaussian process classification. Classification tree [100] involves selecting input variables and forming splits based on the selected variables' values using a greedy algorithm to minimize a cost function. Logistic regression [101] estimates the probability of class membership as a transformation of a multilinear function of the input variables. Gaussian process classification [98] replaces the linear logistic model with a Gaussian process.

Figure 4.13 gives an example to predict the type of tumor using the classification tree. In this example, the type of tumor is dependent on the tumor size and weight. The first level of the tree splits at the tumor size, where if the data is of tumor size greater than 10 mm, the classification tree predicts it as a malignant tumor; while if the size is less or equal to 10 mm, a second level of tree is developed. In this level, the tree splits further on the weight variable, where if the data with size smaller or equal than 10 mm weighs more than 5 g, it falls into malignant type; if not, then it is predicted as benign. It is a simple case, and we can see, in each level, the tree is developed based on both the selection of variables (size or weight) and the particular values (10 mm of the size) to split the data based on the selected variable.

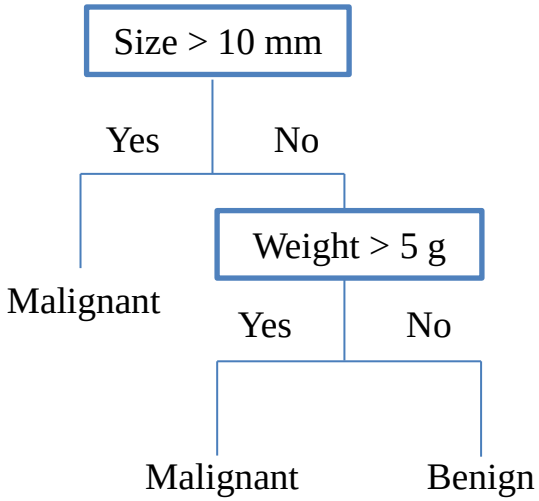

Figure 4.13: Example of a classification tree

The logistic regression approach [101] develops a multilinear function of the input variables and uses the logistic function to transform the classification prediction as a probability restricted to (0, 1). Although the binary classification result in a yes-or-no (type A or B) prediction, the logistic regression gives the estimate as a probability instead. In some cases, the probability might be used directly, but with a predefined cutoff/threshold value, prediction from logistic regression can also be translated into a binary decision. The $h_\theta(x)$ equation in Figure 4.14 illustrates the general logistic regression format. With the given formulation, a cutoff or threshold equal to 0.5 is defined as shown by the dashed line. Therefore, in this case, the data with probability greater than 0.5 is classified into the malignant type and the data with probability smaller than 0.5 is classified as benign. In general, the cutoff is defined in a way where few data points have the probabilities exactly equal to the cutoff value, which minimizes classification failures.

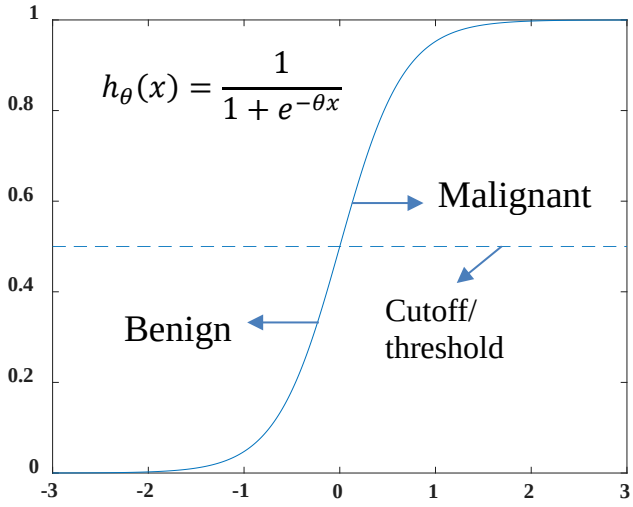

Figure 4.14: Example of a logistic regression

Gaussian process classification (GPC) has a similar implementation as the logistic regression approach. Instead, the multilinear function is replaced by a Gaussian process. The configuration of GPC is equivalent to the one of GPR, except that the predictive probability is not used directly as the output. A predefined cutoff is defined to classify over- or under- predictions of SPPS 1D version 5.1 model.

To choose the most appropriate classification approach from the three, confusion matrix is used as the criteria for checking classification accuracy [102]. Table 4.4 shows the definition of confusion matrix where positive and negative are the binary classification types to be obtained. There are four results based on classification prediction results. The first case has the true condition from the positive type to be predicted correctly as positive and results in the True Positive Rate (TPR). The second case has the true condition from the positive type to be predicted incorrectly as negative and results in the False Negative Rate (FNR). The third case has the true condition from the negative type to be predicted incorrectly as positive and results in the False Positive Rate (FPR). The last case the true

condition from the negative type to be predicted correctly as negative and results in the True Negative Rate (TPR). The True Positive Rate (TPR) or sensitivity and the False Positive Rate (FPR) or selectivity are commonly used to check the prediction accuracy. The TPR is calculated as $\frac{TP}{TP+FN}$, where the TP and FN represent the number of data points categorized into true positive and false negative types, respectively. The FPR is calculated as $\frac{FP}{FP+TN}$, where the TN and FP represent the number of data points categorized into true negative and false positive types, respectively.

Table 4.4: Confusion matrix for classification approach

		Predicted Condition	
		Positive	Negative
True Condition	Positive	True Positive (TP)	False Negative (FN)
	Negative	False Positive (FP)	True Negative (TN)

There are 213 "Positive" cases in our database where the SPPS 1D model is under-predicting the erosion rate compared to the experimental measurement, and 372 "Negative" cases, where the SPPS 1D model is over-predicting. Another criterion based on the confusion definition is the prediction accuracy (ACC). It counts ratio of the total number of true positive and true negative in terms of all the data used for classification. Therefore, a higher accuracy value means a better classification result. The Receiver Operating Characteristics (ROC) of a classifier shows its performance as a tradeoff between selectivity and sensitivity [103]. The area under the ROC curve (AUC) is a convenient way of comparing different classifiers. A random classifier has an area of 0.5, which means for a given set of data, the positive and negative predictions are assigned randomly. The ideal classification approach will generate an area close to one. Figure 4.15 shows the ROC

curves for classification tree, logistic regression and Gaussian process classification approaches for predicting the sign of log-transformed model discrepancy. The corresponding AUC values are listed in Table 4.5. The Gaussian process classification gives the maximum AUC value compared to the other two approaches. Furthermore, by selecting a Gaussian process based approach, we are confining the framework to Bayesian supervised learning area. Therefore, the GPC is used to predict whether an input condition will be over- or under-predicted by the erosion prediction model, SPPS 1D version 5.1, for this dissertation. The GPC combined with the GP regression approach forms the new framework for uncertainty analysis of erosion-rate models.

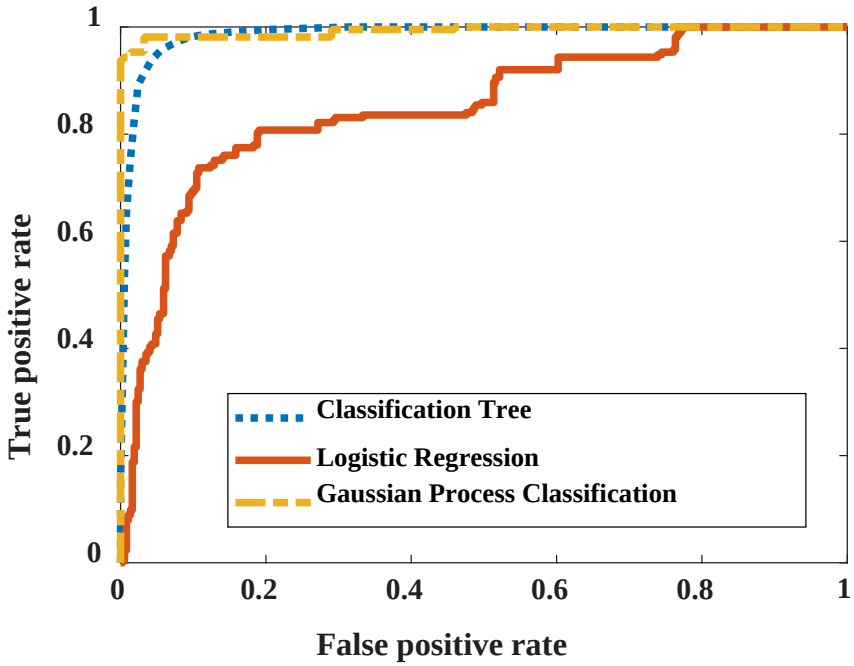

Figure 4.15: ROC curves of the three classification approaches

Table 4.5: AUC values for the three classification approaches

classification approaches	AUC
Classification Tree	0.987
Logistic Regression	0.849
Gaussian Process Classification	0.993

4.6.2 Unbalanced Classification Cost

The ROC curve can also be used to choose the best threshold value for binary classification as well [104]. The best threshold value is chosen in a way that the classifier gives the best tradeoff between selectivity and sensitivity. In terms of the cost generated by failed classification, the best threshold value considers the cost of failing to detect positive classes against the cost of failing to detect negative classes (i.e., raising false alarms). In our study, there are two types of classification failure for the sign prediction:

1. The GPC predicts a positive sign, which means that the SPPS 1D version 5.1 is under-predicting the true erosion rate, but the actual data shows a negative sign (a false positive case).
2. The GPC predicts a negative sign, which means that the SPPS 1D version 5.1 is over-predicting the true erosion rate, but the actual data shows a positive sign (a false negative case).

In field applications, the second type of failure can result in more severe consequences (resulting in great cost) than the first one because productions based on the predictions with the second type error result in faster pipe failure and production lost. Therefore, we can introduce unequal weights for the two types of failures as a guidance for development of Gaussian process classification models. The TPR, FPR and ACC values vary according to

the weights selected. Since false negative can cause integrity issues in the pipeline transportation, greater weights/cautions are added to avoid the second type of failure.

To include the influence of different weights on the classification problem, we introduce a factor, *m*, as the ratio of the weights of the first error type to the second error type. For example, if *m* is equal to one, it means that the two types of errors are treated equally important in the classification problem. However, if *m* is equal to three, it means that the first error type is three times more important than the second error type. Following this definition, the classification models (GPC models) using three different *m* values are trained. The results along with the one from the original classification model are summarized in Table 4.6. It can be observed that with increasing *m* values, the classification threshold is decreasing, which indicates more instances are predicted as under-predicted and results in a reduction of the first error type. Accordingly, the TPR and FPR values are increasing. However, the prediction accuracy (ACC) is not significantly changing. This finding relates to the tendency of the classification model to balance between the two error types, which suggests a minimal reduction in prediction accuracy with introduction of unequal weights. The difference in weights reflects our biased concern on the pipeline failures caused by the first type of error. In practical applications, the *m* value can be tweaked by the end users based on the production demands.

Table 4.6: Classification errors with unequal weights

M	**1**	**3**	**5**	**10**
Threshold	0.62	0.20	0.20	0.20
TPR	0.77	0.94	0.94	0.95
FPR	0.05	0.17	0.18	0.18
ACC	0.88	0.87	0.87	0.87

4.6.3 Results as a Combination of GPM and GPC

With the introduction of the Gaussian process classification approach, the framework for erosion discrepancy prediction is updated as shown in Figure 4.16. Based on the updated framework, the log transformed model discrepancy is the output from the GPM regression model and the sign of the model discrepancy is predicted by the GPC model. The results of the GPM regression model and GPC model are combined to estimate the model discrepancy and experimental erosion rate.

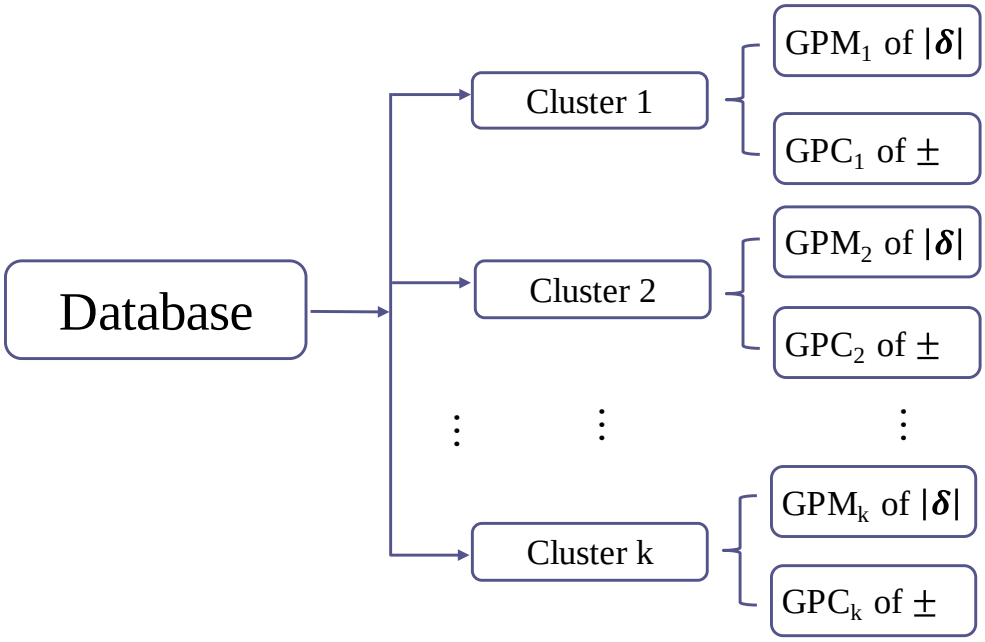

Figure 4.16: Updated framework for erosion discrepancy prediction

Applying the new framework to the clusters obtained in section 4.5.3.3, the area metric for each cluster has been calculated. The results presented in Section 4.5.3 did not consider the uncertainty from data for illustration and comparison of the proposed clustering approaches. However, to compare the previous results to the new framework which combines the Gaussian process classification approach, the AM value for OCIL based clustering is recalculated where data uncertainty is incorporated.

Figure 4.17 shows the bar plot of the AM values for each cluster using the previous and the new framework. The overall AM values using the previous framework is 24.5. By introducing the log transformation and combining with the Gaussian process classification, the overall AM values decreases to 15.4. The results based on the new framework reduces the overall AM by 37% compared to the one without log transformation. In summary, log transformation combined with classification approach can better capture the impact of operating conditions on model discrepancy values.

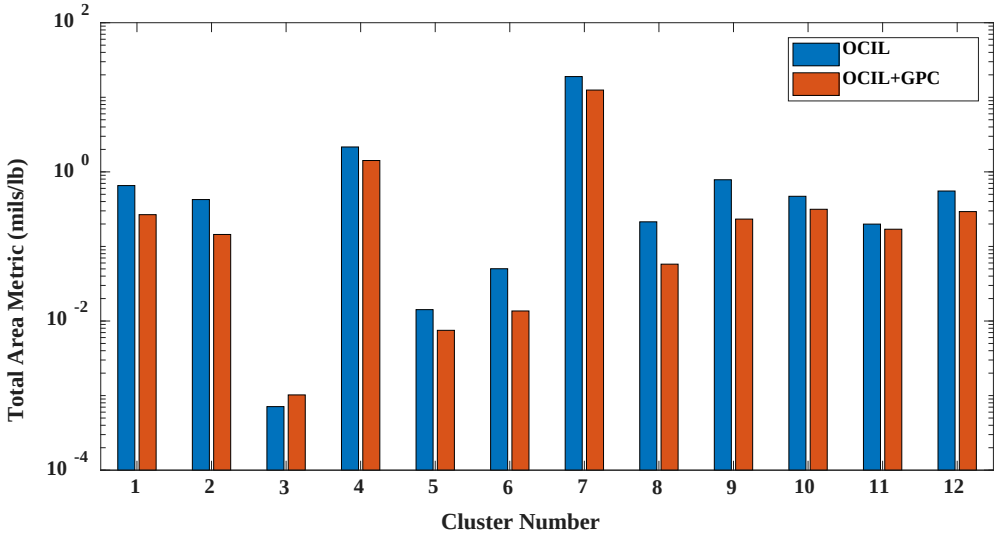

Figure 4.17: Area metric value for each cluster with OCIL clustering using/not using log-transformed model discrepancy and Gaussian process classification

4.7 A Bi-objective Optimization Approach to Reducing Uncertainty in Pipeline Erosion Predictions

The Gaussian process (GP) model estimations of erosion discrepancy can be evaluated considering two factors: (1) the mean prediction of GP model, which quantifies the prediction accuracy, and is generally defined by the squared residual between the mean prediction of GP model and the target, and (2) the confidence on the GP model predictions, which is indicated by the covariance function and can be quantified using the overall

prediction variance (Eq. (4.18)). The two factors can be quantified using area metric (AM, [85]). An accurate GP model should yield the minimum mean squared error (MSE) and the minimum variance. However, in our current study, the hyperparameters were obtained by minimizing the negative log marginal likelihood based on the Maximum Likelihood Estimation approach (MLE [43]). Although MLE is considered the gold standard for statistical parameter estimation, it cannot guarantee the two aforementioned objectives are satisfied at the same time. Furthermore, for non-convex marginal likelihood functions, optimization approaches like conjugated gradient is sensitive to the selection of initial values, and may lead to local optima.

$$\min_{\theta} \frac{\sum_{i=1}^{N} \hat{\sigma}_i^2}{N} \tag{4.18}$$

where $\hat{\sigma}_i^2$ stands for the estimated variance of the model discrepancy for the i^{th} data point.

In this section, we present a bi-objective optimization approach for training GP models of erosion prediction uncertainty. The objectives are the mean squared error, and the overall prediction variance. The ε-constrained approach [105] is used for generating the Pareto optimal set, where the Pareto front shows the tradeoff between the two objectives. The Bayesian optimization algorithm [106] is employed to solve the resulting optimization problems. Spectral mixture kernel [83] with a special initiation scheme is used to estimate model uncertainty of erosion-rate predictions, which can be solved more efficiently with the introduction of Bayesian optimization approach.

Bayesian optimization, a method used with black-box models with moderate dimensions, is well-suited for the optimization of hyperparameters in machine learning approaches [106], and it has been shown that is less likely to be trapped at local minima [107]. Bayesian optimization approach sequentially evaluates the objective function as a

black-box deterministic function. The approach uses acquisition function (α_n) to search for new data points to evaluate the objective function. Acquisition function provides a balanced sampling between exploration and exploitation.

For estimating GP model hyperparameters, the objective function can only be approximated using Gaussian process modeling. Figure 4.18 shows the flowchart of Bayesian optimization algorithm to determine the hyperparameters. In Figure 4.18, the GP model used as the objective function in the Bayesian optimization is referred as GP2 to differentiate it from the GP model used for estimating erosion model discrepancy. The posterior distribution of GP2 reveals areas not modeled well (with large uncertainty) and the objective function values at sampled points reveal the region where the minimum value may lie. The algorithm starts by training GP2 given initial *n* sample points. A new sample point with the maximum α_k is selected. The new sample and its corresponding objective function value are then used to update the distribution of GP2. The acquisition function based on $n + 1$ data points are calculated and utilized to determine the next sampling point. The whole process is repeated until the difference in the objective function values at the latest two samples is smaller than a threshold ϵ (Figure 4.18).

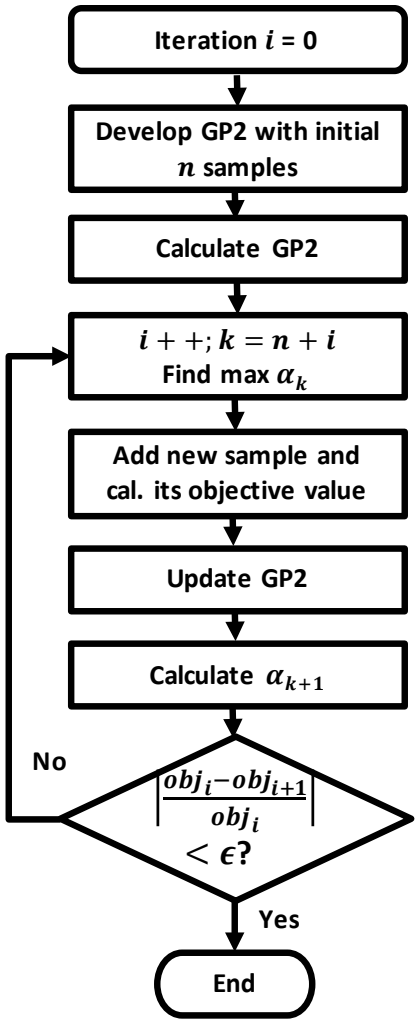

Figure 4.18: Bayesian optimization algorithm used to determine the hyperparameters

Another kernel function, Spectral mixture kernel [83] (Eq.(4.19)) with a special initiation scheme is used in the GM model to predict model uncertainty of erosion-rate predictions for our database. Spectral mixture (SM) kernel contains *Q* scaled mixture of Gaussian distributions, and in this way, a wider range of spectral density can be covered and any stationary kernels can be approximated with high accuracy.

$$k_{SM}(x, x') = \sum_{q=1}^{Q} w_q cos(2\pi(x - x')\mu_q) \prod_{d=1}^{D} exp\left(-2\pi^2 (x - x')^2 v_q^{(d)}\right) \quad (4.19)$$

where w_q's are the weights indicating the relative importance of each mixture component, the inverse means $1/\mu_q$ are the period of components and the inverse standard deviation $1/\sqrt{v_q}$ stands for the length scale which controls the influence from each input dimension. The three sets of hyperparameters, which are w_q, μ_q, and v_q, are initialized based on data-dominated priors [108].

The hyperparameters in the kernel function for the covariance and the constant value used in the mean function form the set of hyperparameters (θ) that are optimized using the data for training the GP model.

The same dataset with 585 samples are used for training and testing the GPM. The function `bayesopt` in MATLAB is used to develop the Bayesian optimization approach. Cross validation is used to evaluate the generality of the developed GPMs.

The optimization problem is solved using training data set constructed by a four-fold cross validation. The hyperparameter values obtained with the highest marginal likelihood from the Spectral mixture kernel initialization (based on data-dominated priors) are used as the initial values for θ to be optimized by Bayesian optimization approach. To evaluate the objective function efficiently in a Bayesian optimization process, the expected improvement with time-weighting is used as the acquisition function [109]. The Bayesian optimization process is continued until the difference of the objective function values at the latest two evaluations is smaller than 1×10^{-3}.

The optimum objective function values of the minimum MSE (Eq. (4.8)) and minimum VAR (Eq. (4.18)) yielded 6.03×10^{-7} $(\text{mils/lb})^2$ and 1.74×10^{-8} $(\text{mils/lb})^2$, respectively. The corresponding VAR and MSE values were 1.41×10^{-1} $(\text{mils/lb})^2$ (Eq. (4.18)) and 3.48×10^{-6} $(\text{mils/lb})^2$ (Eq. (4.8)). The minimization of MSE with the VAR as the ε-constraint yields

the Pareto front shown in Figure 4.19. The corresponding MSE and VAR values obtained when hyperparameters are estimated using MLE with the same initialization scheme are also calculated for comparison, and they are 8.66×10^{-4} $(\text{mils/lb})^2$ and 3.40×10^{-3} $(\text{mils/lb})^2$. These values sit far above the Pareto front, revealing the advantage of constructing the problem as a bi-objective optimization problem and a potential disadvantage of using MLE to achieve both precision and reliability for prediction of erosion model discrepancy.

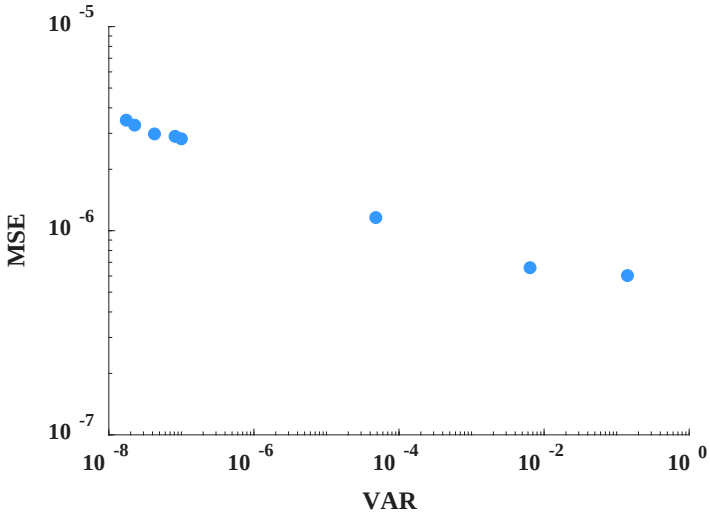

Figure 4.19: Pareto front obtained for the bi-objective problem

The corresponding overall area metric values, for the overall dataset without clustering and without the consideration of data uncertainty, changes from 0.62 (for the left most data point) to 5.54 (for the right most data point), which shows a great reduction in the overall AM values considering the application of Spectral kernel and Bayesian optimization approach.

The root mean square error (RMSE) of erosion model discrepancy for the database is 3.32 mils/lb, indicating for per pound of sand particles transported in the pipeline, there are 3.32 mils (thousandth of an inch) length loss of pipe inner wall incorrectly predicted by

SPPS 1D version 5.1 model. Considering the case with natural gas transported at a rate of 3.0×10^{8} standard cubic feet per day (a very typical production rate in oil and gas transportation), the yearly thickness loss calculated is less than 20 mils. According to ANSI/ASME Standard B31.3 (applies to major facilities onshore and offshore worldwide), the minimum design wall thickness is 0.11 inch (110 mils) [110]. Therefore, this miscalculation is significant, and the uncertainty will accelerate when the model is applied to estimate erosion rate under a long period of time. The RMSEs of the erosion model discrepancy using the optimum GP models obtained by the bi-objective optimization method range from 7.76×10^{-4} to 1.86×10^{-3} mils/lb. Given the same rate of gas transported in the pipeline, for unit sand particles transported, the uncertainty of erosion rate is at most off by 1.86×10^{-3} mils on average. It can be concluded that the predictions obtained from the bi-objective problem are accurate with small prediction biases.

4.8 Conclusion

This section introduced clustering methods to Gaussian processing modeling to estimate the model prediction uncertainties based on a database with a wide range of input conditions. A clustering approach for datasets with mixed attributes is adopted for identification of data with similar characteristics. A new initialization scheme is proposed for the clustering approach. This scheme is shown to reduce the computational burden faced in clustering studies due to random initialization. For each cluster, model discrepancy predicted by GPM is added to the prediction from the model to remove model's bias. The prediction results based on the novel clustering approach are shown to be more reliable in the model uncertainty quantification as tighter confidence intervals are observed. Furthermore, to deal with the wide range of model discrepancies, Gaussian model

classification is introduced. The new approach also manifests the importance of using unequal weights for different classification errors. Lastly, we revisited the hyperparameter optimization using a bi-objective optimization framework. Gaussian process modeling trained using bi-objective optimization outperform the GP model trained using the MLE based approach in terms of precision and reliability for the prediction of erosion model uncertainty. The proposed framework can also be applied to other models and used as a guide for future model development and experimental designs.

CHAPTER 5

DIMENSIONAL ANALYSIS

5.1 Introduction

The experimental data used in model validation and uncertainty quantification are normally collected in a laboratory environment. For example, due to cost and space limitations, most experiments are conducted using small pipe diameters (from one to four inches) while in the field conditions, the pipe diameters generally exceed eight inches. Hence, the predictions of erosion models are routinely extrapolated to conditions where experimental data is not available. The quantification of the uncertainty is especially important during the design phase for subsea applications, as predicted erosion rate allowance is one of the important factors in determining the maximum production capacity of the facility.

To develop a framework capable of quantifying uncertainty of the model's prediction of erosion-rate under a wide range of input conditions, especially focusing on regions where experimental data is scarce or not available, dimensional analysis is introduced. Dimensional analysis (DA) is a method for grouping and reducing the number of independent variables that affect a given physical phenomenon [111]. It can suggest the representation of a process using dimensionless numbers, and most importantly, provide an insight into the form of the physical relationship between the response and independent variables. Furthermore, dimensional variables are generally collected from a limited scale

in laboratory sittings. Using dimensionless numbers, the laboratory results can scale to application scale and conditions [112].

To quantify the model uncertainty and relate to input conditions, correlations between the two are developed. In recent years, machine learning models have been proposed in quantifying complex physical phenomena using dimensionless numbers. Considering the process complexity, linear and polynomial correlations may fail to map the dimensionless numbers to the key design parameters. Shaikh and Al-Dahhan [113] has implemented Artificial Neural Networks (ANNs) to derive correlations for gas holdup with dimensionless numbers. Their ANN model gave an average absolute relative error (AARD) of 15% which is smaller than the ones generated from correlations without dimensional analysis. The ANNs have also been applied for the prediction of pressure drop across rotating packed beds [114] with gas, liquid and rotational Reynolds number as the input variables. The ANN model resulted in a highly accurate prediction of pressure drop in terms of AARD and mean square error (4.7 and 2.0×10^{-5}). Bansal et al. [115] presented an improved prediction of gas-liquid interfacial area in trickle bed reactors using Support Vector Regression (SVR) model. They also draw an interesting conclusion that using dimensionless numbers as input variables may not necessarily lead to better models in terms of prediction accuracy.

5.2 Application of Buckingham Pi Theorem for Identifying Dimensions Numbers Relevant for Erosion Process

The process to determine the dimensionless numbers contains three main steps:

1) Compile relevant independent variables. The compiling of relevant variables relies on the prior knowledge and understanding of the erosion process [116]. For

example, viscosity should be considered as one of the relevant independent variables in characterizing laminar flow, but not in characterizing turbulent flow based on prior knowledge of the two flow types. Compiling the correct set of relevant independent variables enables determining all potentially relevant dimensionless numbers.

2) Form Pi numbers. Once the relevant variables are determined, Buckingham Pi theorem [117] is applied based on the dimensions of the relevant variables and the basis dimensions considered. By forming the sets of repeating variables, dimensionless numbers from each distinct set of repeating variables are obtained.
3) Identify unique dimensionless numbers. They are identified by removing the recurrent dimensionless numbers from the aggregation of dimensionless numbers from all the sets of repeating variables and by retaining one of the dimensionless numbers with reciprocal and power relationships to each other.

5.2.1 Compile Relevant Independent Variables

Based on the analysis of erosion process, the thickness loss of pipeline is due to impingement of sand particles on the inner wall of the pipeline. The interaction of sand particles with the multiphase flow determines the momentum of sand particles during the impingement. Assumptions in this analysis include (1) the erosion takes place at standard atmospheric conditions with constant pressure and temperature (which is also the assumption of the SPPS 1D version 5.1 model [4]), (2) temporal changes in erosion rate is negligible, and (3) impact from particle hardness is negligible. Particle hardness is not considered because particles transported in pipeline are mostly sand, and experimental

studies suggest that an increase in hardness of particles has little impact on the erosion rate when compared to hardness of the pipeline [118].

For multiphase flow, sand particles travel at velocities proportional to the velocity of their entrained phase. Therefore, variables influential in characterizing flow regimes are included, i.e., superficial velocities, viscosities and densities of both gas and liquid flows, gravitational acceleration, and surface tension between the liquid and gas phases. The outcome of the sand particles impacting the wall are also dependent on the movement of the sand particles and the wall roughness and material [27]. To quantify these interactions, variables of particle size, density and sharpness, and pipeline hardness, roughness and density are incorporated. Furthermore, the movement of the sand particles is influenced by the pipeline geometry. Therefore, pipeline geometry type and diameter are considered. The list of relevant variables considered in the analysis is given in Table 5.1. The dimensions of each variable are also provided in terms of mass [M], length [L] and time [T].

Table 5.1: List of relevant variables and their dimensions

Variable	Symbol	Dimensions
Pipe roughness	ε	None
Pipe geometry	G	None
Hardness of the pipe material	H	None
Pipe diameter	D	[L]
Density of sand particles	ρ_p	$[ML^{-3}]$
Particle size	d_p	[L]
Particle sharpness	sf_s	None
Liquid viscosity	μ_l	$[ML^{-1}T^{-1}]$
Gas viscosity	μ_g	$[ML^{-1}T^{-1}]$
Liquid density	ρ_l	$[ML^{-3}]$
Gas density	ρ_g	$[ML^{-3}]$
Liquid velocity	v_l	$[LT^{-1}]$
Gas velocity	v_g	$[LT^{-1}]$
Gravitation constant	g	$[LT^{-2}]$
Surface tension	σ	$[MT^{-2}]$

Pipe roughness, geometry and material hardness are already dimensionless variables, so they are not included in forming Pi numbers. Geometry of the pipe is considered as a categorical variable in developing GPMs and is not included here. Particle sharpness is considered as an empirical factor and is not included as well. The remaining 11 independent variables are then used to form dimensionless numbers in analyzing erosion process.

5.2.2 Form Pi Numbers

With the 11 independent variables considered, mass [M], length [L] and time [T] act as the fundamental dimensions. We construct all possible sets of repeating variables, and identify the corresponding eight dimensionless numbers for each reaerating variable set using Buckingham Pi Theorem. To apply Buckingham Pi Theorem, the unit matrix of the repeating variable set is defined as the units of the three repeating variables and the remaining eight variables. An echelon form of the unit matrix [119] is used to construct the eight dimensionless numbers for this set. The echelon form is constructed by applying Gaussian elimination on the rows of the unit matrix.

A dimensionless group is defined as the group of eight dimensionless numbers that are constructed by using a single set of repeating variables. For example, suppose a repeating variable set is composed of variables σ, D and g. In Table 5.2, the unit matrix of the set is given where the first three columns correspond to the repeating variables and their dimensions and the following eight columns are the remaining variables and their dimensions.

The eight dimensionless numbers corresponding to this set of repeating variables are then obtained by using the echelon form, which is shown in Table 5.3. In the echelon form, the numbers in each column starting from the fourth column corresponds to the exponents

of the three repeating variables. The multiplication of the three repeating variables with one column of the indicated exponent yields the numerator of one dimensionless number. The corresponding variable of that column gives the denominator of that dimensionless number. For example, the values in the column corresponding to variable d_p are [0, 1, 0] (Table 5.3). The corresponding dimensionless number is $\frac{\sigma^0 D^1 g^0}{d_p}$, i.e, $\frac{D}{d_p}$. Similarly, the values of the column that correspond to the variable ρ_p are [1, -2, -1], and, the dimensionless number formed is $\frac{\sigma^1 D^{-2} g^{-1}}{\rho_p}$, i.e, $\frac{\sigma}{D^2 \rho_p g}$ (inverse of Bond number). In total, eight dimensionless numbers are obtained as shown in Table 5.4. These eight dimensionless numbers form one dimensionless group for the set with repeating variables σ, D and g. To construct other dimensionless groups, the process is repeated for each one of the repeating variable sets.

Table 5.2: Unit matrix with repeating variables σ, D and g

	$\boldsymbol{\sigma}$	$\boldsymbol{D}$	$\boldsymbol{g}$	d_p	ρ_p	ρ_g	ρ_l	μ_g	μ_l	v_g	v_l
M	1	0	0	0	1	1	1	1	1	0	0
L	0	1	1	1	-3	-3	-3	-1	-1	1	1
T	-2	0	-2	0	0	0	0	-1	-1	-1	-1

Table 5.3: Echelon form of the unit matrix with repeating variables σ, D and g

	$\boldsymbol{\sigma}$	$\boldsymbol{D}$	$\boldsymbol{g}$	d_p	ρ_p	ρ_g	ρ_l	μ_g	μ_l	v_g	v_l
$\boldsymbol{\sigma}$	1	0	0	0	1	1	1	1	1	0	0
$\boldsymbol{D}$	0	1	0	1	-2	-2	-2	-0.5	-0.5	0.5	0.5
$\boldsymbol{g}$	0	0	1	0	-1	-1	-1	-0.5	-0.5	0.5	0.5

Table 5.4: Dimensionless numbers with repeating variables σ, D and g

1	2	3	4	5	6	7	8
$\frac{d_p}{D}$	$\frac{\rho_p D^2 g}{\sigma}$	$\frac{\rho_g D^2 g}{\sigma}$	$\frac{\rho_l D^2 g}{\sigma}$	$\frac{\mu_g \sqrt{Dg}}{\sigma}$	$\frac{\mu_l \sqrt{Dg}}{\sigma}$	$\frac{v_g}{\sqrt{Dg}}$	$\frac{v_l}{\sqrt{Dg}}$

To construct sets of repeating variables for applying Buckingham Pi theorem, three out of the eleven variables are selected so that the three variables incorporate all three fundamental dimensions. For example, when one of the repeating variables is flow viscosity (including all M, L and T dimensions), then the other two variables can be selected randomly. While when superficial flow velocity is selected as the first repeating variable (only containing dimensions of L and T), at least one of the two other selected variables must contain a mass dimension (e.g. ρ_g or σ).

As can be seen from the last column of Table 5.1, there are six different compositions of the fundamental dimensions. The first composition is of the length dimension only (d_p, D). The second contains densities (ρ_p, ρ_g, ρ_l). The third and fourth are gas and liquid viscosities (μ_g, μ_l), and the superficial flow velocities (v_g, v_l). The last two compositions include gravitational acceleration constant (g) and the surface tension (σ). Based on the given dimensions, 81 repeating variable sets are constructed using these six compositions.

5.2.3 Identify Unique Dimensionless Numbers

Though the dimensionless groups are generated using different sets of repeating variables, there are many dimensionless numbers repeated several times in different dimensionless groups. For example, the ratio of diameters, $\frac{D}{d_p}$, appears in the set with repeating variables σ, D and g and is also obtained from the set with repeating variables σ, d_p and ρ_g. To identify the unique dimensionless numbers, all the dimensionless numbers from different dimensionless groups are combined and only one instances of repeating dimensionless numbers are kept in the combined set.

An examination of combined set of dimensionless numbers revealed that some of the dimensionless numbers contained the same independent variables in a form that can be obtained by algebraic modifications. For example, the ratio of diameters, $\frac{D}{d_p}$, is also obtained as $\frac{d_p}{D}$. Another example is the case where one dimensionless number might be the root or power of another one: both gas Weber number ($\frac{D\rho_g V_g^2}{\sigma}$) and its square root ($v_g\sqrt{\frac{D\rho_g}{\sigma}}$) was found in the combination set. Only one of these dimensionless numbers are retained in the combination set. According to the commonly used definition for dimensionless numbers, we keep the standard format of these dimensionless numbers.

5.3 Application of GPM

To improve prediction from erosion models, we introduce model discrepancy term and use GPM to model how model discrepancy changes with operating conditions. The erosion model prediction is then corrected by the model discrepancy term estimated using the trained GPM. However, there are more than 100 unique dimensionless numbers in the combination set. Therefore, a feature selection approach is applied to reduce the number of dimensionless numbers that will be used as inputs in GPM for estimating model discrepancy (GPM_1). The feature selection method is also used to identify two additional sets of dimensionless numbers that are strongly related to erosion rate predictions (GPM_2) and to observed erosion rates (GPM_3), respectively. The differences between these three sets are then used to provide insight for improving the analyzed erosion model. If the same set of dimensionless numbers are identified from the three models, it indicates that the erosion model incorporates the correct variables but fails to capture certain underlying

relationships of the variables. The prediction from the erosion model can be corrected by adding the model discrepancy term where the corresponding GPM captures the missing relationships. On the other hand, if different sets of dimensionless numbers are identified from the three models, the dimensionless numbers generated using GPM_1 may be used to develop physical explanations for the model discrepancies in the erosion model. The analysis of these three sets of dimensionless numbers provides a systematic way for erosion model improvement studies.

Using the identified influential dimensionless numbers from GPM_1 as inputs, a new GPM is trained (GPM_4) to predict model discrepancy. The resultant erosion predictions (corrected by the predicted model discrepancy calculated using GPM_4) are obtained and referred as P1. The prediction capability of P1 is compared to the erosion model (referred as P2). The overall process is illustrated in Figure 5.1. We stipulate that the performance of P1 should be better than P2, as the erosion model is not a perfect representation of the erosion process under the observed erosion rates [120].

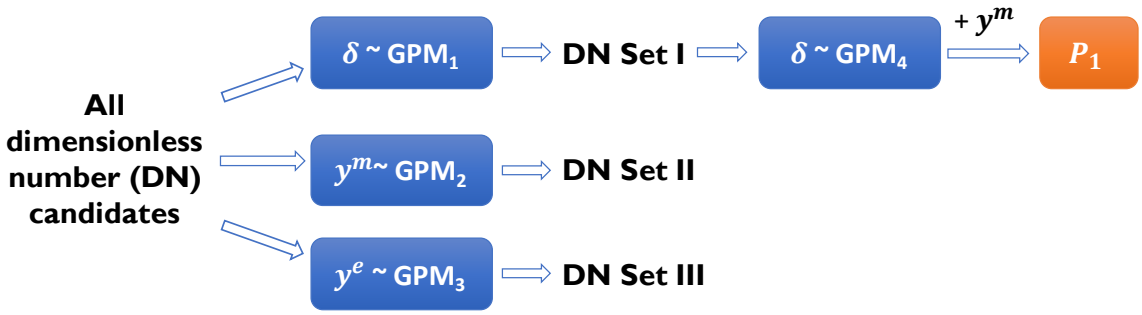

Figure 5.1: Framework of GPM predictions using dimensionless numbers

5.4 Feature Selection

Feature selection approaches determine whether a candidate feature should be included or not considering all candidate features without altering features' original form [121] (as

compared to dimensionality reduction approaches). The basic idea of feature selection is to rank the contributions of features to the accuracy of a model [122]. In this study, the automatic relevance determination (ARD) approach with a sensitivity analysis is used for feature selection.

Gaussian Process modeling has an embedded feature selection method - automatic relevance determination (ARD) [54]. Using the squared exponential (SE) kernel function for the covariance function of the GPM (Eq.(5.1)), the strength of the relationship between the features and the output are related to the optimum values of the length scale hyperparameter (l). This hyperparameter, which has the same dimension as the number of features, controls the fluctuation of GPM output with each dimension. After training the GPM, the optimum value of each length scale indicates the importance of each feature as the output of GPM varies in inverse proportion to the length scale. In other words, features with small length scale values are more important than the ones with large length scale values. By comparing the values of length scales for different features, the ARD method determines the feature rankings.

$$f \sim \mathcal{GP}(m, k),$$
$$m(x) = a, \text{ and } k(x, x') = \sigma_y^2 \exp\left(-\frac{(x - x')^2}{2l^2}\right), \tag{5.1}$$

Figure 5.2 gives an example function with an input of two dimensions. As can be seen from Figure 5.2, the output varies more rapidly with changes in input x_1 than in input x_2. The optimum values of the length scale hyperparameters for the GPM are [1, 3]. The dimension with smaller length scale value, x_1, contributes more to the changes in the output (y), while for the dimension with larger length scale value, the influence is smaller (comparing changes in y with changes in x_1 in Figure 5.2).

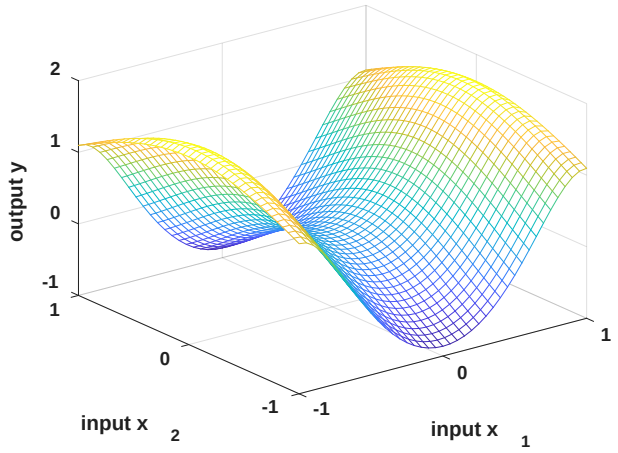

Figure 5.2: Illustration of function with two-dimensional input using ARD

In a recent study, Blix and Eltoft [123] introduced a sensitivity analysis for accurately assessing the results of ARD method. Using the trained GPM, the sensitivity of GPM output to each feature is calculated. The sensitivity of the model output to the j^{th} feature is calculated as the expected value of the squared derivative of the predicted mean function with respect to its arguments as shown in Eq. (5.2).

$$s_j = \int \left(\frac{\partial \phi(x)}{\partial x_j}\right)^2 p(x)dx \tag{5.2}$$

In Eq. (5.2), $\phi(x)$ is the mean function from GPM, $p(x)$ is the probability density function over the dimensionless numbers x and s_j is the sensitivity of dimensionless number j.

The empirical estimate of the sensitivity for the j^{th} dimensionless number is written *viz*. Eq. (5.3).

$$\hat{s}_j = \frac{1}{N}\sum_{n=1}^{N}\left(\frac{\partial \phi\left(x^{(n)}\right)}{\partial x_j}\right)^2 \tag{5.3}$$

where N is the number of training data.

We write the mean function as a linear combination of M kernel functions as $m\left(x^{(n)}\right) = \mathrm{K}(X, x_n)^T \mathrm{K}^{-1}\delta = \mathrm{K}(X, x_n)^T \alpha = \sum_{m=1}^{M} \alpha_m \mathrm{K}(x_m, x_n)^T$, where $\mathrm{K}(X_m, x_n)$ is

the squared exponential covariance function with length scale l, x_m and x_n are the m^{th} and n^{th} data from the training and test data. Then, Eq.(5.4) defines the empirical estimate of the sensitivity of the GPM output to the j^{th} feature. The prediction from GPM (mean function) fluctuates the most due to the changes in the feature with the largest sensitivity value.

$$\hat{s}_j = \frac{1}{N}\sum_{n=1}^{N}\left(\sum_{m=1}^{M}\alpha_m \frac{\left(x_{m,j} - x_{n,j}\right)}{l_j^2} k(x_m, x_n)\right)^2 \tag{5.4}$$

These concepts are illustrated using the function given in Figure 5.3. This function changes in x_1 direction and is constant in x_2 direction. The optimum values of length scales and the estimated values of sensitivities are listed in Table 5.5. Both metrics indicate that the changes in x_1 direction changes the output more significantly than the changes in x_2 direction. However, the absolute differences of the two metrics (length scales and sensitivities) between two directions vary significantly. The ratio of length scale values of x_1 to x_2 is five orders of magnitude smaller than the one of the sensitivities estimated, which demonstrates the enhanced ability of sensitivity estimates for separating important features from the non-important ones. Similar conclusions hold for multiple features.

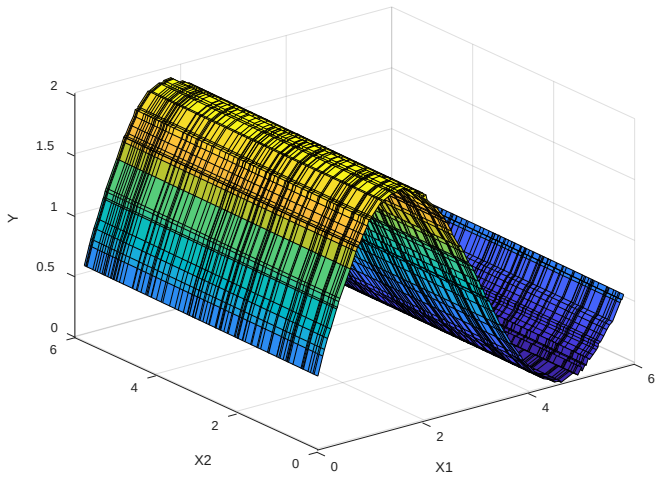

Figure 5.3: Illustration of sensitivity analysis

Table 5.5: Results obtained for length scale and sensitivity

	length scale	sensitivity
x_1	0.82	0.62
x_2	2.8	3.4×10^{-6}
Ratio	3.4	1.8×10^{5}

In this section, we identified relevant dimensionless numbers by ranking the values of length scales, i.e., using the ARD approach. The GPM with optimized hyperparameters is further assessed using the outlined sensitivity analysis [123]. As previously outlined, the model discrepancy is estimated using the mean function of the trained GPM. By conducting the outlined sensitivity analysis of the mean function to dimensionless numbers (i.e., the features), we verify that the dimensionless numbers identified using the ARD approach are indeed significant contributors to the changes in the model discrepancy predictions.

5.5 Unique Formulations of Dimensionless Numbers

For erosion process in multiphase flow, 81 sets of repeating variables are formed, which yielded 81 dimensionless groups and 648 dimensionless numbers. Hence, the cardinality of the initial combination set was 648. Applying the unique dimensionless number identification methods outlined in Section 5.2.3, the size of the combination set reduces to 108, i.e., one hundred eight unique dimensionless numbers are identified (see Appendix Table C.1). The unique dimensionless numbers belong to one of the 15 dimensionless number forms given in Table 5.6. The unique dimensionless numbers can be constructed from the 15 dimensionless number forms using variables from different phases, e.g. gas or liquid phases. For example, the density variable in Ohnesorge number can be one of the following: liquid-phase, gas-phase or sand-particle density. With the viscosity variable being selected from one of the two phases (gas or liquid phase) and the diameter variable as either pipe or particle diameter, the Ohnesorge number can lead to a total of 12 unique dimensionless numbers.

Table 5.6 reveals that eight standard dimensionless number forms are identified. They are Ohnesorge, Capillary, Froude, Morton, Weber, Reynold, Bond and Galileo numbers. Three other forms can be constructed as combinations of two standard dimensionless numbers as indicated in Table 5.6. The remaining four dimensionless number forms are ratios (see Table 5.6). Out of these dimensionless number forms, Froude, Weber, and Reynold numbers are normally used for multiphase flow analysis [124]. The other dimensionless number forms and their impacts are investigated and discussed in Section 5.6 once the feature selection approach has been applied, i.e., once we identify the most influential dimensionless numbers. Though not all of the unique dimensionless numbers formulations may be significant in quantifying the erosion rate, the identification of the

unique dimensionless numbers provides a comprehensive list of dimensionless numbers to study for locating influential ones. A similar analysis can be conducted if more relevant variables are included or there are changes in the selections of relevant variables.

Table 5.6: Unique formulations of dimensionless numbers

	Number	Definition		Number	Definition		Number	Definition
1	Ohnesorge (Oh)	$\frac{\mu}{\sqrt{\sigma d \rho}}$	6	Froude and Capillary	$\frac{\mu\sqrt{dg}}{\sigma}$	11	Galileo (Ga)	$\frac{D^3\rho^2 g}{\mu^2}$
2	Capillary (Ca)	$\frac{\mu V}{\sigma}$	7	Froude and Reynold	$\frac{\mu g}{\rho V^3}$	12	Ratio of diameter	$\frac{d_p}{D}$
3	Froude (Fr)	$\frac{V}{\sqrt{dg}}$	8	Froude and Weber	$\frac{g\sigma}{V^4\rho}$	13	Ratio of viscosity	$\frac{\mu_l}{\mu_g}$
4	Morton (Mo)	$\frac{g\mu^4}{\rho\sigma^3}$	9	Reynold (Re)	$\frac{\mu}{d\rho V}$	14	Ratio of density	$\frac{\rho_g}{\rho_l}$
5	Weber (We)	$\frac{d\rho V^2}{\sigma}$	10	Bond (Bo)	$\frac{gd^2\rho}{\sigma}$	15	Ratio of velocity	$\frac{v_g}{v_l}$

5.6 Results

5.6.1 Dimensionless numbers obtained

Following the dimensional analysis described in Section 5.2, the unique dimensionless numbers for mist, annular, churn, and slug flow using standard and angle head ER probes have been identified.

There are 108 unique dimensionless numbers identified for mist, annular, and churn flows. Using the operating conditions of experiments (585 data points) in the database, we calculate the values of these 108 dimensionless numbers. This yields a matrix with 585 rows each of which corresponds to a single operating condition (data point) and 108 columns each of which corresponds to a single dimensionless number. Three columns of the resulting matrix have the same values due to the operating conditions in the database.

Therefore, only one of these columns, i.e., one instance of the three dimensionless numbers, is kept in the matrix. Furthermore, it was observed that many of the columns are strongly correlated with each other (with correlation coefficient values greater than ±0.95). The strongly correlated columns generally correspond to dimensionless numbers belong to the same dimensionless number forms (Table 5.6). Only one of the highly correlated dimensionless numbers is kept in the matrix for the feature selection process.

As a comparison of identifying the most relevant dimensionless numbers for the model discrepancy, a similar analysis has been conducted for the SPPS 1D version 5.1 flow-regime dependent model, and the experimental measurements, where the ARD combined with sensitivity analysis has been applied.

5.6.2 Dimensionless Numbers Obtained for Mist Flow

Table 5.7 gives the influential dimensionless numbers identified for the GPMs developed for the model discrepancy (GPM_1), the SPPS 1D model (GPM_2) and experimental data (GPM_3) in mist flow. The reason only the first eight most influential dimensionless numbers are presented is due to the consideration of the number of relevant dimensional variables used for dimensional analysis (11 in total) and the number of fundamental dimensions (3 in total).

The three models share the same set of the most relevant dimensionless numbers. These dimensionless numbers have been shown relevant in erosion analysis. Weber number represents a measure of inertial forces to interfacial forces and controls the onset of liquid entrainment. Entrainment fraction is important in erosion process as it determines the ratio of liquid droplets entrained in the gas core. This fraction may also be considered proportional to the sand particles that are traveling in liquid droplets in the gas core. Sand

particles transported in gas core have greater momentum and result in more severe impingement and thickness loss. Froude number has also been found important in quantifying entrainment fraction in multiphase flow [125]. Ohnesorge number relates the viscous forces to inertial and surface tension forces. It is used in analyzing atomization and deposition of liquid droplets [126]. The atomization and deposition of liquid droplets have been found important in determination of entrainment factor [125]. Reynolds number describes the strength of sand particles especially in bend geometry [127] and determines the proper model used for flow regime prediction in multiphase flow [128]. Bond number represents the relative significance of gravitational force and interfacial tension. Mist flow forms when the annular film is totally thinned by the shear force exerted by the high velocity gas on the interface [129]. The interface between the two phases is not smooth and consists of a multitude of waves induced by the gas core. The waves may vary in amplitude and wavelength and the breakup of the large amplitude waves cause the liquid phase to be entrained as droplets in the gas core [130]. The interfacial structures suggested by the Bond number determine the fraction entrained.

Table 5.7: The most relevant dimensionless numbers identified for mist flow

	δ ~ GPM$_1$		y^m ~ GPM$_2$		y^e ~ GPM$_3$	
	Number	**Definition**	**Number**	**Definition**	**Number**	**Definition**
1	Oh	$\frac{\mu_g}{\sqrt{\sigma d_p \rho_l}}$	Oh	$\frac{\mu_g}{\sqrt{\sigma d_p \rho_l}}$	Oh	$\frac{\mu_g}{\sqrt{\sigma d_p \rho_l}}$
2	Fr	$\frac{v_g}{\sqrt{Dg}}$	We	$\frac{D\rho_l V_g^2}{\sigma}$	Fr	$\frac{v_g}{\sqrt{Dg}}$
3	We	$\frac{D\rho_l V_g^2}{\sigma}$	Fr	$\frac{v_g}{\sqrt{Dg}}$	We	$\frac{D\rho_l V_g^2}{\sigma}$
4	Fr and Re	$\frac{\mu_l g}{\rho_l v_g^3}$	Fr and Re	$\frac{\mu_l g}{\rho_l v_g^3}$	Fr and Re	$\frac{\mu_l g}{\rho_l v_g^3}$
5	Oh	$\frac{\mu_g}{\sqrt{\sigma D \rho_g}}$	Oh	$\frac{\mu_g}{\sqrt{\sigma D \rho_g}}$	Oh	$\frac{\mu_g}{\sqrt{\sigma D \rho_g}}$
6	Oh	$\frac{\mu_g}{\sqrt{\sigma d_p \rho_g}}$	Oh	$\frac{\mu_g}{\sqrt{\sigma d_p \rho_g}}$	Oh	$\frac{\mu_g}{\sqrt{\sigma d_p \rho_g}}$
7	Bo	$\frac{gD^2\rho_g}{\sigma}$	Bo	$\frac{gD^2\rho_g}{\sigma}$	Bo	$\frac{gD^2\rho_g}{\sigma}$
8	Oh	$\frac{\mu_l}{\sqrt{\sigma d_p \rho_g}}$	Oh	$\frac{\mu_l}{\sqrt{\sigma d_p \rho_g}}$	Oh	$\frac{\mu_l}{\sqrt{\sigma d_p \rho_g}}$

The bar plot of sensitivity values for each parameter is shown in Figure 5.4. The sensitivity values are normalized for easy comparison. Figure 5.4 reveals that the contributions from the first dimensionless number are dominant for all three cases. The reason Ohnesorge number is dominate is due to the introduction of liquid flow and the formulation of liquid droplets in the mist flow. Ohnesorge number which relates the viscous forces to inertial and surface tension forces indicates the atomization and deposition of liquid droplets [126] in this flow.

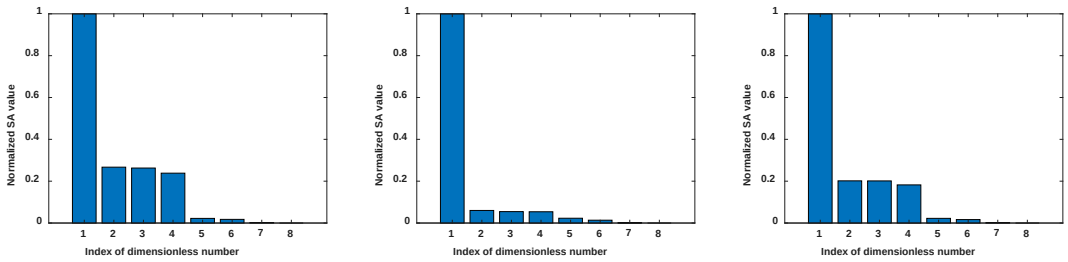

(a) (b) (c)

Figure 5.4: Normalized sensitivity values for mist flow (a) δ ~ GPM$_1$, (b) y^m ~ GPM$_2$, (c) y^e ~ GPM$_3$

Though the three models share the same set of the most relevant dimensionless numbers, GPM$_1$ and GPM$_3$ have the same level of sensitivity to the eight dimensionless numbers. These results suggest that the SPPS 1D version 5.1 considers the proper set of independent variables when calculating erosion rate in mist flow using the flow-dependent approach, and that the difference between SPPS 1D model predictions (GPM$_2$) and experimental data (GPM$_3$) can be correctly quantified by the GPM developed to estimate model discrepancy term (GPM$_4$, Figure 5.1).

5.6.3 Dimensionless Numbers Obtained for Annular Flow

Table 5.8 gives the influential dimensionless numbers identified for the GPMs developed for the model discrepancy (GPM$_1$), the SPPS 1D model (GPM$_2$) and experimental data (GPM$_3$) in annular flow. The bar plot of sensitivity values for influential dimensionless numbers is shown in Figure 5.5. Again, in Figure 5.5, the sensitivity values are normalized. Figure 5.5 reveals that the contributions from first dimensionless number (Table 5.8) are dominant for GPM$_1$ and GPM$_3$, whereas sensitivity values for GPM$_2$ in Figure 5.5 indicate significant influences from the first two dimensionless numbers (Table 5.8).

Table 5.8: The most relevant dimensionless numbers identified for annular flow

	δ ~ GPM$_1$		y^m ~ GPM$_2$		y^e ~ GPM$_3$	
	Number	**Definition**	**Number**	**Definition**	**Number**	**Definition**
1	Oh	$\frac{\mu_l}{\sqrt{\sigma d_p \rho_g}}$	Oh	$\frac{\mu_l}{\sqrt{\sigma d_p \rho_g}}$	Oh	$\frac{\mu_l}{\sqrt{\sigma d_p \rho_g}}$
2	We	$\frac{d_p \rho_g V_g^2}{\sigma}$	Oh	$\frac{\mu_g}{\sqrt{\sigma D \rho_l}}$	Oh	$\frac{\mu_g}{\sqrt{\sigma D \rho_l}}$
3	Fr	$\frac{v_g}{\sqrt{Dg}}$	Bo	$\frac{gD^2\rho_g}{\sigma}$	**Fr and Re**	$\boldsymbol{\frac{\mu_l g}{\rho_g v_g^3}}$
4	We	$\frac{d_p \rho_l V_g^2}{\sigma}$	Fr	$\frac{v_g}{\sqrt{Dg}}$	Bo	$\frac{gD^2\rho_g}{\sigma}$
5	Oh	$\frac{\mu_g}{\sqrt{\sigma D \rho_l}}$	We	$\frac{d_p \rho_g V_g^2}{\sigma}$	**Mo**	$\boldsymbol{\frac{g\mu_g^4}{\rho_g \sigma^3}}$
6	**Ca=$\frac{\text{We}}{\text{Re}}$**	$\boldsymbol{\frac{\mu_l V_l}{\sigma}}$	**Fr and Re**	$\boldsymbol{\frac{\mu_l g}{\rho_g v_g^3}}$	Fr	$\frac{v_g}{\sqrt{Dg}}$
7	Bo	$\frac{gD^2\rho_g}{\sigma}$	**Mo**	$\boldsymbol{\frac{g\mu_g^4}{\rho_g \sigma^3}}$	We	$\frac{d_p \rho_g V_g^2}{\sigma}$
8	**We**	$\boldsymbol{\frac{D\rho_g V_g^2}{\sigma}}$	We	$\frac{d_p \rho_l V_g^2}{\sigma}$	We	$\frac{d_p \rho_l V_g^2}{\sigma}$

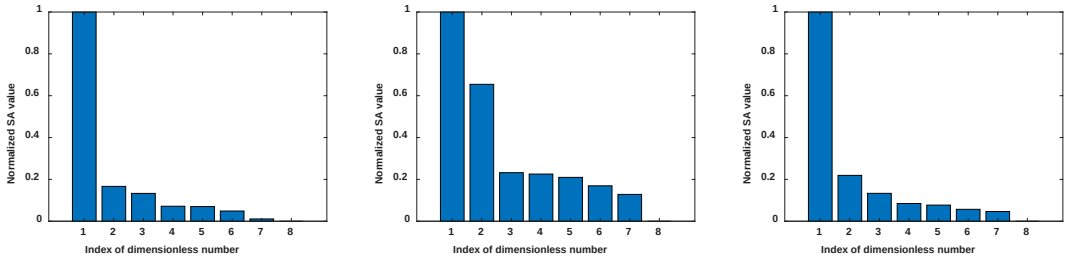

(a) (b) (c)

Figure 5.5: Normalized sensitivity values for annular flow (a) δ ~ GPM$_1$, (b) y^m ~ GPM$_2$, (c) y^e ~ GPM$_3$

The dimensionless numbers identified differ for the three models (highlighted in bold in Table 5.8). Although GPM_2 and GPM_3 share the same set of influential dimensionless numbers, the sensitivities to the eight dimensionless numbers identified are different. The inclusion of Morton number is due to its combination with the Bond number in characterizing the shape of droplets. The most relevant dimensionless numbers for predicting model discrepancy (GPM_1) include the liquid Capillary number, which can be derived by combining Weber and Reynolds numbers. Inclusion of this dimensionless number may be due to the biased consideration of gas velocity in SPPS 1D version 5.1 model using flow-regime dependent approach for calculating erosion rate. In the model, the impact velocity of the representative sand particle has a strong dependence on the value of superficial gas velocity, which mimics the higher impingement velocity of particles transported with fast gas flow rates resulting in greater erosion rates. The order of magnitude of both the measured and predicted erosion rate is positively correlated to the superficial gas velocity. However, as revealed by the inclusion of liquid Capillary number as an influential dimensionless number for GPM_1, the introduction of liquid flow influences the erosion rate by changing the flow regime formed.

In different flow regimes, the liquid dispersion in the gas flows varies along with the movement of sand particles. In annular flow, when the liquid flow rate increases, the sand particles must penetrate the thin liquid film developed around the wall of the pipeline to impinge with the pipeline, which generally leads to a smaller erosion rate. The SPPS 1D version 5.1 model considers the influence of liquid flow rates and consequently the impact of flow regime on erosion process. However, as the sensitivity analysis indicate, the prediction is still mostly dependent on the gas phase flow rate. These results signal potential

avenues for improvements in flow regime determination and in modeling the impact of liquid phase properties on erosion process rate calculations.

5.6.4 Dimensionless Numbers Obtained for Churn Flow

Table 5.9 gives the influential dimensionless numbers identified for the GPMs developed for the model discrepancy (GPM_1), the SPPS 1D model (GPM_2) and experimental data (GPM_3) in churn flow. The bar plot of normalized sensitivity values for influential dimensionless numbers is shown in Figure 5.6. All plots in Figure 5.6 indicate that only the first dimensionless number contributes to the predictions.

Table 5.9: The most relevant dimensionless numbers identified for churn flow

	δ ~ GPM_1		y^m ~ GPM_2		y^e ~ GPM_3	
	Number	**Definition**	**Number**	**Definition**	**Number**	**Definition**
1	Ratio of velocities	$\frac{v_g}{v_l}$	Ratio of velocities	$\frac{v_g}{v_l}$	Ratio of velocities	$\frac{v_g}{v_l}$
2	Oh	$\frac{\mu_l}{\sqrt{\sigma d_p \rho_l}}$	Oh	$\frac{\mu_l}{\sqrt{\sigma d_p \rho_l}}$	Oh	$\frac{\mu_l}{\sqrt{\sigma d_p \rho_l}}$
3	We	$\frac{d_p \rho_l V_g^2}{\sigma}$	We	$\frac{d_p \rho_l V_g^2}{\sigma}$	We	$\frac{d_p \rho_l V_g^2}{\sigma}$
4	We	$\frac{d_p \rho_g V_g^2}{\sigma}$	We	$\frac{d_p \rho_g V_g^2}{\sigma}$	We	$\frac{d_p \rho_g V_g^2}{\sigma}$
5	Oh	$\frac{\mu_l}{\sqrt{\sigma d_p \rho_g}}$	Oh	$\frac{\mu_l}{\sqrt{\sigma d_p \rho_g}}$	Oh	$\frac{\mu_l}{\sqrt{\sigma d_p \rho_g}}$
6	Fr	$\frac{v_g}{\sqrt{d_p g}}$	Fr	$\frac{v_g}{\sqrt{d_p g}}$	Fr	$\frac{v_g}{\sqrt{d_p g}}$
7	Bo	$\frac{g D^2 \rho_g}{\sigma}$	Bo	$\frac{g D^2 \rho_g}{\sigma}$	Bo	$\frac{g D^2 \rho_g}{\sigma}$
8	Fr	$\frac{v_g}{\sqrt{Dg}}$	Fr	$\frac{v_g}{\sqrt{Dg}}$	Fr	$\frac{v_g}{\sqrt{Dg}}$

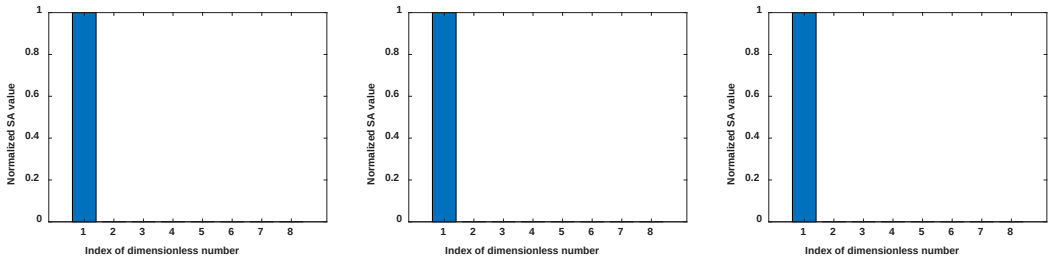

(a) (b) (c)

Figure 5.6: Normalized sensitivity values for churn flow (a) δ ~ GPM_1, (b) y^m ~ GPM_2, (c) y^e ~ GPM_3

The three models share the same set of the most relevant dimensionless numbers, and their outputs have the same levels of sensitivities to the eight dimensionless numbers. The most influential dimensionless number for all three models is the ratio of superficial liquid and gas velocities, which may indicate a problem in churn flow modeling. The difference between SPPS 1D version 5.1 model and experimental data may be correctly quantified by the model discrepancy term estimated using GPM_4 (Figure 5.1), however a more appropriate modeling of erosion rate in churn flow may be developed to address the issue.

5.6.5 Dimensionless Numbers Obtained for Slug Flow Measured by ER probe

There are 92 unique dimensionless numbers identified for slug flow measured by the two approaches. Furthermore, it was observed that many of the columns are strongly correlated with each other (with correlation coefficient values greater than ±0.95). Removing the constant and highly correlated dimensionless numbers yields 22 dimensionless numbers. The GPMs are developed for the model discrepancy (GPM_1), the SPPS 1D model (GPM_2) and experimental data (GPM_3) of erosion rate measurements made by ER probe in slug flow (will be referred to as slug (1)). Table 5.10 gives the influential dimensionless numbers identified for each model using ADR. The bar plots of

normalized sensitivity values for dimensionless variables are given in Figure 5.7, which reveals that the influence of the first dimensionless number is dominant for all three models.

Table 5.10: The most relevant dimensionless numbers identified for slug flow measured by ER probe

	δ ~ GPM$_1$		y^m ~ GPM$_2$		y^e ~ GPM$_3$	
	Number	**Definition**	**Number**	**Definition**	**Number**	**Definition**
1	Fr	$\frac{v_g}{\sqrt{d_p g}}$	Fr	$\frac{v_g}{\sqrt{d_p g}}$	Fr	$\frac{v_g}{\sqrt{d_p g}}$
2	Fr and Re	$\frac{\mu_l g}{\rho_g v_g^3}$	Fr and Re	$\frac{\mu_l g}{\rho_g v_g^3}$	Fr and Re	$\frac{\mu_l g}{\rho_g v_g^3}$
3	Ratio of velocities	$\frac{v_g}{v_l}$	Ratio of velocities	$\frac{v_g}{v_l}$	Ratio of velocities	$\frac{v_g}{v_l}$
4	We	$\frac{d_p \rho_g V_g^2}{\sigma}$	We	$\frac{d_p \rho_g V_g^2}{\sigma}$	We	$\frac{d_p \rho_g V_g^2}{\sigma}$
5	Fr	$\frac{v_l}{\sqrt{Dg}}$	Fr	$\frac{v_l}{\sqrt{Dg}}$	Fr	$\frac{v_l}{\sqrt{Dg}}$
6	Oh	$\frac{\mu_l}{\sqrt{\sigma d_p \rho_g}}$	Oh	$\frac{\mu_l}{\sqrt{\sigma d_p \rho_g}}$	Oh	$\frac{\mu_l}{\sqrt{\sigma d_p \rho_g}}$
7	Oh	$\frac{\mu_g}{\sqrt{\sigma d_p \rho_g}}$	Oh	$\frac{\mu_g}{\sqrt{\sigma d_p \rho_g}}$	Oh	$\frac{\mu_g}{\sqrt{\sigma d_p \rho_g}}$
8	Re	$\frac{\mu_l}{D \rho_g v_l}$	Re	$\frac{\mu_l}{D \rho_g v_l}$	Re	$\frac{\mu_l}{D \rho_g v_l}$

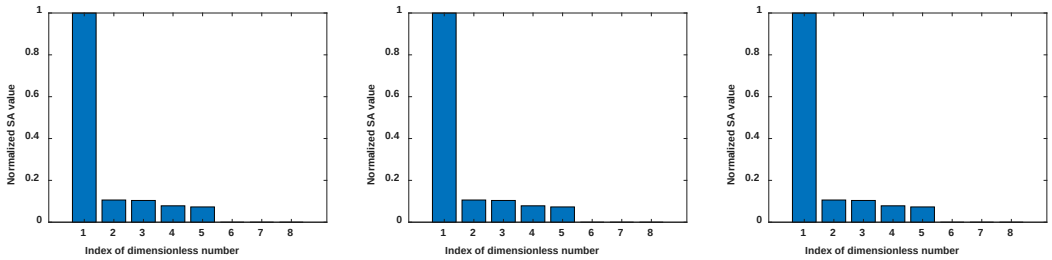

(a) (b) (c)

Figure 5.7: Normalized sensitivity values for slug flow measured by ER probe (a) δ ~ GPM$_1$, (b) y^m ~ GPM$_2$, (c) y^e ~ GPM$_3$

Again, the ratio of velocity has been identified as one of the most relevant dimensionless numbers as it is normally used to quantify the characteristics of gas-liquid multiphase system [131]. The three models share the same set of the most relevant dimensionless numbers, and their outputs show the same level of sensitivities to the eight dimensionless numbers. These results suggest that the SPPS 1D considers the proper set of independent variables when predicting erosion rate in slug flow, and that the difference between the predictions of SPPS 1D version 5.1 model and experimental erosion rate can be correctly quantified by the model discrepancy term. However, as indicted by the mean error in percentage (a positive value, in Table 2.6), the slug model in SPPS 1D version 5.1 tends to under-predict erosion rate collected using ER probe. Therefore, it is suggested that the relationship of independent variables to the erosion rate is checked for the slug flow case in SPPS 1D version 5.1 flow-dependent approach.

5.6.6 Dimensionless Numbers Obtained for Slug Flow Measured by Angle Head ER probe

Table 5.11 gives the influential dimensionless numbers identified for the GPMs developed for the model discrepancy (GPM_1), the SPPS 1D model (GPM_2) and experimental data (GPM_3) in slug flow measured by angle head ER probe (will be referred to as slug (2)). The bar plots of normalized sensitivity values for dimensionless numbers are summarized in Figure 5.8, which suggest that the influence of the first dimensionless number is dominant.

Table 5.11: The most relevant dimensionless numbers identified for slug flow measured by angle head ER probe

	δ ~ GPM1		y^m ~ GPM2		y^e ~ GPM3	
	Number	**Definition**	**Number**	**Definition**	**Number**	**Definition**
1	Fr	$\frac{v_g}{\sqrt{Dg}}$	Fr	$\frac{v_g}{\sqrt{Dg}}$	Fr	$\frac{v_g}{\sqrt{Dg}}$
2	Fr and Re	$\frac{\mu_l g}{\rho_g v_g^3}$	Fr and Re	$\frac{\mu_l g}{\rho_g v_g^3}$	Fr and Re	$\frac{\mu_l g}{\rho_g v_g^3}$
3	Ratio of velocities	$\frac{v_g}{v_l}$	Ratio of velocities	$\frac{v_g}{v_l}$	Ratio of velocities	$\frac{v_g}{v_l}$
4	Fr	$\frac{v_l}{\sqrt{Dg}}$	Fr	$\frac{v_l}{\sqrt{Dg}}$	Fr	$\frac{v_l}{\sqrt{Dg}}$
5	We	$\frac{d_p \rho_g V_g^2}{\sigma}$	We	$\frac{d_p \rho_g V_g^2}{\sigma}$	We	$\frac{d_p \rho_g V_g^2}{\sigma}$
6	Re	$\frac{\mu_l}{D \rho_g v_l}$	Re	$\frac{\mu_l}{D \rho_g v_l}$	Re	$\frac{\mu_l}{D \rho_g v_l}$
7	Oh	$\frac{\mu_l}{\sqrt{\sigma d_p \rho_g}}$	Oh	$\frac{\mu_l}{\sqrt{\sigma d_p \rho_g}}$	Oh	$\frac{\mu_l}{\sqrt{\sigma d_p \rho_g}}$
8	Oh	$\frac{\mu_g}{\sqrt{\sigma d_p \rho_g}}$	Oh	$\frac{\mu_g}{\sqrt{\sigma d_p \rho_g}}$	Oh	$\frac{\mu_g}{\sqrt{\sigma d_p \rho_g}}$

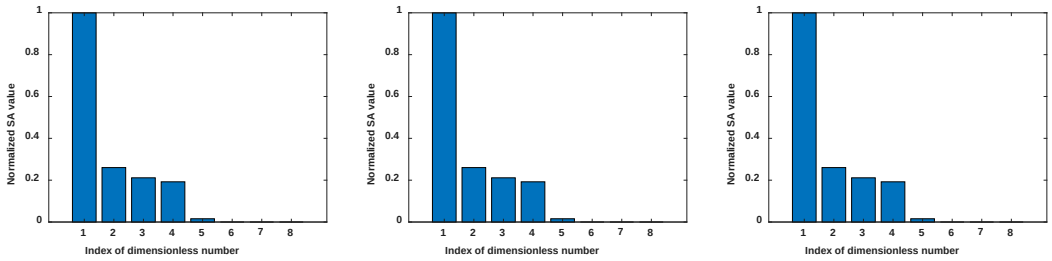

(a) (b) (c)

Figure 5.8: Normalized sensitivity values for slug flow measured by angle head ER probe (a) δ ~ GPM1, (b) y^m ~ GPM2, (c) y^e ~ GPM3

Comparable to the results obtained for the regular ER probe, the three models share the same set of the most relevant dimensionless numbers, and show the same level of

sensitivities to the eight dimensionless numbers. The first identified dimensionless number for the two measurement approaches is Froude number calculated using different length scales. For data collected using angle head ER probe, the length scale used for calculating Froude number is pipe diameter opposed to particle diameter for ER probe case. The angle head ER probe is used to measure erosion rate in the straight part of the pipeline, and for this case, the distribution of particles in the pipeline is more dependent on the pipeline diameter [132]. The results suggest that the SPPS 1D prediction of erosion rate considers the proper set of independent variables and the difference between the erosion-rate predictions of SPPS 1D model and experimental data can be correctly quantified by the model discrepancy term calculated using GPM_4.

5.6.7 Dimensionless Numbers Obtained for Data Collected in Horizontal to Horizontal Orientation

We repeat the overall analysis using only the data points collected in horizontal to horizontal orientation that were not observed to exhibit slug flow. There are 91 data points with these specifications. The initial dimensional analysis yielded 102 unique dimensionless numbers. By removing the constant and highly correlated dimensionless numbers reduced this number to 37 dimensionless numbers. Table 5.12 gives the influential dimensionless numbers identified for the GPMs developed for the model discrepancy (GPM_1), the SPPS 1D model (GPM_2) and experimental data (GPM_3) with data collected in horizontal to horizontal orientation. The bar plots of normalized sensitivity values for dimensionless numbers are given in Figure 5.9. It can be seen from Figure 5.9 that only the first two dimensionless numbers contribute to the model predictions for GPM_1 and GPM_2, while the first dimensionless number dominates the predictions for GPM_1.

Table 5.12: The most relevant dimensionless numbers identified for data collected in horizontal to horizontal orientation

	δ ~ GPM1		y^m ~ GPM2		y^e ~ GPM3	
	Number	**Definition**	**Number**	**Definition**	**Number**	**Definition**
1	Oh	$\frac{\mu_l}{\sqrt{\sigma d_p \rho_l}}$	Ratio of diameters	$\frac{d_p}{D}$	Ratio of diameters	$\frac{d_p}{D}$
2	Ratio of diameters	$\frac{d_p}{D}$	Oh	$\frac{\mu_l}{\sqrt{\sigma d_p \rho_l}}$	Fr	$\frac{v_g}{\sqrt{Dg}}$
3	Fr	$\frac{v_g}{\sqrt{Dg}}$	Fr	$\frac{v_g}{\sqrt{Dg}}$	Oh	$\frac{\mu_l}{\sqrt{\sigma d_p \rho_l}}$
4	Oh	$\frac{\mu_l}{\sqrt{\sigma d_p \rho_g}}$	Oh	$\frac{\mu_l}{\sqrt{\sigma d_p \rho_g}}$	Oh	$\frac{\mu_l}{\sqrt{\sigma d_p \rho_g}}$
5	We	$\frac{d_p \rho_g V_g^2}{\sigma}$	We	$\frac{d_p \rho_g V_g^2}{\sigma}$	Oh	$\frac{\mu_l}{\sqrt{\sigma D \rho_g}}$
6	Oh	$\frac{\mu_l}{\sqrt{\sigma D \rho_g}}$	Oh	$\frac{\mu_l}{\sqrt{\sigma D \rho_g}}$	We	$\frac{d_p \rho_g V_g^2}{\sigma}$
7	Re	$\frac{\mu_l}{D \rho_g v_g}$	Re	$\frac{\mu_l}{D \rho_g v_g}$	Ratio of velocities	$\frac{v_g}{v_l}$
8	Ratio of velocities	$\frac{v_g}{v_l}$	Ratio of velocities	$\frac{v_g}{v_l}$	Re	$\frac{\mu_l}{D \rho_g v_g}$

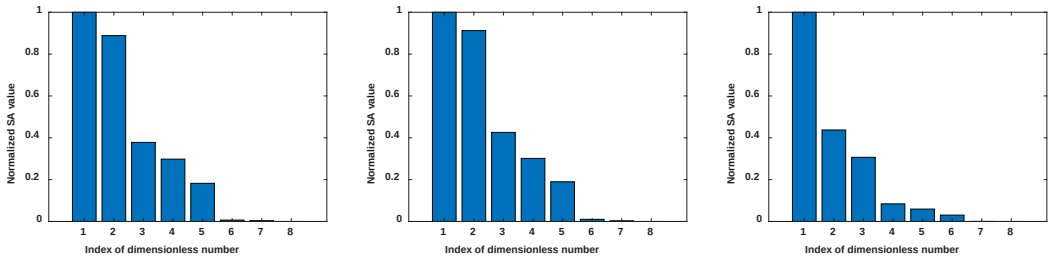

(a) (b) (c)

Figure 5.9: Normalized sensitivity values for data collected in horizontal to horizontal orientation (a) δ ~ GPM1, (b) y^m ~ GPM2, (c) y^e ~ GPM3

The three models share the same set of the most relevant dimensionless numbers, but differ in the order and level of sensitivity to the eight dimensionless numbers. It has been shown that SPPS 1D model fails to correctly model erosion rate for data from horizontal to horizontal orientation. Therefore, the identified dimensionless number in GPM_1 may help explain the discrepancy.

The dimensionless number that differs is liquid Ohnesorge number. With a further study on the entrainment model used in SPPS 1D, we found out that the entrainment fraction used (model developed by Oliemans et al. [133]) is only applicable to vertical orientation. However, this erosion model has been applied to data collected from horizontal orientation. The horizontal orientation exhibits different entrainment characteristics and the former model is not appropriate for modeling the entrainment characteristics at the horizontal orientation. Magrini et al. [134] studied the effect of inclination angle on entrainment fraction and concluded that Pan and Hanratty [125] correlation is the most accurate model for predicting entrainment fraction for horizontal annular flow. Pan and Hanratty [125] model incorporates the balance of droplet deposition and atomization rates, which is related to Ohnesorge number. This analysis, therefore, suggests that a new entrainment model may improve the erosion rate predictions of SPPS 1D version 5.1 for horizontal to horizontal orientations.

5.6.8 Dimensionless Numbers Obtained for Gas Only Flow

We repeat the overall analysis using only the data points collected from gas only flow. There are 63 data points with these specifications. The initial dimensional analysis yielded 72 unique dimensionless numbers. By removing the constant and highly correlated dimensionless numbers reduced this number to 14 dimensionless numbers. Table 5.13

gives the influential dimensionless numbers identified for the GPMs developed for the model discrepancy (GPM_1), the SPPS 1D model (GPM_2) and experimental data (GPM_3) with data collected in gas only flow. Since the number of relevant dimensional variables used for dimensional analysis is 7 and the number of fundamental dimensions is 3, only the first four relevant dimensionless numbers are identified. The bar plots of normalized sensitivity values for dimensionless numbers are given in Figure 5.10. It can be seen from Figure 5.10 that the first dimensionless number contribute the most to all the three model predictions.

Table 5.13: The most relevant dimensionless numbers identified for data collected in horizontal to horizontal orientation

	δ ~ GPM_1		y^m ~ GPM_2		y^e ~ GPM_3	
	Number	**Definition**	**Number**	**Definition**	**Number**	**Definition**
1	Fr and Ca	$\frac{\mu_g\sqrt{d_p g}}{\sigma}$	Fr and Ca	$\frac{\mu_g\sqrt{d_p g}}{\sigma}$	Fr and Ca	$\frac{\mu_g\sqrt{d_p g}}{\sigma}$
2	Fr	$\frac{v_g}{\sqrt{Dg}}$	Fr	$\frac{v_g}{\sqrt{Dg}}$	Fr	$\frac{v_g}{\sqrt{Dg}}$
3	Ratio of diameter	$\frac{d_p}{D}$	Ratio of diameter	$\frac{d_p}{D}$	Ratio of diameter	$\frac{d_p}{D}$
4	Ratio of density	$\frac{\rho_P}{\rho_g}$	Ratio of density	$\frac{\rho_P}{\rho_g}$	Ratio of density	$\frac{\rho_P}{\rho_g}$

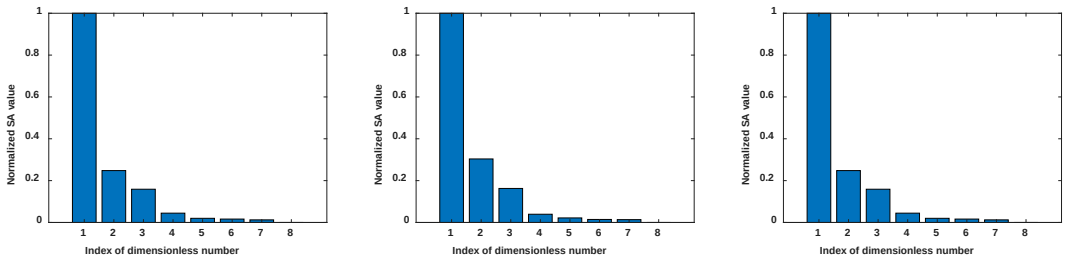

(a) (b) (c)

Figure 5.10: Normalized sensitivity values for data collected in gas only flow (a) δ ~ GPM_1, (b) y^m ~ GPM_2, (c) y^e ~ GPM_3

The three models share the same set of the most relevant dimensionless numbers, and the order and level of sensitivity to the four dimensionless numbers. These results suggest that the SPPS 1D considers the proper set of independent variables when predicting erosion rate in gas only flow, and that the difference between the predictions of SPPS 1D version 5.1 model and experimental erosion rate can be correctly quantified by the model discrepancy term.

5.6.9 Dimensionless Numbers Obtained for Liquid Only Flow

The last dimensional analysis is applied to data points collected from liquid only flow. There are 12 data points from liquid flow. The initial dimensional analysis yielded 72 unique dimensionless numbers. By removing the constant and highly correlated dimensionless numbers reduced this number to 8 dimensionless numbers. Table 5.14 gives the influential dimensionless numbers identified for the GPMs developed for the model discrepancy (GPM_1), the SPPS 1D model (GPM_2) and experimental data (GPM_3) with data collected in liquid only flow. Since the number of relevant dimensional variables used for dimensional analysis is 7 and the number of fundamental dimensions is 3, only the first four relevant dimensionless numbers are identified. The bar plots of normalized sensitivity values for dimensionless numbers are given in Figure 5.11. It can be seen from Figure 5.11 that the first dimensionless number contribute the most to all the three model predictions.

Table 5.14: The most relevant dimensionless numbers identified for liquid only flow

	δ ~ GPM1		y^m ~ GPM2		y^e ~ GPM3	
	Number	**Definition**	**Number**	**Definition**	**Number**	**Definition**
1	Fr	$\frac{v_l}{\sqrt{Dg}}$	Fr	$\frac{v_l}{\sqrt{Dg}}$	Fr	$\frac{v_l}{\sqrt{Dg}}$
2	Re	$\frac{\mu_l}{D\rho_l v_l}$	Re	$\frac{\mu_l}{D\rho_l v_l}$	Re	$\frac{\mu_l}{D\rho_l v_l}$
3	Re	$\frac{\mu_l}{d_p\rho_l v_l}$	Re	$\frac{\mu_l}{d_p\rho_l v_l}$	Re	$\frac{\mu_l}{d_p\rho_l v_l}$
4	Ga	$\frac{d_p^3\rho_l^2 g}{\mu_l^2}$	Ga	$\frac{d_p^3\rho_l^2 g}{\mu_l^2}$	Ga	$\frac{d_p^3\rho_l^2 g}{\mu_l^2}$

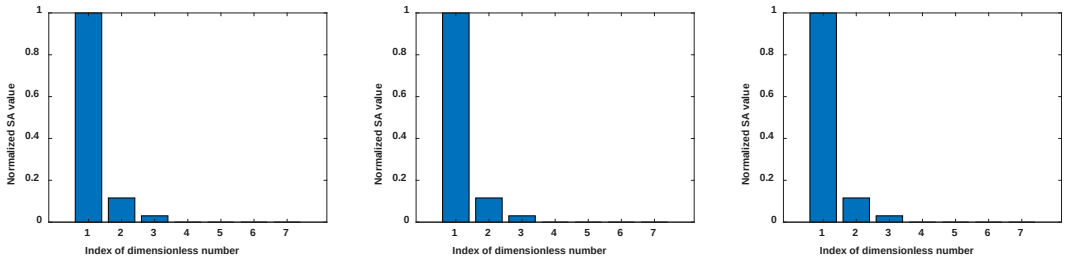

(a) (b) (c)

Figure 5.11: Normalized sensitivity values for data collected in liquid only flow (a) δ ~ GPM1, (b) y^m ~ GPM2, (c) y^e ~ GPM3

The three models share the same set of the most relevant dimensionless numbers, and the order and level of sensitivity to the four dimensionless numbers. These results suggest that the SPPS 1D considers the proper set of independent variables when predicting erosion rate in liquid only flow, and that the difference between the predictions of SPPS 1D version 5.1 model and experimental erosion rate can be correctly quantified by the model discrepancy term.

5.7 Prediction results using the identified dimensionless numbers

Using the identified dimensionless numbers, new GPMs are trained to predict the model discrepancy in each flow regime and orientation. The predicted model discrepancy is added to the erosion-rate prediction calculated using flow-regime dependent approach of SPPS 1D version 5.1. The results are compared to the experimentally measured erosion rates. For this assessment, three performance metrics are calculated: (1) area metric (see section 4.4) [135], (2) root mean squared error (RMSE) (see section 4.4), and (3) number of outliers. Area metric (AM) is defined as the integral of disagreement area between the estimated erosion rate and experimentally measured erosion rate. A smaller area metric represents a more reliable prediction of the model discrepancy. RMSE is commonly used for evaluating model predictability. The check on number of outliers ensures prediction reliability. For this analysis, an outlier is defined as an experimental measurement falling outside of the 95% confidence interval of the GPM corrected predictions.

Table 5.13 shows the results obtained for all flow regimes and orientations considered. The GPMs trained using identified dimensionless numbers as inputs yields smaller AM, RMSE values, and number of outliers compared to the prediction of SPPS 1D version 5.1 model. The last row in Table 5.13 includes the AM and RMSE values obtained when only the prediction of SPPS 1D version 5.1 model flow-regime dependent approach is used in calculating these values. It can be seen by introducing the model discrepancy term, the AM value is improved 80% and RMSE value is reduced by 33%.

Table 5.15: Comparison of prediction results

GPM adjusted prediction	No.	AM	RMSE	Number of outliers
Mist	146	15.67	0.08	10
Annular	89	0.49	1.8×10^{-2}	14
Churn	16	1.7×10^{-2}	1.0×10^{-3}	2
Slug (1)	100	9.4×10^{-3}	1.5×10^{-4}	3
Slug (2)	68	5.4×10^{-2}	2.6×10^{-3}	3
Horizontal data	91	7.8×10^{-2}	5.0×10^{-3}	12
Gas	63	11.13	0.46	24
Liquid	12	8.7×10^{-3}	0.0071	3
In total	585	27.46	0.16	71
y^m	585	129.15	0.24	-

5.8 Comparison to Model Developed using Dimensional Variables

As a comparison to our previous studies in section 4.5, we compared the uncertainty prediction results to that obtained from dimensional variables. The comparison indicates that using dimensionless numbers can improve the erosion-rate uncertainty prediction with reduction in the prediction uncertainty for Annular, Churn and Slug flows (in terms of AM and RMSE value).

5.9 Conclusion

This section applies dimensional analysis and Gaussian processing modeling to quantify the uncertainty in the erosion process qualitatively and quantitatively. Dimensional analysis is implemented for the identification of important operating conditions. The dimensionless groups identified in the multiphase flow provided the most influential variables in the quantification of erosion-rate model discrepancy. The model discrepancy adjusted GPM predictions are more comparable to the experimental data with

smaller prediction uncertainties. The results also suggest possible model improvement opportunities and design of experiments involving the identified dimensionless groups.

CHAPTER 6

CONCLUSIONS AND FUTURE WORK

6.1 Conclusions

In this dissertation, a framework to quantify prediction uncertainty and its confidence interval for erosion models under a wide range of input conditions has been introduced. A large database of erosion rate measurements, consisting of measurement approaches used, flow regimes and experimental set-up details, is assembled from open literature. The application of the developed framework is demonstrated on one of the well-known erosion models, which is used extensively in oil and gas industry for erosion-rate predictions [27].

To the best of our knowledge, this work is the first-time data mining approaches have been used to quantify erosion prediction uncertainty. The framework presented in this dissertation can be used for uncertainty quantification of other erosion models, and the findings can be applied by both model developers and model users as a guideline. For example, model developers can use the framework to analyze their models to identify input regions with large model-uncertainty estimates, which can then trigger additional experimental campaigns or model refinement studies to reduce these estimates for the identified regions. Model users may opt to design their processes with higher safety margins in regions with high model-uncertainty estimates, or plan and adjust production according to the regions with high or low model-uncertainty estimates.

6.2 Identification of Areas with High Uncertainty

Based on the aforementioned approaches for the uncertainty quantification in the erosion-rate modeling, future work may involve compiling regions with large uncertainties for all the tested regions. Since we use cross-validation to develop the GP models, the test data points in each fold are estimated with model interpolation. If data density in the interpolated space is low, it can lead to greater uncertainties in these hyperspaces. Therefore, the future work may focus on developing a “heat map” for highly uncertain regions based on the collected database. A “heat map” will provide a way to differentiate operating conditions with high uncertainties and those with small or even negligible uncertainties. We can utilize the results and analysis from such a heat map as suggestions for future erosion experimental design to achieve reliable estimation of erosion model uncertainties.

For field application of the proposed framework, the GP models are more likely to be extrapolated to regions where experimental data is scare or unavailable. To estimate the model’s capability in extrapolated regions, a guideline in terms of the mean value and the confidence interval can be provided. Gaussian process models based on a non-parametric Bayesian framework, tends to make stable mean predictions with large prediction uncertainties when the models are extrapolated to regions with very low density of data. The model’s predictive capability will decrease gradually with the increased distance to the data available. Beyond a certain distance, the prediction from GP models might not be informative to indicate the model uncertainty. To define the to-be-extrapolated regions, the mean value from the mean functions and the confidence interval converted from the covariance functions can be used. Based on the estimated mean and confidence interval values, the bounds of the hyperspace outside of which GP models become unreliable can

be obtained. From that, a list of operating condition ranges suitable for extrapolation of GP models can be generated.

REFERENCES

[1] C.J. Roy, W.L. Oberkampf, A comprehensive framework for verification, validation, and uncertainty quantification in scientific computing, Comput. Methods Appl. Mech. Eng. 200 (2011) 2131–2144. doi:10.1016/j.cma.2011.03.016.

[2] D.L. Shrestha, Uncertainty analysis in rainfall-runoff modelling: application of machine learning techniques, 2009.

[3] Y.I. Oka, K. Okamura, T. Yoshida, Practical estimation of erosion damage caused by solid particle impact: Part 1: Effects of impact parameters on a predictive equation, Wear. 259 (2005) 95–101. doi:10.1016/j.wear.2005.01.039.

[4] Q.H. Mazumder, Development and Validation of a Mechanistic Model to Predict Erosion in Single-Phase and Multiphase Flow, The University of Tulsa, 2004.

[5] T.J. Danielson, Sand Transport Modeling in Multiphase Pipelines, in: Offshore Technol. Conf., Houston, TX, USA, 2007: pp. 1–11.

[6] B. Singh, P. Jukes, R. Wittkower, B. Poblete, Offshore Integrity Management 20 years On-An Overview of Lessons Learnt Post Piper Alpha, Offshore Technol. Conf. 20051. (2009) 1–30. doi:10.4043/20051-MS.

[7] S. Shirazi, B. McLaury, J. Shadley, E. Rybicki, Generalization of the API RP 14E Guideline for erosive services, J. Pet. Technol. (1995) 693–698. doi:10.2118/28518-PA.

[8] M.M. Salama, OTC 8898 An Alternative to API 14E Erosional Velocity Limits for Sand Laden Fluids fl Ji ; JE ;, (1998).

[9] J. Davalath, M. Hurtado, R. Keig, Flow assurance management for Bijupira and Salema field development, in: Proc. 34th Annu. Offshore Technol. Conf., Houston, USA, 2002.

[10] H.C. Meng, K.C. Ludema, Wear models and predictive equations: their form and content, Wear. 181–183 (1995) 443–457. doi:10.1016/0043-1648(95)90158-2.

[11] H. Arabnejad, A. Mansouri, S.A. Shirazi, B.S. Mclaury, T. Erosion, Evaluation of Solid Particle Erosion Equations and Models for Oil and Gas, SPE Annu. Tech. Conf. Exhib. (2015). doi:10.2118/174987-MS.

[12] API RP 14E Recommended Practice for Design and Installation of Offshore Production Platform Piping Systems, in: Am. Pet. Inst., Washington, DC, USA, 1981: p. 22.

[13] M.M. Salama, E.S. Venkatesh, Evaluation of API RP 14E Erosional Velocity Limitations

for Offshore Gas Wells, in: 15th Annu. OCT, Houston, TX, USA, 1983: pp. 371–376.

[14] A.T. Bourgoyne, Experimental Study of Erosion in Diverter Systems Due to Sand Production, SPE/IADC Drill. Conf. (1989). doi:10.2118/18716-MS.

[15] K.R. Ahlert, Effects of particle impingement angle and surface wetting on solid particle erosion of AISI 1018 steel, The University of Tulsa., 1994.

[16] J.K. Edwards, B.S. McLaury, S.A. Shirazi, SUPPLEMENTING A CFD CODE WITH EROSION PREDICTION CAPABILITIES, in: 1998 ASME Fluids Eng. Div. Summer Meet., Washington, DC, USA, 1998.

[17] AEA Technology, CFX-4.2 Manual, 1997.

[18] J. Wang, S.A. Shirazi, A CFD Based Correlation for Erosion Factor for Long-Radius, J. Energy Resour. Technol. 125 (2003) 26–34. doi:10.1115/1.1514674.

[19] Y. Zhang, E.P. Reuterfors, B.S. McLaury, S.A. Shirazi, E.F. Rybicki, Comparison of computed and measured particle velocities and erosion in water and air flows, Wear. 263 (2007) 330–338. doi:10.1016/j.wear.2006.12.048.

[20] Y. Zhang, B.S. McLaury, S. a. Shirazi, Improvements of Particle Near-Wall Velocity and Erosion Predictions Using a Commercial CFD Code, J. Fluids Eng. 131 (2009) 031303. doi:10.1115/1.3077139.

[21] G.V. Messa, S. Malavasi, The effect of sub-models and parameterizations in the simulation of abrasive jet impingement tests, Wear. 370–371 (2017) 59–72. doi:10.1016/j.wear.2016.10.022.

[22] E. Gharaibah, Y. Zhang, G.E. Oil, G.F. Assurance, SPE-181737-MS Sand Management and Erosion Prediction Models for Oil and Gas Applications - Experimental and Numerical Validation Studies, (2016) 1–13.

[23] R. Zhang, H. Liu, Numerical Simulation of Solid Particle Erosion in a 90 Degree Bend for Gas Flow, Vol. 6A Pipeline Riser Technol. (2014) V06AT04A044. doi:10.1115/OMAE2014-23656.

[24] DNV-GL, Recommended Practice, RP O501: Erosive Wear in Piping Systems, Det Norske Veritas, Revision 4.2- 2007, 2007.

[25] G. Grant, W. Tabakoff, An experimental investigation of the erosive characteristics of 2024 aluminum alloy, Dept. of Aerospace Engineering, University of Cincinnati, 1973.

[26] DNV-GL, Integrity management of subsea production systems, (2014) 1–61. http://rules.dnvgl.com/docs/pdf/DNVGL/RP/2014-11/DNVGL-RP-0002.pdf.

[27] Q.H. Mazumder, S.A. Shirazi, B.S. McLaury, J.R. Shadley, E.F. Rybicki, Development and validation of a mechanistic model to predict solid particle erosion in multiphase flow,

Wear. 259 (2005) 203–207. doi:10.1016/j.wear.2005.02.109.

[28] M. Parsi, M. Kara, P. Sharma, D.N. V Gl, B.S. Mclaury, S.A. Shirazi, Comparative Study of Different Erosion Model Predictions for Single-Phase and Multiphase Flow Conditions, in: Offshore Technol. Conf., Houston, Texas, USA, 2016.

[29] K.A. Bikbaev, V.I. Krasnov, M.I. Maksimenko, V. Berezin, I.B. Zhilinskii, N.T. Otroshko, Main factors affecting gas abrasive wear of elbows in pneumatic conveying pipes, Chem. Pet. Eng. 9 (1973) 73–75.

[30] G.C. Tolle, D.R. Greenwood, Design of Fittings to Reduce Wear Caused by Sand Erosion, 1977.

[31] M. Ishi, K. Mishima, G. Grant, W. Tabakoff, M.M. Salama, An Alternative to API 14E Erosional Velocity Limits for Sand Laden Fluids, Int. J. Heat Mass Transf. 32 (1998) 1835–1846.

[32] A.Z. Antezana, Erosion Studies with Electrical Resistance (ER) Probes in Multiphase Annular Flow, University of Tulsa, 2004.

[33] T. Evans, H. Bennett, Y. Sun, J. Alvarez, E. Babaian-Kibala, J.W. Martin, Studies of Inhibition and Monitoring of Metal Loss in Gas Systems Containing Solids, in: NACE Int., 2004.

[34] E.P. Reuterfors, Particle velocity and erosion measurements for direct impingement of water and air flows, The University of Tulsa, 2007.

[35] M. Pyboyina, Experimental investigation and computational fluid dynamics simulations of erosion on electrical resistance probes, The University of Tulsa, 2006.

[36] P.K. Nuguri, Experimental investigation and modeling of erosion for gas dominant multiphase flows with sand, The University of Tulsa, 2007.

[37] R. Dosila, Effects of Low Liquid Loading on Solid Particle Erosion for Gas Dominant Multiphase Flows, The University of Tulsa, 2008. http://library.utulsa.edu//record=b2294290.

[38] J.C. Rodriguez, Effects of liquid viscosity and sand size on erosion in slug multiphase flow, The University of Tulsa, 2008.

[39] C. Fan, Evaluation of solid particle erosion in gas dominant flows using electrical resistance probes, The University of Tulsa, 2010.

[40] J. Throneberry, Solid particle erosion in slug flow, The University of Tulsa, 2010.

[41] N.R. Kesana, Erosion in Multiphase Pseudo Slug Flow with Emphasis on Sand Sampling and Pseudo Slug Characteristics, University of Tulsa, 2013.

[42] R.E. Vieira, Sand Erosion Model Improvement for Elbows in Gas Production, Multiphase

Annular and Low-Liquid Flow, University of Tulsa, 2014.

[43] A.A. Giunta, J.M. McFarland, L.P. Swiler, M.S. Eldred, The promise and peril of uncertainty quantification using response surface approximations, Struct. Infrastruct. Eng. 2 (2006) 175–189. doi:10.1080/15732470600590507.

[44] S.A. Shirazi, J.R. Shadley, B.S. McLaury, E.F. Rybicki, A Procedure to Predict Solid Particle Erosion in Elbows and Tees, J. Press. Vessel Technol. 117 (1995) 45. doi:10.1115/1.2842089.

[45] D. Barnea, A unified model for predicting flow-pattern transitions for the whole rangeof pipe inclinations, Int. J. Multiph. Flow. 13 (1987) 1–12.

[46] J.M. Throneberry, Y. Zhang, B.S. McLaury, S. a Shirazi, E.F. Rybicki, Solid-Particle Erosion in Slug Flow, SPE Annu. Tech. Conf. Exhib. 6 (2010) 4847–4862. doi:10.2118/135402-MS.

[47] W.L. Oberkampf, M.F. Barone, Measures of agreement between computation and experiment: Validation metrics, J. Comput. Phys. 217 (2006) 5–36. doi:10.1016/j.jcp.2006.03.037.

[48] W. Dai, S. Cremaschi, Quantifying Model Uncertainty in Scarce Data Regions - A Case Study of Particle Erosion in Pipelines, Comput. Aided Chem. Eng. 37 (2015) 1811–1816. doi:10.1016/B978-0-444-63577-8.50147-9.

[49] A.I. Khuri, S. Mukhopadhyay, Response surface methodology, Wiley Interdiscip. Rev. Comput. Stat. 2 (2010) 128–149. doi:10.1002/wics.73.

[50] J.C. Helton, F.J. Davis, Latin hypercube sampling and the propagation of uncertainty in analyses of complex systems, Reliab. Eng. Syst. Saf. 81 (2003) 23–69. doi:10.1016/S0951-8320(03)00058-9.

[51] R.L. Iman, J.C. Helton, J.E. Campbell, An Approach to Sensitivity Analysis of Computer Models: Part I-Introduction, Input Variable Selection and Preliminary Variable Assessment, J. Qual. Technol. 13 (1981) 174–183.

[52] S.T. Tokdar, R.E. Kass, Importance sampling: A review, Wiley Interdiscip. Rev. Comput. Stat. 2 (2010) 54–60. doi:10.1002/wics.56.

[53] E. Aune, J. Eidsvik, Y. Pokern, Iterative numerical methods for sampling from high dimensional Gaussian distributions, Stat. Comput. 23 (2013) 501–521. doi:10.1007/s11222-012-9326-8.

[54] C.E. Rasmussen, C.K.I. Williams, Gaussian processes for machine learning, The MIT Press, 2006.

[55] R. Jin, W. Chen, T.W. Simpson, Comparative Studies of Metamodeling Techniques Under

Multiple Modeling Criteria, Struct. Multidiscip. Optim. 23 (2001) 1–13. doi:10.2514/6.2000-4801.

[56] Z. Jiang, W. Chen, Y. Fu, R.-J. Yang, Reliability-Based Design Optimization with Model Bias and Data Uncertainty, SAE Int. J. Mater. Manuf. 6 (2013) 502–516. doi:10.4271/2013-01-1384.

[57] W.C. Thacker, M. Iskandarani, R.C. Gonçalves, A. Srinivasan, O.M. Knio, Pragmatic aspects of uncertainty propagation : A conceptual review, Ocean Model. 95 (2015) 25–36. doi:10.1016/j.ocemod.2015.09.001.

[58] A. Mchutchon, C.E. Rasmussen, Gaussian Process Training with Input Noise, Adv. Neural Inf. Process. Syst. (2011) 1341–1349. http://papers.nips.cc/paper/4295-gaussian-process-training-with-input-noise.

[59] T. Doiron, J. Stoup, Uncertainty and dimensional calibrations, J. Res. Natl. Inst. Stand. Technol. 102 (1997) 647. doi:10.6028/jres.102.044.

[60] H.W. Coleman, W.G. Steele, Experimentation, Validation, and Uncertainty Analysis for Engineers: Third Edition, 2009. doi:10.1002/9780470485682.

[61] S. Bell, A Beginner's Guide to Uncertainty of Measurement, Meas. Good Pract. Guid. (1999) 41. doi:10.1111/j.1468-3148.2007.00360.x.

[62] C. a Peters, Statistics for Analysis of Experimental Data Princeton University Statistics for Analysis of Experimental Data, Environ. Eng. Process. Lab. Man. (2001) 1–25. doi:10.1145/2901739.2901780.

[63] R.J. Moffat, Using Uncertainty Analysis in the Planning of an Experiment, J. Fluids Eng. 107 (1985) 173. doi:10.1115/1.3242452.

[64] J.L. Peube, Fundamentals of Fluid Mechanics and Transport Phenomena, 2010. doi:10.1002/9780470611500.

[65] R.I. Rawski, P.T. Sanecki, K.M. Kijowska, P.M. Skitat, D.E. Saletnik, Regression analysis in analytical chemistry. Determination and validation of linear and quadratic regression dependencies, South African J. Chem. 69 (2016). doi:10.17159/0379-4350/2016/v69a20.

[66] R.E. Vieira, N.R. Kesana, C.F. Torres, B.S. McLaury, S.A. Shirazi, E. Schleicher, U. Hampel, Experimental Investigation of Horizontal Gas-Liquid Stratified and Annular Flow Using Wire-Mesh Sensor, J. Fluids Eng. 136 (2014) 121301. doi:10.1115/1.4027799.

[67] H.E. Rincon, Testing and Prediction of Erosion-Corrosion for Corrosion Resistant Alloys Used in the Oil and Gas Production Industry, (2008).

[68] H. Arabnejad, A. Mansouri, S.A. Shirazi, B.S. Mclaury, Development of mechanistic

erosion equation for solid particles, 333 (2015) 1044–1050. doi:10.1016/j.wear.2015.01.031.

[69] R.J. Martin, Leverage, influence and residuals in regression models when observations are correlated, Commun. Stat. - Theory Methods. 21 (1992) 1183–1212. doi:10.1080/03610929208830840.

[70] S.J. Sheather, Density Estimation, Stat. Sci. 19 (2004) 588–597. doi:10.1214/088342304000000297.

[71] A.I.J. Forrester, A. Sbester, A.J. Keane, Engineering Design via Surrogate Modelling, John Wiley & Sons, Ltd, Chichester, UK, 2008. doi:10.1002/9780470770801.

[72] M. Molga, C. Smutnicki, Test functions for optimization needs, Test Funct. Optim. Needs. (2005) 1–43.

[73] J.H. Friedman, Multivariate Adaptive Regression Splines, 19 (1991) 1–67.

[74] H. Dette, A. Pepelyshev, Generalized latin hypercube design for computer experiments, Technometrics. 52 (2010) 421–429. doi:10.1198/TECH.2010.09157.

[75] E.N. Ben-Ari, D.M. Steinberg, Modeling Data from Computer Experiments: An Empirical Comparison of Kriging with MARS and Projection Pursuit Regression, Qual. Eng. 19 (2007) 327–338. doi:10.1080/08982110701580930.

[76] M.D. Shields, J. Zhang, The generalization of Latin hypercube sampling, Reliab. Eng. Syst. Saf. 148 (2016) 96–108. doi:10.1016/j.ress.2015.12.002.

[77] N.M. Razali, Y.B. Wah, Power comparisons of Shapiro-Wilk , Kolmogorov-Smirnov, Lilliefors and Anderson-Darling tests, J. Stat. Model. Anal. 2 (2011) 21–33. doi:doi:10.1515/bile-2015-0008.

[78] J. Pearl, Statistics and causal inference: A review, Test. 12 (2003) 281–345. doi:10.1007/BF02595718.

[79] R.E. Vieira, Sand Erosion Model Improvement for Elbows in Gas Production, Multiphase Annular and Low-Liquid Flow, The University of Tulsa, 2014.

[80] H. Khanouki, Development of Erosion Equations for Solid Particle and Liquid Droplet Impact, The University of Tulsa, 2015.

[81] E. Amirian, J.Y. Leung, S. Zanon, P. Dzurman, Integrated cluster analysis and artificial neural network modeling for steam-assisted gravity drainage performance prediction in heterogeneous reservoirs, Expert Syst. Appl. 42 (2015) 723–740. doi:10.1016/j.eswa.2014.08.034.

[82] L. Vinet, A. Zhedanov, A ‘missing’ family of classical orthogonal polynomials, J. Phys. A Math. Theor. 44 (2011) 085201. doi:10.1088/1751-8113/44/8/085201.

[83] A.G. Wilson, R.P. Adams, Gaussian Process Covariance Kernels for Pattern Discovery and Extrapolation, in: Proc. 30th Int. Conf. Mach. Learn., 2013: p. 15. http://arxiv.org/abs/1302.4245.

[84] T.M. Mitchell, Machine Learning, McGraw-Hill, Inc., New York, NY, USA, 1997.

[85] S. Ferson, W.L. Oberkampf, Validation of imprecise probability models, Int. J. Reliab. Saf. 3 (2009). doi:10.1504/IJRS.2009.026832.

[86] A.G. Barnston, Correspondence among the Correlation, RMSE, and Heidke Forecast Verification Measures; Refinement of the Heidke Score, Weather Forecast. 7 (1992) 699–709. doi:10.1175/1520-0434(1992)007<0699:CATCRA>2.0.CO;2.

[87] Y. Cheung, H. Jia, Categorical-and-numerical-attribute data clustering based on a unified similarity metric without knowing cluster number, Pattern Recognit. 46 (2013) 2228–2238.

[88] A.M. Ansari, N.D. Sylvester, C. Sarica, O. Shoham, J.P. Brill, A Comprehensive Mechanistic Model for Upward Two-Phase Flow in Wellbores, SPE Prod. Facil. 9 (1994) 143–152. doi:http://dx.doi.org/10.2118/20630-PA.

[89] A. Rodriguez, A. Laio, Clustering by Fast Search and Find of Density Peaks, Science (80-.). 344 (2014) 1492–1496. doi:10.1126/science.1242072.

[90] B. McLaury, S. Shirazi, Generalization of API RP 14E for erosive service in multiphase production, SPE Annu. Tech. Conf. Exhib. (1999) 423–432. doi:10.2118/56812-ms.

[91] A. Faghri, Y. Zhang, Transport phenomena in multiphase systems, Burlington: Elsevier Academic Press, 2006.

[92] R. Okita, Effects of Viscosity and Particle Size on Erosion Measurement and Predictions, The University of Tulsa, 2010.

[93] M. Ishi, K. Mishima, Droplet entrainment correlation in annular two-phase flow, Int. J. Heat Mass Transf. 32 (1989) 1835–1846.

[94] Y. Taitel, D. Barnea, Two-Phase Slug Flow, Academic Press Inc., 1990.

[95] B.S. McLaury, S.A. Shirazi, E.F. Rybicki, Sand Erosion In Multiphase Flow For Slug And Annular Flow Regimes, in: Corros. 2010, San Antonio, Texas, 2010: pp. 1–16.

[96] Mazumder, A Mechanistic Model To Predict Sand Erosion in Multiphase Flow in Elbows Downstream of Vertical Pipes, Corrosion. (2004) 1–15.

[97] S. Sankararaman, Y. Ling, C. Shantz, S. Mahadevan, Uncertainty Quantification in Fatigue Damage Prognosis, Int. Conf. Progn. Heal. Manag. (2009) 1–13.

[98] H. Nickisch, C.E. Rasmussen, Approximations for Binary Gaussian Process Classification, J. Mach. Learn. Res. 9 (2008) 2035–2078.

http://www.jmlr.org/papers/volume9/nickisch08a/nickisch08a.pdf.

[99] J.Q. Shi, T. Choi, Gaussian Process Regression Analysis for Functional Data, 2014. doi:10.1007/s13398-014-0173-7.2.

[100] J. Morgan, Classification and Regression Tree Analysis, Bu.Edu. (2014) 16. http://www.bu.edu/sph/files/2014/05/MorganCART.pdf.

[101] D. Freedman, Statistical models: theory and practice, 2009.

[102] M. Sokolova, G. Lapalme, A systematic analysis of performance measures for classification tasks, Inf. Process. Manag. 45 (2009) 427–437. doi:10.1016/j.ipm.2009.03.002.

[103] C.D. Brown, H.T. Davis, Receiver operating characteristics curves and related decision measures: A tutorial, Chemom. Intell. Lab. Syst. 80 (2006) 24–38. doi:10.1016/j.chemolab.2005.05.004.

[104] R. Fluss, D. Faraggi, B. Reiser, Estimation of the Youden Index and its associated cutoff point, Biometrical J. 47 (2005) 458–472. doi:10.1002/bimj.200410135.

[105] Y.Y. Haimes, L.S. Lasdon, D.A. Wismer, On a Bicriterion Formulation of the Problems of Integrated System Identification and System Optimization, IEEE Journals Mag. 47 (1971) 296–297. doi:10.1109/TSMC.1971.4308298.

[106] B. Shahriari, K. Swersky, Z. Wang, R.P. Adams, N. De Freitas, Taking the human out of the loop: A review of Bayesian optimization, Proc. IEEE. 104 (2016) 148–175. doi:10.1109/JPROC.2015.2494218.

[107] A.D. Bull, A.B.C.A. Uk, Convergence Rates of Efficient Global Optimization Algorithms, J. Mach. Learn. Res. 12 (2011) 2879–2904.

[108] A.G. Wilson, Covariance kernels for fast automatic pattern discovery and extrapolation with Gaussian processes, Dissertation. (2014). http://mlg.eng.cam.ac.uk/andrew/andrewgwthesis.pdf.

[109] J. Snoek, H. Larochelle, R.R.P. Adams, Practical Bayesian Optimization of Machine Learning Algorithms, Adv. Neural Inf. Process. Syst. (2012) 1–9. doi:2012arXiv1206.2944S.

[110] ANSI/ASME, ANSI/ASME Standard B31.3, Standard for Chemical Plant and Petroleum Refinery Piping, New York, NY, USA, 2002.

[111] F. White, Fluid Mechanics, McGraw-Hill,New York. (2010) 862. doi:10.1111/j.1549-8719.2009.00016.x.Mechanobiology.

[112] M.C. Ruzicka, On dimensionless numbers, Chem. Eng. Res. Des. 86 (2008) 835–868. doi:10.1016/j.cherd.2008.03.007.

[113] A. Shaikh, M. Al-Dahhan, Development of an artificial neural network correlation for prediction of overall gas holdup in bubble column reactors, Chem. Eng. Process. Process Intensif. 42 (2003) 599–610. doi:10.1016/S0255-2701(02)00209-X.

[114] M. Lashkarbolooki, B. Vaferi, D. Mowla, Using Artificial Neural Network to Predict the Pressure Drop in a Rotating Packed Bed, Sep. Sci. Technol. 47 (2012) 2450–2459. doi:10.1080/01496395.2012.665975.

[115] S. Bansal, S. Roy, F. Larachi, Support vector regression models for trickle bed reactors, Chem. Eng. J. 207–208 (2012) 822–831. doi:10.1016/j.cej.2012.07.081.

[116] J. Strong, Scale-up of Pharmaceutical Manufacturing Operations of Solid Dosage Forms, in: Dev. Solid Oral Dos. Forms, 2009: pp. 615–636. doi:10.1016/B978-0-444-53242-8.00027-8.

[117] J. Bertrand, Sur l'homogénéité dans les formules de physique, Comptes Rendus. 86 (1878) 916–920.

[118] R. Okita, Y. Zhang, B.S. McLaury, S. a. Shirazi, Experimental and Computational Investigations to Evaluate the Effects of Fluid Viscosity and Particle Size on Erosion Damage, J. Fluids Eng. 134 (2012) 061301. doi:10.1115/1.4005683.

[119] P.A. Ramachandran, Advanced transport phenomena : analysis, modeling and computations, Cambridge : Cambridge University Press., 2014.

[120] W.L. Oberkampf, S.M. DeLand, B.M. Rutherford, K. V. Diegert, K.F. Alvin, Error and uncertainty in modeling and simulation, Reliab. Eng. Syst. Saf. 75 (2002) 333–357. doi:10.1016/S0951-8320(01)00120-X.

[121] D. Mladeni, Feature Selection for Dimensionality Reduction, Subspace, Latent Struct. Featur. Sel. 3940 (2006) 84–102. doi:10.1007/11752790_5.

[122] G. Chandrashekar, F. Sahin, A survey on feature selection methods, Comput. Electr. Eng. 40 (2014) 16–28. doi:10.1016/j.compeleceng.2013.11.024.

[123] K. Blix, T. Eltoft, Evaluation of Feature Ranking and Regression Methods for Oceanic Chlorophyll-a Estimation, IEEE J. Sel. Top. Appl. Earth Obs. Remote Sens. (2018). doi:10.1109/JSTARS.2018.2810704.

[124] B.J. Azzopardi, Multiphase Flow, Multiph. Flow. I (2006). doi:10.1615/AtoZ.m.multiphase_flow.

[125] L. Pan, T.J. Hanratty, Correlation of entrainment for annular flow in horizontal pipes, 28 (2002) 385–408.

[126] A.H. Lefebvre, Atomization and spray, Corp., New York. 1989 (1989).

[127] Q.H. Mazumder, S-bend erosion in particulated multiphase flow with air and sand, J.

Comput. Multiph. Flows. 8 (2016) 157–166. doi:10.1177/1757482X16668363.

[128] A. Okhovat, S. Zeinali Heris, M.A. Haj Asgarkhani, K. Mohamadi Fard, Modeling and simulation of erosion–corrosion in disturbed two-phase flow through fluid transport pipelines, Arab. J. Sci. Eng. 39 (2014) 1497–1505. doi:10.1007/s13369-013-0771-2.

[129] Petalas, N. and Aziz, K., A Mechanistic Model for Multiphase Flow in Pipes, Soc. Pet. Eng. [Successor to Pet. Soc. Canada]. 39 (2000). doi:10.2118/00-06-04.

[130] N. Hall Taylor, G.F. Hewitt, P.M.C. Lacey, The motion and frequency of large disturbance waves in annular two-phase flow of air-water mixtures, Chem. Eng. Sci. 18 (1963) 537–552. doi:10.1016/0009-2509(63)85014-9.

[131] R. Belt, B. Djoric, S. Kalali, E. Duret, D. Larrey, Comparison of commercial multiphase flow simulators with experimental and field databases, 15th Int. Conf. Multiph. Prod. Technol. (2011) 413–427. https://www.onepetro.org/conference-paper/BHR-2011-I2.

[132] N.R. Kesana, S. a. Grubb, B.S. McLaury, S. a. Shirazi, Ultrasonic Measurement of Multiphase Flow Erosion Patterns in a Standard Elbow, J. Energy Resour. Technol. 135 (2013) 032905. doi:10.1115/1.4023331.

[133] R.V.A. Oliemans, B.F.M. Pots, N. Trompé, Modelling of annular dispersed two-phase flow in vertical pipes, Int. J. Multiph. Flow. 12 (1986) 711–732. doi:10.1016/0301-9322(86)90047-9.

[134] K.L. Magrini, C. Sarica, A. Al-Sarkhi, H.-Q. Zhang, Liquid Entrainment in Annular Gas/Liquid Flow in Inclined Pipes, SPE Annu. Tech. Conf. Exhib. (2010). doi:10.2118/134765-MS.

[135] S. Ferson, W.L. Oberkampf, L. Ginzburg, Model validation and predictive capability for the thermal challenge problem, Comput. Methods Appl. Mech. Eng. 197 (2008) 2408–2430. doi:10.1016/j.cma.2007.07.030.

APPENDIX A

Database

The detailed operating conditions for data points collected in the database are given in the tables below.

Table A.1. Operating conditions of 669 data points before preprocessing steps

No	EXP	MA	GEO	D (inch)	h_B (vicker)	d_p (μm)	ρ_g (kg/m^3)	V_{sg} (m/s)	μ_l (cp)	V_{sl} (m/s)	σ (dyne/cm)	PO	ANG	ERR (mils/lb)
1	Antezana [32]	ER	Tee	1.0	330	150	4	29	1	2.8E-01	73	VER	NA	9.8E-03
2	Antezana [32]	ER	Tee	1.0	330	150	4	23	1	3.0E-01	73	VER	NA	4.1E-03
3	Antezana [32]	ER	Tee	1.0	330	150	4	15	1	2.9E-01	73	VER	NA	5.6E-04
4	Antezana [32]	ER	Tee	1.0	330	150	4	30	1	1.3E-01	73	VER	NA	1.0E-02
5	Antezana [32]	ER	Tee	1.0	330	150	4	30	1	1.3E-01	73	VER	NA	1.0E-02
6	Antezana [32]	ER	Tee	1.0	330	150	4	23	1	1.3E-01	73	VER	NA	2.8E-03
7	Antezana [32]	ER	Tee	1.0	330	150	4	29	1	2.8E-01	73	HOR	NA	3.7E-03
8	Antezana [32]	ER	Tee	1.0	330	150	4	23	1	3.0E-01	73	HOR	NA	2.0E-03
9	Antezana [32]	ER	Tee	1.0	330	150	4	15	1	2.9E-01	73	HOR	NA	3.1E-04
10	Antezana [32]	ER	Tee	1.0	330	150	4	30	1	1.3E-01	73	HOR	NA	8.2E-03
11	Antezana [32]	ER	Tee	1.0	330	150	4	23	1	1.3E-01	73	HOR	NA	1.7E-03
12	Bikbaev [29]	WL	Long elbow	2.0	120	295	1	50	1	0.0E+00	73	VER	NA	2.3E-01
13	Bikbaev [29]	WL	Long elbow	2.0	120	295	1	50	1	0.0E+00	73	VER	NA	2.0E-01
14	Bikbaev [29]	WL	Long elbow	2.0	120	295	1	50	1	0.0E+00	73	VER	NA	1.7E-01
15	Bikbaev [29]	WL	Long elbow	2.0	120	295	1	50	1	0.0E+00	73	VER	NA	1.2E-01
16	Bikbaev [29]	WL	Long elbow	2.0	120	295	1	55	1	0.0E+00	73	VER	NA	5.2E-01
17	Bikbaev [29]	WL	Long elbow	2.0	120	295	1	55	1	0.0E+00	73	VER	NA	2.7E-01
18	Bikbaev [29]	WL	Long elbow	2.0	120	295	1	55	1	0.0E+00	73	VER	NA	2.3E-01
19	Bikbaev [29]	WL	Long elbow	2.0	120	295	1	55	1	0.0E+00	73	VER	NA	2.4E-01

20	Bikbaev [29]	WL	Long elbow	2.0	120	295	1	33	1	0.0E+00	73	VER	NA	9.5E-02
21	Bikbaev [29]	WL	Long elbow	2.0	120	295	1	39	1	0.0E+00	73	VER	NA	1.4E-01
22	Bikbaev [29]	WL	Long elbow	2.0	120	295	1	50	1	0.0E+00	73	VER	NA	2.4E-01
23	Bikbaev [29]	WL	Long elbow	2.0	120	295	1	50	1	0.0E+00	73	VER	NA	4.0E-01
24	Bourgoyne [14]	UTL	Long elbow	2.1	140	350	1	72	1	5.3E-01	73	VER	NA	9.6E-01
25	Bourgoyne [14]	UTL	Long elbow	2.1	140	350	1	84	1	1.2E-01	73	VER	NA	1.3E+00
26	Bourgoyne [14]	UTL	Long elbow	2.1	140	350	1	84	1	5.3E-01	73	VER	NA	1.7E+00
27	Bourgoyne [14]	UTL	Long elbow	2.1	140	350	1	86	1	5.3E-01	73	VER	NA	2.3E+00
28	Bourgoyne [14]	UTL	Long elbow	2.1	140	350	1	89	1	1.2E-01	73	VER	NA	1.9E+00
29	Bourgoyne [14]	UTL	Long elbow	2.1	140	350	1	92	1	1.2E-01	73	VER	NA	1.8E+00
30	Bourgoyne [14]	UTL	Long elbow	2.1	140	350	1	92	1	5.3E-01	73	VER	NA	2.2E+00
31	Bourgoyne [14]	UTL	Long elbow	2.1	140	350	1	107	1	5.3E-01	73	VER	NA	1.9E+00
32	Bourgoyne [14]	UTL	Tee	2.1	140	350	1	70	1	5.3E-01	73	VER	NA	3.6E-02
33	Bourgoyne [14]	UTL	Tee	2.1	140	350	1	76	1	1.2E-01	73	VER	NA	3.8E-02
34	Bourgoyne [14]	UTL	Tee	2.1	140	350	1	81	1	5.3E-01	73	VER	NA	2.4E-02
35	Bourgoyne [14]	UTL	Elbow	2.1	120	350	1	32	1	0.0E+00	73	VER	NA	1.4E-01
36	Bourgoyne [14]	UTL	Elbow	2.1	120	350	1	47	1	0.0E+00	73	VER	NA	8.8E-02
37	Bourgoyne [14]	UTL	Elbow	2.1	120	350	1	72	1	0.0E+00	73	VER	NA	2.5E-01
38	Bourgoyne [14]	UTL	Elbow	2.1	120	350	1	93	1	0.0E+00	73	VER	NA	5.0E-01
39	Bourgoyne [14]	UTL	Elbow	2.1	120	350	1	98	1	0.0E+00	73	VER	NA	6.3E-01

40	Bourgoyne [14]	UTL	Elbow	2.1	120	350	1	98	1	0.0E+00	73	VER	NA	6.3E-01
41	Bourgoyne [14]	UTL	Elbow	2.1	120	350	1	103	1	0.0E+00	73	VER	NA	6.7E-01
42	Bourgoyne [14]	UTL	Elbow	2.1	120	350	1	122	1	0.0E+00	73	VER	NA	3.8E+00
43	Bourgoyne [14]	UTL	Elbow	2.1	120	350	1	167	1	0.0E+00	73	VER	NA	3.3E+00
44	Bourgoyne [14]	UTL	Elbow	2.1	120	350	1	169	1	0.0E+00	73	VER	NA	3.4E+00
45	Bourgoyne [14]	UTL	Elbow	2.1	120	350	1	177	1	0.0E+00	73	VER	NA	4.3E+00
46	Bourgoyne [14]	UTL	Elbow	2.1	120	350	1	177	1	0.0E+00	73	VER	NA	4.5E+00
47	Bourgoyne [14]	UTL	Elbow	2.1	120	350	1	178	1	0.0E+00	73	VER	NA	4.0E+00
48	Bourgoyne [14]	UTL	Elbow	2.1	120	350	1	203	1	0.0E+00	73	VER	NA	4.7E+00
49	Bourgoyne [14]	UTL	Elbow	2.1	120	350	1	205	1	0.0E+00	73	VER	NA	3.7E+00
50	Bourgoyne [14]	UTL	Elbow	2.1	120	350	1	222	1	0.0E+00	73	VER	NA	4.1E+00
51	Bourgoyne [14]	UTL	Elbow	2.1	120	350	1	108	1	0.0E+00	73	VER	NA	1.3E+00
52	Bourgoyne [14]	UTL	Elbow	2.1	120	350	1	109	1	0.0E+00	73	VER	NA	1.1E+00
53	Bourgoyne [14]	UTL	Elbow	2.1	120	350	1	108	1	0.0E+00	73	VER	NA	9.8E-01
54	Bourgoyne [14]	UTL	Elbow	2.1	120	350	1	104	1	0.0E+00	73	VER	NA	1.2E+00
55	Bourgoyne [14]	UTL	Elbow	2.1	120	350	1	108	1	0.0E+00	73	VER	NA	1.4E+00
56	Bourgoyne [14]	UTL	Elbow	2.1	120	350	1	108	1	0.0E+00	73	VER	NA	1.2E+01
57	Bourgoyne [14]	UTL	Elbow	2.1	120	350	1	107	1	0.0E+00	73	VER	NA	8.6E-01
58	Bourgoyne [14]	UTL	Elbow	2.1	120	350	1	111	1	0.0E+00	73	VER	NA	1.0E+00
59	Bourgoyne [14]	UTL	Elbow	2.1	120	350	1	107	1	0.0E+00	73	VER	NA	1.1E+00

60	Bourgoyne [14]	UTL	Elbow	2.1	120	350	1	106	1	0.0E+00	73	VER	NA	9.2E-01
61	Bourgoyne [14]	UTL	Elbow	2.1	120	350	1	103	1	0.0E+00	73	VER	NA	7.1E-01
62	Dosila [36]	ER	Elbow	2.0	330	150	1	29	10	1.8E-03	73	VER	NA	2.4E-03
63	Dosila [36]	ER	Elbow	2.0	330	150	1	29	10	1.5E-03	73	VER	NA	1.9E-03
64	Dosila [36]	ER	Elbow	2.0	330	150	1	29	10	2.4E-03	73	VER	NA	2.1E-03
65	Dosila [36]	ER	Elbow	2.0	330	150	1	29	10	8.2E-03	73	VER	NA	2.4E-03
66	Dosila [36]	ER	Elbow	2.0	330	150	1	29	10	2.7E-03	73	VER	NA	2.0E-03
67	Dosila [36]	ER	Elbow	2.0	330	150	1	29	10	4.0E-03	73	VER	NA	1.5E-03
68	Dosila [36]	ER	Elbow	2.0	330	150	1	29	10	1.9E-03	73	VER	NA	2.8E-03
69	Dosila [36]	ER	Elbow	2.0	330	150	1	29	10	1.7E-03	73	VER	NA	3.2E-03
70	Dosila [36]	ER	Elbow	2.0	330	150	1	29	10	2.2E-03	73	VER	NA	4.1E-03
71	Dosila [36]	ER	Elbow	2.0	330	150	1	29	10	2.2E-03	73	VER	NA	1.9E-03
72	Dosila [36]	ER	Elbow	2.0	330	150	1	29	10	3.1E-03	73	VER	NA	7.2E-04
73	Dosila [36]	ER	Elbow	2.0	330	150	1	29	10	1.5E-03	73	VER	NA	3.6E-03
74	Dosila [36]	ER	Elbow	2.0	330	150	1	29	10	3.1E-03	73	VER	NA	1.9E-03
75	Dosila [36]	ER	Elbow	2.0	330	150	1	29	10	1.2E-03	73	VER	NA	2.7E-03
76	Dosila [36]	ER	Elbow	2.0	330	150	1	29	10	2.0E-03	73	VER	NA	3.4E-03
77	Dosila [36]	ER	Elbow	2.0	330	150	1	29	10	3.0E-03	73	VER	NA	2.9E-03
78	Dosila [36]	ER	Elbow	2.0	330	150	1	29	10	3.7E-03	73	VER	NA	2.3E-03
79	Dosila [36]	ER	Elbow	2.0	330	150	1	29	10	7.0E-03	73	VER	NA	1.2E-03
80	Dosila [36]	ER	Elbow	2.0	330	150	1	29	10	3.8E-02	73	VER	NA	1.4E-03
81	Dosila [36]	ER	Elbow	2.0	330	150	1	29	10	1.2E-02	73	VER	NA	1.2E-03
82	Dosila [36]	ER	Elbow	2.0	330	150	1	29	10	6.1E-03	73	VER	NA	1.3E-03
83	Dosila [36]	ER	Elbow	2.0	330	150	1	29	10	8.5E-03	73	VER	NA	8.4E-04
84	Dosila [36]	ER	Elbow	2.0	330	150	1	29	10	7.6E-03	73	VER	NA	1.4E-03
85	Dosila [36]	ER	Elbow	2.0	330	150	1	29	10	4.6E-03	73	VER	NA	1.9E-03
86	Dosila [36]	ER	Elbow	2.0	330	150	1	29	10	6.1E-03	73	VER	NA	1.8E-03
87	Dosila [36]	ER	Elbow	2.0	330	150	1	29	10	1.2E-02	73	VER	NA	2.2E-03
88	Dosila [36]	ER	Elbow	2.0	330	150	1	29	10	3.0E-04	73	VER	NA	4.7E-03
89	Dosila [36]	ER	Elbow	2.0	330	150	1	29	10	2.4E-04	73	VER	NA	4.8E-03
90	Dosila [36]	ER	Elbow	2.0	330	150	1	29	10	9.1E-04	73	VER	NA	6.2E-03
91	Dosila [36]	ER	Elbow	2.0	330	150	1	29	10	6.1E-04	73	VER	NA	9.4E-03
92	Dosila [36]	ER	Elbow	2.0	330	150	1	29	10	7.6E-04	73	VER	NA	8.6E-03
93	Dosila [36]	ER	Elbow	2.0	330	300	1	29	10	1.8E-02	73	VER	NA	1.1E-02
94	Dosila [36]	ER	Elbow	2.0	330	300	1	29	10	3.2E-02	73	VER	NA	7.3E-03
95	Dosila [36]	ER	Elbow	2.0	330	300	1	29	10	1.0E-03	73	VER	NA	2.0E-02
96	Dosila [36]	ER	Elbow	2.0	330	300	1	29	10	1.6E-03	73	VER	NA	4.7E-03
97	Dosila [36]	ER	Elbow	2.0	330	300	1	29	10	9.8E-04	73	VER	NA	3.8E-02
98	Dosila [36]	ER	Elbow	2.0	330	300	1	29	10	3.4E-03	73	VER	NA	1.7E-02

99	Dosila [36]	ER	Elbow	2.0	330	300	1	29	10	1.6E-03	73	VER	NA	2.8E-02
100	Dosila [36]	ER	Elbow	2.0	330	300	1	29	10	1.8E-03	73	VER	NA	2.3E-02
101	Dosila [36]	ER	Elbow	2.0	330	300	1	29	10	4.3E-03	73	VER	NA	1.5E-02
102	Dosila [36]	ER	Elbow	2.0	330	300	1	29	10	2.0E-03	73	VER	NA	2.2E-02
103	Dosila [36]	ER	Elbow	2.0	330	300	1	29	10	2.3E-03	73	VER	NA	1.6E-02
104	Dosila [36]	ER	Elbow	2.0	330	300	1	29	10	4.1E-03	73	VER	NA	9.1E-03
105	Dosila [36]	ER	Elbow	2.0	330	300	1	29	10	7.6E-03	73	VER	NA	9.6E-03
106	Dosila [36]	ER	Elbow	2.0	330	300	1	29	10	3.4E-03	73	VER	NA	8.8E-03
107	Dosila [36]	ER	Elbow	2.0	330	300	1	29	10	4.9E-03	73	VER	NA	7.5E-03
108	Dosila [36]	ER	Elbow	2.0	330	300	1	29	10	9.1E-03	73	VER	NA	4.6E-03
109	Dosila [36]	ER	Elbow	2.0	330	300	1	29	10	5.4E-03	73	VER	NA	7.8E-03
110	Dosila [36]	ER	Elbow	2.0	330	150	1	29	1	6.1E-03	73	VER	NA	3.9E-03
111	Dosila [36]	ER	Elbow	2.0	330	150	1	29	1	9.4E-03	73	VER	NA	3.4E-03
112	Dosila [36]	ER	Elbow	2.0	330	150	1	29	1	1.0E-02	73	VER	NA	3.7E-03
113	Dosila [36]	ER	Elbow	2.0	330	150	1	29	1	1.4E-02	73	VER	NA	3.9E-03
114	Dosila [36]	ER	Elbow	2.0	330	150	1	29	1	2.1E-02	73	VER	NA	6.0E-03
115	Dosila [36]	ER	Elbow	2.0	330	150	1	29	1	2.2E-02	73	VER	NA	5.8E-03
116	Dosila [36]	ER	Elbow	2.0	330	150	1	29	1	2.7E-02	73	VER	NA	5.4E-03
117	Dosila [36]	ER	Elbow	2.0	330	150	1	29	1	3.0E-02	73	VER	NA	5.0E-03
118	Dosila [36]	ER	Elbow	2.0	330	150	1	29	1	3.9E-02	73	VER	NA	5.1E-03
119	Dosila [36]	ER	Elbow	2.0	330	150	1	29	1	4.8E-02	73	VER	NA	5.8E-03
120	Dosila [36]	ER	Elbow	2.0	330	150	1	29	1	1.5E-01	73	VER	NA	2.6E-03
121	Dosila [36]	ER	Elbow	2.0	330	150	1	29	1	3.0E-05	73	VER	NA	1.8E-02
122	Dosila [36]	ER	Elbow	2.0	330	150	1	29	1	3.0E-05	73	VER	NA	1.7E-02
123	Dosila [36]	ER	Elbow	2.0	330	150	1	29	1	1.2E-03	73	VER	NA	8.6E-03
124	Dosila [36]	ER	Elbow	2.0	330	150	1	29	1	1.7E-03	73	VER	NA	7.3E-03
125	Dosila [36]	ER	Elbow	2.0	330	150	1	29	1	1.8E-03	73	VER	NA	7.3E-03
126	Dosila [36]	ER	Elbow	2.0	330	150	1	29	1	1.9E-03	73	VER	NA	8.0E-03
127	Dosila [36]	ER	Elbow	2.0	330	150	1	29	1	2.1E-03	73	VER	NA	5.2E-03
128	Dosila [36]	ER	Elbow	2.0	330	150	1	29	1	2.2E-03	73	VER	NA	1.2E-02
129	Dosila [36]	ER	Elbow	2.0	330	150	1	29	1	3.0E-03	73	VER	NA	3.9E-03
130	Dosila [36]	ER	Elbow	2.0	330	150	1	29	1	3.2E-03	73	VER	NA	4.5E-03
131	Dosila [36]	ER	Elbow	2.0	330	300	1	29	1	1.3E-01	73	VER	NA	2.0E-02
132	Dosila [36]	ER	Elbow	2.0	330	300	1	29	1	3.0E-05	73	VER	NA	6.6E-02
133	Dosila [36]	ER	Elbow	2.0	330	300	1	29	1	3.0E-05	73	VER	NA	5.4E-02
134	Dosila [36]	ER	Elbow	2.0	330	300	1	29	1	3.0E-05	73	VER	NA	8.5E-02
135	Dosila [36]	ER	Elbow	2.0	330	300	1	29	1	3.0E-05	73	VER	NA	7.2E-02
136	Dosila [36]	ER	Elbow	2.0	330	300	1	29	1	7.0E-04	73	VER	NA	4.7E-02
137	Dosila [36]	ER	Elbow	2.0	330	300	1	29	1	8.7E-04	73	VER	NA	3.2E-02
138	Dosila [36]	ER	Elbow	2.0	330	300	1	29	1	1.2E-03	73	VER	NA	3.4E-02
139	Dosila [36]	ER	Elbow	2.0	330	300	1	29	1	1.5E-03	73	VER	NA	3.1E-02

140	Dosila [36]	ER	Elbow	2.0	330	300	1	29	1	2.1E-03	73	VER	NA	3.6E-02
141	Dosila [36]	ER	Elbow	2.0	330	300	1	29	1	2.1E-03	73	VER	NA	3.1E-02
142	Dosila [36]	ER	Elbow	2.0	330	300	1	29	1	2.4E-03	73	VER	NA	1.8E-02
143	Dosila [36]	ER	Elbow	2.0	330	300	1	29	1	3.0E-03	73	VER	NA	3.3E-02
144	Dosila [36]	ER	Elbow	2.0	330	300	1	29	1	4.3E-03	73	VER	NA	3.3E-02
145	Dosila [36]	ER	Elbow	2.0	330	300	1	29	1	4.8E-03	73	VER	NA	3.1E-02
146	Dosila [36]	ER	Elbow	2.0	330	300	1	29	1	5.2E-03	73	VER	NA	2.9E-02
147	Dosila [36]	ER	Elbow	2.0	330	300	1	29	1	5.5E-03	73	VER	NA	2.6E-02
148	Dosila [36]	ER	Elbow	2.0	330	300	1	29	1	5.8E-03	73	VER	NA	2.6E-02
149	Dosila [36]	ER	Elbow	2.0	330	300	1	29	1	6.0E-03	73	VER	NA	2.4E-02
150	Dosila [36]	ER	Elbow	2.0	330	300	1	29	1	7.6E-03	73	VER	NA	1.9E-02
151	Dosila [36]	ER	Elbow	2.0	330	300	1	29	1	9.1E-03	73	VER	NA	2.4E-02
152	Dosila [36]	ER	Elbow	2.0	330	300	1	29	1	1.2E-02	73	VER	NA	2.1E-02
153	Dosila [36]	ER	Elbow	2.0	330	300	1	29	1	1.5E-02	73	VER	NA	2.6E-02
154	Dosila [36]	ER	Elbow	2.0	330	300	1	29	1	1.8E-02	73	VER	NA	1.9E-02
155	Dosila [36]	ER	Elbow	2.0	330	300	1	29	1	3.0E-02	73	VER	NA	3.4E-02
156	Dosila [36]	ER	Elbow	2.0	330	300	1	29	1	3.0E-02	73	VER	NA	3.3E-02
157	Dosila [36]	ER	Elbow	2.0	330	300	1	29	1	4.0E-02	73	VER	NA	3.3E-02
158	Dosila [36]	ER	Elbow	2.0	330	300	1	29	1	4.9E-02	73	VER	NA	3.0E-02
159	Dosila [36]	ER	Elbow	2.0	330	300	1	29	1	5.3E-02	73	VER	NA	3.2E-02
160	Evans [33]	ER	Long elbow	4.0	142	150	46	23	1	0.0E+00	73	VER	NA	4.9E-04
161	Evans [33]	ER	Long elbow	4.0	142	150	46	35	1	0.0E+00	73	VER	NA	1.7E-03
162	Evans [33]	ER	Long elbow	4.0	142	150	46	63	1	0.0E+00	73	VER	NA	7.1E-03
163	Evans [33]	ER	Long elbow	4.0	222	150	46	23	1	0.0E+00	73	VER	NA	2.4E-04
164	Evans [33]	ER	Long elbow	4.0	222	150	46	35	1	0.0E+00	73	VER	NA	1.0E-03
165	Evans [33]	ER	Long elbow	4.0	222	150	46	63	1	0.0E+00	73	VER	NA	2.6E-03
166	Evans [33]	ER	Long elbow	4.0	289	150	46	35	1	0.0E+00	73	VER	NA	3.6E-04
167	Fan [39]	ER	Elbow	4.0	330	150	1	23	1	1.3E-02	73	HOR	NA	4.2E-04
168	Fan [39]	ER	Elbow	4.0	330	150	1	23	1	1.3E-02	73	HOR	NA	5.9E-04
169	Fan [39]	ER	Elbow	4.0	330	150	1	23	1	1.6E-02	73	HOR	NA	5.2E-04
170	Fan [39]	ER	Elbow	4.0	330	150	1	23	1	2.6E-02	73	HOR	NA	4.0E-04
171	Fan [39]	ER	Elbow	4.0	330	150	1	23	1	3.2E-02	73	HOR	NA	4.9E-04
172	Fan [39]	ER	Elbow	4.0	330	150	1	23	1	4.3E-02	73	HOR	NA	3.0E-04
173	Fan [39]	ER	Elbow	4.0	330	150	1	23	1	4.8E-02	73	HOR	NA	3.5E-04

174	Fan [39]	ER	Elbow	4.0	330	150	1	23	1	5.8E-02	73	HOR	NA	9.1E-05
175	Fan [39]	ER	Elbow	4.0	330	150	1	23	1	6.9E-02	73	HOR	NA	5.0E-04
176	Fan [39]	ER	Elbow	4.0	330	150	1	23	1	7.3E-02	73	HOR	NA	1.0E-04
177	Fan [39]	ER	Elbow	4.0	330	150	1	23	1	1.4E-02	73	HOR	NA	5.7E-04
178	Fan [39]	ER	Elbow	4.0	330	150	1	23	1	2.4E-02	73	HOR	NA	1.6E-04
179	Fan [39]	ER	Elbow	4.0	330	150	1	23	1	1.0E-02	73	HOR	NA	6.3E-04
180	Fan [39]	ER	Elbow	4.0	330	150	1	23	1	1.8E-02	73	HOR	NA	4.2E-04
181	Fan [39]	ER	Elbow	4.0	330	150	1	23	1	2.8E-02	73	HOR	NA	1.6E-04
182	Fan [39]	ER	Elbow	4.0	330	150	1	23	1	3.7E-02	73	HOR	NA	4.2E-04
183	Fan [39]	ER	Elbow	4.0	330	150	1	23	1	5.0E-02	73	HOR	NA	2.2E-04
184	Fan [39]	ER	Elbow	4.0	330	150	1	23	1	5.6E-02	73	HOR	NA	1.4E-04
185	Fan [39]	ER	Elbow	4.0	330	150	1	23	1	7.9E-02	73	HOR	NA	1.8E-04
186	Fan [39]	ER	Elbow	4.0	330	300	1	23	1	5.7E-02	73	HOR	NA	3.9E-04
187	Fan [39]	ER	Elbow	4.0	330	300	1	23	1	6.8E-02	73	HOR	NA	1.9E-04
188	Fan [39]	ER	Elbow	4.0	330	300	1	23	1	5.3E-02	73	HOR	NA	3.5E-04
189	Fan [39]	ER	Elbow	4.0	330	300	1	23	1	4.2E-02	73	HOR	NA	5.3E-04
190	Fan [39]	ER	Elbow	4.0	330	300	1	23	1	7.4E-02	73	HOR	NA	1.2E-04
191	Fan [39]	ER	Elbow	4.0	330	300	1	23	1	6.0E-02	73	HOR	NA	1.5E-04
192	Fan [39]	ER	Elbow	4.0	330	300	1	23	1	5.2E-02	73	HOR	NA	4.4E-04
193	Fan [39]	ER	Elbow	4.0	330	300	1	23	1	4.2E-02	73	HOR	NA	6.6E-04
194	Fan [39]	ER	Elbow	4.0	330	300	1	23	1	9.4E-03	73	HOR	NA	8.1E-04
195	Fan [39]	ER	Elbow	4.0	330	300	1	23	1	6.7E-03	73	HOR	NA	1.4E-03
196	Fan [39]	ER	Elbow	4.0	330	300	1	23	1	4.3E-03	73	HOR	NA	1.7E-03
197	Fan [39]	ER	Elbow	4.0	330	300	1	23	1	9.1E-03	73	HOR	NA	4.7E-04
198	Fan [39]	ER	Elbow	4.0	330	300	1	23	1	6.1E-03	73	HOR	NA	6.1E-04
199	Fan [39]	ER	Elbow	4.0	330	300	1	23	1	4.0E-03	73	HOR	NA	2.5E-03
200	Fan [39]	ER	Elbow	4.0	330	150	1	15	1	3.4E-03	73	HOR	NA	3.2E-04
201	Fan [39]	ER	Elbow	4.0	330	150	1	15	1	3.4E-03	73	HOR	NA	6.4E-04
202	Fan [39]	ER	Elbow	4.0	330	150	1	15	1	4.9E-03	73	HOR	NA	3.7E-04
203	Fan [39]	ER	Elbow	4.0	330	150	1	15	1	4.6E-03	73	HOR	NA	2.2E-04
204	Fan [39]	ER	Elbow	4.0	330	150	1	15	1	3.4E-03	73	HOR	NA	2.3E-04
205	Fan [39]	ER	Elbow	4.0	330	150	1	15	1	2.4E-03	73	HOR	NA	1.4E-04
206	Fan [39]	ER	Elbow	4.0	330	150	1	15	1	4.3E-03	73	HOR	NA	4.9E-05
207	Fan [39]	ER	Elbow	4.0	330	150	1	15	1	6.1E-03	73	HOR	NA	2.9E-04
208	Fan [39]	ER	Elbow	4.0	330	150	1	15	1	8.8E-03	73	HOR	NA	1.3E-04
209	Fan [39]	ER	Elbow	4.0	330	150	1	15	1	1.1E-02	73	HOR	NA	5.7E-04
210	Fan [39]	ER	Elbow	4.0	330	150	1	15	1	1.2E-02	73	HOR	NA	4.4E-05
211	Fan [39]	ER	Elbow	4.0	330	150	1	15	1	1.5E-02	73	HOR	NA	4.0E-04
212	Fan [39]	ER	Elbow	4.0	330	150	1	15	1	1.9E-02	73	HOR	NA	5.1E-05
213	Fan [39]	ER	Elbow	4.0	330	150	1	15	1	4.0E-03	73	HOR	NA	2.2E-04
214	Fan [39]	ER	Elbow	4.0	330	150	1	15	1	3.4E-03	73	HOR	NA	9.4E-04

215	Fan [39]	ER	Elbow	4.0	330	150	1	15	1	5.8E-03	73	HOR	NA	9.5E-05
216	Fan [39]	ER	Elbow	4.0	330	150	1	15	1	8.5E-03	73	HOR	NA	1.2E-04
217	Fan [39]	ER	Elbow	4.0	330	150	1	15	1	1.2E-02	73	HOR	NA	6.1E-05
218	Fan [39]	ER	Elbow	4.0	330	150	1	15	1	1.5E-02	73	HOR	NA	1.2E-04
219	Fan [39]	ER	Elbow	4.0	330	150	1	15	1	1.4E-02	73	HOR	NA	1.0E-04
220	Fan [39]	ER	Elbow	4.0	330	150	1	15	1	1.8E-02	73	HOR	NA	1.5E-04
221	Fan [39]	ER	Elbow	4.0	330	150	1	15	1	1.8E-02	73	HOR	NA	1.3E-04
222	Fan [39]	ER	Elbow	4.0	330	300	1	15	1	2.0E-02	73	HOR	NA	1.2E-04
223	Fan [39]	ER	Elbow	4.0	330	300	1	15	1	2.0E-02	73	HOR	NA	3.1E-04
224	Fan [39]	ER	Elbow	4.0	330	300	1	15	1	1.6E-02	73	HOR	NA	6.3E-05
225	Fan [39]	ER	Elbow	4.0	330	300	1	15	1	1.4E-02	73	HOR	NA	5.1E-04
226	Fan [39]	ER	Elbow	4.0	330	300	1	15	1	1.2E-02	73	HOR	NA	5.4E-05
227	Fan [39]	ER	Elbow	4.0	330	300	1	15	1	9.8E-03	73	HOR	NA	1.7E-04
228	Fan [39]	ER	Elbow	4.0	330	300	1	15	1	8.8E-03	73	HOR	NA	3.8E-05
229	Fan [39]	ER	Elbow	4.0	330	300	1	15	1	4.6E-03	73	HOR	NA	1.3E-04
230	Fan [39]	ER	Elbow	4.0	330	300	1	15	1	3.4E-03	73	HOR	NA	5.4E-05
231	Fan [39]	ER	Elbow	4.0	330	300	1	15	1	2.3E-02	73	HOR	NA	4.4E-05
232	Fan [39]	ER	Elbow	4.0	330	300	1	15	1	1.9E-02	73	HOR	NA	3.4E-04
233	Fan [39]	ER	Elbow	4.0	330	300	1	15	1	1.6E-02	73	HOR	NA	8.3E-05
234	Fan [39]	ER	Elbow	4.0	330	300	1	15	1	1.4E-02	73	HOR	NA	7.4E-05
235	Fan [39]	ER	Elbow	4.0	330	300	1	15	1	8.5E-03	73	HOR	NA	1.6E-04
236	Fan [39]	ER	Elbow	4.0	330	300	1	15	1	6.1E-03	73	HOR	NA	2.7E-04
237	Fan [39]	ER	Elbow	4.0	330	300	1	15	1	4.0E-03	73	HOR	NA	5.2E-04
238	Fan [39]	ER	Elbow	4.0	330	150	1	23	1	2.2E-02	73	VER	45	6.0E-04
239	Fan [39]	ER	Elbow	4.0	330	150	1	23	1	2.0E-02	73	VER	45	7.8E-04
240	Fan [39]	ER	Elbow	4.0	330	150	1	23	1	1.7E-02	73	VER	45	9.1E-04
241	Fan [39]	ER	Elbow	4.0	330	150	1	23	1	1.3E-02	73	VER	45	9.8E-04
242	Fan [39]	ER	Elbow	4.0	330	150	1	23	1	1.2E-02	73	VER	45	1.2E-03
243	Fan [39]	ER	Elbow	4.0	330	150	1	23	1	9.1E-03	73	VER	45	1.4E-03
244	Fan [39]	ER	Elbow	4.0	330	150	1	23	1	7.9E-03	73	VER	45	1.5E-03
245	Fan [39]	ER	Elbow	4.0	330	150	1	23	1	5.5E-03	73	VER	45	1.8E-03
246	Fan [39]	ER	Elbow	4.0	330	150	1	23	1	3.7E-03	73	VER	45	1.4E-03
247	Fan [39]	ER	Elbow	4.0	330	300	1	23	1	2.2E-02	73	VER	45	1.5E-03
248	Fan [39]	ER	Elbow	4.0	330	300	1	23	1	1.6E-02	73	VER	45	2.7E-03
249	Fan [39]	ER	Elbow	4.0	330	300	1	23	1	1.0E-02	73	VER	45	5.7E-03
250	Fan [39]	ER	Elbow	4.0	330	300	1	23	1	4.3E-03	73	VER	45	5.0E-03
251	Fan [39]	ER	Elbow	4.0	330	150	1	15	1	2.0E-02	73	VER	45	9.7E-04
252	Fan [39]	ER	Elbow	4.0	330	150	1	15	1	1.6E-02	73	VER	45	5.5E-04
253	Fan [39]	ER	Elbow	4.0	330	150	1	15	1	1.4E-02	73	VER	45	5.1E-04
254	Fan [39]	ER	Elbow	4.0	330	150	1	15	1	1.4E-02	73	VER	45	5.9E-04
255	Fan [39]	ER	Elbow	4.0	330	150	1	15	1	1.2E-02	73	VER	45	6.8E-04

256	Fan [39]	ER	Elbow	4.0	330	150	1	15	1	1.1E-02	73	VER	45	2.5E-04
257	Fan [39]	ER	Elbow	4.0	330	150	1	15	1	7.9E-03	73	VER	45	4.7E-04
258	Fan [39]	ER	Elbow	4.0	330	150	1	15	1	5.5E-03	73	VER	45	9.8E-04
259	Fan [39]	ER	Elbow	4.0	330	150	1	15	1	3.4E-03	73	VER	45	3.0E-04
260	Fan [39]	ER	Elbow	4.0	330	300	1	15	1	1.6E-02	73	VER	45	5.1E-04
261	Fan [39]	ER	Elbow	4.0	330	300	1	15	1	8.5E-03	73	VER	45	1.6E-03
262	Fan [39]	ER	Elbow	4.0	330	300	1	15	1	4.0E-03	73	VER	45	3.3E-03
263	Fan [39]	ER	Elbow	4.0	330	300	1	15	1	2.2E-02	73	VER	45	3.9E-04
264	Throneberry [40]	Angle-head ER	Elbow	3.0	330	20	1	30	1	4.6E-01	73	VER	NA	1.2E-03
265	Throneberry [40]	Angle-head ER	Elbow	3.0	330	20	1	15	1	8.0E-01	73	VER	NA	3.7E-05
266	Throneberry [40]	ER	Elbow	3.0	330	20	1	15	1	8.0E-01	73	VER	45	7.5E-06
267	Throneberry [40]	Angle-head ER	Elbow	3.0	330	20	1	46	1	8.0E-01	73	VER	NA	2.2E-03
268	Throneberry [40]	Angle-head ER	Elbow	3.0	330	20	1	46	1	4.9E-01	73	VER	NA	2.3E-03
269	Throneberry [40]	ER	Elbow	3.0	330	20	1	46	1	4.9E-01	73	VER	45	1.0E-04
270	Throneberry [40]	Angle-head ER	Elbow	3.0	330	20	1	38	1	5.0E-01	73	VER	NA	1.5E-03
271	Throneberry [40]	ER	Elbow	3.0	330	20	1	38	1	5.0E-01	73	VER	45	8.2E-05
272	Throneberry [40]	Angle-head ER	Elbow	3.0	330	20	1	15	10	4.6E-01	73	VER	NA	4.4E-05
273	Throneberry [40]	ER	Elbow	3.0	330	20	1	15	10	4.6E-01	73	VER	45	7.4E-06
274	Throneberry [40]	Angle-head ER	Elbow	3.0	330	20	1	30	10	4.5E-01	73	VER	NA	7.3E-04
275	Throneberry [40]	ER	Elbow	3.0	330	20	1	30	10	4.5E-01	73	VER	45	2.9E-05
276	Throneberry [40]	Angle-head ER	Elbow	3.0	330	20	1	15	10	7.5E-01	73	VER	NA	2.0E-05
277	Throneberry [40]	ER	Elbow	3.0	330	20	1	15	10	7.5E-01	73	VER	45	3.6E-06
278	Throneberry [40]	Angle-head ER	Elbow	3.0	330	20	1	30	10	7.3E-01	73	VER	NA	7.1E-04
279	Throneberry [40]	ER	Elbow	3.0	330	20	1	30	10	7.3E-01	73	VER	45	1.7E-05

280	Throneberry [40]	ER	Elbow	3.0	330	300	1	27	1	8.0E-01	73	VER	NA	2.4E-05
281	Throneberry [40]	Angle-head ER	Elbow	3.0	330	20	1	23	10	4.5E-01	73	VER	NA	2.4E-04
282	Throneberry [40]	ER	Elbow	3.0	330	20	1	23	10	4.5E-01	73	VER	45	1.0E-05
283	Throneberry [40]	Angle-head ER	Elbow	3.0	330	20	1	23	10	7.3E-01	73	VER	NA	2.0E-04
284	Throneberry [40]	ER	Elbow	3.0	330	20	1	23	10	7.3E-01	73	VER	45	2.2E-05
285	Throneberry [40]	Angle-head ER	Elbow	3.0	330	20	1	38	10	7.4E-01	73	VER	NA	1.3E-03
286	Throneberry [40]	ER	Elbow	3.0	330	20	1	38	10	7.4E-01	73	VER	45	3.6E-05
287	Throneberry [40]	Angle-head ER	Elbow	3.0	330	20	1	46	10	7.5E-01	73	VER	NA	1.9E-03
288	Throneberry [40]	ER	Elbow	3.0	330	20	1	46	10	7.5E-01	73	VER	45	5.8E-05
289	Throneberry [40]	Angle-head ER	Elbow	3.0	330	20	1	38	10	4.6E-01	73	VER	NA	2.0E-03
290	Throneberry [40]	ER	Elbow	3.0	330	20	1	38	10	4.6E-01	73	VER	45	7.5E-05
291	Throneberry [40]	Angle-head ER	Elbow	3.0	330	20	1	46	10	4.3E-01	73	VER	NA	2.3E-03
292	Throneberry [40]	ER	Elbow	3.0	330	20	1	46	10	4.3E-01	73	VER	45	1.5E-04
293	Throneberry [40]	Angle-head ER	Elbow	3.0	330	20	1	15	40	4.6E-01	73	VER	NA	1.4E-05
294	Throneberry [40]	ER	Elbow	3.0	330	20	1	15	40	4.6E-01	73	VER	45	1.2E-05
295	Throneberry [40]	Angle-head ER	Elbow	3.0	330	20	1	30	40	4.6E-01	73	VER	NA	4.1E-04
296	Throneberry [40]	ER	Elbow	3.0	330	20	1	30	40	4.6E-01	73	VER	45	4.9E-05
297	Throneberry [40]	Angle-head ER	Elbow	3.0	330	20	1	15	40	7.8E-01	73	VER	NA	8.7E-06
298	Throneberry [40]	ER	Elbow	3.0	330	20	1	15	40	7.8E-01	73	VER	45	1.3E-05
299	Throneberry [40]	Angle-head ER	Elbow	3.0	330	300	1	27	1	8.0E-01	73	VER	NA	1.8E-03

300	Throneberry [40]	Angle-head ER	Elbow	3.0	330	20	1	30	40	7.9E-01	73	VER	NA	1.7E-04
301	Throneberry [40]	ER	Elbow	3.0	330	20	1	30	40	7.9E-01	73	VER	45	1.0E-05
302	Throneberry [40]	Angle-head ER	Elbow	3.0	330	20	1	46	40	7.2E-01	73	VER	NA	1.4E-03
303	Throneberry [40]	ER	Elbow	3.0	330	20	1	46	40	7.2E-01	73	VER	45	5.7E-05
304	Throneberry [40]	Angle-head ER	Elbow	3.0	330	20	1	46	40	4.4E-01	73	VER	NA	1.7E-03
305	Throneberry [40]	ER	Elbow	3.0	330	20	1	46	40	4.4E-01	73	VER	45	7.9E-05
306	Throneberry [40]	Angle-head ER	Elbow	3.0	330	20	1	23	40	4.8E-01	73	VER	NA	1.6E-04
307	Throneberry [40]	ER	Elbow	3.0	330	20	1	23	40	4.8E-01	73	VER	45	1.9E-05
308	Throneberry [40]	Angle-head ER	Elbow	3.0	330	20	1	38	40	4.5E-01	73	VER	NA	1.4E-03
309	Throneberry [40]	ER	Elbow	3.0	330	20	1	38	40	4.5E-01	73	VER	45	1.0E-04
310	Throneberry [40]	Angle-head ER	Elbow	3.0	330	20	1	23	40	7.3E-01	73	VER	NA	1.4E-04
311	Throneberry [40]	ER	Elbow	3.0	330	20	1	23	40	7.3E-01	73	VER	45	6.1E-06
312	Throneberry [40]	Angle-head ER	Elbow	3.0	330	20	1	38	40	7.2E-01	73	VER	NA	9.1E-04
313	Throneberry [40]	ER	Elbow	3.0	330	20	1	38	40	7.2E-01	73	VER	45	2.4E-05
314	Throneberry [40]	Angle-head ER	Elbow	3.0	330	300	1	15	10	7.7E-01	73	VER	NA	3.1E-04
315	Throneberry [40]	ER	Elbow	3.0	330	300	1	15	10	7.7E-01	73	VER	45	6.7E-05
316	Throneberry [40]	Angle-head ER	Elbow	3.0	330	300	1	30	10	7.3E-01	73	VER	NA	1.7E-03
317	Throneberry [40]	ER	Elbow	3.0	330	300	1	30	10	7.3E-01	73	VER	45	2.3E-04
318	Throneberry [40]	Angle-head ER	Elbow	3.0	330	300	1	46	10	7.8E-01	73	VER	NA	3.9E-03
319	Throneberry [40]	ER	Elbow	3.0	330	300	1	46	10	7.8E-01	73	VER	45	2.5E-04

320	Throneberry [40]	Angle-head ER	Elbow	3.0	330	300	1	16	1	8.0E-01	73	VER	NA	7.2E-04
321	Throneberry [40]	Angle-head ER	Elbow	3.0	330	300	1	15	40	7.9E-01	73	VER	NA	1.6E-04
322	Throneberry [40]	ER	Elbow	3.0	330	300	1	15	40	7.9E-01	73	VER	45	2.4E-05
323	Throneberry [40]	Angle-head ER	Elbow	3.0	330	300	1	30	40	8.0E-01	73	VER	NA	1.2E-03
324	Throneberry [40]	ER	Elbow	3.0	330	300	1	30	40	8.0E-01	73	VER	45	4.7E-05
325	Throneberry [40]	Angle-head ER	Elbow	3.0	330	300	1	46	40	7.7E-01	73	VER	NA	3.4E-03
326	Throneberry [40]	ER	Elbow	3.0	330	300	1	46	40	7.7E-01	73	VER	45	5.9E-04
327	Throneberry [40]	Angle-head ER	Elbow	3.0	330	20	1	23	1	8.0E-01	73	VER	NA	9.2E-05
328	Throneberry [40]	ER	Elbow	3.0	330	20	1	23	1	8.0E-01	73	VER	45	1.6E-05
329	Throneberry [40]	Angle-head ER	Elbow	3.0	330	20	1	38	1	6.4E-01	73	VER	NA	1.6E-03
330	Throneberry [40]	Angle-head ER	Elbow	3.0	330	300	1	27	1	8.0E-01	73	VER	NA	9.4E-04
331	Throneberry [40]	ER	Elbow	3.0	330	300	1	27	1	8.0E-01	73	VER	45	2.5E-04
332	Throneberry [40]	Angle-head ER	Elbow	3.0	330	300	1	46	1	7.3E-01	73	VER	NA	8.4E-03
333	Throneberry [40]	ER	Elbow	3.0	330	300	1	46	1	7.3E-01	73	VER	45	5.1E-04
334	Throneberry [40]	Angle-head ER	Elbow	3.0	330	20	1	28	1	8.4E-01	73	VER	NA	7.3E-04
335	Throneberry [40]	Angle-head ER	Elbow	3.0	330	20	1	15	1	4.5E-01	73	VER	NA	7.1E-05
336	Throneberry [40]	ER	Elbow	3.0	330	20	1	15	1	4.5E-01	73	VER	45	5.2E-05
337	Throneberry [40]	Angle-head ER	Elbow	3.0	330	20	1	24	1	4.9E-01	73	VER	NA	3.3E-04
338	Throneberry [40]	ER	Elbow	3.0	330	20	1	24	1	4.9E-01	73	VER	45	3.3E-05
339	Rodriguez [38]	Angle-head ER	Elbow	3.0	330	150	1	15	20	4.5E-01	73	VER	NA	1.0E-04

340	Rodriguez [38]	ER	Elbow	3.0	330	150	1	15	20	4.5E-01	73	VER	45	3.0E-05
341	Rodriguez [38]	Angle-head ER	Elbow	3.0	330	150	1	15	1	4.4E-01	73	VER	NA	1.2E-04
342	Rodriguez [38]	ER	Elbow	3.0	330	150	1	15	1	4.4E-01	73	VER	45	2.7E-05
343	Rodriguez [38]	Angle-head ER	Elbow	3.0	330	300	1	27	40	8.0E-01	73	VER	NA	1.7E-03
344	Rodriguez [38]	ER	Elbow	3.0	330	300	1	27	40	8.0E-01	73	VER	45	1.2E-04
345	Rodriguez [38]	Angle-head ER	Elbow	3.0	330	150	1	15	40	4.4E-01	73	VER	NA	3.1E-05
346	Rodriguez [38]	ER	Elbow	3.0	330	150	1	15	40	4.4E-01	73	VER	45	1.1E-05
347	Rodriguez [38]	Angle-head ER	Elbow	3.0	330	300	1	27	40	8.0E-01	73	VER	NA	1.6E-03
348	Rodriguez [38]	ER	Elbow	3.0	330	300	1	27	40	8.0E-01	73	VER	45	5.0E-05
349	Rodriguez [38]	Angle-head ER	Elbow	3.0	330	300	1	27	20	8.0E-01	73	VER	NA	3.7E-03
350	Rodriguez [38]	ER	Elbow	3.0	330	300	1	27	20	8.0E-01	73	VER	45	1.1E-04
351	Rodriguez [38]	Angle-head ER	Elbow	3.0	330	300	1	27	1	8.0E-01	73	VER	NA	2.5E-03
352	Rodriguez [38]	ER	Elbow	3.0	330	300	1	27	1	8.0E-01	73	VER	45	1.8E-04
353	Rodriguez [38]	Angle-head ER	Elbow	3.0	330	300	1	16	1	8.0E-01	73	VER	NA	2.3E-04
354	Rodriguez [38]	ER	Elbow	3.0	330	300	1	16	1	8.0E-01	73	VER	45	1.1E-04
355	Rodriguez [38]	Angle-head ER	Elbow	3.0	330	300	1	16	1	4.4E-01	73	VER	NA	1.6E-04
356	Rodriguez [38]	ER	Elbow	3.0	330	300	1	16	1	4.4E-01	73	VER	45	1.0E-05
357	Rodriguez [38]	Angle-head ER	Elbow	3.0	330	150	1	15	1	4.4E-01	73	VER	NA	8.9E-05
358	Rodriguez [38]	Angle-head ER	Elbow	3.0	330	150	1	15	1	8.0E-01	73	VER	NA	7.4E-05
359	Rodriguez [38]	Angle-head ER	Elbow	3.0	330	150	1	28	20	8.0E-01	73	VER	NA	7.0E-04

360	Rodriguez [38]	ER	Elbow	3.0	330	150	1	28	20	8.0E-01	73	VER	45	1.0E-04
361	Rodriguez [38]	Angle-head ER	Elbow	3.0	330	150	1	28	20	8.0E-01	73	VER	NA	6.2E-04
362	Rodriguez [38]	ER	Elbow	3.0	330	150	1	28	20	8.0E-01	73	VER	45	7.4E-05
363	Rodriguez [38]	Angle-head ER	Elbow	3.0	330	300	1	15	1	4.4E-01	73	VER	NA	3.8E-04
364	Rodriguez [38]	ER	Elbow	3.0	330	300	1	15	1	4.4E-01	73	VER	45	1.5E-04
365	Rodriguez [38]	Angle-head ER	Elbow	3.0	330	300	1	15	1	8.0E-01	73	VER	NA	2.0E-04
366	Rodriguez [38]	ER	Elbow	3.0	330	300	1	15	1	8.0E-01	73	VER	45	8.0E-05
367	Rodriguez [38]	Angle-head ER	Elbow	3.0	330	300	1	15	20	4.4E-01	73	VER	NA	2.0E-04
368	Rodriguez [38]	ER	Elbow	3.0	330	300	1	15	20	4.4E-01	73	VER	45	7.3E-05
369	Rodriguez [38]	Angle-head ER	Elbow	3.0	330	300	1	15	20	4.4E-01	73	VER	NA	2.3E-04
370	Rodriguez [38]	ER	Elbow	3.0	330	300	1	15	20	4.4E-01	73	VER	45	5.6E-05
371	Rodriguez [38]	Angle-head ER	Elbow	3.0	330	300	1	25	1	7.7E-01	73	VER	NA	1.7E-03
372	Rodriguez [38]	ER	Elbow	3.0	330	300	1	25	1	7.7E-01	73	VER	45	1.0E-04
373	Rodriguez [38]	Angle-head ER	Elbow	3.0	330	20	1	25	1	7.8E-01	73	VER	NA	3.7E-04
374	Rodriguez [38]	Angle-head ER	Elbow	3.0	330	20	1	15	1	4.4E-01	73	VER	NA	4.9E-05
375	Rodriguez [38]	Angle-head ER	Elbow	3.0	330	20	1	25	20	7.3E-01	73	VER	NA	1.8E-04
376	Rodriguez [38]	ER	Elbow	3.0	330	20	1	25	20	7.3E-01	73	VER	45	1.8E-05
377	Rodriguez [38]	Angle-head ER	Elbow	3.0	330	300	1	21	1	7.9E-01	73	VER	NA	6.9E-04
378	Rodriguez [38]	ER	Elbow	3.0	330	300	1	21	1	7.9E-01	73	VER	45	1.5E-04
379	Rodriguez [38]	Angle-head ER	Elbow	3.0	330	150	1	21	1	7.9E-01	73	VER	NA	2.5E-04

380	Rodriguez [38]	ER	Elbow	3.0	330	150	1	21	1	7.9E-01	73	VER	45	4.9E-05
381	Rodriguez [38]	Angle-head ER	Elbow	3.0	330	20	1	21	1	7.9E-01	73	VER	NA	9.6E-05
382	Rodriguez [38]	ER	Elbow	3.0	330	20	1	21	1	7.9E-01	73	VER	45	3.7E-05
383	Rodriguez [38]	Angle-head ER	Elbow	3.0	330	300	1	21	20	7.9E-01	73	VER	NA	1.1E-03
384	Rodriguez [38]	Angle-head ER	Elbow	3.0	330	300	1	21	40	8.4E-01	73	VER	NA	6.6E-04
385	Rodriguez [38]	Angle-head ER	Elbow	3.0	330	300	1	21	40	7.9E-01	73	VER	NA	6.6E-04
386	Rodriguez [38]	Angle-head ER	Elbow	3.0	330	300	1	21	1	8.0E-01	73	VER	NA	6.1E-04
387	Rodriguez [38]	ER	Elbow	3.0	330	300	1	21	1	8.0E-01	73	VER	45	1.3E-04
388	Rodriguez [38]	Angle-head ER	Elbow	3.0	330	300	1	15	1	4.4E-01	73	VER	NA	9.8E-05
389	Rodriguez [38]	ER	Elbow	3.0	330	300	1	15	1	4.4E-01	73	VER	45	5.0E-05
390	Rodriguez [38]	Angle-head ER	Elbow	3.0	330	300	1	15	1	8.0E-01	73	VER	NA	3.1E-04
391	Rodriguez [38]	ER	Elbow	3.0	330	300	1	15	1	8.0E-01	73	VER	45	1.3E-04
392	Rodriguez [38]	Angle-head ER	Elbow	3.0	330	150	1	27	1	8.0E-01	73	VER	NA	4.8E-04
393	Rodriguez [38]	ER	Elbow	3.0	330	150	1	27	1	8.0E-01	73	VER	45	3.2E-05
394	Rodriguez [38]	Angle-head ER	Elbow	3.0	330	150	1	15	1	8.0E-01	73	VER	NA	8.6E-05
395	Rodriguez [38]	ER	Elbow	3.0	330	150	1	15	1	8.0E-01	73	VER	45	1.8E-05
396	Rodriguez [38]	Angle-head ER	Elbow	3.0	330	150	1	27	1	7.9E-01	73	VER	NA	3.8E-04
397	Rodriguez [38]	ER	Elbow	3.0	330	150	1	27	1	7.9E-01	73	VER	45	5.3E-05
398	Mazumder [4]	WL	Elbow	1.0	222	150	1	19	1	0.0E+00	73	HOR	NA	5.7E-02
399	Mazumder [4]	WL	Elbow	1.0	222	150	1	19	1	0.0E+00	73	VER	NA	4.8E-02

400	Mazumder [4]	WL	Elbow	1.0	222	150	1	27	1	0.0E+00	73	HOR	NA	7.9E-02
401	Mazumder [4]	WL	Elbow	1.0	222	150	1	27	1	0.0E+00	73	VER	NA	1.2E-01
402	Mazumder [4]	WL	Elbow	1.0	222	150	1	34	1	0.0E+00	73	HOR	NA	1.1E-01
403	Mazumder [4]	WL	Elbow	1.0	222	150	1	34	1	0.0E+00	73	VER	NA	1.9E-01
404	Mazumder [4]	WL	Elbow	1.0	222	150	1	34	1	3.0E-02	73	HOR	NA	7.3E-03
405	Mazumder [4]	WL	Elbow	1.0	222	150	1	27	1	3.0E-02	73	HOR	NA	3.2E-03
406	Mazumder [4]	WL	Elbow	1.0	222	150	1	19	1	3.0E-02	73	HOR	NA	1.3E-03
407	Mazumder [4]	WL	Elbow	1.0	222	150	1	10	1	3.0E-02	73	HOR	NA	1.6E-03
408	Mazumder [4]	WL	Elbow	1.0	222	150	1	34	1	3.0E-01	73	HOR	NA	2.1E-03
409	Mazumder [4]	WL	Elbow	1.0	222	150	1	27	1	3.0E-01	73	HOR	NA	3.7E-03
410	Mazumder [4]	WL	Elbow	1.0	222	150	1	19	1	3.0E-01	73	HOR	NA	1.4E-03
411	Mazumder [4]	WL	Elbow	1.0	222	150	1	10	1	3.0E-01	73	HOR	NA	1.6E-04
412	Mazumder [4]	WL	Elbow	1.0	222	150	1	34	1	3.0E-02	73	VER	NA	2.4E-02
413	Mazumder [4]	WL	Elbow	1.0	222	150	1	27	1	3.0E-02	73	VER	NA	6.4E-03
414	Mazumder [4]	WL	Elbow	1.0	222	150	1	19	1	3.0E-02	73	VER	NA	3.3E-03
415	Mazumder [4]	WL	Elbow	1.0	222	150	1	10	1	3.0E-02	73	VER	NA	2.6E-03
416	Mazumder [4]	WL	Elbow	1.0	222	150	1	34	1	3.0E-01	73	VER	NA	5.8E-02
417	Mazumder [4]	WL	Elbow	1.0	222	150	1	27	1	3.0E-01	73	VER	NA	1.9E-02
418	Mazumder [4]	WL	Elbow	1.0	222	150	1	19	1	3.0E-01	73	VER	NA	3.9E-03
419	Mazumder [4]	WL	Elbow	1.0	222	150	1	10	1	3.0E-01	73	VER	NA	7.5E-04
420	Nuguri [36]	ER	Elbow	3.0	330	150	2	34	1	0.0E+00	73	VER	45	1.2E-02

421	Nuguri [36]	ER	Elbow	3.0	330	150	2	58	1	0.0E+00	73	VER	45	5.7E-02
422	Nuguri [36]	ER	Elbow	2.0	330	150	2	24	1	7.1E-03	73	VER	45	1.7E-03
423	Nuguri [36]	ER	Elbow	2.0	330	150	2	24	1	9.4E-03	73	VER	45	1.4E-03
424	Nuguri [36]	ER	Elbow	2.0	330	150	2	24	1	2.2E-02	73	VER	45	1.9E-03
425	Nuguri [36]	ER	Elbow	2.0	330	150	2	24	1	2.6E-02	73	VER	45	2.0E-03
426	Nuguri [36]	ER	Elbow	2.0	330	150	2	24	1	2.8E-02	73	VER	45	4.3E-03
427	Nuguri [36]	ER	Elbow	2.0	330	150	2	24	1	3.1E-02	73	VER	45	2.2E-03
428	Nuguri [36]	ER	Elbow	2.0	330	150	2	24	1	5.2E-02	73	VER	45	2.3E-03
429	Nuguri [36]	ER	Elbow	2.0	330	150	2	24	1	1.1E-01	73	VER	45	1.5E-03
430	Nuguri [36]	ER	Elbow	2.0	330	150	2	24	1	1.7E-01	73	VER	45	2.4E-03
431	Nuguri [36]	ER	Elbow	2.0	330	300	2	30	1	3.0E-01	73	VER	45	1.1E-02
432	Nuguri [36]	ER	Elbow	2.0	330	150	2	30	1	1.4E-04	73	VER	45	1.1E-02
433	Nuguri [36]	ER	Elbow	2.0	330	150	2	30	1	3.0E-04	73	VER	45	2.1E-02
434	Nuguri [36]	ER	Elbow	2.0	330	150	2	30	1	7.6E-04	73	VER	45	1.4E-02
435	Nuguri [36]	ER	Elbow	2.0	330	150	2	30	1	1.2E-03	73	VER	45	1.7E-02
436	Nuguri [36]	ER	Elbow	2.0	330	150	2	30	1	1.5E-03	73	VER	45	7.1E-03
437	Nuguri [36]	ER	Elbow	2.0	330	150	2	30	1	1.7E-03	73	VER	45	1.1E-02
438	Nuguri [36]	ER	Elbow	2.0	330	150	2	30	1	1.8E-03	73	VER	45	8.6E-03
439	Nuguri [36]	ER	Elbow	2.0	330	150	2	30	1	2.0E-03	73	VER	45	1.1E-02
440	Nuguri [36]	ER	Elbow	2.0	330	150	2	30	1	2.2E-03	73	VER	45	1.7E-02
441	Nuguri [36]	ER	Elbow	2.0	330	150	2	30	1	3.0E-03	73	VER	45	1.1E-02
442	Nuguri [36]	ER	Elbow	2.0	330	150	2	30	1	5.0E-03	73	VER	45	1.1E-02
443	Nuguri [36]	ER	Elbow	2.0	330	150	2	30	1	5.2E-03	73	VER	45	6.7E-03
444	Nuguri [36]	ER	Elbow	2.0	330	150	2	30	1	6.5E-03	73	VER	45	4.2E-03
445	Nuguri [36]	ER	Elbow	2.0	330	150	2	30	1	6.7E-03	73	VER	45	3.8E-03
446	Nuguri [36]	ER	Elbow	2.0	330	150	2	30	1	6.9E-03	73	VER	45	4.3E-03
447	Nuguri [36]	ER	Elbow	2.0	330	150	2	30	1	7.6E-03	73	VER	45	7.1E-03
448	Nuguri [36]	ER	Elbow	2.0	330	150	2	30	1	4.0E-03	73	VER	45	8.3E-03
449	Nuguri [36]	ER	Elbow	2.0	330	150	2	30	1	4.3E-03	73	VER	45	7.7E-03
450	Nuguri [36]	ER	Elbow	2.0	330	150	2	30	1	4.5E-03	73	VER	45	7.8E-03
451	Nuguri [36]	ER	Elbow	2.0	330	150	2	30	1	2.1E-04	73	VER	45	1.4E-02
452	Nuguri [36]	ER	Elbow	2.0	330	150	2	30	1	2.1E-04	73	VER	45	1.5E-02
453	Nuguri [36]	ER	Elbow	2.0	330	150	2	30	1	3.4E-04	73	VER	45	1.5E-02
454	Nuguri [36]	ER	Elbow	2.0	330	150	2	30	1	4.6E-04	73	VER	45	1.8E-02
455	Nuguri [36]	ER	Elbow	2.0	330	150	2	30	1	1.4E-03	73	VER	45	1.6E-02
456	Nuguri [36]	ER	Elbow	2.0	330	150	2	30	1	3.0E-03	73	VER	45	5.5E-03
457	Nuguri [36]	ER	Elbow	2.0	330	150	2	30	1	3.7E-03	73	VER	45	4.2E-03
458	Nuguri [36]	ER	Elbow	2.0	330	150	2	30	1	5.9E-03	73	VER	45	4.4E-03
459	Nuguri [36]	ER	Elbow	2.0	330	150	2	30	1	7.1E-03	73	VER	45	4.2E-03
460	Nuguri [36]	ER	Elbow	2.0	330	150	2	24	1	2.7E-04	73	VER	45	8.4E-03
461	Nuguri [36]	ER	Elbow	2.0	330	150	2	24	1	4.3E-04	73	VER	45	7.3E-03

462	Nuguri [36]	ER	Elbow	2.0	330	150	2	24	1	6.2E-04	73	VER	45	8.3E-03
463	Nuguri [36]	ER	Elbow	2.0	330	150	2	24	1	9.1E-04	73	VER	45	6.3E-03
464	Nuguri [36]	ER	Elbow	2.0	330	150	2	24	1	1.1E-03	73	VER	45	6.7E-03
465	Nuguri [36]	ER	Elbow	2.0	330	150	2	24	1	2.5E-03	73	VER	45	2.7E-03
466	Nuguri [36]	ER	Elbow	2.0	330	150	2	24	1	2.5E-03	73	VER	45	1.5E-03
467	Nuguri [36]	ER	Elbow	2.0	330	150	2	24	1	3.0E-03	73	VER	45	2.8E-03
468	Nuguri [36]	ER	Elbow	2.0	330	150	2	24	1	3.0E-03	73	VER	45	7.6E-03
469	Nuguri [36]	ER	Elbow	2.0	330	150	2	24	1	4.1E-03	73	VER	45	3.6E-03
470	Nuguri [36]	ER	Elbow	2.0	330	150	2	24	1	4.1E-03	73	VER	45	1.4E-03
471	Nuguri [36]	ER	Elbow	2.0	330	150	2	24	1	4.7E-03	73	VER	45	1.8E-03
472	Nuguri [36]	ER	Elbow	2.0	330	300	2	30	1	3.0E-05	73	VER	45	5.6E-02
473	Nuguri [36]	ER	Elbow	2.0	330	300	2	30	1	3.0E-05	73	VER	45	6.3E-02
474	Nuguri [36]	ER	Elbow	2.0	330	300	2	30	1	1.1E-04	73	VER	45	2.5E-02
475	Nuguri [36]	ER	Elbow	2.0	330	300	2	30	1	1.8E-04	73	VER	45	4.5E-02
476	Nuguri [36]	ER	Elbow	2.0	330	300	2	30	1	2.1E-04	73	VER	45	4.4E-02
477	Nuguri [36]	ER	Elbow	2.0	330	300	2	30	1	3.1E-04	73	VER	45	3.1E-02
478	Nuguri [36]	ER	Elbow	2.0	330	300	2	30	1	4.0E-04	73	VER	45	4.5E-02
479	Nuguri [36]	ER	Elbow	2.0	330	300	2	30	1	6.4E-04	73	VER	45	3.2E-02
480	Nuguri [36]	ER	Elbow	2.0	330	300	2	30	1	7.6E-04	73	VER	45	3.4E-02
481	Nuguri [36]	ER	Elbow	2.0	330	300	2	30	1	1.6E-03	73	VER	45	2.1E-02
482	Nuguri [36]	ER	Elbow	2.0	330	300	2	30	1	5.5E-03	73	VER	45	1.3E-02
483	Nuguri [36]	ER	Elbow	2.0	330	300	2	30	1	1.5E-02	73	VER	45	1.8E-02
484	Nuguri [36]	ER	Elbow	2.0	330	300	2	30	1	2.1E-02	73	VER	45	2.0E-02
485	Nuguri [36]	ER	Elbow	2.0	330	300	2	30	1	3.0E-02	73	VER	45	2.1E-02
486	Nuguri [36]	ER	Elbow	2.0	330	300	2	30	1	6.4E-02	73	VER	45	2.7E-02
487	Nuguri [36]	ER	Elbow	2.0	330	300	2	30	1	6.7E-02	73	VER	45	2.7E-02
488	Nuguri [36]	ER	Elbow	2.0	330	300	2	30	1	9.1E-02	73	VER	45	2.5E-02
489	Nuguri [36]	ER	Elbow	2.0	330	300	2	30	1	1.2E-01	73	VER	45	2.1E-02
490	Nuguri [36]	ER	Elbow	2.0	330	300	2	30	1	1.5E-01	73	VER	45	1.8E-02
491	Nuguri [36]	ER	Elbow	3.0	330	150	2	34	1	0.0E+00	73	VER	90	1.2E-03
492	Nuguri [36]	ER	Elbow	3.0	330	150	2	58	1	0.0E+00	73	VER	90	1.0E-02
493	Pyboyina [35]	WL	Elbow	1.0	123	150	3	27	1	3.0E-01	73	VER	NA	1.6E-02
494	Pyboyina [35]	WL	Elbow	1.0	123	150	3	27	1	3.0E-01	73	HOR	NA	7.6E-03
495	Pyboyina [35]	WL	Elbow	1.0	90	150	3	27	1	3.0E-01	73	VER	NA	1.2E-01
496	Pyboyina [35]	WL	Elbow	1.0	123	150	3	27	1	3.0E-02	73	VER	NA	1.2E-02
497	Pyboyina [35]	WL	Elbow	1.0	123	150	3	27	1	3.0E-02	73	HOR	NA	2.4E-03

498	Pyboyina [35]	WL	Elbow	1.0	90	150	3	27	1	3.0E-02	73	VER	NA	3.7E-02
499	Pyboyina [35]	ER	Elbow	2.0	330	150	3	27	1	1.2E-01	73	HOR	45	2.9E-03
500	Pyboyina [35]	ER	Elbow	2.0	330	150	3	23	1	6.1E-02	73	VER	45	8.9E-03
501	Pyboyina [35]	ER	Elbow	2.0	330	150	3	30	1	4.9E-02	73	HOR	45	8.6E-03
502	Pyboyina [35]	ER	Elbow	2.0	330	150	3	30	1	4.9E-02	73	VER	45	1.4E-02
503	Pyboyina [35]	ER	Elbow	2.0	330	150	3	12	1	0.0E+00	73	HOR	45	1.4E-03
504	Pyboyina [35]	ER	Elbow	2.0	330	150	3	19	1	0.0E+00	73	HOR	45	5.4E-03
505	Pyboyina [35]	ER	Elbow	2.0	330	150	3	28	1	0.0E+00	73	HOR	45	1.2E-02
506	Pyboyina [35]	ER	Elbow	2.0	330	150	3	12	1	0.0E+00	73	VER	45	2.0E-03
507	Pyboyina [35]	ER	Elbow	2.0	330	150	3	19	1	0.0E+00	73	VER	45	7.1E-03
508	Pyboyina [35]	ER	Elbow	2.0	330	150	3	28	1	0.0E+00	73	VER	45	1.6E-02
509	Pyboyina [35]	ER	Tee	1.0	330	150	3	19	1	0.0E+00	73	HOR	NA	1.5E-02
510	Pyboyina [35]	ER	Tee	1.0	330	150	3	27	1	0.0E+00	73	HOR	NA	2.2E-02
511	Pyboyina [35]	ER	Tee	1.0	330	150	3	34	1	0.0E+00	73	HOR	NA	1.7E-02
512	Pyboyina [35]	ER	Tee	1.0	330	150	3	19	1	0.0E+00	73	VER	NA	1.3E-02
513	Pyboyina [35]	ER	Tee	1.0	330	150	3	27	1	0.0E+00	73	VER	NA	1.9E-02
514	Pyboyina [35]	ER	Tee	1.0	330	150	3	34	1	0.0E+00	73	VER	NA	2.2E-02
515	Pyboyina [35]	ER	Tee	1.0	330	150	3	25	1	0.0E+00	73	VER	NA	1.6E-02
516	Pyboyina [35]	ER	Tee	1.0	330	150	3	25	1	0.0E+00	73	VER	NA	1.5E-02
517	Salama [31]	NA	Elbow	1.9	160	150	2	8	1	2.0E-01	73	VER	NA	2.2E-03
518	Salama [31]	NA	Long elbow	1.9	160	150	2	30	1	1.0E+00	73	VER	NA	9.4E-03

519	Salama [31]	NA	Long elbow	1.9	160	150	2	30	1	5.0E-01	73	VER	NA	4.4E-02
520	Salama [31]	NA	Long elbow	1.0	160	250	10	14	1	1.5E+00	73	VER	NA	4.1E-03
521	Salama [31]	NA	Long elbow	1.0	160	250	10	15	1	1.5E+00	73	VER	NA	7.5E-03
522	Salama [31]	NA	Long elbow	1.0	160	250	10	34	1	2.1E+00	73	VER	NA	5.1E-02
523	Salama [31]	NA	Long elbow	1.0	160	250	10	35	1	1.0E+00	73	VER	NA	1.2E-01
524	Salama [31]	NA	Long elbow	1.0	160	250	10	34	1	5.0E-01	73	VER	NA	1.3E-01
525	Salama [31]	NA	Long elbow	1.0	160	250	10	37	1	7.0E-01	73	VER	NA	1.4E-01
526	Salama [31]	NA	Long elbow	1.0	160	250	10	39	1	5.0E-01	73	VER	NA	1.4E-01
527	Salama [31]	NA	Long elbow	1.0	160	250	10	44	1	1.5E+00	73	VER	NA	1.9E-01
528	Salama [31]	NA	Long elbow	1.0	160	250	10	51	1	6.0E-01	73	VER	NA	2.4E-01
529	Salama [31]	NA	Long elbow	1.0	160	250	10	52	1	7.0E-01	73	VER	NA	2.4E-01
530	Salama [31]	NA	Elbow	1.9	160	150	2	20	1	5.8E+00	73	VER	NA	9.3E-04
531	Salama [31]	NA	Elbow	1.9	160	150	2	20	1	3.1E+00	73	VER	NA	1.2E-03
532	Salama [31]	NA	Long elbow	1.9	160	150	2	15	1	1.0E+00	73	VER	NA	2.6E-03
533	Salama [31]	NA	Long elbow	1.9	160	150	2	15	1	5.0E+00	73	VER	NA	1.1E-03
534	Salama [31]	NA	Long elbow	1.9	160	150	2	10	1	5.0E+00	73	VER	NA	2.4E-04
535	Salama [31]	NA	Long elbow	1.9	160	150	2	10	1	7.0E-01	73	VER	NA	1.3E-03
536	Salama [31]	NA	Long elbow	1.0	160	250	10	9	1	6.2E+00	73	VER	NA	3.2E-03
537	Tolle [30]	WL	Elbow	2.0	109	300	1	9	1	0.0E+00	73	VER	NA	3.8E-02
538	Tolle [30]	WL	Elbow	2.0	109	300	1	12	1	0.0E+00	73	VER	NA	6.8E-02
539	Tolle [30]	WL	Elbow	2.0	109	300	1	15	1	0.0E+00	73	VER	NA	1.3E-01
540	Tolle [30]	WL	Elbow	2.0	109	300	1	18	1	0.0E+00	73	VER	NA	1.6E-01
541	Tolle [30]	WL	Elbow	2.0	109	300	1	21	1	0.0E+00	73	VER	NA	2.2E-01
542	Tolle [30]	WL	Elbow	2.0	109	300	1	24	1	0.0E+00	73	VER	NA	2.9E-01
543	Tolle [30]	WL	Elbow	2.0	109	300	1	27	1	0.0E+00	73	VER	NA	3.2E-01

544	Tolle [30]	WL	Elbow	2.0	109	300	1	30	1	0.0E+00	73	VER	NA	3.6E-01
545	Kesana [41]	UT	Elbow	3.0	222	150	1	34	1	0.0E+00	73	HOR	NA	3.1E-02
546	Kesana [41]	UT	Elbow	3.0	222	150	1	33	1	0.0E+00	73	HOR	NA	2.1E-02
547	Kesana [41]	UT	Elbow	3.0	222	150	1	29	1	0.0E+00	73	HOR	NA	1.2E-02
548	Kesana [41]	UT	Elbow	3.0	222	150	1	18	1	0.0E+00	73	HOR	NA	8.5E-03
549	Vieira [42]	UT	Elbow	3.0	222	300	1	11	1	0.0E+00	73	VER	42	2.9E-03
550	Vieira [42]	UT	Elbow	3.0	222	300	1	15	1	0.0E+00	73	VER	47	7.0E-03
551	Vieira [42]	UT	Elbow	3.0	222	300	1	23	1	0.0E+00	73	VER	47	1.7E-02
552	Vieira [42]	UT	Elbow	3.0	222	300	1	27	1	0.0E+00	73	VER	47	2.5E-02
553	Vieira [42]	UT	Elbow	3.0	222	150	1	11	1	0.0E+00	73	VER	45	1.3E-03
554	Vieira [42]	UT	Elbow	3.0	222	150	1	15	1	0.0E+00	73	VER	47	2.7E-03
555	Vieira [42]	UT	Elbow	3.0	222	150	1	23	1	0.0E+00	73	VER	47	6.9E-03
556	Vieira [42]	UT	Elbow	3.0	222	150	1	27	1	0.0E+00	73	VER	45	1.3E-02
557	Vieira [42]	UT	Elbow	3.0	222	300	1	49	1	1.8E-01	73	VER	42	4.5E-02
558	Vieira [42]	UT	Elbow	3.0	222	300	1	49	1	4.1E-02	73	VER	42	4.5E-02
559	Vieira [42]	UT	Elbow	3.0	222	300	1	49	1	2.0E-02	73	VER	42	3.4E-02
560	Vieira [42]	UT	Elbow	3.0	222	300	1	49	1	2.0E-02	73	VER	42	3.5E-02
561	Vieira [42]	UT	Elbow	3.0	222	300	1	49	1	1.0E-02	73	VER	42	3.8E-02
562	Vieira [42]	UT	Elbow	3.0	222	300	1	49	1	3.0E-03	73	VER	42	4.3E-02
563	Vieira [42]	UT	Elbow	3.0	222	300	1	41	1	4.1E-02	73	VER	42	3.2E-02
564	Vieira [42]	UT	Elbow	3.0	222	300	1	41	1	2.0E-02	73	VER	42	2.6E-02
565	Vieira [42]	UT	Elbow	3.0	222	300	1	41	1	1.0E-02	73	VER	42	2.6E-02
566	Vieira [42]	UT	Elbow	3.0	222	300	1	41	1	5.0E-03	73	VER	47	3.2E-02
567	Vieira [42]	UT	Elbow	3.0	222	300	1	35	1	8.8E-02	73	VER	47	2.1E-02
568	Vieira [42]	UT	Elbow	3.0	222	300	1	36	1	9.1E-02	73	VER	47	1.4E-02
569	Vieira [42]	UT	Elbow	3.0	222	300	1	34	1	9.8E-02	73	VER	45	2.2E-02
570	Vieira [42]	UT	Elbow	3.0	222	20	1	34	1	9.8E-02	73	VER	42	4.0E-03
571	Vieira [42]	UT	Elbow	3.0	222	150	1	36	1	9.1E-02	73	VER	42	4.5E-03
572	Vieira [42]	UT	Elbow	3.0	222	300	1	27	1	9.8E-02	73	VER	45	1.6E-02
573	Vieira [42]	UT	Elbow	3.0	222	300	1	27	1	4.0E-02	73	VER	45	1.4E-02
574	Vieira [42]	UT	Elbow	3.0	222	300	1	27	1	4.0E-02	73	VER	45	1.1E-02
575	Vieira [42]	UT	Elbow	3.0	222	300	1	27	1	4.0E-02	73	VER	45	1.3E-02
576	Vieira [42]	UT	Elbow	3.0	222	300	1	27	1	1.8E-02	73	VER	42	1.1E-02
577	Vieira [42]	UT	Elbow	3.0	222	300	1	27	1	9.0E-03	73	VER	42	1.6E-02
578	Vieira [42]	UT	Elbow	3.0	222	300	1	27	1	5.0E-03	73	VER	42	2.0E-02
579	Vieira [42]	UT	Elbow	3.0	222	300	1	23	1	9.8E-02	73	VER	45	1.2E-02
580	Vieira [42]	UT	Elbow	3.0	222	20	1	23	1	4.0E-02	73	VER	45	2.3E-03
581	Vieira [42]	UT	Elbow	3.0	222	150	1	23	1	4.0E-02	73	VER	45	6.5E-03
582	Vieira [42]	UT	Elbow	3.0	222	300	1	23	1	4.0E-02	73	VER	45	1.7E-02
583	Vieira [42]	UT	Elbow	3.0	222	300	1	23	1	4.0E-02	73	VER	45	1.5E-02
584	Vieira [42]	UT	Elbow	3.0	222	300	1	23	1	4.0E-02	73	VER	45	1.5E-02

585	Vieira [42]	UT	Elbow	3.0	222	300	1	23	1	9.0E-03	73	VER	45	5.7E-03
586	Vieira [42]	UT	Elbow	3.0	222	300	1	15	1	9.8E-02	73	VER	45	4.9E-03
587	Vieira [42]	UT	Elbow	3.0	222	20	1	15	1	9.8E-02	73	VER	42	1.7E-03
588	Vieira [42]	UT	Elbow	3.0	222	150	1	15	1	9.8E-02	73	VER	42	2.4E-03
589	Vieira [42]	UT	Elbow	3.0	222	300	1	15	1	4.0E-02	73	VER	42	7.2E-03
590	Vieira [42]	UT	Elbow	3.0	222	300	1	15	1	4.0E-02	73	VER	45	9.1E-03
591	Vieira [42]	UT	Elbow	3.0	222	300	1	15	1	4.0E-02	73	VER	45	6.5E-03
592	Vieira [42]	UT	Elbow	3.0	222	300	1	15	1	1.8E-02	73	VER	42	5.4E-03
593	Vieira [42]	UT	Elbow	3.0	222	300	1	15	1	1.2E-02	73	VER	42	5.4E-03
594	Vieira [42]	UT	Elbow	3.0	222	300	1	15	1	8.0E-03	73	VER	42	4.2E-03
595	Vieira [42]	UT	Elbow	3.0	222	300	1	49	1	4.6E-01	73	VER	42	1.3E-02
596	Vieira [42]	UT	Elbow	3.0	222	300	1	27	1	4.8E-01	73	VER	42	4.0E-03
597	Vieira [42]	UT	Elbow	3.0	222	300	1	27	1	8.5E-02	73	VER	42	2.8E-02
598	Vieira [42]	UT	Elbow	3.0	222	300	1	11	1	9.8E-02	73	VER	42	1.4E-03
599	Vieira [42]	UT	Elbow	3.0	222	300	1	49	1	4.6E-01	73	HOR	42	1.3E-04
600	Vieira [42]	UT	Elbow	3.0	222	300	1	49	1	1.8E-01	73	HOR	30	3.1E-04
601	Vieira [42]	UT	Elbow	3.0	222	300	1	49	1	4.0E-02	73	HOR	42	1.6E-03
602	Vieira [42]	UT	Elbow	3.0	222	300	1	49	1	1.8E-02	73	HOR	42	1.8E-03
603	Vieira [42]	UT	Elbow	3.0	222	300	1	49	1	1.0E-02	73	HOR	42	2.2E-03
604	Vieira [42]	UT	Elbow	3.0	222	300	1	49	1	4.0E-03	73	HOR	42	2.6E-03
605	Vieira [42]	UT	Elbow	3.0	222	300	1	40	1	4.0E-02	73	HOR	42	6.0E-04
606	Vieira [42]	UT	Elbow	3.0	222	300	1	40	1	1.8E-02	73	HOR	42	1.2E-03
607	Vieira [42]	UT	Elbow	3.0	222	300	1	40	1	1.8E-02	73	HOR	42	1.1E-03
608	Vieira [42]	UT	Elbow	3.0	222	300	1	40	1	1.0E-02	73	HOR	42	1.3E-03
609	Vieira [42]	UT	Elbow	3.0	222	300	1	40	1	5.0E-03	73	HOR	45	1.5E-03
610	Vieira [42]	UT	Elbow	3.0	222	300	1	35	1	9.1E-02	73	HOR	42	1.2E-04
611	Vieira [42]	UT	Elbow	3.0	222	150	1	34	1	9.8E-02	73	HOR	42	1.0E-04
612	Vieira [42]	UT	Elbow	3.0	222	20	1	34	1	9.8E-02	73	HOR	42	8.4E-05
613	Vieira [42]	UT	Elbow	3.0	222	300	1	27	1	1.3E-01	73	HOR	42	3.9E-05
614	Vieira [42]	UT	Elbow	3.0	222	300	1	30	1	3.0E-02	73	HOR	42	3.1E-04
615	Zhang [20]	ER	DI	0.3	330	150	1	0	1	1.0E+01	73	VER	NA	1.7E-03
616	Zhang [20]	ER	DI	0.3	330	150	1	0	1	5.0E+00	73	VER	NA	3.2E-04
617	Zhang [20]	ER	DI	0.3	330	150	1	0	1	2.5E+00	73	VER	NA	2.3E-05
618	Zhang [20]	ER	DI	0.3	330	25	1	0	1	1.0E+01	73	VER	NA	6.1E-04
619	Reuterfors [34]	ER	DI	0.3	330	150	1	0	1	2.5E+00	73	VER	NA	1.0E-04
620	Reuterfors [34]	ER	DI	0.3	330	150	1	0	1	5.0E+00	73	VER	NA	2.5E-04
621	Reuterfors [34]	ER	DI	0.3	330	150	1	0	1	1.0E+01	73	VER	NA	1.7E-03

622	Reuterfors [34]	ER	DI	0.3	330	20	1	0	1	1.0E+01	73	VER	NA	6.0E-04
623	Bourgoyne [14]	ER	Elbow	0.6	200	195	1	0	1	208E+00	73	VER	NA	8.8E-04
624	Bourgoyne [14]	ER	Elbow	0.6	200	83	1	0	1	2.8E+00	73	VER	NA	1.2E-04
625	Bourgoyne [14]	UTL	Elbow	2.1	120	350	1	0	6	9.5E+00	73	VER	NA	4.0E-05
626	Bourgoyne [14]	UTL	Elbow	2.1	120	350	1	0	6	1.4E+01	73	VER	NA	8.1E-06
627	Kesana [41]	ER	Elbow	3.0	222	20	1	15	1	4.5E-01	73	VER	45	5.3E-05
628	Kesana [41]	ER	Elbow	3.0	222	20	1	24	1	4.9E-01	73	VER	45	3.3E-05
629	Kesana [41]	ER	Elbow	3.0	222	20	1	30	1	4.6E-01	73	VER	45	4.6E-05
630	Kesana [41]	ER	Elbow	3.0	222	20	1	15	1	8.0E-01	73	VER	45	7.5E-06
631	Kesana [41]	ER	Elbow	3.0	222	20	1	46	1	8.0E-01	73	VER	45	4.5E-05
632	Kesana [41]	ER	Elbow	3.0	222	20	1	46	1	5.0E-01	73	VER	45	1.0E-04
633	Kesana [41]	ER	Elbow	3.0	222	150	1	18	1	4.4E-01	73	VER	45	1.0E-05
634	Kesana [41]	ER	Elbow	3.0	222	150	1	27	1	4.4E-01	73	VER	45	3.0E-05
635	Kesana [41]	ER	Elbow	3.0	222	150	1	35	1	4.4E-01	73	VER	45	8.5E-05
636	Kesana [41]	ER	Elbow	3.0	222	150	1	44	1	4.4E-01	73	VER	45	3.9E-04
637	Kesana [41]	ER	Elbow	3.0	222	150	1	48	1	4.4E-01	73	VER	45	6.9E-04
638	Kesana [41]	ER	Elbow	3.0	222	150	1	18	1	7.3E-01	73	VER	45	2.7E-05
639	Kesana [41]	ER	Elbow	3.0	222	150	1	26	1	7.3E-01	73	VER	45	3.0E-05
640	Kesana [41]	ER	Elbow	3.0	222	150	1	34	1	7.3E-01	73	VER	45	5.1E-05
641	Kesana [41]	ER	Elbow	3.0	222	150	1	44	1	7.3E-01	73	VER	45	1.7E-04
642	Kesana [41]	ER	Elbow	3.0	222	150	1	48	1	7.3E-01	73	VER	45	3.1E-04
643	Kesana [41]	ER	Elbow	3.0	222	150	1	17	10	4.8E-01	73	VER	45	3.0E-05
644	Kesana [41]	ER	Elbow	3.0	222	150	1	26	10	4.8E-01	73	VER	45	7.4E-05
645	Kesana [41]	ER	Elbow	3.0	222	150	1	33	10	4.8E-01	73	VER	45	1.1E-04
646	Kesana [41]	ER	Elbow	3.0	222	150	1	43	10	4.8E-01	73	VER	45	2.1E-04
647	Kesana [41]	ER	Elbow	3.0	222	150	1	48	10	4.8E-01	73	VER	45	3.7E-04
648	Kesana [41]	ER	Elbow	3.0	222	150	1	18	10	7.7E-01	73	VER	45	2.7E-05
649	Kesana [41]	ER	Elbow	3.0	222	150	1	26	10	7.7E-01	73	VER	45	6.1E-05
650	Kesana [41]	ER	Elbow	3.0	222	150	1	34	10	7.7E-01	73	VER	45	1.0E-04
651	Kesana [41]	ER	Elbow	3.0	222	150	1	44	10	7.7E-01	73	VER	45	1.7E-04
652	Kesana [41]	ER	Elbow	3.0	222	150	1	48	10	7.7E-01	73	VER	45	2.7E-04
653	Kesana [41]	ER	Elbow	3.0	222	300	1	17	1	4.7E-01	73	VER	45	5.9E-05
654	Kesana [41]	ER	Elbow	3.0	222	300	1	26	1	4.7E-01	73	VER	45	7.9E-05
655	Kesana [41]	ER	Elbow	3.0	222	300	1	35	1	4.7E-01	73	VER	45	3.4E-04
656	Kesana [41]	ER	Elbow	3.0	222	300	1	43	1	4.7E-01	73	VER	45	9.2E-04
657	Kesana [41]	ER	Elbow	3.0	222	300	1	49	1	4.7E-01	73	VER	45	1.9E-03

658	Kesana [41]	ER	Elbow	3.0	222	300	1	18	1	7.3E-01	73	VER	45	4.4E-05
659	Kesana [41]	ER	Elbow	3.0	222	300	1	25	1	7.3E-01	73	VER	45	4.1E-05
660	Kesana [41]	ER	Elbow	3.0	222	300	1	33	1	7.3E-01	73	VER	45	6.0E-05
661	Kesana [41]	ER	Elbow	3.0	222	300	1	44	1	7.3E-01	73	VER	45	1.6E-04
662	Kesana [41]	ER	Elbow	3.0	222	300	1	49	1	7.3E-01	73	VER	45	3.0E-04
663	Kesana [41]	ER	Elbow	3.0	222	300	1	18	10	4.7E-01	73	VER	45	5.5E-05
664	Kesana [41]	ER	Elbow	3.0	222	300	1	26	10	4.7E-01	73	VER	45	1.2E-04
665	Kesana [41]	ER	Elbow	3.0	222	300	1	35	10	4.7E-01	73	VER	45	2.6E-04
666	Kesana [41]	ER	Elbow	3.0	222	300	1	43	10	4.7E-01	73	VER	45	5.8E-04
667	Kesana [41]	ER	Elbow	3.0	222	300	1	49	10	4.7E-01	73	VER	45	1.1E-03
668	Kesana [41]	ER	Elbow	3.0	222	300	1	18	10	7.7E-01	73	VER	45	6.7E-05
669	Kesana [41]	ER	Elbow	3.0	222	300	1	48	10	7.8E-01	73	VER	45	2.5E-04

Table A.2. Operating conditions of 585 data points after preprocessing steps

No	EXP	MA	GEO	D (inch)	h_B (vicker)	d_p (μm)	ρ_g (kg/m^3)	V_{sg} (m/s)	μ_l (cp)	V_{sl} (m/s)	σ (dyne/cm)	PO	ERR (mils/lb)
1	Antezana [32]	ER	Tee	1.0	330	150	4	29	1	2.8E-01	73	VER	9.8E-03
2	Antezana [32]	ER	Tee	1.0	330	150	4	23	1	3.0E-01	73	VER	4.1E-03
3	Antezana [32]	ER	Tee	1.0	330	150	4	15	1	2.9E-01	73	VER	5.6E-04
4	Antezana [32]	ER	Tee	1.0	330	150	4	30	1	1.3E-01	73	VER	1.0E-02
5	Antezana [32]	ER	Tee	1.0	330	150	4	23	1	1.3E-01	73	VER	2.8E-03
6	Antezana [32]	ER	Tee	1.0	330	150	4	29	1	2.8E-01	73	HOR	3.7E-03
7	Antezana [32]	ER	Tee	1.0	330	150	4	23	1	3.0E-01	73	HOR	2.0E-03
8	Antezana [32]	ER	Tee	1.0	330	150	4	23	1	1.3E-01	73	HOR	1.7E-03
9	Bikbaev [29]	WL	Long elbow	2.0	120	295	1	50	1	0.0E+00	73	VER	2.3E-01
10	Bikbaev [29]	WL	Long elbow	2.0	120	295	1	55	1	0.0E+00	73	VER	5.2E-01
11	Bikbaev [29]	WL	Long elbow	2.0	120	295	1	33	1	0.0E+00	73	VER	9.5E-02
12	Bikbaev [29]	WL	Long elbow	2.0	120	295	1	39	1	0.0E+00	73	VER	1.4E-01
13	Bikbaev [29]	WL	Long elbow	2.0	120	295	1	50	1	0.0E+00	73	VER	4.0E-01
14	Bourgoyne [14]	UTL	Long elbow	2.1	140	350	1	72	1	5.3E-01	73	VER	9.6E-01
15	Bourgoyne [14]	UTL	Long elbow	2.1	140	350	1	84	1	1.2E-01	73	VER	1.3E+00
16	Bourgoyne [14]	UTL	Long elbow	2.1	140	350	1	84	1	5.3E-01	73	VER	1.7E+00
17	Bourgoyne [14]	UTL	Long elbow	2.1	140	350	1	86	1	5.3E-01	73	VER	2.3E+00
18	Bourgoyne [14]	UTL	Long elbow	2.1	140	350	1	89	1	1.2E-01	73	VER	1.9E+00
19	Bourgoyne [14]	UTL	Long elbow	2.1	140	350	1	92	1	1.2E-01	73	VER	1.8E+00

20	Bourgoyne [14]	UTL	Long elbow	2.1	140	350	1	92	1	5.3E-01	73	VER	2.2E+00
21	Bourgoyne [14]	UTL	Long elbow	2.1	140	350	1	107	1	5.3E-01	73	VER	1.9E+00
22	Bourgoyne [14]	UTL	Tee	2.1	140	350	1	70	1	5.3E-01	73	VER	3.6E-02
23	Bourgoyne [14]	UTL	Tee	2.1	140	350	1	76	1	1.2E-01	73	VER	3.8E-02
24	Bourgoyne [14]	UTL	Tee	2.1	140	350	1	81	1	5.3E-01	73	VER	2.4E-02
25	Bourgoyne [14]	UTL	Elbow	2.1	120	350	1	32	1	0.0E+00	73	VER	1.4E-01
26	Bourgoyne [14]	UTL	Elbow	2.1	120	350	1	47	1	0.0E+00	73	VER	8.8E-02
27	Bourgoyne [14]	UTL	Elbow	2.1	120	350	1	72	1	0.0E+00	73	VER	2.5E-01
28	Bourgoyne [14]	UTL	Elbow	2.1	120	350	1	93	1	0.0E+00	73	VER	5.0E-01
29	Bourgoyne [14]	UTL	Elbow	2.1	120	350	1	98	1	0.0E+00	73	VER	6.3E-01
30	Bourgoyne [14]	UTL	Elbow	2.1	120	350	1	103	1	0.0E+00	73	VER	6.7E-01
31	Bourgoyne [14]	UTL	Elbow	2.1	120	350	1	122	1	0.0E+00	73	VER	3.8E+00
32	Bourgoyne [14]	UTL	Elbow	2.1	120	350	1	167	1	0.0E+00	73	VER	3.3E+00
33	Bourgoyne [14]	UTL	Elbow	2.1	120	350	1	169	1	0.0E+00	73	VER	3.4E+00
34	Bourgoyne [14]	UTL	Elbow	2.1	120	350	1	177	1	0.0E+00	73	VER	4.3E+00
35	Bourgoyne [14]	UTL	Elbow	2.1	120	350	1	203	1	0.0E+00	73	VER	4.7E+00
36	Bourgoyne [14]	UTL	Elbow	2.1	120	350	1	205	1	0.0E+00	73	VER	3.7E+00
37	Bourgoyne [14]	UTL	Elbow	2.1	120	350	1	222	1	0.0E+00	73	VER	4.1E+00
38	Bourgoyne [14]	UTL	Elbow	2.1	120	350	1	108	1	0.0E+00	73	VER	1.3E+00
39	Bourgoyne [14]	UTL	Elbow	2.1	120	350	1	109	1	0.0E+00	73	VER	1.1E+00

40	Bourgoyne [14]	UTL	Elbow	2.1	120	350	1	104	1	0.0E+00	73	VER	1.2E+00
41	Bourgoyne [14]	UTL	Elbow	2.1	120	350	1	107	1	0.0E+00	73	VER	8.6E-01
42	Bourgoyne [14]	UTL	Elbow	2.1	120	350	1	111	1	0.0E+00	73	VER	1.0E+00
43	Bourgoyne [14]	UTL	Elbow	2.1	120	350	1	106	1	0.0E+00	73	VER	9.2E-01
44	Dosila [37]	ER	Elbow	2.0	330	150	1	29	10	1.8E-03	73	VER	2.4E-03
45	Dosila [37]	ER	Elbow	2.0	330	150	1	29	10	1.5E-03	73	VER	1.9E-03
46	Dosila [37]	ER	Elbow	2.0	330	150	1	29	10	2.4E-03	73	VER	2.1E-03
47	Dosila [37]	ER	Elbow	2.0	330	150	1	29	10	8.2E-03	73	VER	2.4E-03
48	Dosila [37]	ER	Elbow	2.0	330	150	1	29	10	2.7E-03	73	VER	2.0E-03
49	Dosila [37]	ER	Elbow	2.0	330	150	1	29	10	4.0E-03	73	VER	1.5E-03
50	Dosila [37]	ER	Elbow	2.0	330	150	1	29	10	1.9E-03	73	VER	2.8E-03
51	Dosila [37]	ER	Elbow	2.0	330	150	1	29	10	1.7E-03	73	VER	3.2E-03
52	Dosila [37]	ER	Elbow	2.0	330	150	1	29	10	2.2E-03	73	VER	4.1E-03
53	Dosila [37]	ER	Elbow	2.0	330	150	1	29	10	2.2E-03	73	VER	1.9E-03
54	Dosila [37]	ER	Elbow	2.0	330	150	1	29	10	3.1E-03	73	VER	7.2E-04
55	Dosila [37]	ER	Elbow	2.0	330	150	1	29	10	3.1E-03	73	VER	1.9E-03
56	Dosila [37]	ER	Elbow	2.0	330	150	1	29	10	1.2E-03	73	VER	2.7E-03
57	Dosila [37]	ER	Elbow	2.0	330	150	1	29	10	2.0E-03	73	VER	3.4E-03
58	Dosila [37]	ER	Elbow	2.0	330	150	1	29	10	3.0E-03	73	VER	2.9E-03
59	Dosila [37]	ER	Elbow	2.0	330	150	1	29	10	3.7E-03	73	VER	2.3E-03
60	Dosila [37]	ER	Elbow	2.0	330	150	1	29	10	7.0E-03	73	VER	1.2E-03
61	Dosila [37]	ER	Elbow	2.0	330	150	1	29	10	3.8E-02	73	VER	1.4E-03
62	Dosila [37]	ER	Elbow	2.0	330	150	1	29	10	1.2E-02	73	VER	1.2E-03
63	Dosila [37]	ER	Elbow	2.0	330	150	1	29	10	6.1E-03	73	VER	1.3E-03
64	Dosila [37]	ER	Elbow	2.0	330	150	1	29	10	8.5E-03	73	VER	8.4E-04
65	Dosila [37]	ER	Elbow	2.0	330	150	1	29	10	7.6E-03	73	VER	1.4E-03
66	Dosila [37]	ER	Elbow	2.0	330	150	1	29	10	4.6E-03	73	VER	1.9E-03

67	Dosila [37]	ER	Elbow	2.0	330	150	1	29	10	1.2E-02	73	VER	2.2E-03
68	Dosila [37]	ER	Elbow	2.0	330	150	1	29	10	3.0E-04	73	VER	4.7E-03
69	Dosila [37]	ER	Elbow	2.0	330	150	1	29	10	2.4E-04	73	VER	4.8E-03
70	Dosila [37]	ER	Elbow	2.0	330	150	1	29	10	9.1E-04	73	VER	6.2E-03
71	Dosila [37]	ER	Elbow	2.0	330	150	1	29	10	6.1E-04	73	VER	9.4E-03
72	Dosila [37]	ER	Elbow	2.0	330	150	1	29	10	7.6E-04	73	VER	8.6E-03
73	Dosila [37]	ER	Elbow	2.0	330	300	1	29	10	1.8E-02	73	VER	1.1E-02
74	Dosila [37]	ER	Elbow	2.0	330	300	1	29	10	3.2E-02	73	VER	7.3E-03
75	Dosila [37]	ER	Elbow	2.0	330	300	1	29	10	1.0E-03	73	VER	2.0E-02
76	Dosila [37]	ER	Elbow	2.0	330	300	1	29	10	1.6E-03	73	VER	4.7E-03
77	Dosila [37]	ER	Elbow	2.0	330	300	1	29	10	9.8E-04	73	VER	3.8E-02
78	Dosila [37]	ER	Elbow	2.0	330	300	1	29	10	3.4E-03	73	VER	1.7E-02
79	Dosila [37]	ER	Elbow	2.0	330	300	1	29	10	1.6E-03	73	VER	2.8E-02
80	Dosila [37]	ER	Elbow	2.0	330	300	1	29	10	1.8E-03	73	VER	2.3E-02
81	Dosila [37]	ER	Elbow	2.0	330	300	1	29	10	4.3E-03	73	VER	1.5E-02
82	Dosila [37]	ER	Elbow	2.0	330	300	1	29	10	2.0E-03	73	VER	2.2E-02
83	Dosila [37]	ER	Elbow	2.0	330	300	1	29	10	2.3E-03	73	VER	1.6E-02
84	Dosila [37]	ER	Elbow	2.0	330	300	1	29	10	4.1E-03	73	VER	9.1E-03
85	Dosila [37]	ER	Elbow	2.0	330	300	1	29	10	7.6E-03	73	VER	9.6E-03
86	Dosila [37]	ER	Elbow	2.0	330	300	1	29	10	4.9E-03	73	VER	7.5E-03
87	Dosila [37]	ER	Elbow	2.0	330	300	1	29	10	9.1E-03	73	VER	4.6E-03
88	Dosila [37]	ER	Elbow	2.0	330	300	1	29	10	5.4E-03	73	VER	7.8E-03
89	Dosila [37]	ER	Elbow	2.0	330	150	1	29	1	6.1E-03	73	VER	3.9E-03
90	Dosila [37]	ER	Elbow	2.0	330	150	1	29	1	9.4E-03	73	VER	3.4E-03
91	Dosila [37]	ER	Elbow	2.0	330	150	1	29	1	1.0E-02	73	VER	3.7E-03
92	Dosila [37]	ER	Elbow	2.0	330	150	1	29	1	1.4E-02	73	VER	3.9E-03
93	Dosila [37]	ER	Elbow	2.0	330	150	1	29	1	2.1E-02	73	VER	6.0E-03
94	Dosila [37]	ER	Elbow	2.0	330	150	1	29	1	2.2E-02	73	VER	5.8E-03

95	Dosila [37]	ER	Elbow	2.0	330	150	1	29	1	2.7E-02	73	VER	5.4E-03
96	Dosila [37]	ER	Elbow	2.0	330	150	1	29	1	3.0E-02	73	VER	5.0E-03
97	Dosila [37]	ER	Elbow	2.0	330	150	1	29	1	3.9E-02	73	VER	5.1E-03
98	Dosila [37]	ER	Elbow	2.0	330	150	1	29	1	4.8E-02	73	VER	5.8E-03
99	Dosila [37]	ER	Elbow	2.0	330	150	1	29	1	1.5E-01	73	VER	2.6E-03
100	Dosila [37]	ER	Elbow	2.0	330	150	1	29	1	3.0E-05	73	VER	1.8E-02
101	Dosila [37]	ER	Elbow	2.0	330	150	1	29	1	1.2E-03	73	VER	8.6E-03
102	Dosila [37]	ER	Elbow	2.0	330	150	1	29	1	1.7E-03	73	VER	7.3E-03
103	Dosila [37]	ER	Elbow	2.0	330	150	1	29	1	1.8E-03	73	VER	7.3E-03
104	Dosila [37]	ER	Elbow	2.0	330	150	1	29	1	1.9E-03	73	VER	8.0E-03
105	Dosila [37]	ER	Elbow	2.0	330	150	1	29	1	2.1E-03	73	VER	5.2E-03
106	Dosila [37]	ER	Elbow	2.0	330	150	1	29	1	2.2E-03	73	VER	1.2E-02
107	Dosila [37]	ER	Elbow	2.0	330	150	1	29	1	3.0E-03	73	VER	3.9E-03
108	Dosila [37]	ER	Elbow	2.0	330	150	1	29	1	3.2E-03	73	VER	4.5E-03
109	Dosila [37]	ER	Elbow	2.0	330	300	1	29	1	1.3E-01	73	VER	2.0E-02
110	Dosila [37]	ER	Elbow	2.0	330	300	1	29	1	3.0E-05	73	VER	6.6E-02
111	Dosila [37]	ER	Elbow	2.0	330	300	1	29	1	7.0E-04	73	VER	4.7E-02
112	Dosila [37]	ER	Elbow	2.0	330	300	1	29	1	8.7E-04	73	VER	3.2E-02
113	Dosila [37]	ER	Elbow	2.0	330	300	1	29	1	1.2E-03	73	VER	3.4E-02
114	Dosila [37]	ER	Elbow	2.0	330	300	1	29	1	1.5E-03	73	VER	3.1E-02
115	Dosila [37]	ER	Elbow	2.0	330	300	1	29	1	2.1E-03	73	VER	3.6E-02
116	Dosila [37]	ER	Elbow	2.0	330	300	1	29	1	2.1E-03	73	VER	3.1E-02
117	Dosila [37]	ER	Elbow	2.0	330	300	1	29	1	2.4E-03	73	VER	1.8E-02
118	Dosila [37]	ER	Elbow	2.0	330	300	1	29	1	3.0E-03	73	VER	3.3E-02
119	Dosila [37]	ER	Elbow	2.0	330	300	1	29	1	4.3E-03	73	VER	3.3E-02
120	Dosila [37]	ER	Elbow	2.0	330	300	1	29	1	4.8E-03	73	VER	3.1E-02
121	Dosila [37]	ER	Elbow	2.0	330	300	1	29	1	5.2E-03	73	VER	2.9E-02
122	Dosila [37]	ER	Elbow	2.0	330	300	1	29	1	5.5E-03	73	VER	2.6E-02

123	Dosila [37]	ER	Elbow	2.0	330	300	1	29	1	5.8E-03	73	VER	2.6E-02
124	Dosila [37]	ER	Elbow	2.0	330	300	1	29	1	6.0E-03	73	VER	2.4E-02
125	Dosila [37]	ER	Elbow	2.0	330	300	1	29	1	7.6E-03	73	VER	1.9E-02
126	Dosila [37]	ER	Elbow	2.0	330	300	1	29	1	9.1E-03	73	VER	2.4E-02
127	Dosila [37]	ER	Elbow	2.0	330	300	1	29	1	1.2E-02	73	VER	2.1E-02
128	Dosila [37]	ER	Elbow	2.0	330	300	1	29	1	1.5E-02	73	VER	2.6E-02
129	Dosila [37]	ER	Elbow	2.0	330	300	1	29	1	1.8E-02	73	VER	1.9E-02
130	Dosila [37]	ER	Elbow	2.0	330	300	1	29	1	3.0E-02	73	VER	3.4E-02
131	Dosila [37]	ER	Elbow	2.0	330	300	1	29	1	3.0E-02	73	VER	3.3E-02
132	Dosila [37]	ER	Elbow	2.0	330	300	1	29	1	4.0E-02	73	VER	3.3E-02
133	Dosila [37]	ER	Elbow	2.0	330	300	1	29	1	4.9E-02	73	VER	3.0E-02
134	Dosila [37]	ER	Elbow	2.0	330	300	1	29	1	5.3E-02	73	VER	3.2E-02
135	Evans [33]	ER	Long elbow	4.0	142	150	46	23	1	0.0E+00	73	VER	4.9E-04
136	Evans [33]	ER	Long elbow	4.0	142	150	46	35	1	0.0E+00	73	VER	1.7E-03
137	Evans [33]	ER	Long elbow	4.0	142	150	46	63	1	0.0E+00	73	VER	7.1E-03
138	Evans [33]	ER	Long elbow	4.0	222	150	46	23	1	0.0E+00	73	VER	2.4E-04
139	Evans [33]	ER	Long elbow	4.0	222	150	46	35	1	0.0E+00	73	VER	1.0E-03
140	Evans [33]	ER	Long elbow	4.0	222	150	46	63	1	0.0E+00	73	VER	2.6E-03
141	Evans [33]	ER	Long elbow	4.0	289	150	46	35	1	0.0E+00	73	VER	3.6E-04
142	Fan [39]	ER	Elbow	4.0	330	150	1	23	1	1.3E-02	73	HOR	4.2E-04
143	Fan [39]	ER	Elbow	4.0	330	150	1	23	1	1.6E-02	73	HOR	5.2E-04
144	Fan [39]	ER	Elbow	4.0	330	150	1	23	1	2.6E-02	73	HOR	4.0E-04
145	Fan [39]	ER	Elbow	4.0	330	150	1	23	1	3.2E-02	73	HOR	4.9E-04
146	Fan [39]	ER	Elbow	4.0	330	150	1	23	1	4.3E-02	73	HOR	3.0E-04
147	Fan [39]	ER	Elbow	4.0	330	150	1	23	1	4.8E-02	73	HOR	3.5E-04
148	Fan [39]	ER	Elbow	4.0	330	150	1	23	1	5.8E-02	73	HOR	9.1E-05

149	Fan [39]	ER	Elbow	4.0	330	150	1	23	1	6.9E-02	73	HOR	5.0E-04
150	Fan [39]	ER	Elbow	4.0	330	150	1	23	1	7.3E-02	73	HOR	1.0E-04
151	Fan [39]	ER	Elbow	4.0	330	150	1	23	1	1.4E-02	73	HOR	5.7E-04
152	Fan [39]	ER	Elbow	4.0	330	150	1	23	1	2.4E-02	73	HOR	1.6E-04
153	Fan [39]	ER	Elbow	4.0	330	150	1	23	1	1.0E-02	73	HOR	6.3E-04
154	Fan [39]	ER	Elbow	4.0	330	150	1	23	1	1.8E-02	73	HOR	4.2E-04
155	Fan [39]	ER	Elbow	4.0	330	150	1	23	1	2.8E-02	73	HOR	1.6E-04
156	Fan [39]	ER	Elbow	4.0	330	150	1	23	1	3.7E-02	73	HOR	4.2E-04
157	Fan [39]	ER	Elbow	4.0	330	150	1	23	1	5.0E-02	73	HOR	2.2E-04
158	Fan [39]	ER	Elbow	4.0	330	150	1	23	1	5.6E-02	73	HOR	1.4E-04
159	Fan [39]	ER	Elbow	4.0	330	150	1	23	1	7.9E-02	73	HOR	1.8E-04
160	Fan [39]	ER	Elbow	4.0	330	300	1	23	1	5.7E-02	73	HOR	3.9E-04
161	Fan [39]	ER	Elbow	4.0	330	300	1	23	1	6.8E-02	73	HOR	1.9E-04
162	Fan [39]	ER	Elbow	4.0	330	300	1	23	1	5.3E-02	73	HOR	3.5E-04
163	Fan [39]	ER	Elbow	4.0	330	300	1	23	1	4.2E-02	73	HOR	5.3E-04
164	Fan [39]	ER	Elbow	4.0	330	300	1	23	1	7.4E-02	73	HOR	1.2E-04
165	Fan [39]	ER	Elbow	4.0	330	300	1	23	1	6.0E-02	73	HOR	1.5E-04
166	Fan [39]	ER	Elbow	4.0	330	300	1	23	1	5.2E-02	73	HOR	4.4E-04
167	Fan [39]	ER	Elbow	4.0	330	300	1	23	1	9.4E-03	73	HOR	8.1E-04
168	Fan [39]	ER	Elbow	4.0	330	300	1	23	1	6.7E-03	73	HOR	1.4E-03
169	Fan [39]	ER	Elbow	4.0	330	300	1	23	1	4.3E-03	73	HOR	1.7E-03
170	Fan [39]	ER	Elbow	4.0	330	300	1	23	1	9.1E-03	73	HOR	4.7E-04
171	Fan [39]	ER	Elbow	4.0	330	300	1	23	1	6.1E-03	73	HOR	6.1E-04
172	Fan [39]	ER	Elbow	4.0	330	300	1	23	1	4.0E-03	73	HOR	2.5E-03
173	Fan [39]	ER	Elbow	4.0	330	150	1	15	1	3.4E-03	73	HOR	3.2E-04
174	Fan [39]	ER	Elbow	4.0	330	150	1	15	1	4.9E-03	73	HOR	3.7E-04
175	Fan [39]	ER	Elbow	4.0	330	150	1	15	1	4.6E-03	73	HOR	2.2E-04
176	Fan [39]	ER	Elbow	4.0	330	150	1	15	1	2.4E-03	73	HOR	1.4E-04

177	Fan [39]	ER	Elbow	4.0	330	150	1	15	1	4.3E-03	73	HOR	4.9E-05
178	Fan [39]	ER	Elbow	4.0	330	150	1	15	1	6.1E-03	73	HOR	2.9E-04
179	Fan [39]	ER	Elbow	4.0	330	150	1	15	1	8.8E-03	73	HOR	1.3E-04
180	Fan [39]	ER	Elbow	4.0	330	150	1	15	1	1.1E-02	73	HOR	5.7E-04
181	Fan [39]	ER	Elbow	4.0	330	150	1	15	1	1.2E-02	73	HOR	4.4E-05
182	Fan [39]	ER	Elbow	4.0	330	150	1	15	1	1.5E-02	73	HOR	4.0E-04
183	Fan [39]	ER	Elbow	4.0	330	150	1	15	1	1.9E-02	73	HOR	5.1E-05
184	Fan [39]	ER	Elbow	4.0	330	150	1	15	1	4.0E-03	73	HOR	2.2E-04
185	Fan [39]	ER	Elbow	4.0	330	150	1	15	1	5.8E-03	73	HOR	9.5E-05
186	Fan [39]	ER	Elbow	4.0	330	150	1	15	1	8.5E-03	73	HOR	1.2E-04
187	Fan [39]	ER	Elbow	4.0	330	150	1	15	1	1.2E-02	73	HOR	6.1E-05
188	Fan [39]	ER	Elbow	4.0	330	150	1	15	1	1.5E-02	73	HOR	1.2E-04
189	Fan [39]	ER	Elbow	4.0	330	150	1	15	1	1.4E-02	73	HOR	1.0E-04
190	Fan [39]	ER	Elbow	4.0	330	150	1	15	1	1.8E-02	73	HOR	1.5E-04
191	Fan [39]	ER	Elbow	4.0	330	150	1	15	1	1.8E-02	73	HOR	1.3E-04
192	Fan [39]	ER	Elbow	4.0	330	300	1	15	1	2.0E-02	73	HOR	1.2E-04
193	Fan [39]	ER	Elbow	4.0	330	300	1	15	1	2.0E-02	73	HOR	3.1E-04
194	Fan [39]	ER	Elbow	4.0	330	300	1	15	1	1.6E-02	73	HOR	6.3E-05
195	Fan [39]	ER	Elbow	4.0	330	300	1	15	1	1.4E-02	73	HOR	5.1E-04
196	Fan [39]	ER	Elbow	4.0	330	300	1	15	1	1.2E-02	73	HOR	5.4E-05
197	Fan [39]	ER	Elbow	4.0	330	300	1	15	1	9.8E-03	73	HOR	1.7E-04
198	Fan [39]	ER	Elbow	4.0	330	300	1	15	1	8.8E-03	73	HOR	3.8E-05
199	Fan [39]	ER	Elbow	4.0	330	300	1	15	1	4.6E-03	73	HOR	1.3E-04
200	Fan [39]	ER	Elbow	4.0	330	300	1	15	1	3.4E-03	73	HOR	5.4E-05
201	Fan [39]	ER	Elbow	4.0	330	300	1	15	1	2.3E-02	73	HOR	4.4E-05
202	Fan [39]	ER	Elbow	4.0	330	300	1	15	1	1.9E-02	73	HOR	3.4E-04
203	Fan [39]	ER	Elbow	4.0	330	300	1	15	1	1.6E-02	73	HOR	8.3E-05
204	Fan [39]	ER	Elbow	4.0	330	300	1	15	1	1.4E-02	73	HOR	7.4E-05

205	Fan [39]	ER	Elbow	4.0	330	300	1	15	1	8.5E-03	73	HOR	1.6E-04
206	Fan [39]	ER	Elbow	4.0	330	300	1	15	1	6.1E-03	73	HOR	2.7E-04
207	Fan [39]	ER	Elbow	4.0	330	300	1	15	1	4.0E-03	73	HOR	5.2E-04
208	Fan [39]	ER	Elbow	4.0	330	150	1	23	1	2.2E-02	73	VER	6.0E-04
209	Fan [39]	ER	Elbow	4.0	330	150	1	23	1	2.0E-02	73	VER	7.8E-04
210	Fan [39]	ER	Elbow	4.0	330	150	1	23	1	1.7E-02	73	VER	9.1E-04
211	Fan [39]	ER	Elbow	4.0	330	150	1	23	1	1.3E-02	73	VER	9.8E-04
212	Fan [39]	ER	Elbow	4.0	330	150	1	23	1	1.2E-02	73	VER	1.2E-03
213	Fan [39]	ER	Elbow	4.0	330	150	1	23	1	9.1E-03	73	VER	1.4E-03
214	Fan [39]	ER	Elbow	4.0	330	150	1	23	1	7.9E-03	73	VER	1.5E-03
215	Fan [39]	ER	Elbow	4.0	330	150	1	23	1	5.5E-03	73	VER	1.8E-03
216	Fan [39]	ER	Elbow	4.0	330	150	1	23	1	3.7E-03	73	VER	1.4E-03
217	Fan [39]	ER	Elbow	4.0	330	300	1	23	1	2.2E-02	73	VER	1.5E-03
218	Fan [39]	ER	Elbow	4.0	330	300	1	23	1	1.6E-02	73	VER	2.7E-03
219	Fan [39]	ER	Elbow	4.0	330	300	1	23	1	1.0E-02	73	VER	5.7E-03
220	Fan [39]	ER	Elbow	4.0	330	150	1	15	1	2.0E-02	73	VER	9.7E-04
221	Fan [39]	ER	Elbow	4.0	330	150	1	15	1	1.6E-02	73	VER	5.5E-04
222	Fan [39]	ER	Elbow	4.0	330	150	1	15	1	1.4E-02	73	VER	5.1E-04
223	Fan [39]	ER	Elbow	4.0	330	150	1	15	1	1.2E-02	73	VER	6.8E-04
224	Fan [39]	ER	Elbow	4.0	330	150	1	15	1	7.9E-03	73	VER	4.7E-04
225	Fan [39]	ER	Elbow	4.0	330	150	1	15	1	5.5E-03	73	VER	9.8E-04
226	Fan [39]	ER	Elbow	4.0	330	300	1	15	1	1.6E-02	73	VER	5.1E-04
227	Fan [39]	ER	Elbow	4.0	330	300	1	15	1	2.2E-02	73	VER	3.9E-04
228	Rodriguez [38]	Angle-head ER	Tee	3.0	330	20	1	30	1	4.6E-01	73	HOR	1.2E-03
229	Rodriguez [38]	Angle-head ER	Tee	3.0	330	20	1	15	1	8.0E-01	73	HOR	3.7E-05
230	Rodriguez [38]	ER	Elbow	3.0	330	20	1	15	1	8.0E-01	73	HOR	7.5E-06
231	Rodriguez [38]	Angle-head ER	Tee	3.0	330	20	1	46	1	8.0E-01	73	HOR	2.2E-03

232	Rodriguez [38]	Angle-head ER	Tee	3.0	330	20	1	46	1	4.9E-01	73	HOR	2.3E-03
233	Rodriguez [38]	ER	Elbow	3.0	330	20	1	46	1	4.9E-01	73	HOR	1.0E-04
234	Rodriguez [38]	Angle-head ER	Tee	3.0	330	20	1	38	1	5.0E-01	73	HOR	1.5E-03
235	Rodriguez [38]	ER	Elbow	3.0	330	20	1	38	1	5.0E-01	73	HOR	8.2E-05
236	Rodriguez [38]	Angle-head ER	Tee	3.0	330	20	1	15	10	4.6E-01	73	HOR	4.4E-05
237	Rodriguez [38]	ER	Elbow	3.0	330	20	1	15	10	4.6E-01	73	HOR	7.4E-06
238	Rodriguez [38]	Angle-head ER	Tee	3.0	330	20	1	30	10	4.5E-01	73	HOR	7.3E-04
239	Rodriguez [38]	ER	Elbow	3.0	330	20	1	30	10	4.5E-01	73	HOR	2.9E-05
240	Rodriguez [38]	Angle-head ER	Tee	3.0	330	20	1	15	10	7.5E-01	73	HOR	2.0E-05
241	Rodriguez [38]	ER	Elbow	3.0	330	20	1	15	10	7.5E-01	73	HOR	3.6E-06
242	Rodriguez [38]	Angle-head ER	Tee	3.0	330	20	1	30	10	7.3E-01	73	HOR	7.1E-04
243	Rodriguez [38]	ER	Elbow	3.0	330	20	1	30	10	7.3E-01	73	HOR	1.7E-05
244	Rodriguez [38]	ER	Elbow	3.0	330	300	1	27	1	8.0E-01	73	HOR	2.4E-05
245	Rodriguez [38]	Angle-head ER	Tee	3.0	330	20	1	23	10	4.5E-01	73	HOR	2.4E-04
246	Rodriguez [38]	ER	Elbow	3.0	330	20	1	23	10	4.5E-01	73	HOR	1.0E-05
247	Rodriguez [38]	Angle-head ER	Tee	3.0	330	20	1	23	10	7.3E-01	73	HOR	2.0E-04
248	Rodriguez [38]	ER	Elbow	3.0	330	20	1	23	10	7.3E-01	73	HOR	2.2E-05
249	Rodriguez [38]	Angle-head ER	Tee	3.0	330	20	1	38	10	7.4E-01	73	HOR	1.3E-03
250	Rodriguez [38]	ER	Elbow	3.0	330	20	1	38	10	7.4E-01	73	HOR	3.6E-05
251	Rodriguez [38]	Angle-head ER	Tee	3.0	330	20	1	46	10	7.5E-01	73	HOR	1.9E-03
252	Rodriguez [38]	ER	Elbow	3.0	330	20	1	46	10	7.5E-01	73	HOR	5.8E-05
253	Rodriguez [38]	Angle-head ER	Tee	3.0	330	20	1	38	10	4.6E-01	73	HOR	2.0E-03
254	Rodriguez [38]	ER	Elbow	3.0	330	20	1	38	10	4.6E-01	73	HOR	7.5E-05
255	Rodriguez [38]	Angle-head ER	Tee	3.0	330	20	1	46	10	4.3E-01	73	HOR	2.3E-03

256	Rodriguez [38]	ER	Elbow	3.0	330	20	1	46	10	4.3E-01	73	HOR	1.5E-04
257	Rodriguez [38]	Angle-head ER	Tee	3.0	330	20	1	15	40	4.6E-01	73	HOR	1.4E-05
258	Rodriguez [38]	ER	Elbow	3.0	330	20	1	15	40	4.6E-01	73	HOR	1.2E-05
259	Rodriguez [38]	Angle-head ER	Tee	3.0	330	20	1	30	40	4.6E-01	73	HOR	4.1E-04
260	Rodriguez [38]	ER	Elbow	3.0	330	20	1	30	40	4.6E-01	73	HOR	4.9E-05
261	Rodriguez [38]	Angle-head ER	Tee	3.0	330	20	1	15	40	7.8E-01	73	HOR	8.7E-06
262	Rodriguez [38]	ER	Elbow	3.0	330	20	1	15	40	7.8E-01	73	HOR	1.3E-05
263	Rodriguez [38]	Angle-head ER	Tee	3.0	330	300	1	27	1	8.0E-01	73	HOR	1.8E-03
264	Rodriguez [38]	Angle-head ER	Tee	3.0	330	20	1	30	40	7.9E-01	73	HOR	1.7E-04
265	Rodriguez [38]	ER	Elbow	3.0	330	20	1	30	40	7.9E-01	73	HOR	1.0E-05
266	Rodriguez [38]	Angle-head ER	Tee	3.0	330	20	1	46	40	7.2E-01	73	HOR	1.4E-03
267	Rodriguez [38]	ER	Elbow	3.0	330	20	1	46	40	7.2E-01	73	HOR	5.7E-05
268	Rodriguez [38]	Angle-head ER	Tee	3.0	330	20	1	46	40	4.4E-01	73	HOR	1.7E-03
269	Rodriguez [38]	ER	Elbow	3.0	330	20	1	46	40	4.4E-01	73	HOR	7.9E-05
270	Rodriguez [38]	Angle-head ER	Tee	3.0	330	20	1	23	40	4.8E-01	73	HOR	1.6E-04
271	Rodriguez [38]	ER	Elbow	3.0	330	20	1	23	40	4.8E-01	73	HOR	1.9E-05
272	Rodriguez [38]	Angle-head ER	Tee	3.0	330	20	1	38	40	4.5E-01	73	HOR	1.4E-03
273	Rodriguez [38]	ER	Elbow	3.0	330	20	1	38	40	4.5E-01	73	HOR	1.0E-04
274	Rodriguez [38]	Angle-head ER	Tee	3.0	330	20	1	23	40	7.3E-01	73	HOR	1.4E-04
275	Rodriguez [38]	ER	Elbow	3.0	330	20	1	23	40	7.3E-01	73	HOR	6.1E-06
276	Rodriguez [38]	Angle-head ER	Tee	3.0	330	20	1	38	40	7.2E-01	73	HOR	9.1E-04
277	Rodriguez [38]	ER	Elbow	3.0	330	20	1	38	40	7.2E-01	73	HOR	2.4E-05
278	Rodriguez [38]	Angle-head ER	Tee	3.0	330	300	1	15	10	7.7E-01	73	HOR	3.1E-04
279	Rodriguez [38]	ER	Elbow	3.0	330	300	1	15	10	7.7E-01	73	HOR	6.7E-05

280	Rodriguez [38]	Angle-head ER	Tee	3.0	330	300	1	30	10	7.3E-01	73	HOR	1.7E-03
281	Rodriguez [38]	ER	Elbow	3.0	330	300	1	30	10	7.3E-01	73	HOR	2.3E-04
282	Rodriguez [38]	Angle-head ER	Tee	3.0	330	300	1	46	10	7.8E-01	73	HOR	3.9E-03
283	Rodriguez [38]	ER	Elbow	3.0	330	300	1	46	10	7.8E-01	73	HOR	2.5E-04
284	Rodriguez [38]	Angle-head ER	Tee	3.0	330	300	1	16	1	8.0E-01	73	HOR	7.2E-04
285	Rodriguez [38]	Angle-head ER	Tee	3.0	330	300	1	15	40	7.9E-01	73	HOR	1.6E-04
286	Rodriguez [38]	ER	Elbow	3.0	330	300	1	15	40	7.9E-01	73	HOR	2.4E-05
287	Rodriguez [38]	Angle-head ER	Tee	3.0	330	300	1	30	40	8.0E-01	73	HOR	1.2E-03
288	Rodriguez [38]	ER	Elbow	3.0	330	300	1	30	40	8.0E-01	73	HOR	4.7E-05
289	Rodriguez [38]	Angle-head ER	Tee	3.0	330	300	1	46	40	7.7E-01	73	HOR	3.4E-03
290	Rodriguez [38]	ER	Elbow	3.0	330	300	1	46	40	7.7E-01	73	HOR	5.9E-04
291	Rodriguez [38]	Angle-head ER	Tee	3.0	330	20	1	23	1	8.0E-01	73	HOR	9.2E-05
292	Rodriguez [38]	ER	Elbow	3.0	330	20	1	23	1	8.0E-01	73	HOR	1.6E-05
293	Rodriguez [38]	Angle-head ER	Tee	3.0	330	20	1	38	1	6.4E-01	73	HOR	1.6E-03
294	Rodriguez [38]	Angle-head ER	Tee	3.0	330	300	1	27	1	8.0E-01	73	HOR	9.4E-04
295	Rodriguez [38]	ER	Elbow	3.0	330	300	1	27	1	8.0E-01	73	HOR	2.5E-04
296	Rodriguez [38]	Angle-head ER	Tee	3.0	330	300	1	46	1	7.3E-01	73	HOR	8.4E-03
297	Rodriguez [38]	ER	Elbow	3.0	330	300	1	46	1	7.3E-01	73	HOR	5.1E-04
298	Rodriguez [38]	Angle-head ER	Tee	3.0	330	20	1	28	1	8.4E-01	73	HOR	7.3E-04
299	Rodriguez [38]	Angle-head ER	Tee	3.0	330	20	1	15	1	4.5E-01	73	HOR	7.1E-05
300	Rodriguez [38]	ER	Elbow	3.0	330	20	1	15	1	4.5E-01	73	HOR	5.2E-05
301	Rodriguez [38]	Angle-head ER	Tee	3.0	330	20	1	24	1	4.9E-01	73	HOR	3.3E-04
302	Rodriguez [38]	ER	Elbow	3.0	330	20	1	24	1	4.9E-01	73	HOR	3.3E-05

303	Throneberry [40]	Angle-head ER	Tee	3.0	330	150	1	15	20	4.5E-01	73	HOR	1.0E-04
304	Throneberry [40]	ER	Elbow	3.0	330	150	1	15	20	4.5E-01	73	HOR	3.0E-05
305	Throneberry [40]	Angle-head ER	Tee	3.0	330	150	1	15	1	4.4E-01	73	HOR	1.2E-04
306	Throneberry [40]	ER	Elbow	3.0	330	150	1	15	1	4.4E-01	73	HOR	2.7E-05
307	Throneberry [40]	Angle-head ER	Tee	3.0	330	300	1	27	40	8.0E-01	73	HOR	1.7E-03
308	Throneberry [40]	ER	Elbow	3.0	330	300	1	27	40	8.0E-01	73	HOR	1.2E-04
309	Throneberry [40]	Angle-head ER	Tee	3.0	330	150	1	15	40	4.4E-01	73	HOR	3.1E-05
310	Throneberry [40]	ER	Elbow	3.0	330	150	1	15	40	4.4E-01	73	HOR	1.1E-05
311	Throneberry [40]	Angle-head ER	Tee	3.0	330	300	1	27	20	8.0E-01	73	HOR	3.7E-03
312	Throneberry [40]	ER	Elbow	3.0	330	300	1	27	20	8.0E-01	73	HOR	1.1E-04
313	Throneberry [40]	ER	Elbow	3.0	330	300	1	16	1	8.0E-01	73	HOR	1.1E-04
314	Throneberry [40]	Angle-head ER	Tee	3.0	330	300	1	16	1	4.4E-01	73	HOR	1.6E-04
315	Throneberry [40]	ER	Elbow	3.0	330	300	1	16	1	4.4E-01	73	HOR	1.0E-05
316	Throneberry [40]	Angle-head ER	Tee	3.0	330	150	1	15	1	4.4E-01	73	HOR	8.9E-05
317	Throneberry [40]	Angle-head ER	Tee	3.0	330	150	1	15	1	8.0E-01	73	HOR	7.4E-05
318	Throneberry [40]	Angle-head ER	Tee	3.0	330	150	1	28	20	8.0E-01	73	HOR	7.0E-04
319	Throneberry [40]	ER	Elbow	3.0	330	150	1	28	20	8.0E-01	73	HOR	1.0E-04
320	Throneberry [40]	Angle-head ER	Tee	3.0	330	300	1	15	1	4.4E-01	73	HOR	3.8E-04
321	Throneberry [40]	ER	Elbow	3.0	330	300	1	15	1	4.4E-01	73	HOR	1.5E-04
322	Throneberry [40]	Angle-head ER	Tee	3.0	330	300	1	15	1	8.0E-01	73	HOR	2.0E-04

323	Throneberry [40]	ER	Elbow	3.0	330	300	1	15	1	8.0E-01	73	HOR	8.0E-05
324	Throneberry [40]	Angle-head ER	Tee	3.0	330	300	1	15	20	4.4E-01	73	HOR	2.0E-04
325	Throneberry [40]	ER	Elbow	3.0	330	300	1	15	20	4.4E-01	73	HOR	7.3E-05
326	Throneberry [40]	Angle-head ER	Tee	3.0	330	300	1	25	1	7.7E-01	73	HOR	1.7E-03
327	Throneberry [40]	ER	Elbow	3.0	330	300	1	25	1	7.7E-01	73	HOR	1.0E-04
328	Throneberry [40]	Angle-head ER	Tee	3.0	330	20	1	25	1	7.8E-01	73	HOR	3.7E-04
329	Throneberry [40]	Angle-head ER	Tee	3.0	330	20	1	15	1	4.4E-01	73	HOR	4.9E-05
330	Throneberry [40]	Angle-head ER	Tee	3.0	330	20	1	25	20	7.3E-01	73	HOR	1.8E-04
331	Throneberry [40]	ER	Elbow	3.0	330	20	1	25	20	7.3E-01	73	HOR	1.8E-05
332	Throneberry [40]	Angle-head ER	Tee	3.0	330	300	1	21	1	7.9E-01	73	HOR	6.9E-04
333	Throneberry [40]	ER	Elbow	3.0	330	300	1	21	1	7.9E-01	73	HOR	1.5E-04
334	Throneberry [40]	Angle-head ER	Tee	3.0	330	150	1	21	1	7.9E-01	73	HOR	2.5E-04
335	Throneberry [40]	ER	Elbow	3.0	330	150	1	21	1	7.9E-01	73	HOR	4.9E-05
336	Throneberry [40]	Angle-head ER	Tee	3.0	330	20	1	21	1	7.9E-01	73	HOR	9.6E-05
337	Throneberry [40]	ER	Elbow	3.0	330	20	1	21	1	7.9E-01	73	HOR	3.7E-05
338	Throneberry [40]	Angle-head ER	Tee	3.0	330	300	1	21	20	7.9E-01	73	HOR	1.1E-03
339	Throneberry [40]	Angle-head ER	Tee	3.0	330	300	1	21	40	8.4E-01	73	HOR	6.6E-04
340	Throneberry [40]	Angle-head ER	Tee	3.0	330	300	1	21	40	7.9E-01	73	HOR	6.6E-04
341	Throneberry [40]	Angle-head ER	Tee	3.0	330	300	1	21	1	8.0E-01	73	HOR	6.1E-04
342	Throneberry [40]	ER	Elbow	3.0	330	300	1	21	1	8.0E-01	73	HOR	1.3E-04

343	Throneberry [40]	Angle-head ER	Tee	3.0	330	300	1	15	1	4.4E-01	73	HOR	9.8E-05
344	Throneberry [40]	ER	Elbow	3.0	330	300	1	15	1	4.4E-01	73	HOR	5.0E-05
345	Throneberry [40]	Angle-head ER	Tee	3.0	330	300	1	15	1	8.0E-01	73	HOR	3.1E-04
346	Throneberry [40]	ER	Elbow	3.0	330	300	1	15	1	8.0E-01	73	HOR	1.3E-04
347	Throneberry [40]	Angle-head ER	Tee	3.0	330	150	1	27	1	8.0E-01	73	HOR	4.8E-04
348	Throneberry [40]	ER	Elbow	3.0	330	150	1	27	1	8.0E-01	73	HOR	3.2E-05
349	Throneberry [40]	Angle-head ER	Tee	3.0	330	150	1	15	1	8.0E-01	73	HOR	8.6E-05
350	Throneberry [40]	ER	Elbow	3.0	330	150	1	15	1	8.0E-01	73	HOR	1.8E-05
351	Throneberry [40]	Angle-head ER	Tee	3.0	330	150	1	27	1	7.9E-01	73	HOR	3.8E-04
352	Throneberry [40]	ER	Elbow	3.0	330	150	1	27	1	7.9E-01	73	HOR	5.3E-05
353	Mazumder [4]	WL	Elbow	1.0	230	150	1	19	1	0.0E+00	73	HOR	5.7E-02
354	Mazumder [4]	WL	Elbow	1.0	230	150	1	27	1	0.0E+00	73	HOR	7.9E-02
355	Mazumder [4]	WL	Elbow	1.0	230	150	1	34	1	0.0E+00	73	HOR	1.1E-01
356	Mazumder [4]	WL	Elbow	1.0	230	150	1	34	1	3.0E-02	73	HOR	7.3E-03
357	Mazumder [4]	WL	Elbow	1.0	230	150	1	27	1	3.0E-02	73	HOR	3.2E-03
358	Mazumder [4]	WL	Elbow	1.0	230	150	1	19	1	3.0E-02	73	HOR	1.3E-03
359	Mazumder [4]	WL	Elbow	1.0	230	150	1	10	1	3.0E-02	73	HOR	1.6E-03
360	Mazumder [4]	WL	Elbow	1.0	230	150	1	34	1	3.0E-01	73	HOR	2.1E-03
361	Mazumder [4]	WL	Elbow	1.0	230	150	1	27	1	3.0E-01	73	HOR	3.7E-03
362	Mazumder [4]	WL	Elbow	1.0	230	150	1	19	1	3.0E-01	73	HOR	1.4E-03
363	Mazumder [4]	WL	Elbow	1.0	230	150	1	10	1	3.0E-01	73	HOR	1.6E-04
364	Nuguri [36]	ER	Elbow	3.0	330	150	2	34	1	0.0E+00	73	VER	1.2E-02
365	Nuguri [36]	ER	Elbow	3.0	330	150	2	58	1	0.0E+00	73	VER	5.7E-02
366	Nuguri [36]	ER	Elbow	2.0	330	150	2	24	1	7.1E-03	73	VER	1.7E-03
367	Nuguri [36]	ER	Elbow	2.0	330	150	2	24	1	9.4E-03	73	VER	1.4E-03

368	Nuguri [36]	ER	Elbow	2.0	330	150	2	24	1	2.2E-02	73	VER	1.9E-03
369	Nuguri [36]	ER	Elbow	2.0	330	150	2	24	1	2.6E-02	73	VER	2.0E-03
370	Nuguri [36]	ER	Elbow	2.0	330	150	2	24	1	2.8E-02	73	VER	4.3E-03
371	Nuguri [36]	ER	Elbow	2.0	330	150	2	24	1	3.1E-02	73	VER	2.2E-03
372	Nuguri [36]	ER	Elbow	2.0	330	150	2	24	1	5.2E-02	73	VER	2.3E-03
373	Nuguri [36]	ER	Elbow	2.0	330	150	2	24	1	1.1E-01	73	VER	1.5E-03
374	Nuguri [36]	ER	Elbow	2.0	330	150	2	24	1	1.7E-01	73	VER	2.4E-03
375	Nuguri [36]	ER	Elbow	2.0	330	300	2	30	1	3.0E-01	73	VER	1.1E-02
376	Nuguri [36]	ER	Elbow	2.0	330	150	2	30	1	1.4E-04	73	VER	1.1E-02
377	Nuguri [36]	ER	Elbow	2.0	330	150	2	30	1	3.0E-04	73	VER	2.1E-02
378	Nuguri [36]	ER	Elbow	2.0	330	150	2	30	1	7.6E-04	73	VER	1.4E-02
379	Nuguri [36]	ER	Elbow	2.0	330	150	2	30	1	1.2E-03	73	VER	1.7E-02
380	Nuguri [36]	ER	Elbow	2.0	330	150	2	30	1	1.5E-03	73	VER	7.1E-03
381	Nuguri [36]	ER	Elbow	2.0	330	150	2	30	1	1.7E-03	73	VER	1.1E-02
382	Nuguri [36]	ER	Elbow	2.0	330	150	2	30	1	1.8E-03	73	VER	8.6E-03
383	Nuguri [36]	ER	Elbow	2.0	330	150	2	30	1	2.0E-03	73	VER	1.1E-02
384	Nuguri [36]	ER	Elbow	2.0	330	150	2	30	1	2.2E-03	73	VER	1.7E-02
385	Nuguri [36]	ER	Elbow	2.0	330	150	2	30	1	3.0E-03	73	VER	1.1E-02
386	Nuguri [36]	ER	Elbow	2.0	330	150	2	30	1	5.0E-03	73	VER	1.1E-02
387	Nuguri [36]	ER	Elbow	2.0	330	150	2	30	1	5.2E-03	73	VER	6.7E-03
388	Nuguri [36]	ER	Elbow	2.0	330	150	2	30	1	6.5E-03	73	VER	4.2E-03
389	Nuguri [36]	ER	Elbow	2.0	330	150	2	30	1	6.7E-03	73	VER	3.8E-03
390	Nuguri [36]	ER	Elbow	2.0	330	150	2	30	1	6.9E-03	73	VER	4.3E-03
391	Nuguri [36]	ER	Elbow	2.0	330	150	2	30	1	7.6E-03	73	VER	7.1E-03
392	Nuguri [36]	ER	Elbow	2.0	330	150	2	30	1	4.0E-03	73	VER	8.3E-03
393	Nuguri [36]	ER	Elbow	2.0	330	150	2	30	1	4.3E-03	73	VER	7.7E-03
394	Nuguri [36]	ER	Elbow	2.0	330	150	2	30	1	4.5E-03	73	VER	7.8E-03
395	Nuguri [36]	ER	Elbow	2.0	330	150	2	30	1	2.1E-04	73	VER	1.4E-02

396	Nuguri [36]	ER	Elbow	2.0	330	150	2	30	1	3.4E-04	73	VER	1.5E-02
397	Nuguri [36]	ER	Elbow	2.0	330	150	2	30	1	4.6E-04	73	VER	1.8E-02
398	Nuguri [36]	ER	Elbow	2.0	330	150	2	30	1	1.4E-03	73	VER	1.6E-02
399	Nuguri [36]	ER	Elbow	2.0	330	150	2	30	1	3.0E-03	73	VER	5.5E-03
400	Nuguri [36]	ER	Elbow	2.0	330	150	2	30	1	3.7E-03	73	VER	4.2E-03
401	Nuguri [36]	ER	Elbow	2.0	330	150	2	30	1	5.9E-03	73	VER	4.4E-03
402	Nuguri [36]	ER	Elbow	2.0	330	150	2	30	1	7.1E-03	73	VER	4.2E-03
403	Nuguri [36]	ER	Elbow	2.0	330	150	2	24	1	2.7E-04	73	VER	8.4E-03
404	Nuguri [36]	ER	Elbow	2.0	330	150	2	24	1	4.3E-04	73	VER	7.3E-03
405	Nuguri [36]	ER	Elbow	2.0	330	150	2	24	1	6.2E-04	73	VER	8.3E-03
406	Nuguri [36]	ER	Elbow	2.0	330	150	2	24	1	9.1E-04	73	VER	6.3E-03
407	Nuguri [36]	ER	Elbow	2.0	330	150	2	24	1	1.1E-03	73	VER	6.7E-03
408	Nuguri [36]	ER	Elbow	2.0	330	150	2	24	1	2.5E-03	73	VER	2.7E-03
409	Nuguri [36]	ER	Elbow	2.0	330	150	2	24	1	3.0E-03	73	VER	2.8E-03
410	Nuguri [36]	ER	Elbow	2.0	330	150	2	24	1	4.1E-03	73	VER	3.6E-03
411	Nuguri [36]	ER	Elbow	2.0	330	150	2	24	1	4.7E-03	73	VER	1.8E-03
412	Nuguri [36]	ER	Elbow	2.0	330	300	2	30	1	3.0E-05	73	VER	5.6E-02
413	Nuguri [36]	ER	Elbow	2.0	330	300	2	30	1	1.1E-04	73	VER	2.5E-02
414	Nuguri [36]	ER	Elbow	2.0	330	300	2	30	1	1.8E-04	73	VER	4.5E-02
415	Nuguri [36]	ER	Elbow	2.0	330	300	2	30	1	2.1E-04	73	VER	4.4E-02
416	Nuguri [36]	ER	Elbow	2.0	330	300	2	30	1	3.1E-04	73	VER	3.1E-02
417	Nuguri [36]	ER	Elbow	2.0	330	300	2	30	1	4.0E-04	73	VER	4.5E-02
418	Nuguri [36]	ER	Elbow	2.0	330	300	2	30	1	6.4E-04	73	VER	3.2E-02
419	Nuguri [36]	ER	Elbow	2.0	330	300	2	30	1	7.6E-04	73	VER	3.4E-02
420	Nuguri [36]	ER	Elbow	2.0	330	300	2	30	1	1.6E-03	73	VER	2.1E-02
421	Nuguri [36]	ER	Elbow	2.0	330	300	2	30	1	5.5E-03	73	VER	1.3E-02
422	Nuguri [36]	ER	Elbow	2.0	330	300	2	30	1	1.5E-02	73	VER	1.8E-02
423	Nuguri [36]	ER	Elbow	2.0	330	300	2	30	1	2.1E-02	73	VER	2.0E-02

424	Nuguri [36]	ER	Elbow	2.0	330	300	2	30	1	3.0E-02	73	VER	2.1E-02
425	Nuguri [36]	ER	Elbow	2.0	330	300	2	30	1	6.4E-02	73	VER	2.7E-02
426	Nuguri [36]	ER	Elbow	2.0	330	300	2	30	1	6.7E-02	73	VER	2.7E-02
427	Nuguri [36]	ER	Elbow	2.0	330	300	2	30	1	9.1E-02	73	VER	2.5E-02
428	Nuguri [36]	ER	Elbow	2.0	330	300	2	30	1	1.2E-01	73	VER	2.1E-02
429	Nuguri [36]	ER	Elbow	2.0	330	300	2	30	1	1.5E-01	73	VER	1.8E-02
430	Pyboyina [35]	WL	Elbow	1.0	123	150	3	27	1	3.0E-01	73	VER	1.6E-02
431	Pyboyina [35]	WL	Elbow	1.0	90	150	3	27	1	3.0E-01	73	VER	1.2E-01
432	Pyboyina [35]	WL	Elbow	1.0	123	150	3	27	1	3.0E-02	73	VER	1.2E-02
433	Pyboyina [35]	WL	Elbow	1.0	123	150	3	27	1	3.0E-02	73	HOR	2.4E-03
434	Pyboyina [35]	WL	Elbow	1.0	90	150	3	27	1	3.0E-02	73	VER	3.7E-02
435	Pyboyina [35]	ER	Elbow	2.0	330	150	3	27	1	1.2E-01	73	HOR	2.9E-03
436	Pyboyina [35]	ER	Elbow	2.0	330	150	3	23	1	6.1E-02	73	VER	8.9E-03
437	Pyboyina [35]	ER	Elbow	2.0	330	150	3	30	1	4.9E-02	73	HOR	8.6E-03
438	Pyboyina [35]	ER	Elbow	2.0	330	150	3	12	1	0.0E+00	73	HOR	1.4E-03
439	Pyboyina [35]	ER	Elbow	2.0	330	150	3	19	1	0.0E+00	73	HOR	5.4E-03
440	Pyboyina [35]	ER	Elbow	2.0	330	150	3	28	1	0.0E+00	73	HOR	1.2E-02
441	Pyboyina [35]	ER	Tee	1.0	330	150	3	19	1	0.0E+00	73	HOR	1.5E-02
442	Pyboyina [35]	ER	Tee	1.0	330	150	3	27	1	0.0E+00	73	HOR	2.2E-02
443	Pyboyina [35]	ER	Tee	1.0	330	150	3	34	1	0.0E+00	73	HOR	1.7E-02
444	Pyboyina [35]	ER	Tee	1.0	330	150	3	25	1	0.0E+00	73	VER	1.6E-02
445	Salama [31]	NA	Elbow	1.9	160	150	2	8	1	2.0E-01	73	VER	2.2E-03
446	Salama [31]	NA	Long elbow	1.9	160	150	2	30	1	1.0E+00	73	VER	9.4E-03
447	Salama [31]	NA	Long elbow	1.9	160	150	2	30	1	5.0E-01	73	VER	4.4E-02
448	Salama [31]	NA	Long elbow	1.0	330	250	10	14	1	1.5E+00	73	VER	4.1E-03
449	Salama [31]	NA	Long elbow	1.0	330	250	10	15	1	1.5E+00	73	VER	7.5E-03

450	Salama [31]	NA	Long elbow	1.0	330	250	10	34	1	2.1E+00	73	VER	5.1E-02
451	Salama [31]	NA	Long elbow	1.0	330	250	10	35	1	1.0E+00	73	VER	1.2E-01
452	Salama [31]	NA	Long elbow	1.0	330	250	10	34	1	5.0E-01	73	VER	1.3E-01
453	Salama [31]	NA	Long elbow	1.0	330	250	10	37	1	7.0E-01	73	VER	1.4E-01
454	Salama [31]	NA	Long elbow	1.0	330	250	10	39	1	5.0E-01	73	VER	1.4E-01
455	Salama [31]	NA	Long elbow	1.0	330	250	10	44	1	1.5E+00	73	VER	1.9E-01
456	Salama [31]	NA	Long elbow	1.0	330	250	10	51	1	6.0E-01	73	VER	2.4E-01
457	Salama [31]	NA	Long elbow	1.0	330	250	10	52	1	7.0E-01	73	VER	2.4E-01
458	Salama [31]	NA	Elbow	1.9	160	150	2	20	1	5.8E+00	73	VER	9.3E-04
459	Salama [31]	NA	Elbow	1.9	160	150	2	20	1	3.1E+00	73	VER	1.2E-03
460	Salama [31]	NA	Long elbow	1.9	160	150	2	15	1	1.0E+00	73	VER	2.6E-03
461	Salama [31]	NA	Long elbow	1.9	160	150	2	15	1	5.0E+00	73	VER	1.1E-03
462	Salama [31]	NA	Long elbow	1.9	160	150	2	10	1	5.0E+00	73	VER	2.4E-04
463	Salama [31]	NA	Long elbow	1.9	160	150	2	10	1	7.0E-01	73	VER	1.3E-03
464	Salama [31]	NA	Long elbow	1.0	330	250	10	9	1	6.2E+00	73	VER	3.2E-03
465	Tolle [30]	WL	Elbow	2.0	109	300	1	9	1	0.0E+00	73	VER	3.8E-02
466	Tolle [30]	WL	Elbow	2.0	109	300	1	12	1	0.0E+00	73	VER	6.8E-02
467	Tolle [30]	WL	Elbow	2.0	109	300	1	15	1	0.0E+00	73	VER	1.3E-01
468	Tolle [30]	WL	Elbow	2.0	109	300	1	18	1	0.0E+00	73	VER	1.6E-01
469	Tolle [30]	WL	Elbow	2.0	109	300	1	21	1	0.0E+00	73	VER	2.2E-01
470	Tolle [30]	WL	Elbow	2.0	109	300	1	24	1	0.0E+00	73	VER	2.9E-01
471	Tolle [30]	WL	Elbow	2.0	109	300	1	27	1	0.0E+00	73	VER	3.2E-01
472	Tolle [30]	WL	Elbow	2.0	109	300	1	30	1	0.0E+00	73	VER	3.6E-01

473	Kesana [41]	UT	Elbow	3.0	230	150	1	34	1	0.0E+00	73	HOR	3.1E-02
474	Kesana [41]	UT	Elbow	3.0	230	150	1	33	1	0.0E+00	73	HOR	2.1E-02
475	Kesana [41]	UT	Elbow	3.0	230	150	1	29	1	0.0E+00	73	HOR	1.2E-02
476	Kesana [41]	UT	Elbow	3.0	230	150	1	18	1	0.0E+00	73	HOR	8.5E-03
477	Vieira [42]	UT	Elbow	3.0	230	300	1	11	1	0.0E+00	73	VER	2.9E-03
478	Vieira [42]	UT	Elbow	3.0	230	300	1	15	1	0.0E+00	73	VER	7.0E-03
479	Vieira [42]	UT	Elbow	3.0	230	300	1	23	1	0.0E+00	73	VER	1.7E-02
480	Vieira [42]	UT	Elbow	3.0	230	300	1	27	1	0.0E+00	73	VER	2.5E-02
481	Vieira [42]	UT	Elbow	3.0	230	150	1	11	1	0.0E+00	73	VER	1.3E-03
482	Vieira [42]	UT	Elbow	3.0	230	150	1	15	1	0.0E+00	73	VER	2.7E-03
483	Vieira [42]	UT	Elbow	3.0	230	150	1	23	1	0.0E+00	73	VER	6.9E-03
484	Vieira [42]	UT	Elbow	3.0	230	150	1	27	1	0.0E+00	73	VER	1.3E-02
485	Vieira [42]	UT	Elbow	3.0	230	300	1	49	1	1.8E-01	73	VER	4.5E-02
486	Vieira [42]	UT	Elbow	3.0	230	300	1	49	1	4.1E-02	73	VER	4.5E-02
487	Vieira [42]	UT	Elbow	3.0	230	300	1	49	1	2.0E-02	73	VER	3.4E-02
488	Vieira [42]	UT	Elbow	3.0	230	300	1	49	1	1.0E-02	73	VER	3.8E-02
489	Vieira [42]	UT	Elbow	3.0	230	300	1	49	1	3.0E-03	73	VER	4.3E-02
490	Vieira [42]	UT	Elbow	3.0	230	300	1	41	1	4.1E-02	73	VER	3.2E-02
491	Vieira [42]	UT	Elbow	3.0	230	300	1	41	1	2.0E-02	73	VER	2.6E-02
492	Vieira [42]	UT	Elbow	3.0	230	300	1	41	1	1.0E-02	73	VER	2.6E-02
493	Vieira [42]	UT	Elbow	3.0	230	300	1	41	1	5.0E-03	73	VER	3.2E-02
494	Vieira [42]	UT	Elbow	3.0	230	300	1	35	1	8.8E-02	73	VER	2.1E-02
495	Vieira [42]	UT	Elbow	3.0	230	300	1	36	1	9.1E-02	73	VER	1.4E-02
496	Vieira [42]	UT	Elbow	3.0	230	300	1	34	1	9.8E-02	73	VER	2.2E-02
497	Vieira [42]	UT	Elbow	3.0	230	20	1	34	1	9.8E-02	73	VER	4.0E-03
498	Vieira [42]	UT	Elbow	3.0	230	150	1	36	1	9.1E-02	73	VER	4.5E-03
499	Vieira [42]	UT	Elbow	3.0	230	300	1	27	1	9.8E-02	73	VER	1.6E-02
500	Vieira [42]	UT	Elbow	3.0	230	300	1	27	1	4.0E-02	73	VER	1.4E-02

501	Vieira [42]	UT	Elbow	3.0	230	300	1	27	1	1.8E-02	73	VER	1.1E-02
502	Vieira [42]	UT	Elbow	3.0	230	300	1	27	1	9.0E-03	73	VER	1.6E-02
503	Vieira [42]	UT	Elbow	3.0	230	300	1	27	1	5.0E-03	73	VER	2.0E-02
504	Vieira [42]	UT	Elbow	3.0	230	300	1	23	1	9.8E-02	73	VER	1.2E-02
505	Vieira [42]	UT	Elbow	3.0	230	20	1	23	1	4.0E-02	73	VER	2.3E-03
506	Vieira [42]	UT	Elbow	3.0	230	150	1	23	1	4.0E-02	73	VER	6.5E-03
507	Vieira [42]	UT	Elbow	3.0	230	300	1	23	1	4.0E-02	73	VER	1.7E-02
508	Vieira [42]	UT	Elbow	3.0	230	300	1	23	1	9.0E-03	73	VER	5.7E-03
509	Vieira [42]	UT	Elbow	3.0	230	300	1	15	1	9.8E-02	73	VER	4.9E-03
510	Vieira [42]	UT	Elbow	3.0	230	20	1	15	1	9.8E-02	73	VER	1.7E-03
511	Vieira [42]	UT	Elbow	3.0	230	150	1	15	1	9.8E-02	73	VER	2.4E-03
512	Vieira [42]	UT	Elbow	3.0	230	300	1	15	1	4.0E-02	73	VER	7.2E-03
513	Vieira [42]	UT	Elbow	3.0	230	300	1	15	1	1.8E-02	73	VER	5.4E-03
514	Vieira [42]	UT	Elbow	3.0	230	300	1	15	1	1.2E-02	73	VER	5.4E-03
515	Vieira [42]	UT	Elbow	3.0	230	300	1	15	1	8.0E-03	73	VER	4.2E-03
516	Vieira [42]	UT	Elbow	3.0	230	300	1	49	1	4.6E-01	73	VER	1.3E-02
517	Vieira [42]	UT	Elbow	3.0	230	300	1	27	1	4.8E-01	73	VER	4.0E-03
518	Vieira [42]	UT	Elbow	3.0	230	300	1	27	1	8.5E-02	73	VER	2.8E-02
519	Vieira [42]	UT	Elbow	3.0	230	300	1	11	1	9.8E-02	73	VER	1.4E-03
520	Vieira [42]	UT	Elbow	3.0	230	300	1	49	1	4.0E-02	73	HOR	1.6E-03
521	Vieira [42]	UT	Elbow	3.0	230	300	1	49	1	1.8E-02	73	HOR	1.8E-03
522	Vieira [42]	UT	Elbow	3.0	230	300	1	49	1	4.0E-03	73	HOR	2.6E-03
523	Vieira [42]	UT	Elbow	3.0	230	300	1	40	1	4.0E-02	73	HOR	6.0E-04
524	Vieira [42]	UT	Elbow	3.0	230	300	1	40	1	1.8E-02	73	HOR	1.2E-03
525	Vieira [42]	UT	Elbow	3.0	230	300	1	40	1	1.0E-02	73	HOR	1.3E-03
526	Vieira [42]	UT	Elbow	3.0	230	300	1	40	1	5.0E-03	73	HOR	1.5E-03
527	Vieira [42]	UT	Elbow	3.0	230	300	1	35	1	9.1E-02	73	HOR	1.2E-04
528	Vieira [42]	UT	Elbow	3.0	230	150	1	34	1	9.8E-02	73	HOR	1.0E-04

529	Vieira [42]	UT	Elbow	3.0	230	300	1	27	1	1.3E-01	73	HOR	3.9E-05
530	Vieira [42]	UT	Elbow	3.0	230	300	1	30	1	3.0E-02	73	HOR	3.1E-04
531	Zhang [20]	ER	DI	0.3	330	150	1	0	1	1.0E+01	73	VER	1.7E-03
532	Zhang [20]	ER	DI	0.3	330	150	1	0	1	5.0E+00	73	VER	3.2E-04
533	Zhang [20]	ER	DI	0.3	330	150	1	0	1	2.5E+00	73	VER	2.3E-05
534	Zhang [20]	ER	DI	0.3	330	25	1	0	1	1.0E+01	73	VER	6.1E-04
535	Reuterfors [34]	ER	DI	0.3	330	150	1	0	1	2.5E+00	73	VER	1.0E-04
536	Reuterfors [34]	ER	DI	0.3	330	150	1	0	1	5.0E+00	73	VER	2.5E-04
537	Reuterfors [34]	ER	DI	0.3	330	150	1	0	1	1.0E+01	73	VER	1.7E-03
538	Reuterfors [34]	ER	DI	0.3	330	20	1	0	1	1.0E+01	73	VER	6.0E-04
539	Bourgoyne [14]	ER	Elbow	0.6	200	195	1	0	1	2.8E+00	73	VER	8.8E-04
540	Bourgoyne [14]	ER	Elbow	0.6	200	83	1	0	1	2.8E+00	73	VER	1.2E-04
541	Bourgoyne [14]	UTL	Long elbow	2.1	120	350	1	0	6	9.5E+00	73	VER	4.0E-05
542	Bourgoyne [14]	UTL	Long elbow	2.1	120	350	1	0	6	1.4E+01	73	VER	8.1E-06
543	Kesana [41]	ER	Elbow	3.0	230	20	1	15	1	4.5E-01	73	HOR	5.3E-05
544	Kesana [41]	ER	Elbow	3.0	230	20	1	24	1	4.9E-01	73	HOR	3.3E-05
545	Kesana [41]	ER	Elbow	3.0	230	20	1	30	1	4.6E-01	73	HOR	4.6E-05
546	Kesana [41]	ER	Elbow	3.0	230	20	1	15	1	8.0E-01	73	HOR	7.5E-06
547	Kesana [41]	ER	Elbow	3.0	230	20	1	46	1	8.0E-01	73	HOR	4.5E-05
548	Kesana [41]	ER	Elbow	3.0	230	20	1	46	1	5.0E-01	73	HOR	1.0E-04
549	Kesana [41]	ER	Elbow	3.0	230	150	1	18	1	4.4E-01	73	HOR	1.0E-05
550	Kesana [41]	ER	Elbow	3.0	230	150	1	27	1	4.4E-01	73	HOR	3.0E-05
551	Kesana [41]	ER	Elbow	3.0	230	150	1	35	1	4.4E-01	73	HOR	8.5E-05
552	Kesana [41]	ER	Elbow	3.0	230	150	1	44	1	4.4E-01	73	HOR	3.9E-04
553	Kesana [41]	ER	Elbow	3.0	230	150	1	48	1	4.4E-01	73	HOR	6.9E-04

554	Kesana [41]	ER	Elbow	3.0	230	150	1	18	1	7.3E-01	73	HOR	2.7E-05
555	Kesana [41]	ER	Elbow	3.0	230	150	1	26	1	7.3E-01	73	HOR	3.0E-05
556	Kesana [41]	ER	Elbow	3.0	230	150	1	34	1	7.3E-01	73	HOR	5.1E-05
557	Kesana [41]	ER	Elbow	3.0	230	150	1	44	1	7.3E-01	73	HOR	1.7E-04
558	Kesana [41]	ER	Elbow	3.0	230	150	1	48	1	7.3E-01	73	HOR	3.1E-04
559	Kesana [41]	ER	Elbow	3.0	230	150	1	17	10	4.8E-01	73	HOR	3.0E-05
560	Kesana [41]	ER	Elbow	3.0	230	150	1	26	10	4.8E-01	73	HOR	7.4E-05
561	Kesana [41]	ER	Elbow	3.0	230	150	1	33	10	4.8E-01	73	HOR	1.1E-04
562	Kesana [41]	ER	Elbow	3.0	230	150	1	43	10	4.8E-01	73	HOR	2.1E-04
563	Kesana [41]	ER	Elbow	3.0	230	150	1	48	10	4.8E-01	73	HOR	3.7E-04
564	Kesana [41]	ER	Elbow	3.0	230	150	1	18	10	7.7E-01	73	HOR	2.7E-05
565	Kesana [41]	ER	Elbow	3.0	230	150	1	26	10	7.7E-01	73	HOR	6.1E-05
566	Kesana [41]	ER	Elbow	3.0	230	150	1	34	10	7.7E-01	73	HOR	1.0E-04
567	Kesana [41]	ER	Elbow	3.0	230	150	1	44	10	7.7E-01	73	HOR	1.7E-04
568	Kesana [41]	ER	Elbow	3.0	230	150	1	48	10	7.7E-01	73	HOR	2.7E-04
569	Kesana [41]	ER	Elbow	3.0	230	300	1	17	1	4.7E-01	73	HOR	5.9E-05
570	Kesana [41]	ER	Elbow	3.0	230	300	1	26	1	4.7E-01	73	HOR	7.9E-05
571	Kesana [41]	ER	Elbow	3.0	230	300	1	35	1	4.7E-01	73	HOR	3.4E-04
572	Kesana [41]	ER	Elbow	3.0	230	300	1	43	1	4.7E-01	73	HOR	9.2E-04
573	Kesana [41]	ER	Elbow	3.0	230	300	1	49	1	4.7E-01	73	HOR	1.9E-03
574	Kesana [41]	ER	Elbow	3.0	230	300	1	18	1	7.3E-01	73	HOR	4.4E-05
575	Kesana [41]	ER	Elbow	3.0	230	300	1	25	1	7.3E-01	73	HOR	4.1E-05
576	Kesana [41]	ER	Elbow	3.0	230	300	1	33	1	7.3E-01	73	HOR	6.0E-05
577	Kesana [41]	ER	Elbow	3.0	230	300	1	44	1	7.3E-01	73	HOR	1.6E-04
578	Kesana [41]	ER	Elbow	3.0	230	300	1	49	1	7.3E-01	73	HOR	3.0E-04
579	Kesana [41]	ER	Elbow	3.0	230	300	1	18	10	4.7E-01	73	HOR	5.5E-05
580	Kesana [41]	ER	Elbow	3.0	230	300	1	26	10	4.7E-01	73	HOR	1.2E-04
581	Kesana [41]	ER	Elbow	3.0	230	300	1	35	10	4.7E-01	73	HOR	2.6E-04

582	Kesana [41]	ER	Elbow	3.0	230	300	1	43	10	4.7E-01	73	HOR	5.8E-04
583	Kesana [41]	ER	Elbow	3.0	230	300	1	49	10	4.7E-01	73	HOR	1.1E-03
584	Kesana [41]	ER	Elbow	3.0	230	300	1	18	10	7.7E-01	73	HOR	6.7E-05
585	Kesana [41]	ER	Elbow	3.0	230	300	1	48	10	7.8E-01	73	HOR	2.5E-04

APPENDIX B

Data Uncertainty Results

Results for Branin function

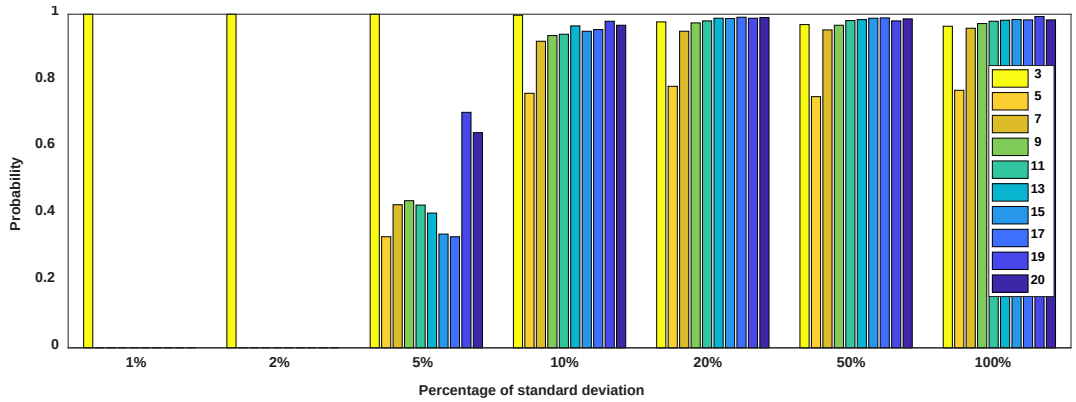

Figure B.1. Probability of passing SW-test of Branin function (α = 0.01)

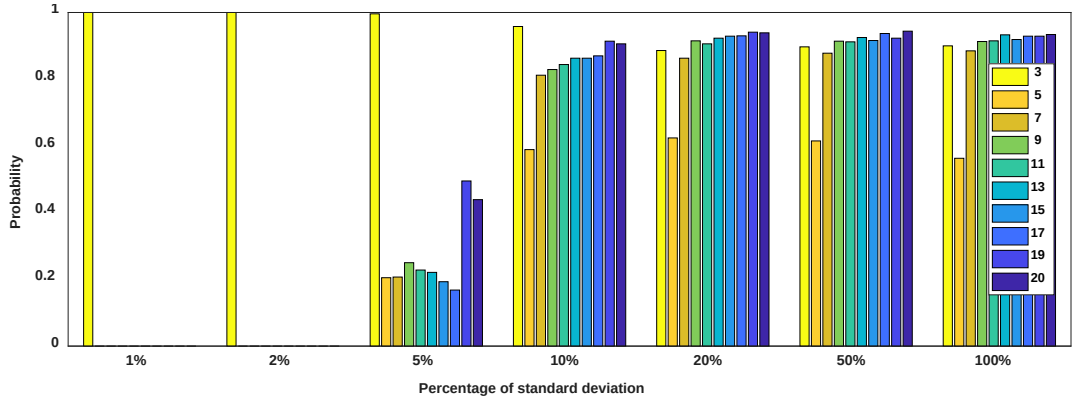

Figure B.2. Probability of passing SW-test of Branin function (α = 0.05)

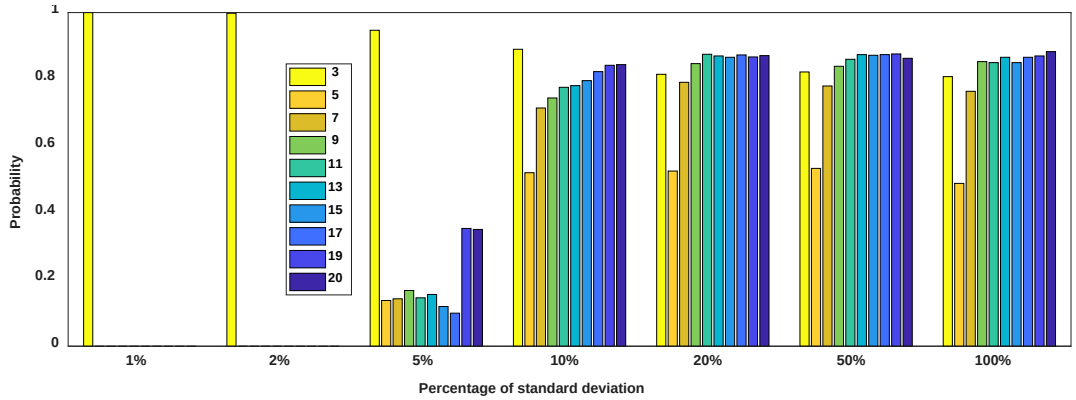

Figure B.3. Probability of passing SW-test of Branin function (α = 0.1)

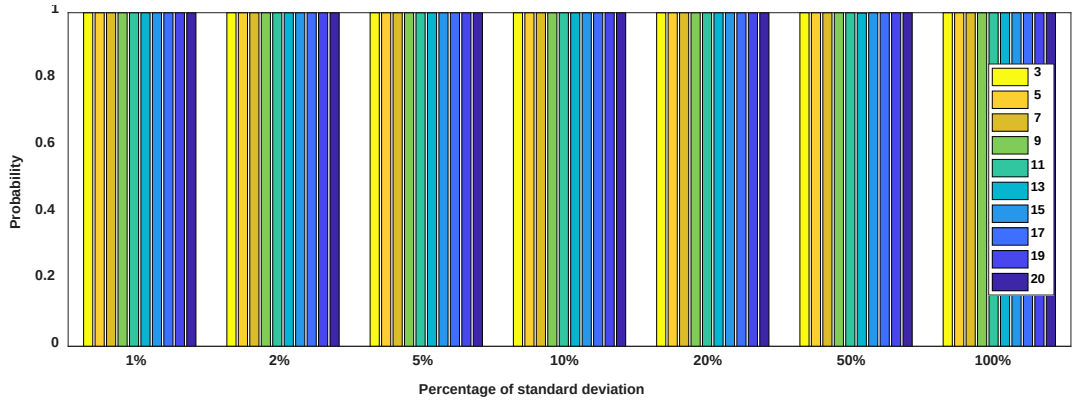

Figure B.4. Probability of passing t-test of Branin function (α = 0.01)

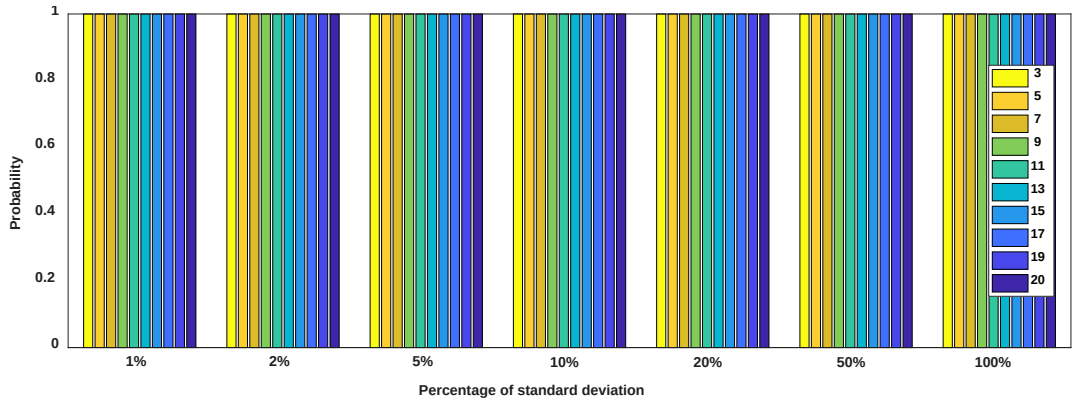

Figure B.5. Probability of passing t-test of Branin function (α = 0.05)

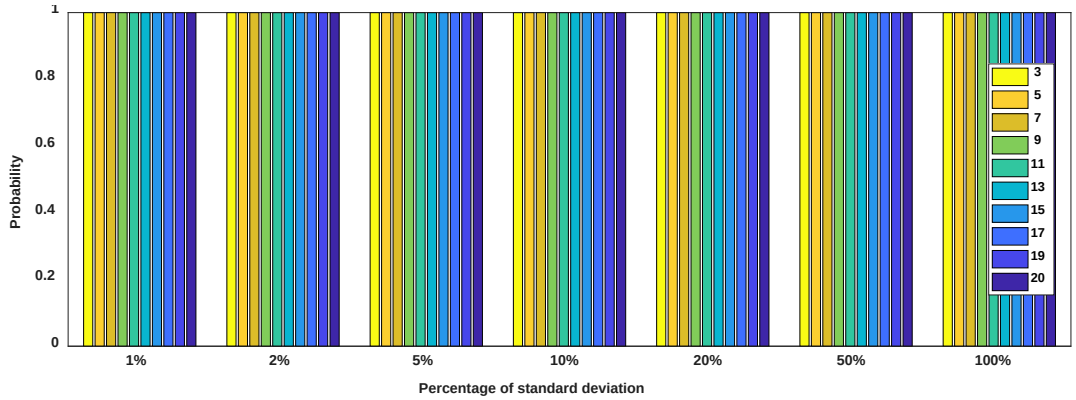

Figure B.6. Probability of passing t-test of Branin function (α = 0.1)

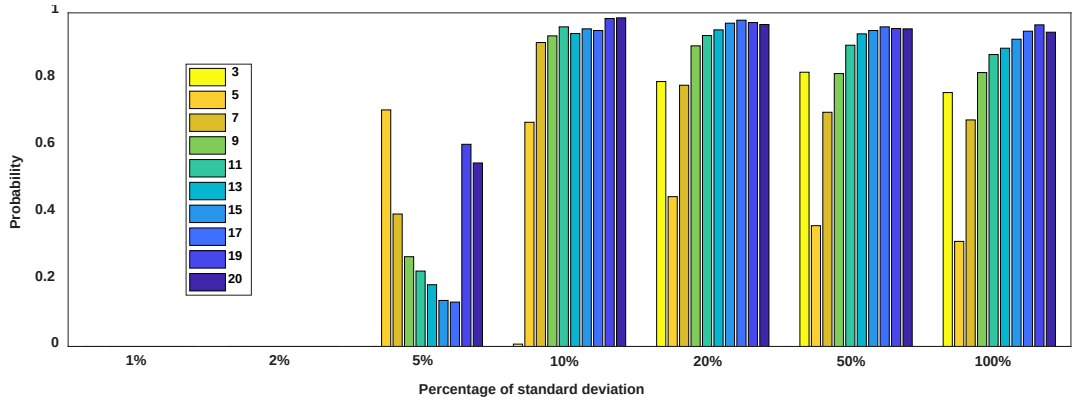

Figure B.7. Probability of passing χ^2-test of Branin function (α = 0.01)

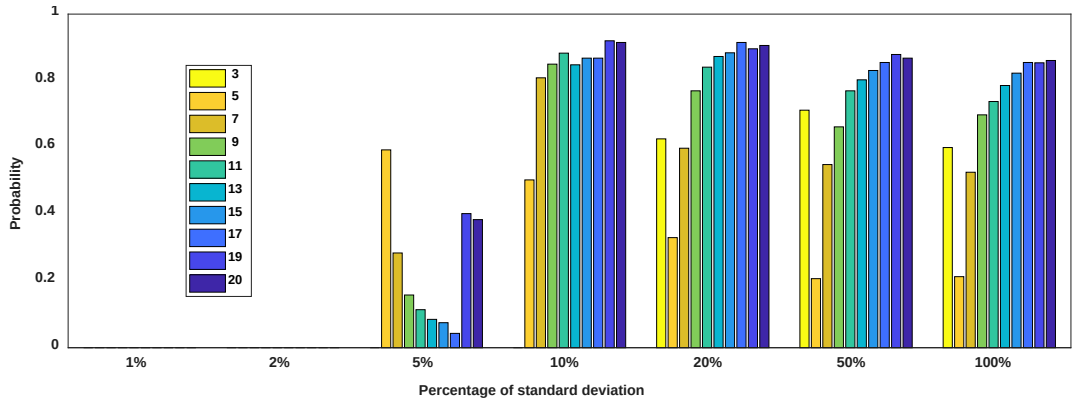

Figure B.8. Probability of passing χ^2-test of Branin function (α = 0.05)

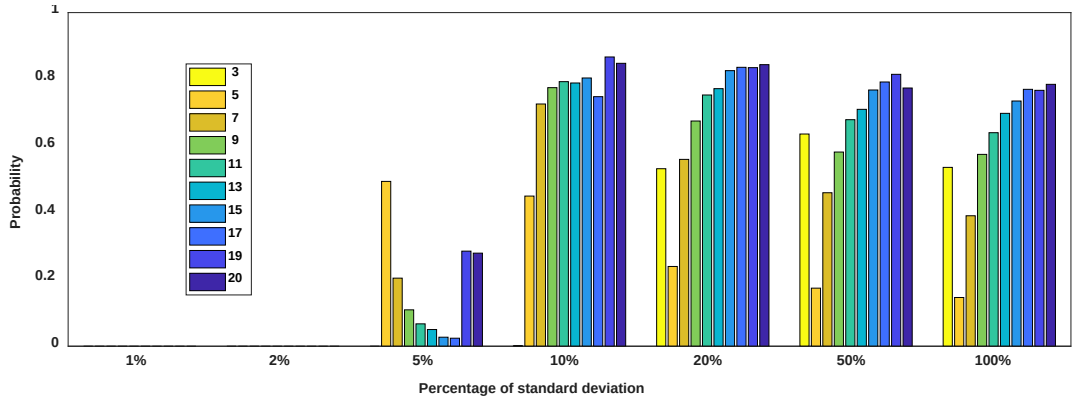

Figure B.9. Probability of passing χ^2-test of Branin function (α = 0.1)

Results for Three-hump Camel function

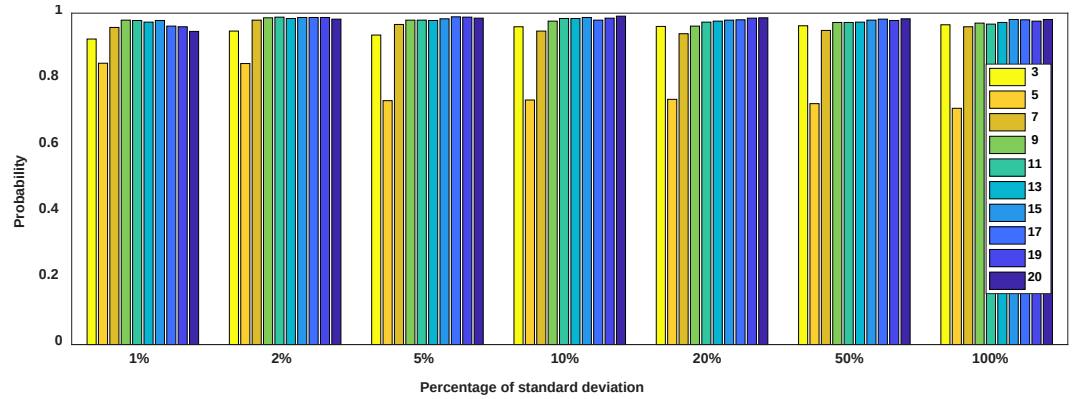

Figure B.10. Probability of passing SW-test (α = 0.01)

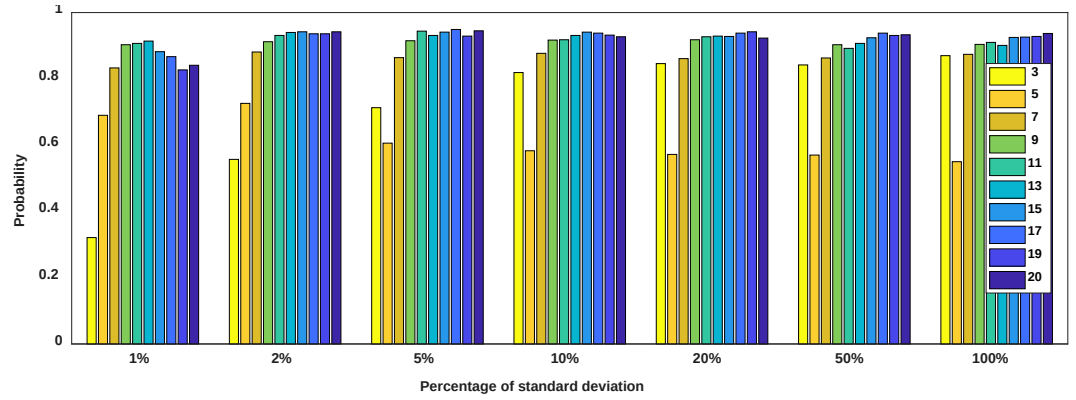

Figure B.11. Probability of passing SW-test (α = 0.05)

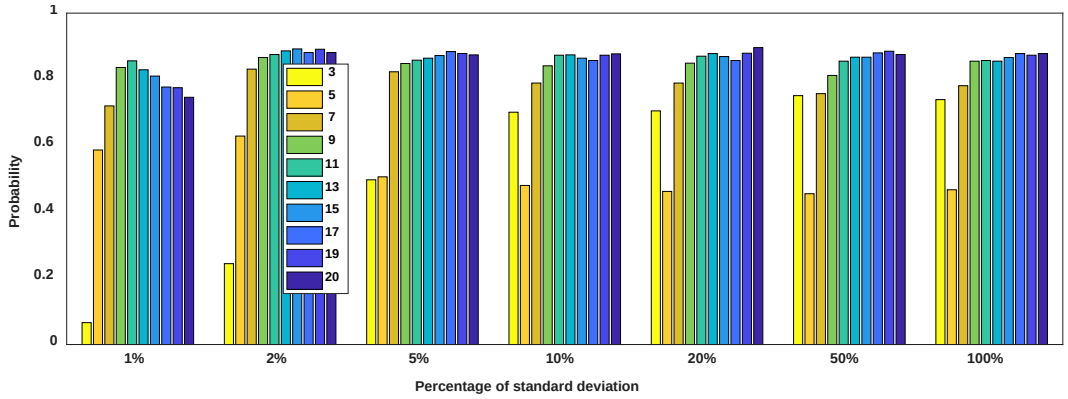

Figure B.12. Probability of passing SW-test (α = 0.1)

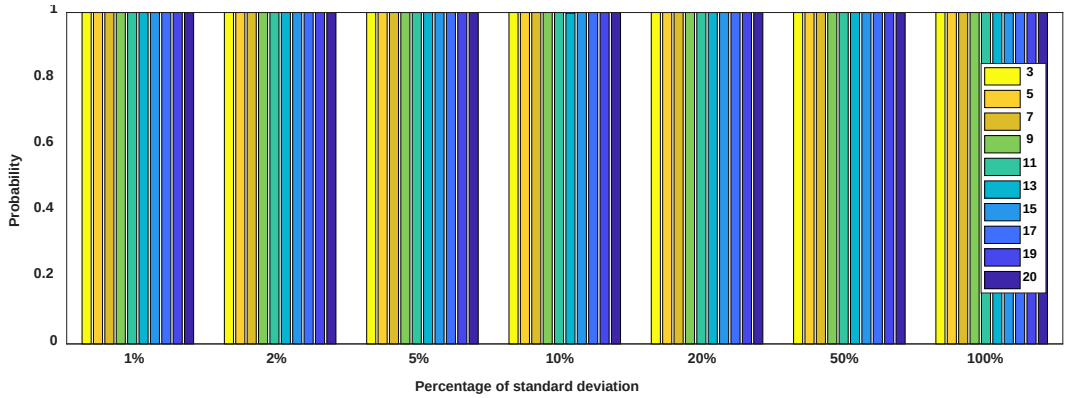

Figure B.13. Probability of passing t-test (α = 0.01)

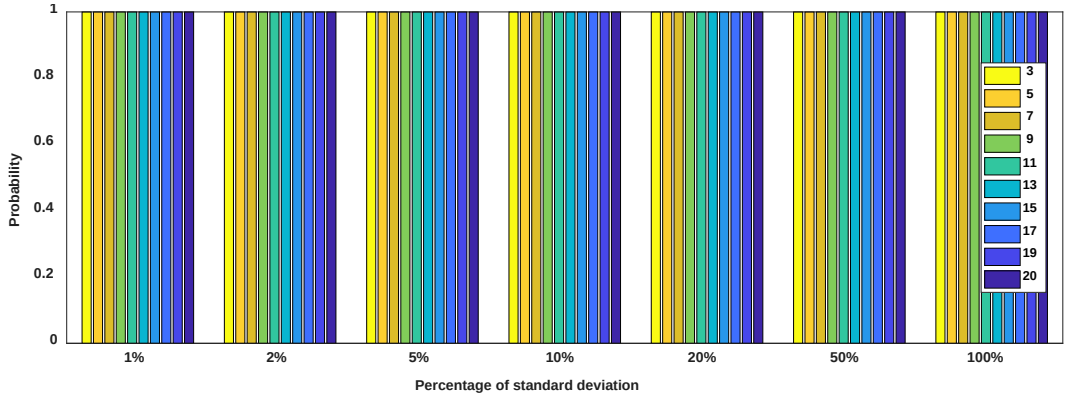

Figure B.14. Probability of passing t-test (α = 0.05)

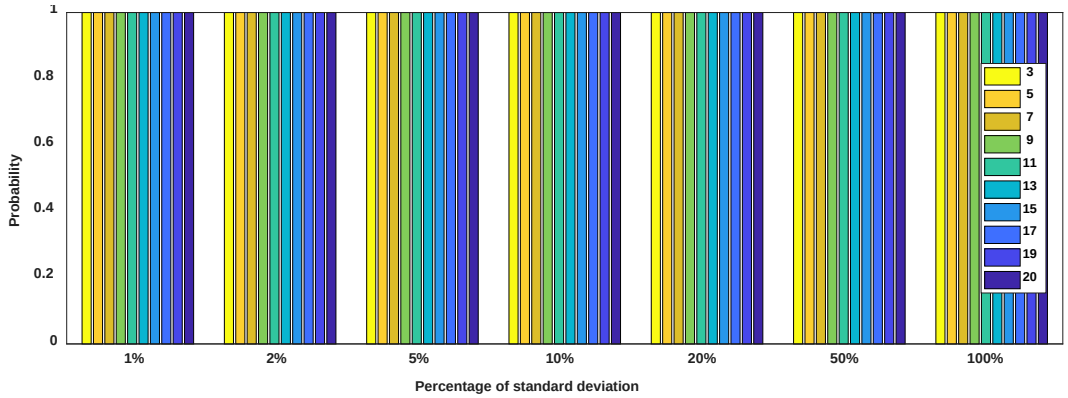

Figure B.15. Probability of passing t-test (α = 0.1)

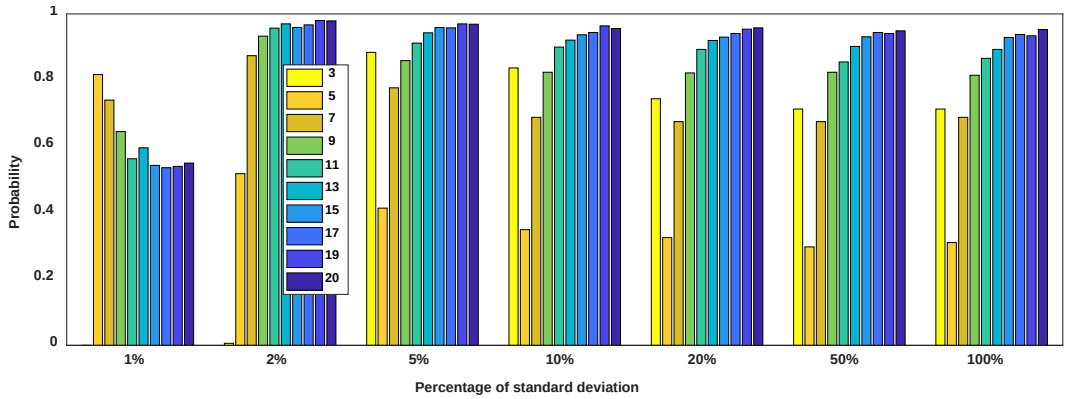

Figure B.16. Probability of passing χ^2-test (α = 0.01)

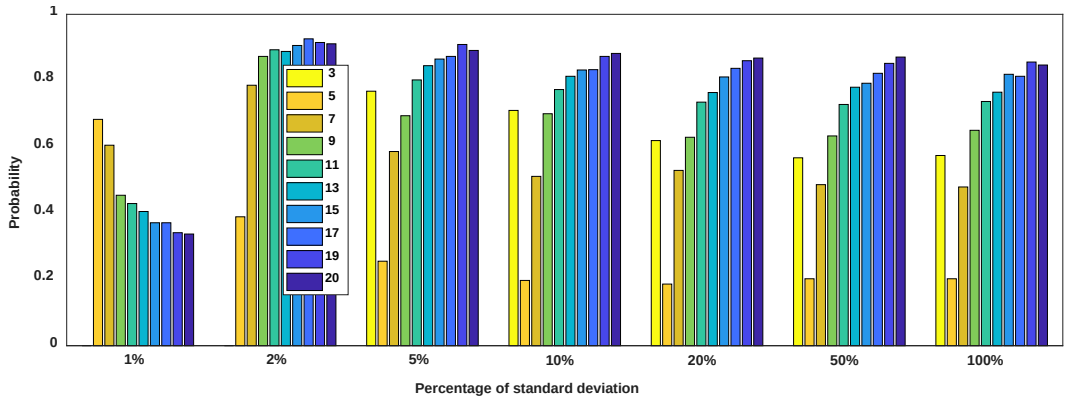

Figure B.17. Probability of passing χ^2-test (α = 0.05)

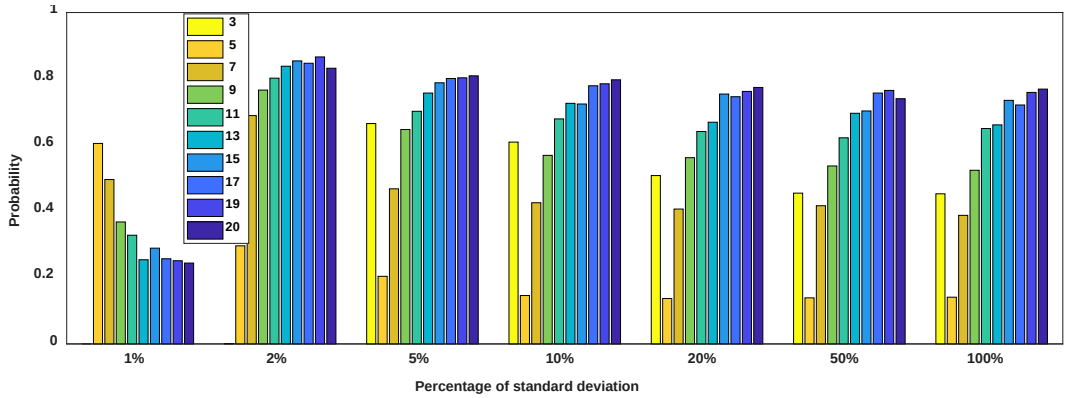

Figure B.18. Probability of passing χ^2-test (α = 0.1)

Results for Friedman function

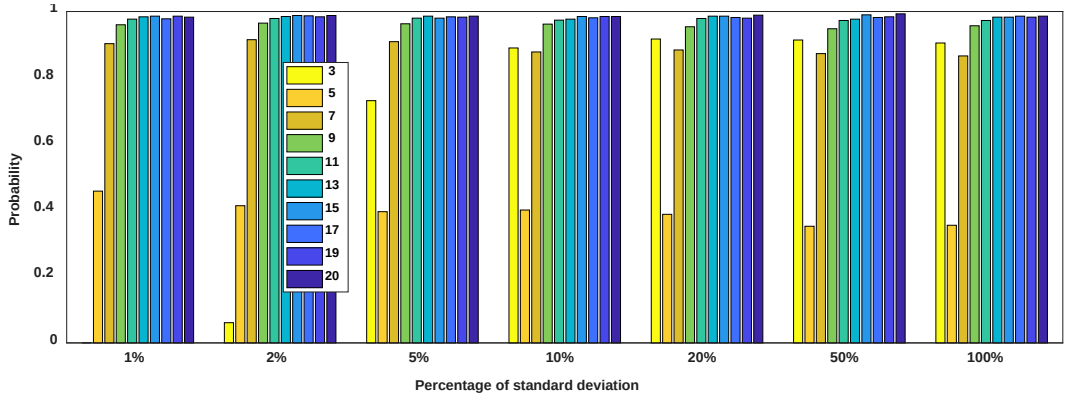

Figure B.19. Probability of passing SW-test (α = 0.01)

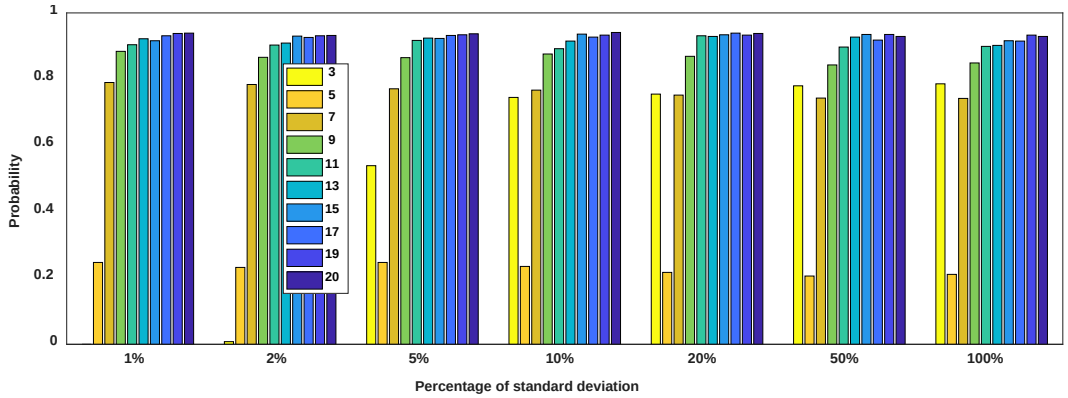

Figure B.20. Probability of passing SW-test (α = 0.05)

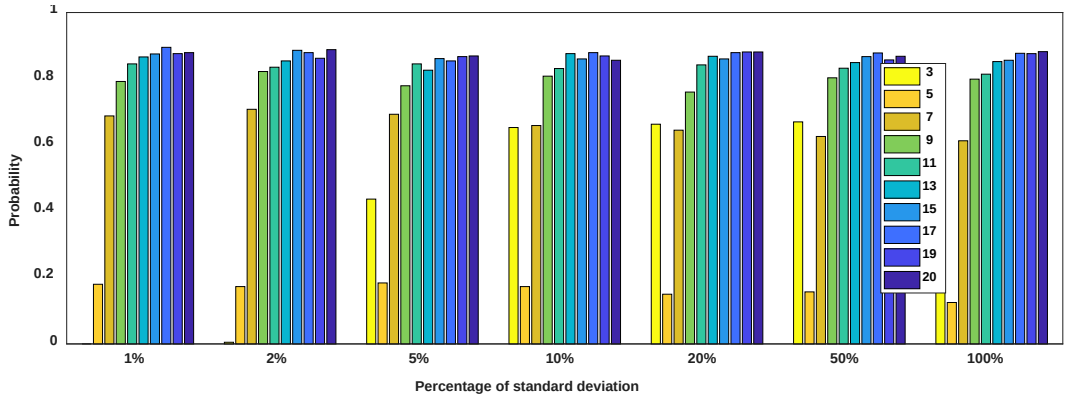

Figure B.21. Probability of passing SW-test (α = 0.1)

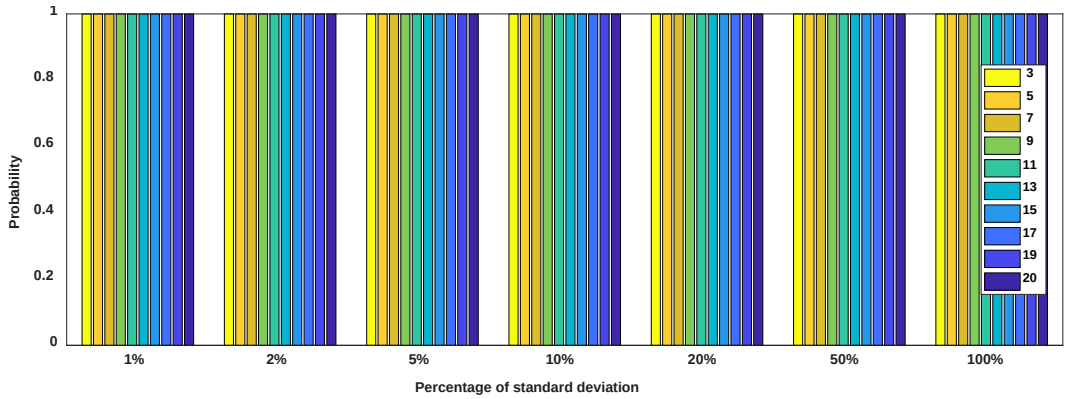

Figure B.22. Probability of passing t-test (α = 0.01)

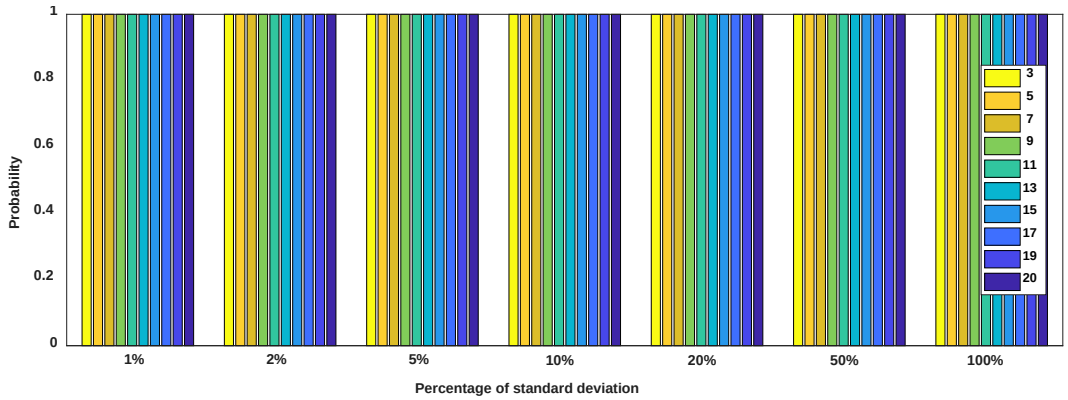

Figure B.23. Probability of passing t-test (α = 0.05)

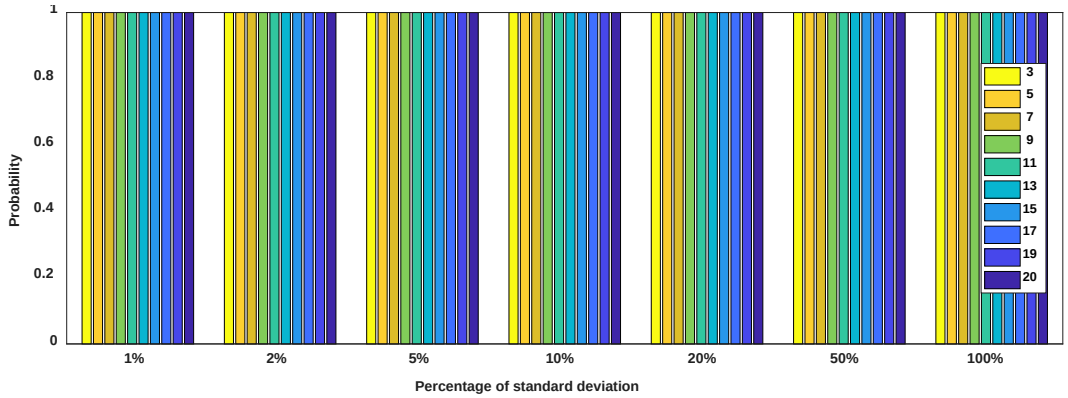

Figure B.24. Probability of passing t-test (α = 0.1)

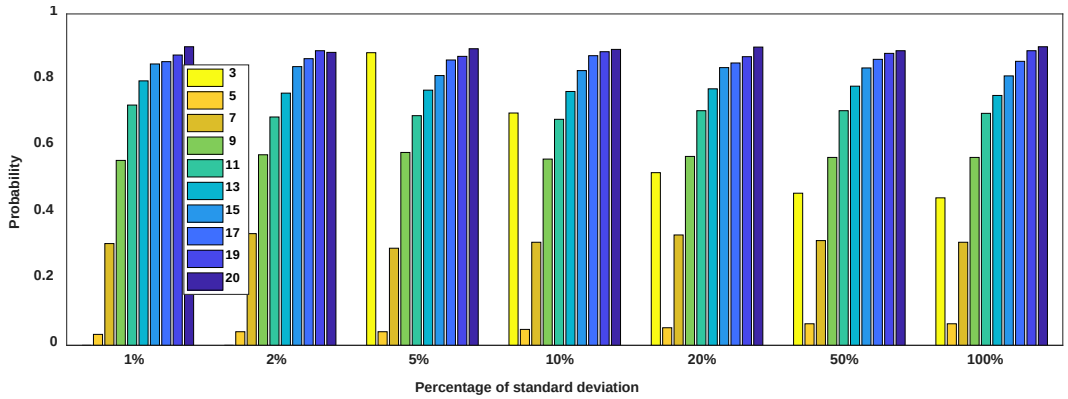

Figure B.25. Probability of passing χ^2-test (α = 0.01)

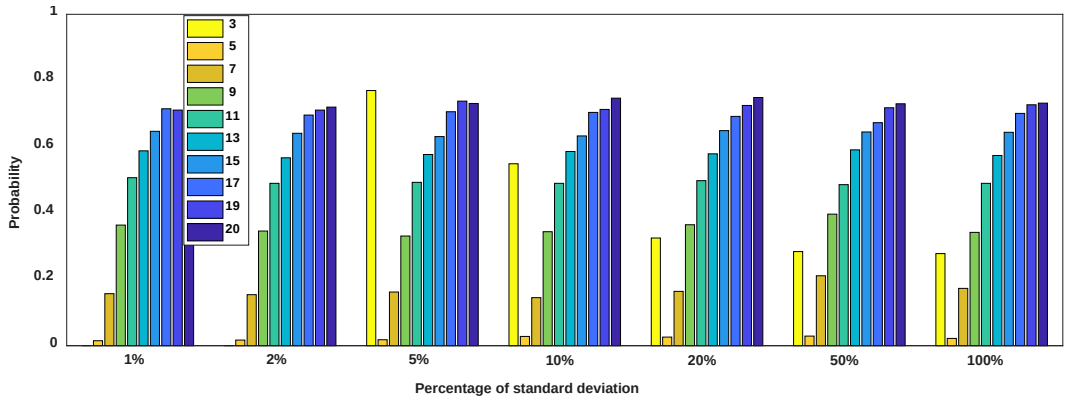

Figure B.26. Probability of passing χ^2-test (α = 0.05)

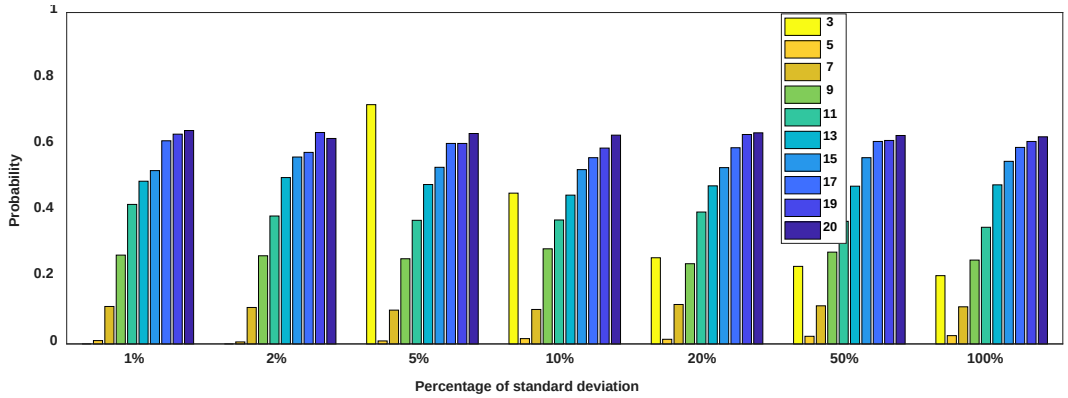

Figure B.27. Probability of passing χ^2-test (α = 0.1)

Results for Dette & Pepelyshev's eight dimension function

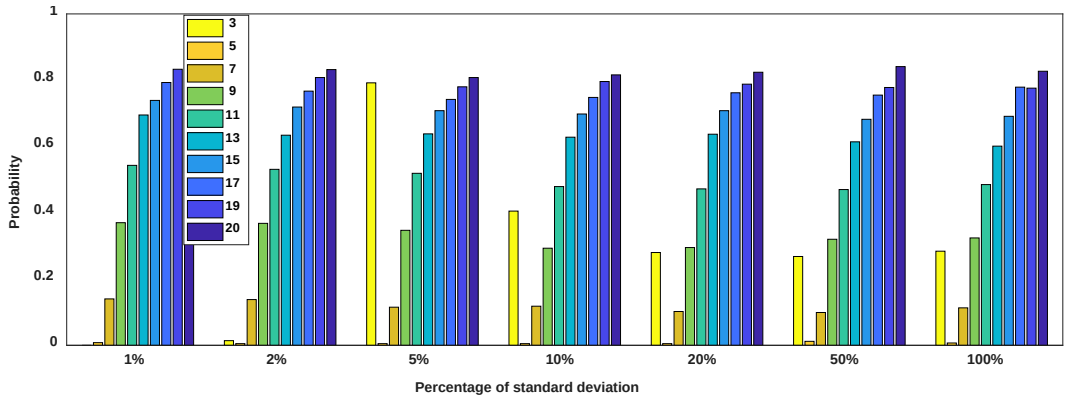

Figure B.28. Probability of passing SW-test (α = 0.01)

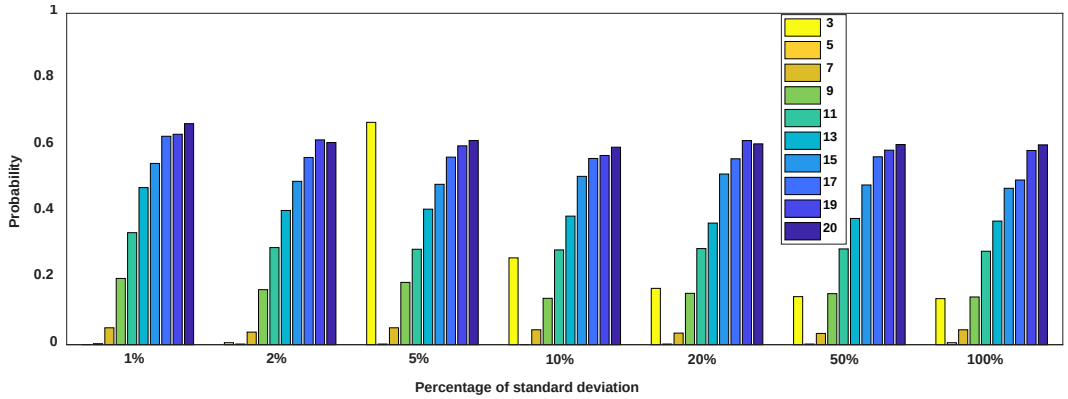

Figure B.29. Probability of passing SW-test (α = 0.05)

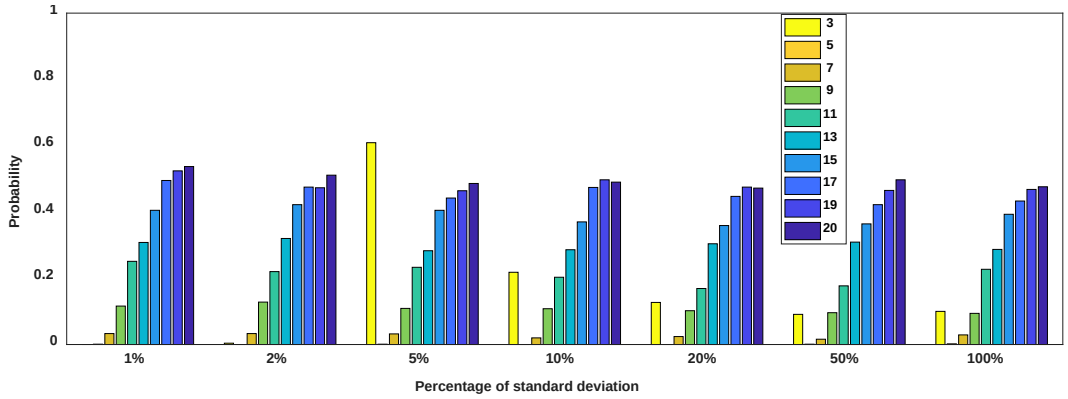

Figure B.30. Probability of passing SW-test (α = 0.1)

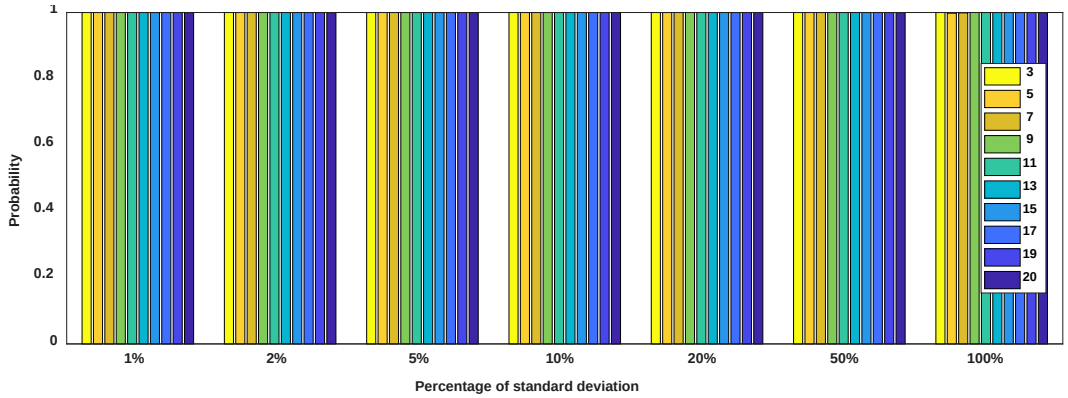

Figure B.31. Probability of passing t-test (α = 0.01)

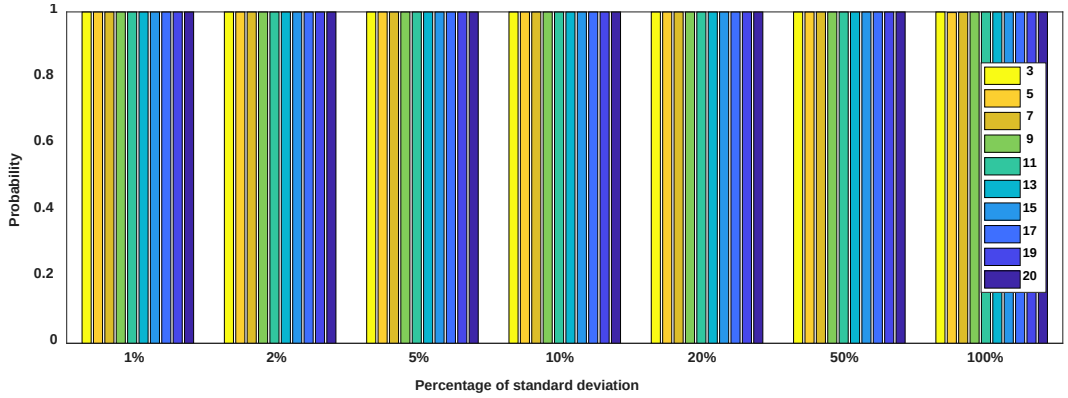

Figure B.32. Probability of passing t-test (α = 0.05)

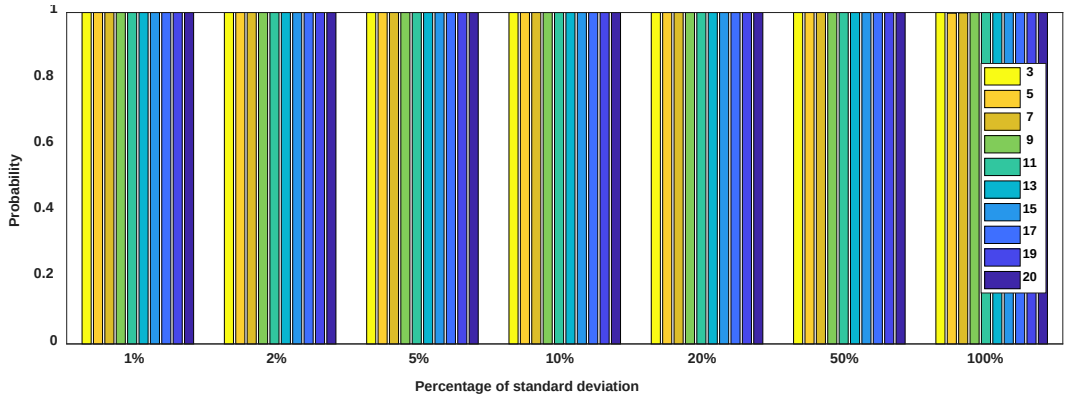

Figure B.33. Probability of passing t-test (α = 0.1)

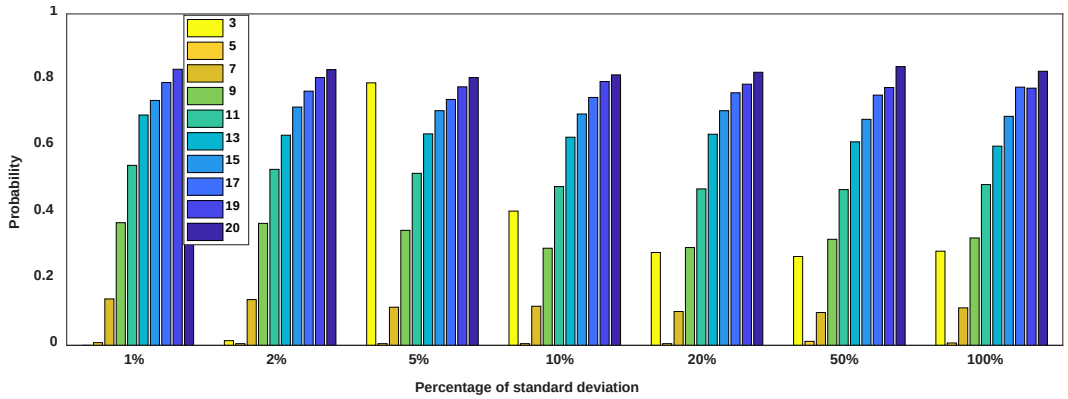

Figure B.34. Probability of passing χ^2-test (α = 0.01)

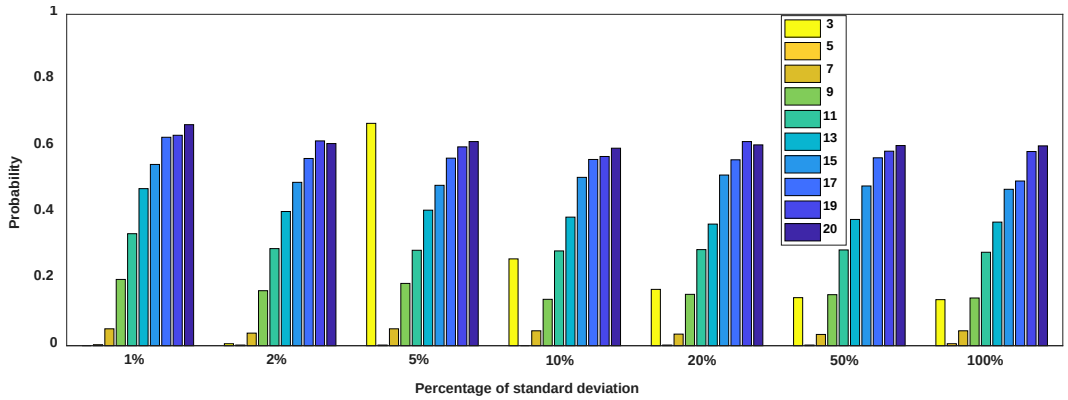

Figure B.35. Probability of passing χ^2-test (α = 0.05)

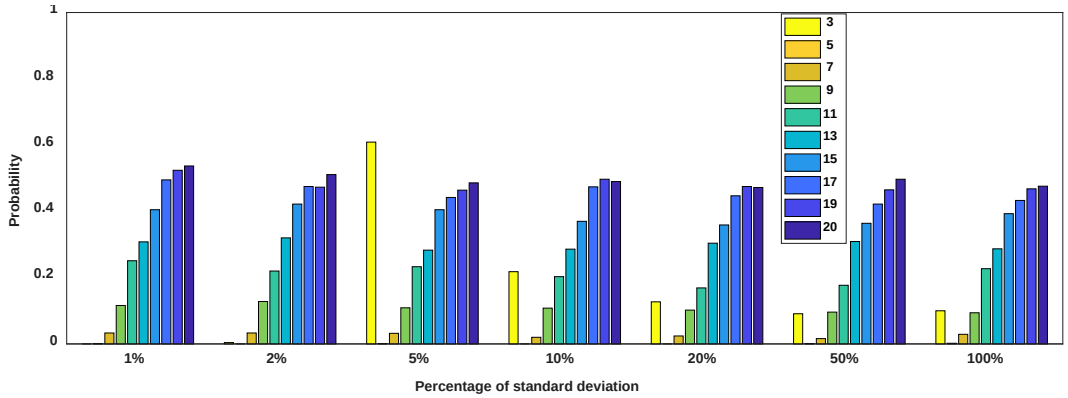

Figure B.36. Probability of passing χ^2-test (α = 0.1)

Results for Piston simulation function

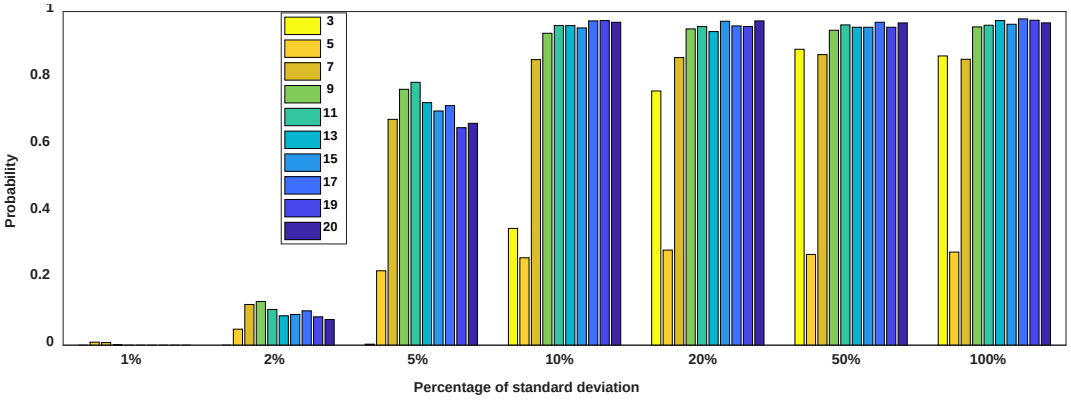

Figure B.37. Probability of passing SW-test (α = 0.01)

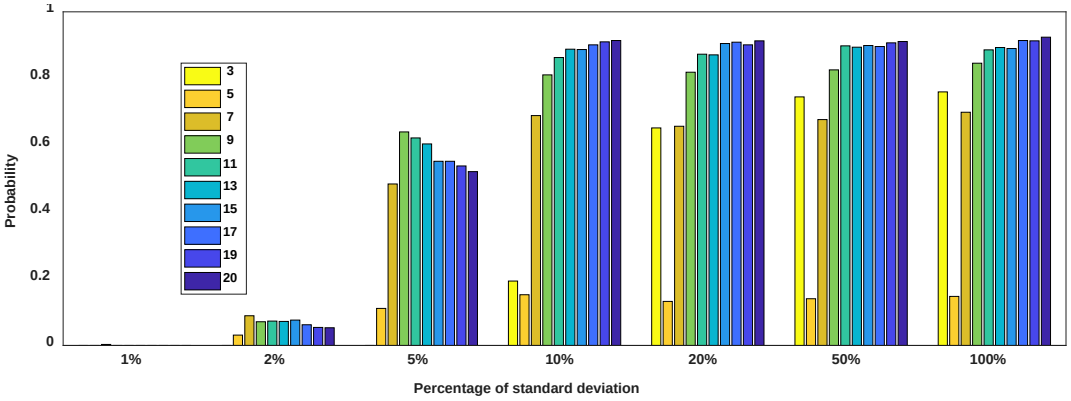

Figure B.38. Probability of passing SW-test (α = 0.05)

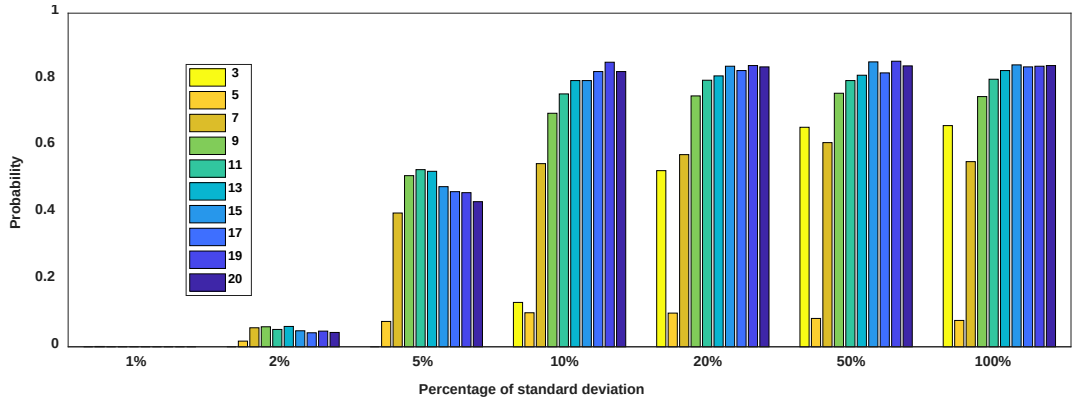

Figure B.39. Probability of passing SW-test (α = 0.1)

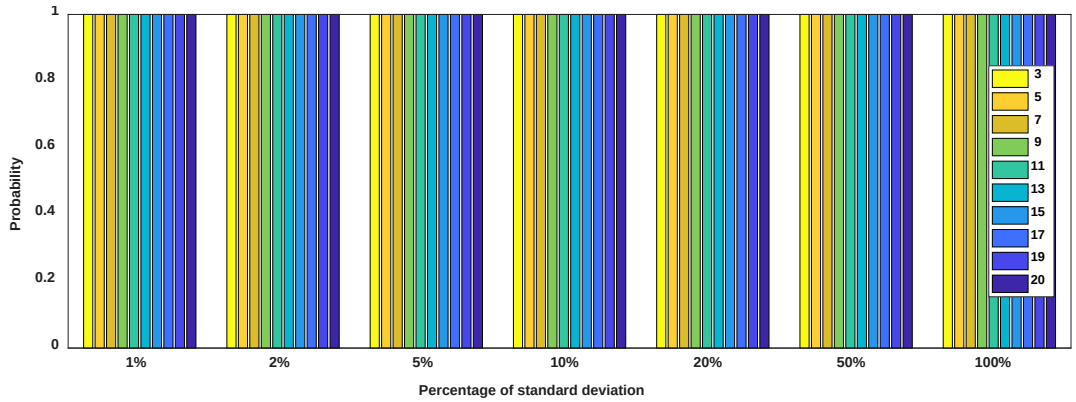

Figure B.40. Probability of passing t-test (α = 0.01)

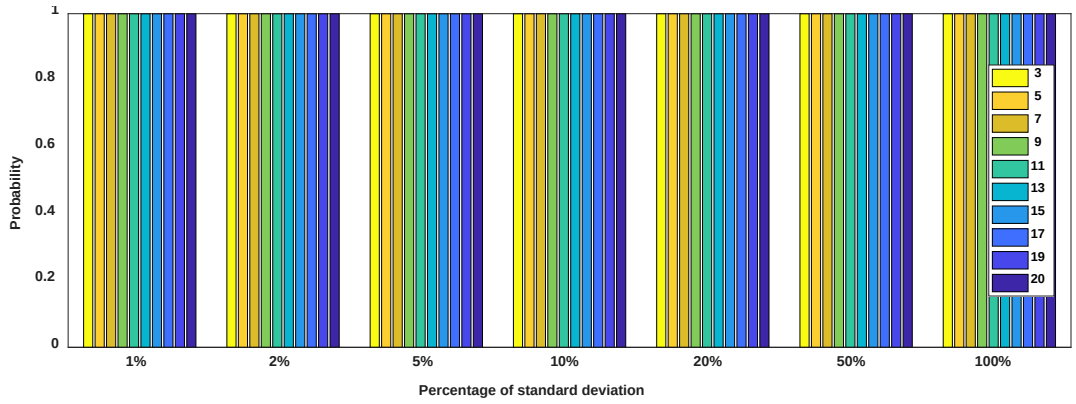

Figure B.41. Probability of passing t-test (α = 0.05)

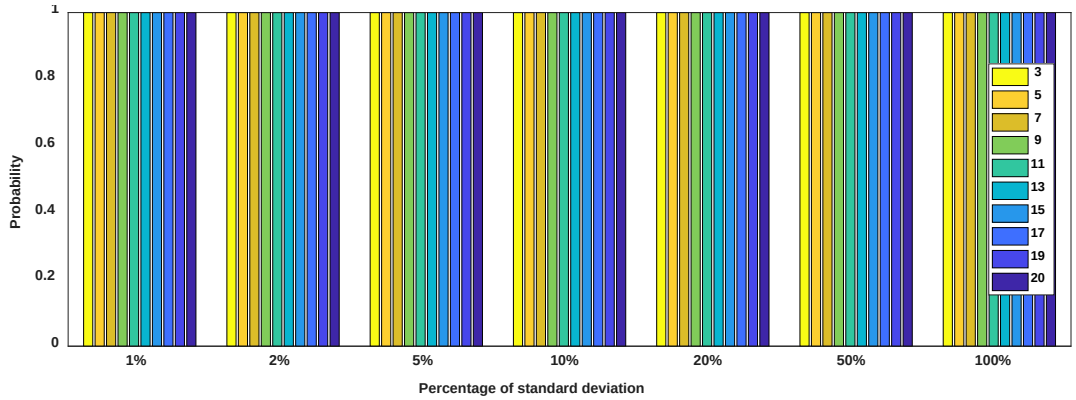

Figure B.42. Probability of passing t-test (α = 0.1)

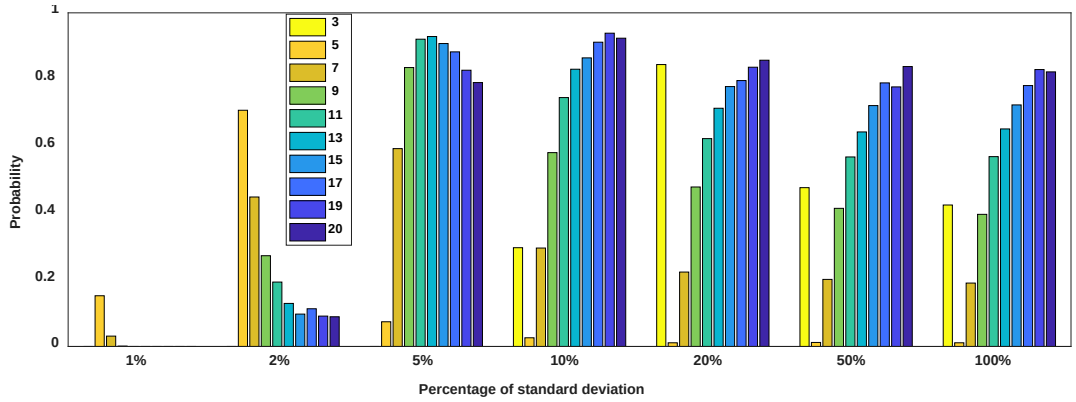

Figure B.43. Probability of passing χ^2-test (α = 0.01)

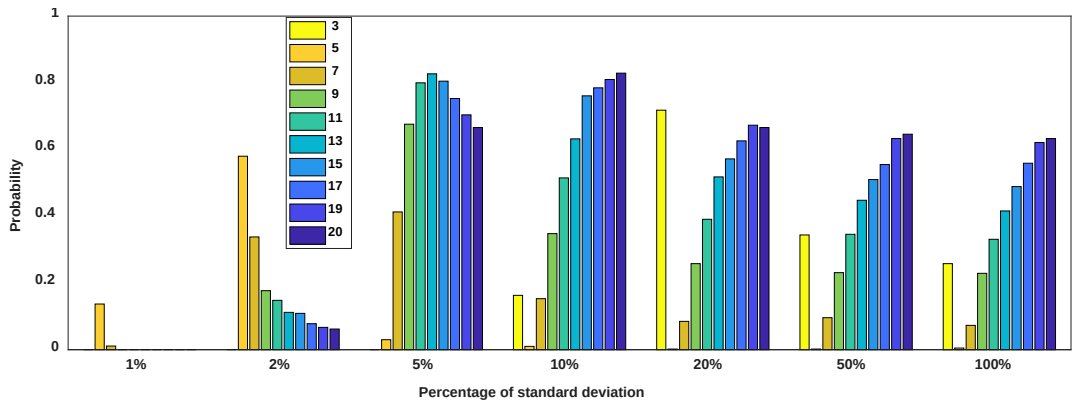

Figure B.44. Probability of passing χ^2-test (α = 0.05)

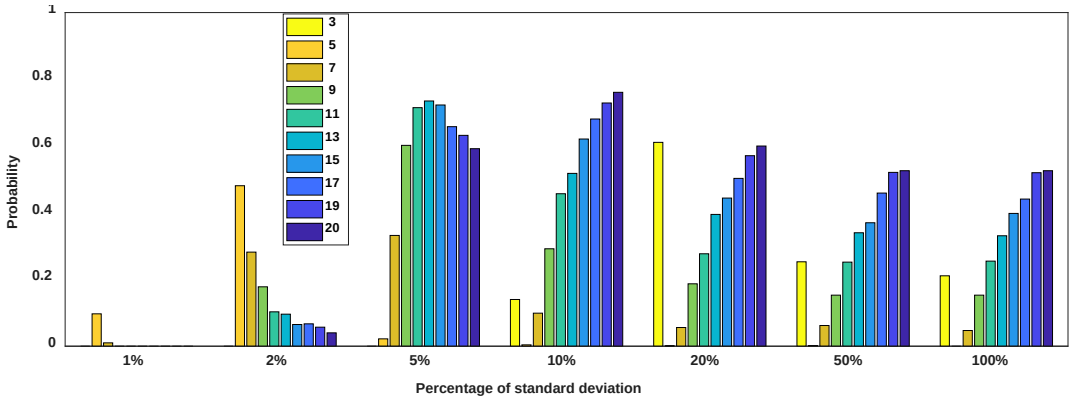

Figure B.45. Probability of passing χ^2-test ($\alpha = 0.1$)

APPENDIX C

Dimensionless Numbers Identified

Table C.1: Dimensionless numbers identified for multiphase flow

#	Dimension	Definition
1	Oh	$\frac{\mu_l}{\sqrt{\sigma d_p \rho_g}}$
2	Ratio of viscosities	$\frac{\mu_l}{\mu_g}$
3	Oh	$\frac{\mu_g}{\sqrt{\sigma d_p \rho_g}}$
4	Ratio of velocities	$\frac{v_g}{v_l}$
5	Mo	$\frac{g\mu_l^4}{\rho_p \sigma^3}$
6	Fr	$\frac{v_g}{\sqrt{Dg}}$
7	Mo	$\frac{g\mu_g^4}{\rho_g \sigma^3}$
8	Oh	$\frac{\mu_l}{\sqrt{\sigma d_p \rho_l}}$
9	Mo	$\frac{g\mu_l^4}{\rho_l \sigma^3}$
10	Mo	$\frac{g\mu_l^4}{\rho_g \sigma^3}$
11	Oh	$\frac{\mu_g}{\sqrt{\sigma d_p \rho_l}}$
12	Oh	$\frac{\mu_l}{\sqrt{\sigma d_p \rho_p}}$
13	Fr	$\frac{v_l}{\sqrt{Dg}}$
14	Ratio of densities	$\frac{\rho_g}{\rho_l}$
15	Oh	$\frac{\mu_g}{\sqrt{\sigma d_p \rho_p}}$
16	Ga	$\frac{d_p^3 \rho_g^2 g}{\mu_l^2}$

(Continued)

#	Dimension	Definition
17	Fr and Ca	$\frac{\mu_g\sqrt{d_p g}}{\sigma}$
18	Ratio of densities	$\frac{\rho_g}{\rho_p}$
19	Fr and Ca	$\frac{\mu_l\sqrt{d_p g}}{\sigma}$
20	Bo	$\frac{g d_p^2 \rho_g}{\sigma}$
21	Ga	$\frac{d_p^3 \rho_l^2 g}{\mu_l^2}$
22	Oh	$\frac{\mu_l}{\sqrt{\sigma D \rho_g}}$
23	Ga	$\frac{d_p^3 \rho_l^2 g}{\mu_g^2}$
24	Ga	$\frac{d_p^3 \rho_g^2 g}{\mu_g^2}$
25	Bo	$\frac{g d_p^2 \rho_l}{\boldsymbol{\sigma}}$
26	Ga	$\frac{d_p^3 \rho_p^2 g}{\mu_l^2}$
27	Oh	$\frac{\mu_g}{\sqrt{\sigma D \rho_g}}$
28	Fr	$\frac{v_g}{\sqrt{d_p g}}$
29	Ga	$\frac{d_p^3 \rho_p^2 g}{\mu_g^2}$
30	Oh	$\frac{\mu_l}{\sqrt{\sigma D \rho_l}}$
31	Bo	$\frac{g d_p^2 \rho_p}{\sigma}$
32	Oh	$\frac{\mu_g}{\sqrt{\sigma D \rho_l}}$

(Continued)

#	Dimension	Definition
33	Oh	$\frac{\mu_l}{\sqrt{\sigma D \rho_p}}$
34	Fr	$\frac{v_l}{\sqrt{d_p g}}$
35	Fr and Re	$\frac{\mu_l g}{\rho_g v_g^3}$
36	Oh	$\frac{\mu_g}{\sqrt{\sigma D \rho_p}}$
37	Fr and Re	$\frac{\mu_g g}{\rho_g v_g^3}$
38	Fr and We	$\frac{g\sigma}{{v_g}^4 \rho_g}$
39	Fr and Re	$\frac{\mu_l g}{\rho_l v_g^3}$
40	Fr and Ca	$\frac{\mu_g \sqrt{Dg}}{\sigma}$
41	Fr and Re	$\frac{\mu_g g}{\rho_l v_g^3}$
42	Fr and Re	$\frac{\mu_l g}{\rho_g v_l^3}$
43	Fr and We	$\frac{g\sigma}{{v_g}^4 \rho_l}$
44	Fr and Re	$\frac{\mu_l g}{\rho_p v_g^3}$
45	Fr and Re	$\frac{\mu_g g}{\rho_g v_l^3}$
46	Fr and Re	$\frac{\mu_g g}{\rho_p v_g^3}$
47	Fr and Ca	$\frac{\mu_l \sqrt{Dg}}{\sigma}$
48	Fr and We	$\frac{g\sigma}{{v_g}^4 \rho_p}$

(Continued)

#	Dimension	Definition
49	Fr and We	$\frac{\boldsymbol{g\sigma}}{\boldsymbol{v_l{}^4\rho_g}}$
50	Fr and Re	$\frac{\mu_l g}{\rho_l v_l^3}$
51	Ca	$\frac{\mu_g V_g}{\sigma}$
52	Fr and Re	$\frac{\mu_g g}{\rho_l v_l^3}$
53	Ratio of diameters	$\frac{d_p}{D}$
54	Fr and We	$\frac{g\sigma}{v_l{}^4\rho_l}$
55	Fr and Re	$\frac{\mu_l g}{\rho_p v_l^3}$
56	Fr and Re	$\frac{\mu_g g}{\rho_p v_l^3}$
57	Fr and We	$\frac{g\sigma}{v_l{}^4\rho_p}$
58	Ca	$\frac{\mu_l V_g}{\sigma}$
59	We	$\frac{d_p\rho_g V_g^2}{\sigma}$
60	Ca	$\frac{\mu_g V_l}{\sigma}$
61	Re	$\frac{\mu_l}{d_p\rho_g v_g}$
62	Ca	$\frac{\mu_l V_l}{\sigma}$
63	Re	$\frac{\mu_g}{d_p\rho_g v_g}$
64	We	$\frac{d_p\rho_g V_l^2}{\sigma}$

(Continued)

#	Dimension	Definition
65	We	$\frac{d_p \rho_l V_g^2}{\sigma}$
66	Re	$\frac{\mu_l}{d_p \rho_g v_l}$
67	We	$\frac{d_p \rho_p V_g^2}{\sigma}$
68	Re	$\frac{\mu_g}{d_p \rho_g v_l}$
69	We	$\frac{d_p \rho_l V_l^2}{\sigma}$
70	Ga	$\frac{D^3 \rho_g^2 g}{\mu_l^2}$
71	Re	$\frac{\mu_l}{d_p \rho_l v_g}$
72	Ga	$\frac{D^3 \rho_g^2 g}{\mu_g^2}$
73	We	$\frac{d_p \rho_p V_l^2}{\sigma}$
74	Re	$\frac{\mu_g}{d_p \rho_l v_g}$
75	Re	$\frac{\mu_l}{d_p \rho_l v_l}$
76	Bo	$\frac{g D^2 \rho_g}{\sigma}$
77	Ga	$\frac{D^3 \rho_l^2 g}{\mu_l^2}$
78	Re	$\frac{\mu_l}{d_p \rho_p v_g}$
79	Re	$\frac{\mu_g}{d_p \rho_l v_l}$
80	Ga	$\frac{D^3 \rho_l^2 g}{\mu_g^2}$

(Continued)

#	Dimension	Definition
81	Re	$\frac{\mu_g}{d_p \rho_p v_g}$
82	We	$\frac{D \rho_g V_g^2}{\sigma}$
83	Bo	$\frac{g D^2 \rho_l}{\sigma}$
84	Ga	$\frac{D^3 \rho_p^2 g}{\mu_l^2}$
85	Re	$\frac{\mu_l}{d_p \rho_p v_l}$
86	Ga	$\frac{D^3 \rho_p^2 g}{\mu_g^2}$
87	Bo	$\frac{g D^2 \rho_p}{\sigma}$
88	Re	$\frac{\mu_g}{d_p \rho_p v_l}$
89	We	$\frac{D \rho_g V_l^2}{\sigma}$
90	We	$\frac{D \rho_l V_g^2}{\sigma}$
91	We	$\frac{D \rho_p V_g^2}{\sigma}$
92	We	$\frac{D \rho_l V_l^2}{\sigma}$
93	We	$\frac{D \rho_p V_l^2}{\sigma}$
94	Re	$\frac{\mu_l}{D \rho_g v_g}$
95	Re	$\frac{\mu_g}{D \rho_g v_g}$
96	Re	$\frac{\mu_l}{D \rho_g v_l}$

(Continued)

#	Dimension	Definition
97	Re	$\frac{\mu_g}{D\rho_g v_l}$
98	Re	$\frac{\mu_l}{D\rho_l v_g}$
99	Re	$\frac{\mu_g}{D\rho_l v_g}$
100	Re	$\frac{\mu_l}{D\rho_l v_l}$
101	Re	$\frac{\mu_l}{D\rho_p v_g}$
102	Re	$\frac{\mu_g}{D\rho_l v_l}$
103	Re	$\frac{\mu_g}{D\rho_p v_g}$
104	Re	$\frac{\mu_l}{D\rho_p v_l}$
105	Re	$\frac{\mu_g}{D\rho_p v_l}$

Table C.2: Dimensionless numbers identified for gas only flow

#	Dimension	Definition
1	Fr	$\frac{v_g}{\sqrt{Dg}}$
2	Ratio of densities	$\frac{\rho_P}{\rho_g}$
3	Ga	$\frac{d_p^3 \rho_g^2 g}{\mu_g^2}$
4	Fr	$\frac{v_g}{\sqrt{d_p g}}$
5	Ga	$\frac{d_p^3 \rho_p^2 g}{\mu_g^2}$
6	Fr and Re	$\frac{\mu_g g}{\rho_g v_g^3}$
7	Ratio of diameters	$\frac{d_p}{D}$
8	Fr and Re	$\frac{\mu_g g}{\rho_p v_g^3}$
9	Re	$\frac{\mu_g}{d_p \rho_g v_g}$
10	Ga	$\frac{D^3 \rho_g^2 g}{\mu_g^2}$
11	Ga	$\frac{D^3 \rho_p^2 g}{\mu_g^2}$
12	Re	$\frac{\mu_g}{d_p \rho_p v_g}$
13	Re	$\frac{\mu_g}{D \rho_g v_g}$
14	Re	$\frac{\mu_g}{D \rho_p v_g}$

Table C.3: Dimensionless numbers identified for liquid only flow

#	Dimension	Definition
1	Fr	$\frac{v_l}{\sqrt{Dg}}$
2	Ga	$\frac{d_p^3 \rho_l^2 g}{\mu_l^2}$
3	Fr	$\frac{v_l}{\sqrt{d_p g}}$
4	Fr and Re	$\frac{\mu_l g}{\rho_l v_l^3}$
5	Ratio of diameter	$\frac{d_p}{D}$
6	Re	$\frac{\mu_l}{d_p \rho_l v_l}$
7	Ga	$\frac{D^3 \rho_l^2 g}{\mu_l^2}$
8	Re	$\frac{\mu_l}{D \rho_l v_l}$